Electrochemical Surface-Enhanced Raman Spectroscopy
Used In The Characterization of Langmuir Blodgett/Langmuir
Schaefer Biomimetic Membranes

By
Soraya Timica Merchant

A Thesis Submitted to
Saint Mary's University, Halifax, Nova
Scotia in Partial Fulfillment of the
Requirements for the Degree of Master of
Science in Applied Science.

June, 2014, Halifax, Nova Scotia

Approved: Dr. Christa Brosseau
Associate professor
Supervisor

Approved: Dr. Colleen Barber
Professor
Committee member

Approved: Dr. Marc Lamoureux
Associate professor
Committee member

Approved: Dr. Maria-Victoria Meli
Associate professor
External examiner

Date: June 24th 2014

Table of contents

1 Introduction

1.1 Alzheimer's Disease

2 Literature Review

2.2 Properties of cell membranes

2.6 Electrochemical and spectroscopic methods for the characterization of cell membranes

3 Theory

3.3 Raman spectroscopy

Electrochemical Surface-Enhanced Raman Spectroscopy Used In The

Characterization of Langmuir Blodgett/Langmuir Schaefer Biomimetic Membranes

By Soraya Merchant

Abstract

June 24th 2014

In recent years, the classification of Alzheimer's Disease (AD) as a pore-forming disease has been a highly debated topic. It has been postulated that aggregated species, such as amyloid beta (Aβ), derived from a transmembrane protein in neurons, known as amyloid precursor protein (APP), interacts with cell membranes to give toxic effects. One postulated theory suggests that aggregate insertion into cell membranes form non- specific channels that cause a loss of cellular homeostasis. In this investigation, the aim is to produce a defect-free biomimetic model membrane that can be used in future work to validate the AD amyloid pore-hypothesis. The model consists of the deposition of a lipid bilayer by the Langmuir-Blodgett/Langmuir-Schaefer (LB-LS) method onto an electrode surface consisting of silver colloids thus affording the use of the non-invasive, sensitive method of Surface-Enhanced Raman Spectroscopy (SERS). By coupling SERS with electrochemistry (EC-SERS), the membrane properties and quality were monitored.

Acknowledgements

This thesis is dedicated to the persons who have supported, guided and motivated me throughout my life endeavors. Firstly, I would like to thank God for his bounteous blessings and my faith grows deeper every day. My deceased father, Mr. Lesroy Merchant an educator in his own right, has instilled in me that good moral, a sound education, humility, and love is the key to a fulfilled life. My mother, Mrs. Maygwen Merchant, who taught me about balancing life activities, organizational skills, and prioritizing has given me the basic tools for managing or succeeding at any task set before me. To my sister, Miss Janel Merchant, the rest of my family, and close friends, I am indebted to your never failing love and encouragement. My passion for Chemistry came from the educators throughout my academic life that inspired or mentored me. They include Mr. Morrison Burn, my high school teacher; Dr. Kathy Singfield, my university professor; and Dr. Christa Brosseau, my supervisor. Special recognition must be given to the members of my supervisory committee, Dr. Marc Lamoureux and Dr. Colleen Barber, for their direction and assistance. Also I would like to thank Sasha Power for her contributions to the initial Langmuir Blodgett/Langmuir Schaefer experiments which has been a building block to this research project. Finally yet most importantly, to my better half, Bjorn Carr, a sincere thanks for your love, for believing in me even when I lacked the confidence to do so, and firmly standing by me through my difficult times.

List of tables and figures

Figures

List of tables

List of symbols and abbreviations

Δ	change
γ	surface tension
ε_o	permittivity of free space
Π	surface pressure
ρ	density
Ψ	electrical potential
1-ODT	1-octadecanethiol
6-MHA	6-mercaptohexanoic acid
12-MDA	12- mercaptododecanoic acid
A	area
AD	Alzheimer's disease
AFM	atomic force microscopy
AgNP	silver nanoparticle
alpha HL	alpha-hemolysin
APP	amyloid precursor protein
ATP	adenosine triphosphate
$A\beta$	amyloid beta
C	capacitance
c	concentration of analyte
CCB	calcium channel blocker
CCD	charged-coupled device
CE	chemical enhancement

CE	counter electrode
cosθ	contact angle
CV	cyclic voltammetry
d	distance
dAMP	2´-Deoxyadenosine 5´-phosphate
DC	differential capacitance
DMPC	1,2-Dimyristoyl-*sn*-glycero-3-phosphocholine
DOPC	1,2-dioleoyl-*sn*-glycero-3-phosphocholine
DPPC	1,2-dipalmitoyl-*sn*-glycero-3-phosphocholine
EC-SERS	electrochemical surface-enhanced raman spectroscopy
EM	electromagnetic
EM	electron microscopy
F	Faraday's constant
F	force
FRAP	fluorescence recovery after photobleaching
FSB	floating supported bilayers
G	gauche
G	Gibbs free energy
g	gravity
Glu	glutamine
h	height
h-BLM	hybrid bilayer lipid membrane
I	current

IHP	inner Helmholtz plane
IR	infrared spectroscopy
IRRAS	infrared reflection adsorption spectroscopy
k	relative permittivity of a material
LB	Langmuir-Blodgett
LB-LS	Langmuir- Blodgett/Langmuir-Schaefer
L-C	liquid-condensed phase
L_d	liquid-disordered state
L-E	liquid-expanded phase
LS	Langmuir Schaefer
LSPR	localized surface plasmon resonance
n	number of electrons
NP	nanoparticle
OCP	open circuit potential
OHP	outer Helmholtz plane
PM-IRRAS	polarization modulation infrared reflection adsorption spectroscopy
pzc	potential of zero charge
R	gas constant
RE	reference electrode
RH	relative humidity
SAM	self-assembled monolayer
s-BLM	supported bilayer lipid membrane
SCE	saturated calomel electrode
SECM	scanning electrochemical microscopy

SEIRS	surface enhanced infrared absorption spectroscopy
SERS	surface-enhanced raman spectroscopy
SHE	standard hydrogen electrode
S_o	solid-ordered state
SPM	scanning probe microscopy
SSCE	silver/silver chloride electrode
STM	scanning tunneling microscopy
T	temperature
t	thickness
T	trans
t-BLM	tethered bilayer lipid membrane
T_m	transition temperature
trp	tryptophan
v	stretching vibration
v_{as}	asymmetric stretching
VDPS	variable dynamic point sample
v_s	symmetric stretching
w	width
WE	working electrode
XPS	x-ray photoelectron spectroscopy
Z	charge on migrating species

Introduction

1.1 Alzheimer's Disease

1.1.1 Definition and impact on society

Alzheimer's Disease (AD) is a progressive illness that has been classified both as a form of dementia and a type of protein-misfolding disorder.[1,2] AD falls under the broad heading of dementia because it results in a decline in mental stability.[1] Symptoms of AD include but are not limited to a reduction in the following: memory, communication, language, ability to focus, reasoning, judgement, ability to learn new information and visual perception.[1,2] As AD progresses, a patient's physical health deteriorates due to a decline in physical activities as a result of decreased brain function. In the late stages of AD, patients are unable to feed and dress themselves, control their bladder or bowel functions, and require assistance for most everyday tasks. The reduction in bodily function, mental stability, and physical activity eventually weakens the immune system of AD patients, and therefore AD patients are more susceptible to infections. The main cause of death among AD patients is pneumonia.[1,2]

The classification of AD as a protein-misfolding disease stems from early research where the microscopic view of an AD patient`s brain cells showed discrete insoluble structures outside dead neurons which were termed senile plaques and neurofribrillary tangles.[3,4,5] These misfolded fragments are derived from the proteolytic cleavage of a transmembrane protein, amyloid precursor protein (APP) by specific enzymes.[3] There are two ways in which APP can

be cleaved but only one pathway produces the specific AD fragments.[3] One pathway involves APP being cleaved in the extracellular matrix by an enzyme called α-secretase; this is referred to as the non- amyloidogenic pathway. The other pathway involves the sequential cleavage of APP, first by β-secretase in the extracelluar matrix followed by interior membrane cleavage by γ-secretase. This particular pathway is referred to as the amyloidogenic pathway; it results in the formation of the senile plaques consisting of peptides, typically 37-49 units in length, called amyloid beta (Aβ). In addition, this pathway results in neurofribrillary tangles which consist of hyperphosphorylated tau protein. Figure 1 is a simplified illustration of the two possibile pathways for cleavage of APP.[3]
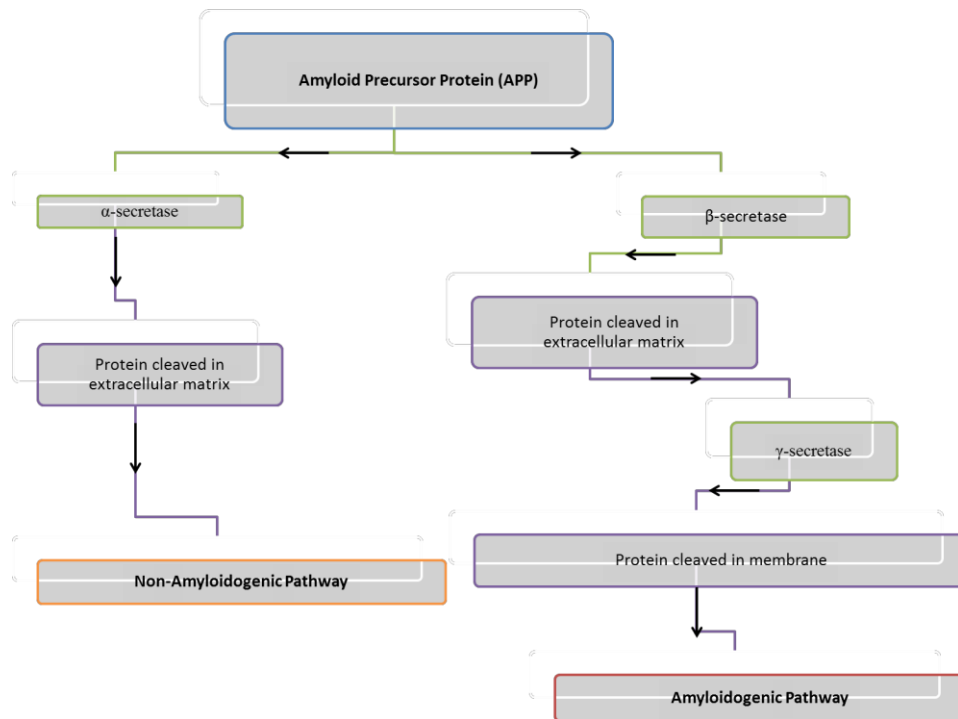
Figure 1: A flow chart illustration adapted from Nunan (2000) showing the two possible pathways for APP proteolytic cleavage. Only one pathway, the amyloidogenic pathway produces the aggregates believed to cause toxic effects in Alzheimer's disease.[3]

The growing awareness of AD is due to the increased social and economic burdens on developed nations due to the rising numbers of persons affected by this disease.[6] A 2012 Alzheimer Society of Canada study showed that as of that year over 700,000 Canadians were diagnosed with a cognitive impairment such as AD.[7] This figure is estimated to double to 1.4 million by the year 2031.[7] The report calculated that the total healthcare cost of dementia in Canada was CD$33 billion per year and this figure is estimated to rise to CD$293 billion by 2040.[7] A more recent study done in 2014 by the Alzheimer Society of Canada showed that 747,000 Canadians are presently diagnosed with AD but this figure is expected to be higher since 50% of Canadians wait too long for the appropriate medical assessment and diagnosis.[7] In March 2013 the Alzheimer`s Association of the United States of America stated that cases of AD increased by 68% between 2000 and 2010, and that presently approximately 5 million Americans are living with AD.[8] In addition, the total estimated direct cost of caring for persons with AD amounted to US $203 billion in 2013. This cost was divided into the categories of medical aid (US$35 billion), medical care (US$107 billion), out-of-pocket expenses (US$34 billion), and other costs (US$27 billion).[8] The total estimated cost of caring for persons with AD in the United States of America has now risen to US $214 billion.[8] The social burdens of AD on the family unit include the emotional strain of persons taking care of a family member with AD (referred to as unpaid caregivers), the adjustment or change of the family structure and day-to-day activities required to provide adequate support for the affected person, and the personal frustration or depression of the AD patient.[9] In some instances, family members reduce their hours of work or leave their jobs to provide personal homecare for AD family members.[10]

Developed countries such as Canada, the United States of America, and Western Europe face their own social burdens due to rising numbers of AD cases.[6] The following modifications are presently made by developed countries to cope with the demands of AD: a) establishing dedicated care facilities with specific educational and coping strategies for families who require additional assistance, b) attracting, training and retaning caregivers to staff such facilities, and c) providing programs designed to reduce the psychological and physical stress of caregivers.[6,11] Thus, the demographics and social structure of a country can be altered when a significant portion of the population is diagnosed with AD and another significant portion of the population is tasked to care for AD patients.[9]

1.1.2 Theories of origin, toxicity and membrane interaction

Hensley and his research group infer that AD is related to one or all of the following three theories based on amyloid toxicity: (1) oxidative stress, (2) Aβ misfolding and fibrillization and (3) innate immune system failure.[12] The oxidative stress theory involves the interaction of free radicals present in the body with cell membranes leading to protein oxidization and lipid peroxidation, resulting in a loss of cellular homeostasis. The Aβ misfolding and fibrillization theory postulates that the formation of insoluble misfolded proteins somehow leads to the death of neurons. Evidence to support this theory lies in the fact that healthy neurons do not possess Aβ aggregates in their direct extracellular medium while dead neurons do. Finally, the immune system failure theory suggests that since misfolded proteins are a natural occurrence in the body, and there exists a clearing mechanism for such structures, the accumulation of these

species is a result of a failure in this clearing mechanism.[12]

Presently researchers believe that the more plausible and valid origin for AD is related to the Aβ misfolding-fibrillization theory and therefore in this thesis emphasis was placed on this theory. [13-15] This assumptions is referred to as the "amyloid pore-hypothesis" which proposes that the interaction of Aβ aggregates with membranes leads to membrane insertion of the Aβ aggregates and the formation of channels, pores or defects, which allow unregulated passage of ions.[16,17] The resulting chemical imbalance in the intracellular medium results in cell toxicity.[16] The amyloid pore-hypothesis came about via two main observations. First was the change in conductance across lipid bilayers after being exposed to Aβ aggregates.[18,19] An influx of Ca^{2+} ions was observed in the intracelluar medium of exposed cell membranes and thus it was deduced that channels were likely created in the bilayer structures.[20] The second observation was derived from microscopic images showing that pore-like structures formed on the surface of cell membranes when exposed to Aβ aggregates.[21] Soluble prefibrillar (intermediate) Aβ aggregates possessing anti-parallel β-sheet structure were deemed the most toxic species.[22,23] Experimental trials comparing Aβ aggregates with toxic pore-forming bacterial peptides possessing β-sheet structure (i.e. alpha-hemolysin; alpha HL) showed similar spherical arrangements on cell membranes.[24,25] It was then hypothesized that since these prefibrillar aggregates have similar β-sheet structures and similar arrangements on cell membranes to alpha HL, the most likely route to exerting toxicity lies within the creation of

pores in cell membranes.[24,25]   Figure 2, taken from the work by Lashuel and associates, shows the circular structures formed by mutated proteins derived from APP for AD and α-synuclein for Parkinson's Disease, another protein-folding disorder.[26]

Each square is 30.5 nm x 30.5 nm
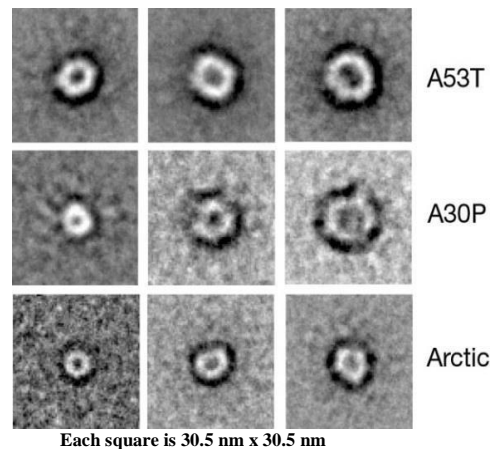
Reprinted by permission from Macmillan Publishers Ltd: Nature, Lashuel, H. et al, *Amyloid pores from pathogenic mutation*, copyright 2002

Figure 2: Image showing digitized electron micrographs of circular pore- like structures formed from: Artic-aggregates derived from mutated APP; AD, A30P and A53T-aggregates derived from mutated α-synuclein; Parkinson's Disease.[26]

Although there are several claims supporting the amyloid pore-hypothesis there is to date insufficient evidence to validate this theory. For example Connelly and associates observed circular pore-like structures on a lipid bilayer surface.[21] The scientific technique of atomic force microscopy (AFM) used in their investigations could not traverse the entire bilayer, thus it was not discerned if these structures formed complete transmembrane pores or simply f o r m e d gaps in the top leaflet. Another example supporting the uncertainty of pore-formation was also seen in the research of Green *et al.*[27] In their experiment, both vesicles adsorbed on a solid substrate and vesicles in solution were exposed to

aggregates and examined by AFM and electron microscopy (EM). The vesicles either broke apart into smaller pieces or had holes on the top leaflet. There was no evidence to indicate that the defects observed spanned the two lipid layers forming complete pores in an intact lipid bilayer.

There are various thoughts on how the presence of amyloid beta (Aβ) peptide leads to cell membrane instability. One theory suggests that the β-sheet aggregate structures consisting of mainly hydrophobic amino acids become imbedded in the non- polar region of the cell membrane becaust it is said to be more thermodynamically stable and energetically favourable.[28,29] The insertion of these β-sheet structures into membranes can lead to channels, pore-formation, or overall instability in the cell membrane.[28] Victor Munoz outlines other explanations for aggregate-membrane interactions leading to cell membrane defects:[30]

(a) Aggregates interact with specific cellular components and disrupt membrane structure.

(b) Channel hypothesis – protofibrils form non-specific membrane pores resulting in an imbalance in cellular content.

(c) Independent pore-formation that alters membrane fluidity

(d) Aggregates react with ions to produce hydrogen peroxide that causes lipid and protein decomposition

(e) Loss of function- where aggregated proteins create extra bulk in cells and cause inflammatory responses.

To examine the accuracy of these theories and to investigate the Aβ-membrane interaction, good quality, defect-free model cell membranes are essential.

1.1.3 Drawbacks in therapeutic remedies

The route to finding a cure or even a treatment for AD has been based largely on the Aβ aggregate-membrane interaction theory of toxicity.[31] Extensive research therefore has been focused on understanding the structures of the Aβ pre-fibrillar intermediates and characterizing their interactions with cellular membranes.[32-37]

The isolation and characterization of a definite structure for the prefibrillar Aβ species has been difficult due to its nanoscale size.[38] In addition, these amyloid intermediates exist in a dynamic equilibrium with each other and thus a "pure" form has proved difficult to isolate.[39] This is also a good explanation for the variability observed in results using Aβ in different pore-formation experiments.[39] Various experimental conditions used to form Aβ aggregates consequently gave rise to differences in aggregate phase composition, which can result in different types of pores and hence differing levels of toxicity.[16,39,40] Connelly showed that the circular arrangements formed on lipid bilayers exposed to Aβ aggregates were heterogeneous in nature and existed as either tetramers, pentamers or hexamers where the exterior and interior core features were different for each type of circular arrangement.[21]

In recent years work has been done to characterize the pores or channels formed by Aβ aggregates.[41-43] Results from computer model simulations indicated that the pores are heterogeneous with a pore-opening ranging from 1-2 nm and an estimated pore length of 6-13 nm.[44] In in these computer simulation studies the Aβ channels span the entire length of the model membrane with portions also extending out into the bulk solution.[44] The internal core environment is very hydrophilic and has an overall negative charge due to the presence of glutamine (Glu), which causes the pores to attract positively charged ions.[44,46] The size of the pore and the negative amino acid residues present in the pore core dictate the type and mobility of ions which may pass through the pores. For example, Ca^{2+} ions have low mobility due to their high binding affinity for Glu residues while K^+ ions have high mobility due to a lower binding affinity to Glu residues. [45,46] Thus since the internal core environment attracts Ca^{2+} ions readily, research has been focused on reducing the entry of Ca^{2+} ions into the pores. To regulate the Ca^{2+} content in cells, therapeutic efforts were explored by utilizing Calcium Channel Blockers (CCB's).[47,48] CCB`s interact with calcium channels (e.g. N-type) present in cell membranes inhibiting entry of Ca^{2+} ions and countering the effect of Aβ pores or channels.[49] However, the use of CCB's in clinical trials gave differing results where some trials showed prevention of cognitive decline in patients, and in other cases the use of CCB's failed.[48] Experimental research utilizing CCB's in the presence of neurons exposed to Aβ aggregates showed the same inconsistent results where CCB's were found to work

only occassionally.[49]

Other researchers speculated that since AD was a type of protein-misfolding disease, using specific chaperones to stabilize misfolded proteins or antibodies to prevent the formation of Aβ deposits could be a useful therapeutic route.[31,50] These chaperones would bind specifically to misfolded proteins and prevent aggregation.[31,50] Inhibitors were designed specifically to target enzymes that would bring about proteolytic cleavage of APP, which would in essence prevent the initial production of the Aβ aggregates.[31,50] Once more, these attempts were futile. The use of chaperones in patients caused meningoencephalitis.[51] In addition, experiments involving mice that lacked the γ-secretase enzyme died during trials. Clearly, these enzymes had other specific functions for growth and development.[52] The continued development of therapeutic remedies and an eventual cure for AD is ongoing with the use of increasingly more modern and sophisticated approaches.

1.2 Objective of thesis

There is experimental evidence that does not support the amyloid pore-hypothesis and in addition, present attempts towards the development of therapeutic remedies for AD remain ineffective.[21,27,51,52] A therapeutic remedy is based on a clear understanding of the mechanism of a particular disease and thus to achieve a successful remedy, the exact disease mechanism must be known.[53] The aim of this research project was to fabricate and characterize an intact defect-free model lipid bilayer system which will set the foundation for use in

future investigations aimed at exploring the pore-hypothesis for AD. This system will have the capability of showing any changes, defects or disturbances to the lipid bilayer brought about by the presence of other molecules, ions or aggregates. In this research, the Langmuir-Blodgett/Langmuir-Schaefer (LB-LS) technique will be used for the formation of a lipid bilayer on a solid substrate. In addition, the coupling of two major techniques, surface-enhanced Raman spectroscopy (SERS) and electrochemistry will be exploited to gain increased sensitivity whereby determining possible film formation on the surface of the working electrode, and affording information such as molecular orientation of lipid bilayer components.

1.3 Scope of Investigation

The Langmuir-Blodgett/Langmuir-Schaefer technique can be used to create lipid bilayers.[54] This technique is fairly straightforward and allows for the formation of ordered monolayers at an air-water interface which can then be transferred onto a solid substrate.[54] The correct sequential steps, i.e. vertical transfer followed by a horizontal touch, will afford the formation of a bilayer system with the desired orientation of the amphiphilic molecules.[55] The desired orientation is a hydrophobic region sandwiched by two hydrophilic regions, analogous to a biological cell membrane. Modern Langmuir-Blodgett instruments have user friendly software which allows for the close monitoring of the formation and transfer of monolayers; this aspect is very useful in terms of obtaining and maintaining optimal experimental conditions.[55] In the proposed research, electrochemistry and surface-enhanced Raman spectroscopy (SERS) will be

coupled together to give electrochemical surface-enhanced Raman spectroscopy (EC-SERS). In this particular method the working electrode surface is comprised of nanoparticles which affords the use of SERS; a non-invasive, distance-dependent, sensitive, molecular fingerprinting method of analysis.[56] In SERS, vibrational signals of a molecule are obtained when the analyte is brought to within nanoscale distance from a roughened metal surface and irradiated with laser energy.[56] The use of electrochemistry can simulate electric field conditions that a real cell membrane typically experiences. In addition, the electrochemical technique of cyclic voltammetry (CV) can provide information on film thickness, porosity and defects present in a deposited layer on the electrode surface.[57] To test the quality of the bilayer formed, a molecule will be used to probe the membrane for any defects, by monitoring changes in permeability to ions or molecules. This molecule will be termed the *probe molecule* and for the purpose of this work the probe molecule must be SERS active. A SERS signal will be observed for probe molecules that permeate the lipid bilayer or travel through gaps (defects) present in the lipid bilayer because now the probe molecules are closer to the SERS substrate. On the other hand, a defect-free lipid bilayer will give no SERS signal for the probe molecules since they are not close enough to the SERS substrate to provide a signal. Figure 3 shows a schematic diagram illustrating this point.
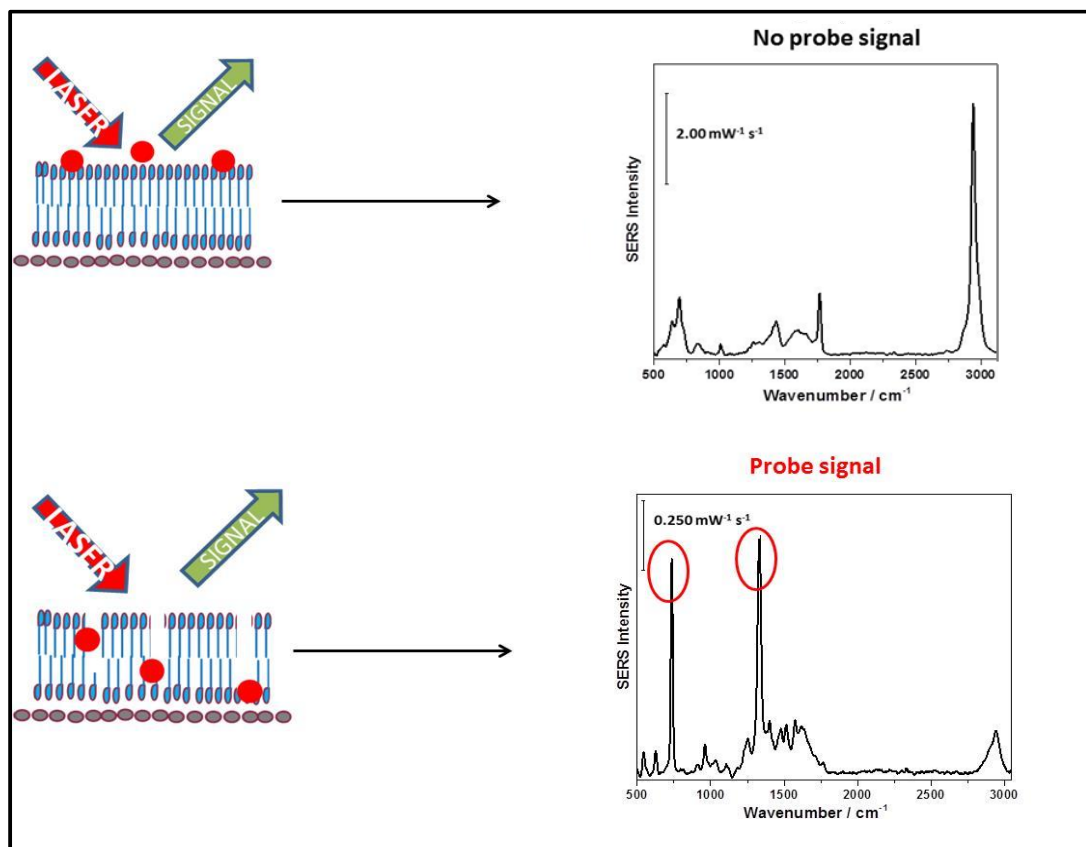
Figure 3: Schematic diagram of research design showing a magnified view of the working electrode surface that consists of a lipid bilayer deposited on a nanoparticle SERS substrate. No probe signal will derive from a good quality membrane or non-permeating probe molecules while a probe signal will derive from a poor quality membrane or permeating probe molecules.

2 Literature Review

2.1 Introduction

This section addresses all the main topics and techniques encompassed in this research project. Each section highlights the basic concepts that facilitated the design of experiments and evaluation of data. In addition, an up-to-date review of recent literature in the field is presented.

2.2 Properties of cell membranes

2.2.1 Components of cell membranes

Biological cells are the basic unit of living things.[58] Some of the fundamental functions of these complex and highly organized structures include: housing and replication of genetic information, providing, storing and using energy, carrying out mechanical activities and chemical reactions, responding to stimuli, and self-regulation. Cells vary in size, structure and composition which enable them to perform diverse functions.[58]

The cell membrane, also known as the plasma membrane has the main function of separating the internal cellular matrix from the external environment.[58] Examples of other functions of the plasma membrane include: providing a selectively permeable barrier, aiding in the transportation of specific molecules and responding to external stimuli.[58] The plasma membrane consists of lipids, proteins and carbohydrates, all of which enable the membrane to perform specific tasks.[58] The ratio of each of these components depends on the function and location of the cell within the organism. For example, neurons have a low percentage of protein since their main function is to provide electrical resistance which is achieved by incorporation of a high percentage of lipids.[58] One common model of the plasma membrane is referred to as the "*fluid-mosaic model*", proposed by Dr. S. Jonathan Singer and Garth Nicolson in 1972.[58] This model consists of protein and carbohydrate moving through a sea of lipids which forms a sandwich-like structure where the hydrophilic portions encase the hydrophobic region.[58] The idea of such a model implies that not all the

molecules within the plasma membrane are stationary. The sandwich-like arrangement of the lipids is a result of shielding of the hydrophobic region from the surrounding aqueous solution, thus giving rise to the well known term "*lipid bilayer*".[58]

Lipids found in cell membranes are amphiphilic molecules which consist of a hydrophobic and a hydrophilic region.[58] The most prevalent lipids in cell membranes fall under the category of phospholipids.[58] The glycerol backbone in phospholipids has three carbon atoms that are esterified; two carbon atoms are esterified to long chain fatty acids, and the third carbon atom is esterified to a phosphate group. The long chain fatty acids comprise the hydrophobic region of the bilayer. Phospholipids that have double bonds within the fatty acid chains are termed unsaturated lipids, while those with no double bonds are termed saturated lipids. Unsaturated fatty acid chains increase the fluidity of membranes because the double bond structure affords a less dense packing of the lipid molecules within the membrane. The hydrophilic region of the lipid molecules, also called the polar head region, consists of the esterified portion along with the phosphate group which has a negative charge. The modification of the phosphate group by the addition of other functional groups or molecules gives rise to a variety of lipids.[58] Figure 4 provides an example of a phosphatidylcholine, a class of phospholipids where the phosphate group is attached to a choline moiety. Other types of membrane lipids include sphingolipids, which contain long hydrocarbon chains attached to an amino alcohol, and cholesterol which is a type of sterol.[58]
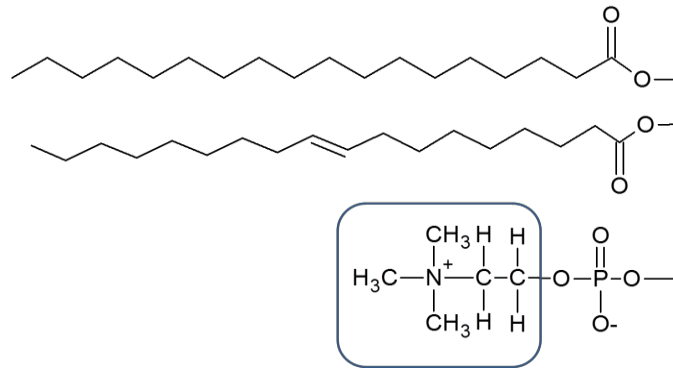
Figure 4: The structure of 1-palmitoyl-2-oleoyl-sn-glycero-3-phosphocholine.

Proteins exist in every area of the plasma membrane and are categorized based on their location. These categories are[58,59]:

1) integral (intrinsic) proteins- proteins which span the entire membrane and have sections protruding into the intracellular and extracellular matrix

2) peripheral (extrinsic) proteins- proteins which are located on the surface of the hydrophilic region of the membrane

3) lipid-anchored proteins- proteins which are covalently attached to lipid molecules and are present on the hydrophilic surface of the bilayer.

Integral membrane proteins consist of a hydrophobic and a hydrophilic region. These proteins sit comfortably within the lipid bilayer, stabilized by the hydrophobic interactions between the protein and lipid tails. The hydrophilic portion of these proteins has the ability to interact with species in solution. Thus integral proteins are well suited for their roles as channels where the hydrophilic portion of proteins extending into aqueous solution interact with specific molecules causing a conformational change of the

entire protein structure that results in a closed or open channel conformation.[58,59] Peripheral proteins interact at the membrane surface via electrostatic interactions or hydrogen-bonding with the lipid polar head or another charged molecule in the membrane. There is some literature debate that in some cases there might be a small section of peripheral protein that is imbedded slightly in the hydrophobic region of the membrane. These proteins aid in signal transduction or add mechanical support for membranes during shape change.[58,59] Lipid-anchored proteins can be attached either through a hydrocarbon chain or through a short oligosaccharide and their functions include participation in enzyme reaction processes or acting as cell receptor sites.[58,59]

Carbohydrates in cell membranes are either covalently attached to lipids (glycolipids) to proteins (glycoproteins).[58,59] Glycoproteins have short chain branched oligosaccharides that protrude outwards from the plasma membrane surface. The chief function of these structures is to participate in cell-cell interactions and cell-foreign material interactions. Glycolipids are comprised of short-chained oligosaccharides whose functions include energy storage and cellular signalling.[58,59]

2.2.2 Properties of cell membranes

The bilayer motif is maintained by the hydrophobic interactions of the alkyl chains of the lipids, the electrostatic interactions of the polar head regions and the shielding of the hydrophobic region from the aqueous environment which is thermodynamically favourable.[58,59] Another feature of cell membranes is the

movement of lipid components within the membrane. Lipid molecules undergo different types of movement within the cell membrane. Lateral diffusion, where lipid molecules move crosswise within one lipid layer occurs rapidly at a frequency of 10^7/sec.[59] Transverse diffusion or "flip-flop" is another type of lipid movement where lipid molecules move from one leaflet to the other. This type of lipid movement is more thermodynamically unfavourable since a polar head group will be required to pass through the hydrophobic region. The frequency of lipid flip-flop ranges from 10^{-4}-10^3/sec.[59] Finally, lipids can also stay in place but rotate about a fixed position and this movement is referred to as rotational diffusion, occuring at a frequency of 10^8/sec.[59] Proteins are also mobile within the cell membrane and their movements depend upon the fluidity of the membrane and the size of protein.[58] For those proteins that appear to be immobile, the cell membrane possesses a fibrillar network that holds such proteins in place.[58] Overall, this creates domains within the cell membrane and the purpose of these domains is to keep particular proteins close to each other in order to facilitate membrane reactions.[58] This dynamic movement or restriction of lipid components highlights another feature of cell membranes; asymmetry can exist between the two lipid layers. This feature correlates to the different types of reactions or processes that occur in the intracellular and extracellular matrices of cells.[58,59]

The amount and type of lipid components and the local temperature can dictate the ordering of lipids within the cell membrane.[58,59] Lipid bilayers can be described based on the packing of components which can give insight into characteristics such as the composition or fluidity of the membrane. At low

temperatures lipid components are tightly packed; rigid with little movement and highly ordered so that the alkyl chains are almost perpendicular to the plane of the membrane. This state is called the gel phase or solid-ordered state (S_o).[58,59] At higher temperatures the lipid components have increased motion; the area that each component occupies increases and the membrane thickness decreases. Since the lipid components are not tightly packed the membrane disorder increases. This state is called the liquid crystalline or liquid-disordered state (L_d).[58,59] Lipid bilayers that change from a gel phase to a liquid crystalline phase experience a characteristic phase transition and the temperature at which this occurs is called the transition temperature or melting temperature, T_m.[58,59] The change from one state to then next requires an alteration of the interactions that stabilize the lipid bilayer structure. Such interactions depend on the lipid chain length, lipid chain saturation and type of lipid polar head; all of which can affect the value of T_m.[58,59,60] T_m can be used as a means of identifying lipid bilayer composition and fluidity. For example, the T_m for a pure 1,2-dipalmitoyl-*sn*-glycero-3-phosphocholine (DPPC) lipid bilayer whose lipid tails are saturated with 16 carbon atoms for each tail is roughly 42°C.[61] On the other hand the T_m a pure for 1,2-dioleoyl-*sn*-glycero-3-phosphocholine (DOPC) lipid bilayer whose lipid tails are unsaturated with 18 carbon atoms for each tail, is roughly -22°C.[61] From this example it is clear that the presence of unsaturation in the lipid tails lowers the T_m. Temperature is only one method of changing the physical or chemical properties of lipid bilayers. The reactions or interactions of hormones, enzymes or neurotransmitters as well as the hydrolysis of certain glycolipids can cause conformational changes in membrane associated proteins and possible

19

changes in the fluidity of cell membranes.[58,59]

Although the plasma membrane is approximately 50-100 Å thick, the nature of its hydrophobic region rather than the thickness hinders the movement of certain molecules or ions across it.[58] As a result, the plasma membrane is sometimes referred to as a *resistor*.[58] Typically, cell membrane resistivity values range from 10^2 Ω·cm to 10^5 Ω·cm.[58] Given that some ions are prevented from crossing the cell membrane and other ions are actively assisted across the membrane, a potential difference is established.[58] The movement of ions across cell membranes leading towards an accumulation of positive or negative charges on the inner or outer surfaces of the membranes establishes an electric field across the membrane. The electric field exerts a force on ions moving through the cell membrane and plays a role in the direction of charged species across the membrane.[58] Thus if the extracellular matrix becomes more negatively charged than the intracellular matrix, the electric field difference draws positive ions into the extracellular matrix. Hence, the plasma membrane is also deemed a *capacitor*. The capacitance of biological cell membranes ranges between 0.5-1.3 $\mu F/cm^2$.[58] The resistivity and capacitance of the cell membrane generates a *membrane potential*. The membrane potential for biological cells falls within the range of -10 mV to -100 mV with respect to the exterior of cells.[58]

2.2.3 Cholesterol and membrane fluidity

As mentioned in the previous section, increasing the temperature above the T_m and introducing double bonds into the lipid tails will increase the fluidity of the cell membrane.[58,59] Cholesterol (Figure 5), a member of the sterol family and

20

also classified as a lipid, increases or decreases the fluidity of the membrane.[58,59] Thus, in its presence a membrane can accommodate the change from a gel ordered phase to the liquid phase more readily.[62] Cholesterol has a small hydrophilic region that consists of an OH group and a hydrophobic region consisting of the sterol ring moiety and alkyl chain unit. In the cell membrane cholesterol is oriented so that its hydrophilic and hydrophobic regions align with those of the lipid molecules, which alters the packing of the lipid molecules (Refer to Figure 5).[63-65]
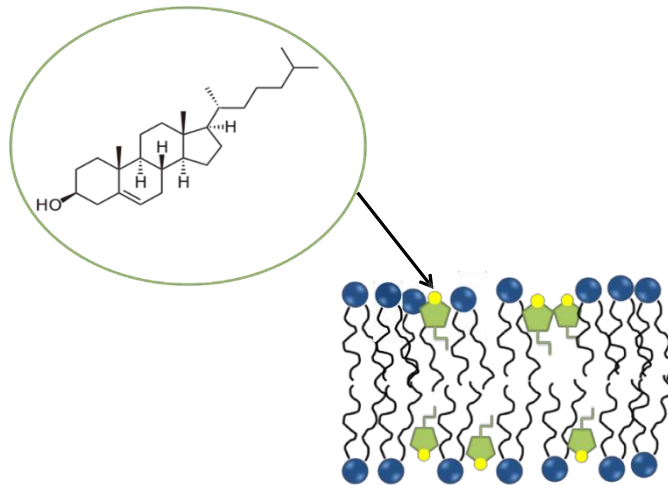
Figure 5: A diagram showing the structure of cholesterol and its approximate orientation within a lipid bilayer.[63-65]

Since the hydrophilic region of cholesterol is small compared to the rest of its structure, it is situated mainly in the hydrophobic region of the lipid bilayer.[63] Cholesterol is said to have a condensing effect since its presence in lipid bilayers decreases the area per molecule of the lipids.[66] Also researchers have shown that when cholesterol forms complexes with other lipid components, it increases lipid bilayer thickness due to apparent lipid chain lengthening and/or straightening.[66,67]

Membrane fluidity is important as it allows reactions to be carried out more

easily by lipid components e.g. proteins might be required to travel from one area of the membrane to another to complete a biological process or form specialized structures.[58] The fluidity of cell membranes is also important in cellular processes such as cell growth, secretion, and division.[58]

2.2.4 Movement of molecules across cell membranes

The physical structure of cell membranes acts as a natural barrier to many ions and molecules. Depending on the function of the cell, membrane processes control the passage of molecules in order to maintain a particular environment within the intracellular medium.[58] The movement of ions and molecules across the membrane depends on the charge, size, and concentration gradient. Hence, transport across a membrane will occur via one of the following processes: passive diffusion, facilitated diffusion and active transport.[58,59]

Passive diffusion occurs when molecules can cross the cell membrane without the aid of transporter molecules or some dedicated process. The molecules move based on a concentration gradient where migration is from an area of high concentration to that of low concentration. Passage of uncharged molecules across a cell membrane can be described using the following thermodynamic Equation 1:[58,59]

$$\Delta G = G_2 - G_1 = RT\ln\frac{[c_2]}{[c_1]} \qquad [1]$$

ΔG is the chemical potential difference based on the Gibbs free energy, G, of each side of the membrane and the concentration, c, of a particular species on each side of the membrane.[58,59] For charged molecules, the charge of the migrating

molecule and the electrochemical potential plays a role in the movement of species across the membrane. For example, if the extracellular matrix is more positive than the intracellular matrix, there will be a pull of positively charged molecules into the interior of the cell. Equation 1 can be modified to give a new equation, Equation 2, which describes the movement of charged molecules across a cell membrane:[58,59]

$$\Delta G = G_2 - G_1 = \text{RTln}\frac{[c_2]}{[c_1]} + ZF\Delta\psi \qquad [2]$$

The additional terms in equation 2 take into account the charge of the migrating species, Z; Faraday's constant, F, for determining the total charge based on the number of molecules present; and $\Delta\psi$, the electrical potential difference across the membrane.[58,59]

Cell membranes are very permeable to small neutral molecules such as oxygen, carbon dioxide, nitrogen, and water, while large polar molecules such as sugars, amino acids, and phosphorylated compounds have low permeability.[58,59] For molecules that cannot diffuse spontaneously across the membrane, facilitated diffusion is required for entry of these species into cells. In many cases, this facilitated diffusion takes place via ion channels, either voltage-gated, where entry of ions is based on the difference in electrical charge on the two sides of the membrane; or chemically-gated, where binding of specific molecules to particular integral membrane proteins causes a protein conformational change which allows entry of ions.[58,59]

Similar to facilitated diffusion, active diffusion also relies on conformational changes of integral proteins for entry of specific molecules. However, unlike

passive and facilitated diffusion, active diffusion has two distinguishing features: 1) it acts against the concentration gradient, taking molecules from an area of low concentration to an area of high concentration, and 2) it requires energy to perform its function; energy can be provided by the hydrolysis of adenosine triphosphate (ATP).[58,59] For example, gastric H^+,K^+-ATPase, an integral protein found in the parietal cells located in the inner lining of the stomach wall, uses the energy derived from the hydrolysis of ATP to pump H^+ ions out of the mucosal cells (lower H^+ ion concentration) into the interior of the stomach (higher H^+ ion concentration) in exchange for K^+ ions.[59]

2.3 Biomimetic membranes

2.3.1 Formation and types of model membranes

Biomimicry is defined by the Oxford English Dictionary as, *"the design and production of materials, structures, and systems that are modelled on biological entities and processes".*[68] The possibilities for this particular field are vast and can be applied to most, if not all scientific areas. For example, dendrites present on neurons have numerous branch-like features that aid in rapid electrical signal transduction.[69] This biological architecture was used in the design of nanoparticles covered with dendritic features to aid in drug delivery to specific cells in the body.[69] Another example of biomimicry is the design of microfluidic devices called "organ-on-chips" which are engineered to mimic the tissue arrangement and environment in organs so that a specific cell physiology can be studied, or an investigation into organ-specific diseases can be

performed.[70] In all biomimicry designs the aim is to have the model system be as closely related to the biological system it represents as possible. One aspect of this thesis project involves the fabrication of lipid bilayers to mimic cell membranes. These biomimetic membranes must have similar properties to cell membranes in order to provide credible results. Table 1 is an example of how biomimetic membranes can have comparable properties to that of biological cell membranes.[58]

Properties	Biological Cell Membranes	Unmodified Lipid Bilayers
Thickness (Å)	60-130	60-90
Resistivity (Ω·cm)	10^2-10^5	10^6-10^8
Capacitance ($\mu F/cm^2$)	0.5-1.3	0.3-1.3
Resting Potential (mV)	10-90	0-140
Water permeability (10^{-4}cm/sec)	0.25-58	2.3-24

Table 1: An adapted table showing the comparison of physical and electrical properties between biological cell membranes and unmodified lipid bilayers.[58]

There are different biomimetic models for cell membranes and the design varies according to the biological process of interest e.g. model bilayer systems have been tailored to study ligand-receptor interactions[71], viral attack[72], and enzymatic reactivity of membrane proteins[73]. Initial model membranes were derived from two main processes: black lipid membrane fabrication and liposome formation.[74] The black lipid membrane procedure involves the formation of the lipid bilayer at a micrometer-sized aperture formed from hydrophobic material such as Teflon® in aqueous solution.[74] Stabilization of the lipid bilayer structure is accomplished by hydrophobic interactions between the lipid tails and the hydrophobic material forming the aperture, and hydrogen bonding or electrostatic

interactions between the polar head region of the lipids and the aqueous solution.[74] There are two ways to form a black lipid membrane; painting the aperture with an organic solution of the desired lipid components under aqueous solution, or by lowering or raising a hydrophobic aperture between two sections, one containing an aqueous solution and the other a lipid monolayer formed on an aqueous solution.[74] Liposome formation involves dissolving lipid components in organic solvents, removing the organic solvent to form dry lipid, redispersing the dried lipids in aqueous solution, and then collecting the resulting small vesicles.[74] The main advantage of the black lipid membrane and liposome technique is that both sides of the lipid bilayer are in contact with aqueous solution.[74] The drawbacks of the two previous methods include: difficulty in manipulating the lipid bilayers; in the case of black lipid membranes it can be difficult to incorporate more than one bulky analyte molecule (e.g. pore-forming protein) within the lipid bilayer, stability, lack of ability to create asymmetric bilayers, and the limitation of optical techniques for characterizing such membranes, especially in the case of black lipid membranes.[74] Figure 6 is a simplified diagram illustrating (a) a black lipid membrane at an aperture, and (b) liposome formation.
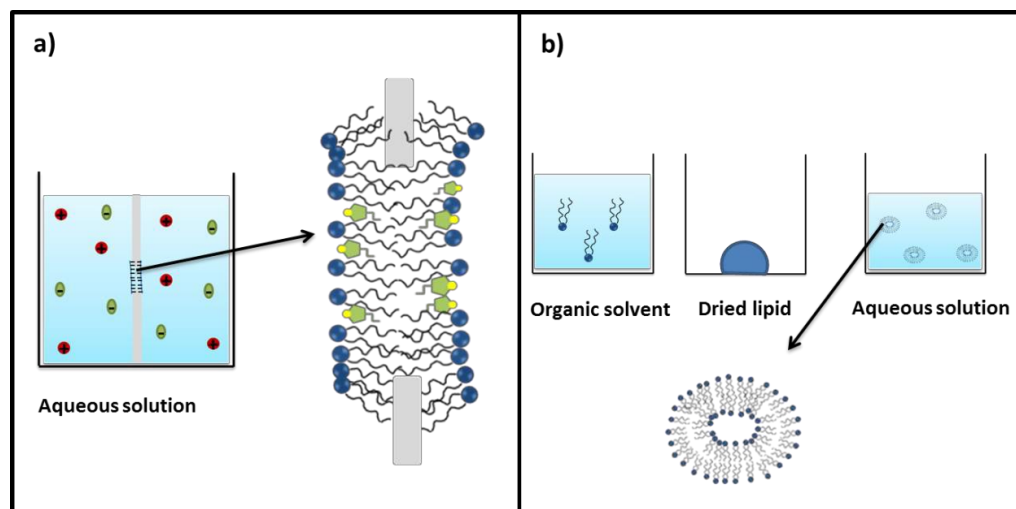
Figure 6: a) a black lipid membrane formed at a hydrophobic aperture in aqueous solution. b) liposomes formed by sequential steps of dissolving, drying, and redispersing in appropriate solvents or solutions.

Recent applications of model membranes have required the formation of lipid bilayers on solid supports.[74] Lipid bilayers can be directly attached to a solid support, separated from the solid support by another layer, or tethered to a solid support via specific molecules.[74] Examples of supported bilayer lipid membranes (s-BLMs) include:

a) tethered bilayer lipid membranes (t-BLMs) - Lipid bilayers are anchored to solid substrates via specific units such as alkyl polymer chains that are bonded to the solid substrate at one end, and bonded to lipid components at the other.[74]

b) floating bilayer lipid membranes (f-BLMs) - Lipid bilayers are separated by a water layer from a lipid covered solid substrate or a solid substrate modified to afford a hydrophilic surface. The water separating these two structures gives the appearance of a lipid bilayer 'floating' on top of the surface.[75]

27

hybrid bilayer lipid membranes (h-BLMs) - The lipid bilayer structure is comprised of two leaflets; one leaflet contains non-lipid components and the other has lipid components. The lower leaflet is a non-lipid monolayer (such as closely packed alkyl chains) that is directly attached to the solid support at one end while the other end is in direct contact with the top lipid containing leaflet.[74] Figure 7 shows a schematic representation of examples of various supported lipid bilayer architectures. The lipid bilayers are held in place on the solid support via interactions which include steric forces, electrostatic interactions, chemical bonding, and Van der Waals interactions.[74] The choice of solid support is often dictated by the analytical technique intended to characterize the lipid bilayer or the biological process under investigation.[74] Examples of solid supports include metal and metal oxides, nanoparticles, polymer cushions, fused silica, and borosilicate glass.[74] More recently lipid bilayers have been formed on the surface of solid supports in a layer-by-layer fusion using the technique of Langmuir-Blodgett/Langmuir-Schaefer (LB-LS) deposition, layer- by-layer vesicle fusion, or a combination of the LB-LS method and vesicle fusion.[74]
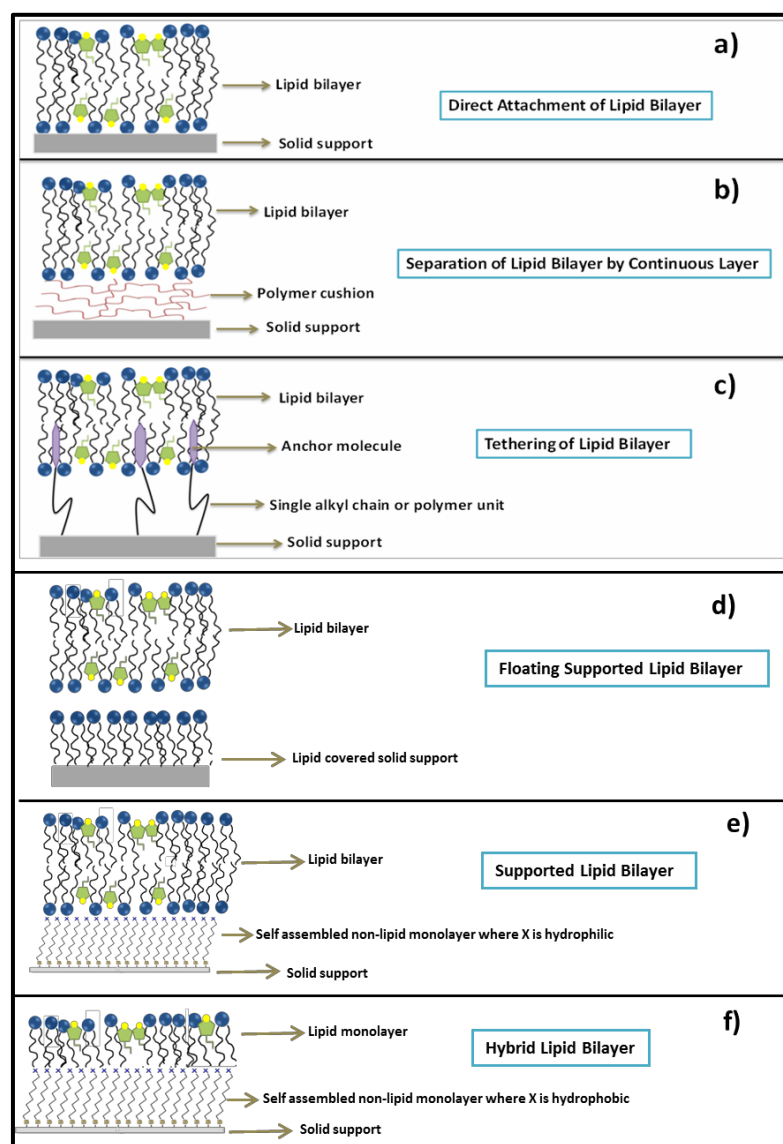
Figure 7: A schematic diagram illustrating the various ways in which a biomimetic membrane can be fabricated onto a solid support. a), b), d), e), and f) can be achieved by both LB-LS, layer-by-layer vesicle fusion, or a combination of both techniques, while c) is best attained by layer-by-layer vesicle fusion.

The advantages of using a solid support include increased stability, ease of anchoring specific proteins in order to probe their reactivity, improved surface coverage, and mobility of lipid components and fluidity if the lipid bilayer is maintained by an underlying water film.[74] In addition, sophisticated surface

analytical techniques such as Atomic Force Microscopy (AFM) or Surface Enhanced Raman Spectroscopy (SERS) can be used to probe interactions at the lipid bilayer surface.[74] Drawbacks of using a solid support include direct contact of the lipid bilayer with the solid support which can lead to unwanted effects e.g. denaturing of proteins; decreased fluidity of the membrane compared to black lipid method, and interactions used to stabilize bilayer-solid support system may require specific pH and ionic strength conditions that stray from that of the biological process under investigation.[74]

2.3.2 Characterization of model membranes

The analytical technique employed to characterize biomimetic membranes depends on the method used to create the membrane and the biological process being studied. Early unsupported membranes or liposomes were usually examined using simple optical microscopy techniques such as light or fluorescence microscopy, or electrochemical methods such as the surface charge through zeta potential or electrical conductance measurements.[74,76,77] As technology advanced and membranes could be formed on more diverse solid supports, more sophisticated and unconventional methods were developed.[74]

A main concern for model membranes is the reduction in fluidity of the fabricated lipid bilayer when compared to biological cell membranes.[74] Fluorescence Recovery After Photobleaching (FRAP) is a technique used to analyze or monitor the movement of lipid components within a lipid bilayer.[78] In FRAP, fluorescent dyes are covalently bonded to target molecules within the

bilayer and then a section of the sample is subjected to high intensity radiation that will cause fluorescence followed by photobleaching. This results in a dark region within the bilayer. The diffusion and migration of lipid components within this dark region is then evaluated.[78]

Biomimetic membranes can be studied using powerful microscopic techniques that provide high resolution images of the topography of the lipid bilayer surfaces.[79] Scanning Tunneling Microscopy (STM) and Atomic Force Microscopy (AFM) use very sensitive tips to scan the surfaces of bilayers, providing micro and nanometer scale resolution.[80,81] The images and data obtained using these methods can confirm bilayer formation or show the structures of pores or aggregates on the membrane surface.[82] Green and associates used AFM to probe the surfaces of mica supported lipid bilayers exposed to human amylin peptide.[27] The AFM images in this experiment revealed defects (small holes) in the lipid bilayer after injection of the amylin peptide solution. Mayer *et al.* used AFM to image the surfaces of their s-BLMs containing cytochrome *c* oxidase. The goal of the experiment was to determine how compact the lipid bilayer was and the location of the anchored cytochrome *c* oxidase molecules within the lipid bilayer.[83] Other techniques can provide additional information on the properties of model membranes. IRRAS (infrared reflection adsorption spectroscopy) or PM-IRRAS (polarization modulation infrared reflection adsorption spectroscopy) are spectroscopic methods exploiting the reflection and absorption of radiant energy to probe lipid component orientation and conformation within lipid bilayers[84], while X-Ray and Neutron Scattering,

centred on observing how a sample scatters X-rays and neutrons respectively, resolve the composition, location, and distance between components in biomimetic model membranes.[74,84]

Besides lipid composition and location, the behaviour of specific lipid components (e.g. channel proteins) is another area of interest in the investigation of biomimetic membranes. Electrochemical techniques, for example cyclic voltammetry (CV) are regularly used to obtain information regarding the redox behaviour of specific membrane components.[57] CV involves cycling the potential of the working electrode which supports the bilayer between set voltages and measuring the resulting current.[57] Recently, modern techniques such as computer modelling and molecular dynamic simulations have been used to predict, comprehend and offer possible explanations for lipid bilayer behaviour and function.[85] This includes information such as hydration of lipid components, pore-formation and structures of pores, orientation of cholesterol in lipid bilayers, mechanisms for movement of lipid components within the bilayer, and the orientation of water molecules with respect to lipid components for a supported lipid bilayer system.[21,86,87] Other modern techniques, for instance Raman spectroscopy and SERS use vibrational information to provide insight into composition, structural orientation, and inter and intra lipid component interactions.[88,89] Leverette and Dluhy utilized SERS to investigate the structural orientation of lipid components in a supported lipid bilayer system.[90] The spectral data from this experiment showed that lipid components were oriented perpendicular to the metal surface and that disorder in the support

layer was due to attachment of the lipid bilayer. Ianoul *et al*. employed Raman spectroscopy to study the effect of antimicrobial peptides on model cell membranes.[91] Raman spectra showed that for zwitterionic lipids, the presence of antimicrobial peptides had no effect on the alkyl stretch vibrations. Alternatively, anionic lipids exhibited spectral changes for the alkyl vibrations and the conclusion of the experiment was that a charged polar head is required for adsorption of the antimicrobial peptides onto the bilayer surface.[91]

Although there are many ways to characterize model membranes each technique comes with its own set of drawbacks. Depending on these limitations, the quality of data can be affected such that the intended aim may not always be attained. Often however, steps can be taken to overcome these drawbacks, or supplement the results by using complementary techniques to increase the validity of the data. For example, AFM provides good resolution and a three-dimensional surface profile of the lipid bilayer, however AFM is highly dependent on technical expertise and typically requires years of experience with operational use.[81] Lack of experience with such an instrument can lead to greater occurrences of image artifacts. Such artifacts can be misinterpreted as useful or novel structures. Moreover, it can be difficult to image biological membranes due to tip contact interference.[81]

2.3.3 Application of model membranes

The main application of model membranes is to provide a means by which biological processes can be understood or investigated; thus the applications are

vast. Enzymatic reactions, protein structure and function, pore-formation, understanding specific channel operations, membrane interactions with toxins, and the kinetics of antibody binding to antigens are just some of the ways in which model membranes are exploited.[74,92] Presently the direction towards using model membranes as sensing platforms is of great interest. Model membranes can be fabricated to detect specific pathogens, viruses, biological warfare agents, or precursors to neural degenerative diseases. Biomimetic membranes or immobilized liposomes have also been incorporated into chromatographic columns to aid in separation of biological molecules for investigating drug interactions, or predicting how the absorption of drugs might occur in vivo.[74,93-95]

2.4 Self-assembled monolayers

2.4.1 Introduction

The choice of solid support utilized in this research project was modified with a self-assembled monolayer (SAM) consisting of simple alkanethiols. This next section highlights the formation of SAMs from solution, their chemical and physical properties, advantages and disadvantages regarding their use, and techniques used to characterize their surfaces. Such knowledge is important for the successful and efficient exploitation of these assemblies in the present research project.

2.4.2 Self-assembled monolayers: formation and properties

SAMs are formed from the spontaneous adsorption of certain molecules from solution or vapour phase onto a solid substrate.[96] The monolayer formed

completely covers the surface and yields a thickness somewhere within the range of 1-3 nm.[96] The solid substrate can include metals, metal oxides, glass, silicon or carbon. There are many types of SAMs but for the purpose of this study, SAMs formed from simple alkanethiols will be the focus.[96]

Alkanethiols consist of an alkyl chain that has a thiol group at one end and a desired functional group at the other; $SH(CH_2)_nX$.[96] Alkanethiols have been used with metal substrates such as copper, palladium, and mercury due to the high affinity of the sulphur atom for these metal surfaces.[96] Also, electrodes are typically made from these metals affording the use of electrochemical techniques for further characterization or extension of their applications. However, chiefly silver and gold are used as solid substrates for alkanethiol SAMs, and it has been proven experimentally that a metal- sulphur bond forms during the adsorption process on these metals.[97-99] The terminal group, X, is chosen to achieve desired surface chemistry. Some examples of terminal functional groups include OH, COOH, CH_3, and $C_6H_4(OH)_2$. Figure 8 shows a simple one-dimensional representation of an alkanethiol SAM.[96]
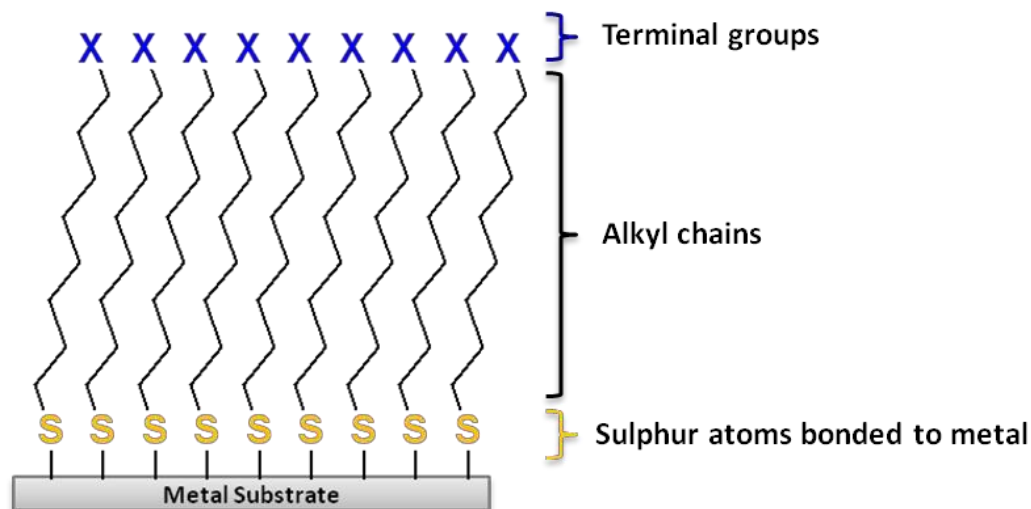
Figure 8: A 1-dimensional representation of a good quality SAM derived from alkanethiols. The diagram demonstrates two main features; the tight packing of the molecules, and a very well-organized assembly.

The formation and stability of SAMs relies on several factors: affinity of molecules for the solid substrate, the amount and type of impurities present, Van der Waals or electrostatic forces existing between adsorbed molecules, alkyl chain length, terminal functional group, experimental conditions, and elapsed time for SAM formation.[96,100]

Spontaneous adsorption of alkanethiols from solution onto a solid substrate is a common, easy and cost effective route to forming SAMs.[96] The solvent chosen is typically ethanol because it dissolves molecules of varying degrees of polarity, it is inexpensive, volatile, and high purity grades are available.[96] Other solvents can be used but care must be taken to choose a solvent that does not have a stronger affinity for the solid substrate; adsorption of the solvent onto the solid substrate can yield an incomplete, defective layer.[96] Other solvent effects include strong interactions between solvent and

alkanethiols, oxidation of the SAM, or poor solubility of the alkanethiol in the solvent. In these cases, SAM formation is incomplete or does not occur.[96] Concentrations of alkanethiols are typically in the μM to mM range and the substrate of choice is incubated in this solution for typically 12-18 hrs.[96] Adjustments such as increased alkanethiol concentration in solution and increased incubation time ensure maximum coverage of the solid substrate and a higher probability of a complete, compact SAM. Once the alkanethiol monolayer is formed, desorption of the alkanethiol from the substrate surface does not occur easily due to the strong interaction with the surface.[96]

There are several factors that could prevent the proper formation of a SAM. For example, impurities present both on the substrate and in solution can prevent the adsorption of molecules onto the substrate.[96] In addition, alkyl chain length can play an important role in SAM formation. Longer alkyl chains compared to shorter chains have more extensive hydrophobic regions and therefore stronger Van der Waals interactions which is a driving force for faster SAM formation.[96,100] Shorter alkyl chains have the added disadvantage of bringing terminal groups closer to the substrate surface and providing a possibility for interaction of these groups with the substrate.[101] Ma and co-workers proposed a mechanism of SAM formation for alkanethiols using a time-dependent study of 11-mercaptoundecanoic acid adsorbing onto roughened silver.[102] This study showed that during monolayer formation the SAM went from disordered, where the deprotonated COOH terminal groups were interacting with the metal substrate, to a well-formed monolayer with very little to no terminal group-metal interaction within approximately 2 hrs. They continued by stating that the Ag-S

bond was stronger than the COO-Ag interaction and displacement of COO⁻ groups from the surface will eventually occur. In these studies it was shown that the COO-Ag bond can be reduced readily by lowering the pH of the solution and applying a negative potential to the Ag surface. In basic solution the COO-Ag bond persists for a longer time before complete SAM formation.[102] Thus, for shorter alkanethiols, pH conditions, incubation times and surface charge are important considerations for preventing a poorly formed SAM. Temperature and the presence of oxygen can hamper the formation of an alkanethiol SAM. Cooler temperatures (i.e. below 25°C) decrease the rate of formation of the monolayer; while oxygen in the solvent can cause oxidation of the thiols to sulfonates. If the temperature of the solution is kept above 25°C and oxygen is removed by degassing the solvent with an inert gas, the quality of the SAM can be improved.[96]

Tight molecule packing and the extensive hydrophobic region of a SAM creates a barrier to the passage of molecules and limits interactions with the substrate surface.[96] Not all molecules are prevented from reaching the surface; water molecules and small ions can penetrate the monolayer, forming channels.[103] A well-formed alkanethiol SAM with a methyl terminal group has a spacing of about 3 Å between hydrogen atoms of neighbouring alkyl chains, and this allows the passage of water molecules or desolvated ions.[103] The size of the channels can be greater than 3 Å due to bigger bulkier terminal groups or defects present within the SAM.[103] For example, large branched terminal amides create steric bulk and hinder the formation of a dense, well-formed SAM.[103] Another feature of SAMs is

the orientation of the C-C-S moiety.[104,105]   The orientation of this moiety dictates the conformation of the alkyl chain. When this moiety is relatively straight and is almost perpendicular to the substrate surface it is said to be in the *trans* conformation. When the moiety is bent, a section of the chain is almost parallel to the substrate surface and the chain is said to be in a *gauche* conformation.[104] Figure 9 represents a comparison between the *trans* and *gauche* formations.
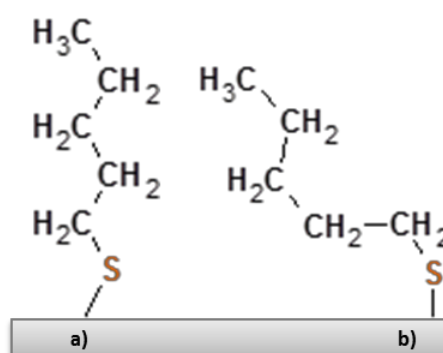
Figure 9: a) shows the almost perpendicular orientation of the *trans* conformation, and b) shows the bent configuration of the *gauche* conformation.[104]

The terminal groups of SAMs can interact with water molecules and other species present in solution via electrostatic interactions, hydrogen bonding, or covalent bonding.[96,106]   Deprotonated carboxylic groups are known to interact with hydrophilic molecules such as lipids, proteins, positively charged ions, and water molecules.[96,106-108]   The reactivity of carboxyl terminated alkanethiol SAMs cannot be compared directly to their counterparts of free unadsorbed carboxylic groups since upon adsorption of the alkanethiol the strength of the acid group decreases due to possible hydrogen bonding between neighbouring carboxylic groups which stabilizes the protonated form.[109,110]

Defects present in a SAM give rise to an uneven, disordered monolayer, which might be undesirable depending on its desired role.[96,103] If the substrate surface is uneven and poorly formed, the SAM may in turn be uneven and poorly formed. "Pinholes" are gaps or spaces formed within the SAM. The surfaces of substrates are exposed when pinholes are present and as a result unwanted electron transfer processes can occur.[96,103] For example, in electrochemistry where electron transfer processes are investigated for electroactive species, SAMs are used as barriers to prevent redox species from directly interacting with the electrode surface, hence reducing false readings in current output.[96] Other defects arise from chains that are severely tilted, or bent towards the surface of the substrate, forming disorder in the monolayer structures.[103] SAMs are also affected by other factors that can degrade their stability. For SAMs that are formed on the surface of a working electrode in an electrochemical cell, reductive desorption can occur at very negative potentials.[111] In addition, SAMs are sensitive to oxygen and over time oxidation of the metal-sulphur bond can occur.[96] pH also affects these monolayers where in some cases desorption occurs in acidic solutions, and in other cases some monolayers are stable under both acidic and basic conditions.[112]

2.4.3 Applications of self-assembled monolayers

The applications of SAMs are immense and only a few will be highlighted in this section. The reason for the wide assortment of applications originates from the varied terminal functional groups and/or modification of the alkyl

chains.[96]   For example, the alkyl chain moiety can consist of polymer chains with monomer units of ring compounds, and a target terminal group such as an antibody.[96]   In addition, to enhance SAM versatility, components of the monolayer can be varied, i.e. monolayers are not exclusively homogenous but can be heterogeneous.[57,96]

One major application of SAMs is as sensors for the detection of biological and non-biological molecules. For example, gold electrodes modified with alkanethiols with terminal groups possessing carboxyl terminals are used to selectively detect trivalent cations from divalent cations.[96,113] Martin and co-workers applied this type of molecular selection to separate a mixture of 1,5-naphthalene disulfonate and methyl viologen that was passed through gold nanotubes modified with a carboxyl terminated SAM. At high pH the deprotonated carboxyl groups of the SAM attracted the positively charged methyl viologen molecules.[96]

SAMs act as a protective layer separating biological molecules from direct contact with the metal surface.[74,96]   For example, using SAMs as a solid support for lipid bilayers prevents surface-induced denaturation of circulating proteins which can cause biofouling. In addition, SAMs are used as protective coatings on metal surfaces such as medical implant materials to prevent the adsorption of specific compounds or to prevent corrosion.[57,96]

Outside the realm of biology, SAMs are added to the surfaces of nanoparticles to control their growth, reduce aggregation, or stabilize their structures.[114] From time to time composite nanoparticles such as CdSe are used

as semiconductor materials and are synthesized in the presence of surfactant molecules. The surfactant molecules form a SAM on the metal complex that aids in controlling growth and reducing defects of the CdSe nanoparticles in solution.[114]

2.5 Langmuir monolayers and films

2.5.1 Langmuir monolayer formation and properties

A Langmuir monolayer refers to a one molecule thick insoluble monolayer formed at the interface of two adjoining bulk phases (usually an air-water interface).[54,55] The term Langmuir pays tribute to Irving Langmuir for his original experimental contributions in the 1900s on theoretical concepts and behaviour concerning insoluble monolayers at the air-liquid interface.[115] At the air-liquid interface Langmuir films are formed on the surface of the liquid which is referred to as the subphase.[54,115] In order for the monolayer to remain as an insoluble film on the surface of the subphase, the molecules of the monolayer must be amphiphilic. The hydrophilic head group of the amphiphile is in contact with the subphase while the hydrophobic portion protrudes out into the air, preventing the amphiphile from being completely solubilized in the subphase. The amphiphile can be deposited onto the subphase via two methods: (i) directly onto the surface as either a liquid or solid or (ii) as a solution where the amphiphile is dissolved in a volatile liquid. In the latter case, evapouration of the solvent must occur before the monolayer is formed via compression.[54,115] One main application of Langmuir films is their use as an in vitro model to study membrane interactions.[115]

Langmuir monolayers are typically formed in specialized instruments that

can monitor the surface tension of the subphase during the slow and steady compression of the molecules located at the interface.[55] During compression, the Langmuir film typically goes through four phases: gaseous phase, liquid-expanded (L-E) phase, liquid-condensed (L-C) phase, and a two-dimensional solid phase.[55] Figure 10 illustrates the different monolayer phases during compression. The gaseous phase occurs immediately after the deposition of the amphiphiles onto the subphase surface. The molecules are widely spaced out with very little to no forces existing between them, and sometimes exist in a nearly flat orientation on the surface of the subphase. In the L-E phase the compression of the molecules has begun, and the molecules are now closer to each other and experience attractive interactions such as chain intertwining. Also the vertical alignment of the hydrophobic tails commences in the L-E phase. However, the majority of the molecules are still randomly ordered. Further compression results in the L-C phase where the area that each molecule occupies decreases and neighbouring chains interact with each other. The final two-dimensional solid phase has tightly packed, well-aligned molecules, with the hydrophobic regions oriented perpendicular to the plane of the subphase surface.[55] The hydrocarbon chain attractive forces (Van der Waals) play an important role in stabilizing the monolayer in the solid phase.[115] The compression of a monolayer beyond its solid phase can lead to what is termed a "monolayer collapse". In a monolayer collapse molecules are forced out from the surface of the liquid to the end of the hydrophobic region yielding undesirable multilayers (Figure 10).[55,115] Monolayer collapse results in an immediate and profound drop in surface

pressure.
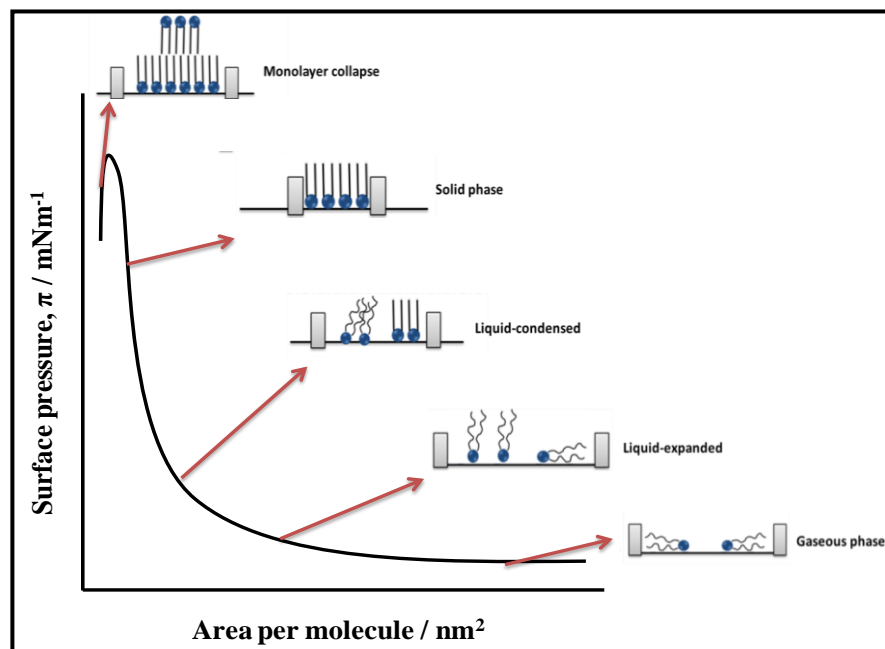
Figure 10: The slow and steady compression of amphiphiles at the air-water interface by barriers shown in grey yields the main phases of a monolayer formation that can be detected in a compression isotherm. Further compression of the solid phase results in a collapsed monolayer.

The addition of amphiphiles to a clean subphase surface reduces the surface tension.[115] The change in the surface tension of the subphase surface due to the addition of a monolayer is called the surface pressure, Π, of the film. The surface pressure is brought about by the lateral forces generated between the molecules in the monolayer.[115] Film balances that involve the partial immersion and wetting of a solid (e.g. platinum, quartz or filter paper) in the subphase measure the changes in surface tension. The dimensions and properties of the solid, along with gravity, g, surface tension, γ, and buoyancy effects acting on the solid yields an equation that gives the total downward force on the immersed solid, shown in Equation 3.[115]

$$\mathbf{F} = \rho_s glwt + 2\gamma(t+w)\cos\theta - \rho_l gtwh \qquad [3]$$

The dimensions of the solid include its length, l, width, w, and thickness, t; in addition the density of the material, ρ_s, must be taken into account. The surface tension and buoyancy effects take into account the depth, h, that the solid is immersed in a subphase of density, ρ_l, and the contact angle, $\cos\theta$, formed between solid and liquid.[115] Any changes in the surface tension will alter the forces acting on the immersed solid. Since the surface pressure of a film is the two-dimensional analog of a gaseous pressure, it is calculated as the change in force per unit length.[115] Thus relating surface pressure to changes in surface tension, rearrangement of Equation 3, assuming complete wetting of the immersed solid ($\cos\theta = 0$), yields Equation 4 for a stationary immersed solid.[115]

$$\Pi = -\Delta\gamma = -[\Delta\mathbf{F}/2(t+w)] \qquad [4]$$

Factors that may affect the proper formation of a Langmuir monolayer include: contamination of the subphase or the solvent used to dissolve the amphiphile, short hydrophobic tails that cannot stabilize the molecule sufficiently at the air-water interface, a hydrophilic head that has a very weak or very strong interaction with the subphase, the concentration of amphiphile deposited on subphase, compression of a monolayer too quickly, strong to moderate vibrations during compression, incomplete evapouration of solvent used to dissolve amphiphile, or fluctuating temperatures during monolayer formation.[115] Another undesirable problem with monolayers formed at the air-water interface is micelle formation. Instead of staying at the air-water interface, the amphiphiles form circular moieties where the hydrophobic tails are in the interior and the

hydrophilic heads comprise the surface. The micelles are therefore soluble and found in the subphase below the air-water interface.[55,115]

2.5.2 Langmuir-Blodgettry

A compressed monolayer at the air-water interface exerts a particular surface pressure. This value is dependent on the nature of both the amphiphile and subphase.[115] A compressed monolayer can be transferred onto a solid substrate at a constant compressed monolayer pressure; this is referred to as Langmuir-Blodgettry.[115] This ensures that the molecules are packed tightly and transferred effectively as a single monolayer onto the substrate. The nature of the solid substrate, whether hydrophilic or hydrophobic, must be taken into consideration to afford transfer of the monolayer in the correct orientation if the substrate is either fully immersed or partially immersed in the subphase.[115]

There are different ways to transfer a monolayer unto a solid substrate. For example, one method of Langmuir-Blodgettry involves a hydrophilic substrate that is fully immersed in the subphase before monolayer formation.[115] Here the substrate is well wetted and after the monolayer is formed and compressed, the substrate is slowly brought through the air-water interface while the surface pressure is held constant.[115] The monolayer is transferred onto the substrate with the hydrophilic head adsorbed directly onto the solid substrate and the hydrophobic tails oriented perpendicular to the plane of the substrate.[115] Depending on the nature of the amphiphile, multilayers can be achieved by successive depositions of the solid substrate.[116] Multilayers can be formed by

the following deposition styles: a) Y-type, b) X-type, and c) Z-type (Figure 11).[116] In the Y-type deposition, the solid substrate is passed through a monolayer in successive up and down strokes yielding alternating monolayer films. X-type depositions involve only downward strokes, hence typically hydrophobic solid substrates are used and monolayer films are all in the same direction. Z-type multifilms also yield monolayer films in the same direction, but deposition occurs only by upward strokes and the solid substrate is typically hydrophilic. For X-type and Z-type depositions, the tail-head interaction of the molecules in the monolayer film must be stronger than the tail-tail or head-head interaction in order to stabilize the multilayer formed. If the tail-head interaction is not strong enough then the multilayer can rearrange to form a Y-type multilayer, i.e. alternating monolayer films.[116]
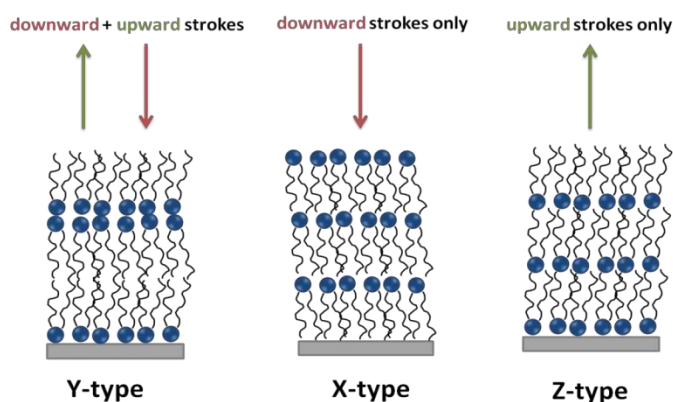
Figure 11: Diagram showing the various types of monolayer deposition. The Y-type deposition yields alternating monolayer films while the X-type and Z-type depositions forms monolayer films in the same direction.

A thin film of water is also transferred with the monolayer.[115,117] This water can be rapidly expelled in a few seconds during monolayer transfer onto the

substrate, or slowly expelled with drying overtime after monolayer transfer. The rate of monolayer transfer and the strength of attraction between the hydrophilic region of the amphiphile and the solid substrate both determine the speed at which the film of water is expelled.[115,117] For example, if the amphiphile has a strong attraction for the solid substrate and the monolayer transfer rate is slow, the water film can be pushed out to facilitate the strong interaction between the amphiphile and solid substrate.[115,117]

The Langmuir-Blodgett technique is a very sensitive method and hence there are a number of factors or conditions that should be maintained and/or controlled in order to afford reproducible results and a successful monolayer transfer. These factors include the dimensions of the solid substrate, nature of the subphase, nature of the amphiphile, attraction of amphiphile to subphase, surface pressure at deposition, number of layers deposited, and the rate of substrate withdrawl through the monolayer. A poor transfer of a compressed monolayer onto a solid substrate can lead to irregular, clumpy or patchy films on the solid substrate. A poor monolayer transfer can be due to fluctuating surface pressures at the air-water interface or too fast withdrawl of the solid substrate through the monolayer.[55,115]

Although the Y-type deposition (with the manipulation of a hydrophilic solid support) can theoretically be used to obtain a lipid bilayer structure, it has been proven experimentally that the Y-type deposition was unsuccessful in the formation of 1,2-Dimyristoyl-*sn*-glycero-3-phosphocholine (DMPC) lipid bilayers.[117] Downward strokes followed by upward strokes gave only DMPC

monolayers that were directly attached to solid substrates. It was deduced that for a DMPC lipid monolayer at an air-liquid interface, a stronger interaction existed between the DMPC polar head groups and the liquid subphase than the interaction between DMPC polar head groups within a lipid bilayer structure.[117] Thus the force involved in the upward stroke of the Y-type deposition (transfer of the second lipid leaflet) is not sufficient to pull the DMPC monolayer from the air-liquid interface.[117] To overcome this drawback, an alternative technique, the Langmuir-Schaefer method can be used to transfer a second lipid leaflet.[115,117] The Langmuir-Schaefer technique involves a horizontal touch of a solid substrate to the surface of a subphase containing a compressed monolayer, and in this technique the solid substrate is not totally submerged in the subphase.[115,117] The compressed monolayer at the air-liquid interface is transferred to the solid substrate via electrostatic interactions, Van der Waals forces, or covalent bonding depending on the nature of solid substrate.

2.5.3 Applications of Langmuir monolayers and Langmuir films

Modern instruments equipped with sophisticated software are designed to investigate, monitor, and analyze floating monolayers and the deposition of monolayer films.[55,118] Also, modern Langmuir film instruments allow for the determination of molecular size, shape and packing; derived from values such as surface pressure, molecular weight, concentration and volume of sample used.[55,118] One application of Langmuir monolayers is for membrane modelling where various lipid components are chosen to construct a monolayer leaflet in order to study specific reactions e.g. protein aggregate-membrane interactions or

the role of cholesterol in membranes.[55,119] Another application of Langmuir films is in surfactant chemistry; the role of a surfactant in a monolayer can be understood and monitored.[55]

Monolayers deposited via Langmuir-Blodgettry have fascinating and varied applications. In molecular electronics, components or surfaces of electronic devices are often modified using Langmuir-Blodgettry.[55] Nanosized particles are deposited on surfaces to enhance the efficiency of the device or component, e.g. increase processing speed. Another Langmuir-Blodgettry application is the deposition of multilayers of specific organic molecules in laser devices. The presence of the multilayers formed by the X-type or Z-type deposition extends the frequency range of the laser.[55] One widely used application of deposited monolayers is for the fabrication of chemical and biological sensors. A specific monolayer is deposited on a solid surface that will attract target species in solution.[55] For example, Capone *et al.* used Langmuir-Blodgettry to deposit iron oxide nanoparticles onto the surfaces of chemoresistive gas sensors to improve the detection of gases such as NO_2 and CO.[120]

2.6 Electrochemical and spectroscopic methods for the characterization of cell membranes

2.6.1 Characterization of cell membranes by electrochemical methods

Advancement in the fields of both self-assembled and Langmuir monolayers has led to new avenues of research where deposited lipid bilayers

or lipid monolayers on electrode surfaces have been studied.[57,121,122] For example, studies have included the binding effects due to the adsorption of ions or molecules on membranes, understanding how membrane channels function, cell membrane permeability, and electron transport.[123-126] An example of an electrochemical method that has been used to characterize lipid bilayers is differential capacitance (DC). This technique describes the electrical double layer or film formed on an electrode surface based on its thickness and polarizability. As the electrode potential is varied, the surface charge of the electrical double layer changes.[57,127] Brosseau *et al.* applied this method for determining the approximate thickness of a supported membrane, investigating how compact the membrane was, and determining the level to which the membrane contained any gaps or defects.[128] Another electrochemical technique is cyclic voltammetry (CV). In this technique, the potential is cycled within a set range at the working electrode, and the current response is measured. This current response can be used to deduce possible film formation on the working electrode surface.[57,122] A journal paper published in the early 1990s by Andrew Nelson showed that a comparison between the control CVs (mercury electrode in the presence of redox species and electrolyte) and the CVs of lipid monolayer coated mercury electrodes showed a reduction in current response as a result of the redox species not being able to permeate the lipid surface.[129] These studies also showed that monolayer permeation of the redox species can be increased by altering the pH, ionic composition (whether univalent or divalent ions) and ionic strength of the electrolyte solution, and varying the applied electrode potential. Most

importantly the research done by Nelson demonstrated that adsorbed lipid monolayers at a metal electrode surface can be stable within set experimental conditions e.g. pH or applied voltage and also the lipid monolayer remains adsorbed to the metal surface. Nelson's work provided a new avenue for probing processes involving cell membranes, and the potential use of solid metal electrodes which can afford the application of spectroscopic techniques that required a solid metal surface (e.g. SERS).[129] This is evident in the numerous experiments that followed which either employed CV for studying membrane processes, or utilized Raman and SERS to investigate bilayer structures adsorbed on metal electrodes. An example of the application of CV for studying a cell membrane process was the work done by Wilkop *et al*. where they investigated pore-formation by bacterial toxins using CV.[130] In their research, control results showed that an electrode modified with a lipid bilayer in a supporting electrolyte with a redox probe present showed a significant reduction in current response when compared to that of the supporting electrolyte and redox probe only. When the bacterial toxins were introduced to the lipid bilayer system an increased current response was observed. They hypothesized that pore-formation allowed the redox probe and ions in the electrolyte to reach the surface of the working electrode and increase the current response.[130]

Electrochemical methods as highlighted above provide very useful results concerning biomimetic membranes. On the other hand, there are drawbacks to electrochemical methods; they do not provide structural

information or elemental composition, and in some cases information regarding the orientation of molecules on the electrode surface can be limited. Bruno Pettinger substantiated this point in his statement explaining why coupling electrochemical methods with Raman spectroscopy is beneficial, *"Data are needed with reference to surface states, surface energy band structures, surface composition and structure, and the type of bonding and the chemical identity of surface species. Such data are much beyond the scope of standard electrochemical investigations but are accessible with the methods of modern optical or electronic spectroscopies".[131]*

2.6.2 Characterization of cell membranes by Raman and Surface Enhanced Raman spectroscopy (SERS)

Raman spectroscopy and surface enhanced Raman spectroscopy (SERS) are spectroscopic methods which can provide insight into the identity, orientation, and structure of molecules.[56] Both methods are extensively used in the literature for the characterization of biomimetic model membranes. Ianoul *et al.* studied the interactions between lactoferricin B derivatives and model cell membranes using normal Raman spectroscopy.[91] In the Raman spectra, changes in signal intensities of peaks representing the alkyl chain region of the lipid components were used to ascertain if the lactoferricin B derivatives adsorbed or penetrated the model cell membranes. This work clearly indicated that Raman spectroscopy was sensitive enough to detect the binding of molecules to a model membrane surface.[91] Leverette *et al.* used SERS to identify peaks and determine the orientation of molecules present in a lipid bilayer supported on a SAM surface.

The emphasis was placed on studying the changes in a SAM upon adsorption of a lipid bilayer. The paper suggested that changes in peak intensities and shifts in peak positions observed for the SAM were a result of the bending or distortion of the alkyl chains in the SAM due to lipid bilayer adsorption.[91]

Data obtained from journal articles using both Raman spectroscopy and SERS for membrane studies provides a valuable resource for peak assignment of lipid components. This data will aid in the analysis of the findings obtained from the current research project. One crucial point to bear in mind when using literature Raman peak values is that the corresponding SERS values are either approximately the same or sometimes found within 10-20 wavenumbers (cm^{-1}).[132,133] Additionally, infrared spectroscopy (IR) wavenumbers in some instances are similar to Raman wavenumbers, and hence IR values are sometimes used as a reference point.[134] Table 2 gives examples of Raman and SERS peak values for a select few phospholipid vibrational modes.

Band Assignment	Raman Wavenumber Approximation (cm^{-1})	SERS Wavenumber Approximation (cm^{-1})	Functional Group
$v_s N^+(CH_3)_3$	717-719, 877, 930	715, 855	Choline[134-136,229]
$v_{as} N^+(CH_3)_3$	970	970	Choline[134-136,230]
$v_s(CH_2)$	2817-2881, 2889-2908	2843, 2873, 2926	Methylene in lipid tail[89,136]
$v_{as}(CH_2)$	2876-2908, 2929-2940	2880	Methylene in lipid tail[89,136]
$v_s(PO_2^-)$	1072-1086	1080	Phosphate[134-136,230]
$v_{as}(PO_2^-)$	1220-1250	1230-1250	Phosphate[134-136,230]
C=O	~1740	~1700	Carbonyl ester[134-136,228]
C-C	1060-1095	1065	Lipid tail[134-136,89]

Table 2: Examples for Raman and SERS band assignment for phospholipids. *v*, stretching vibrations; *as*, asymmetric; and *s*, symmetric.

2.6.3 Characterization of cell membranes by electrochemical Surface

Enhanced Raman Spectroscopy (EC-SERS)

Since SERS requires the use of a metallic surface, combining SERS with traditional electrochemical methods is straightforward. The combination of spectroscopic and electrochemical methods is termed spectroelectrochemistry.[122] The type of electrochemical method varies with the process under investigation or the structural composition of the species being examined.[122,57] Some researchers have used electrochemical and spectroscopic methods separately and combined the data to give an overall result.[137] Others have used these techniques simultaneously (EC-SERS) to comprehend the in situ dynamics of a process.[138] To validate the novelty of the proposed research project, emphasis was placed on journal articles employing the EC-SERS method to study biomimetic membranes.

EC-SERS has been used to explore the stability, organization and binding effects of SAMs, lipid monolayers and lipid bilayers on electrode surfaces.[122,139] Recently interest has grown in applying the EC-SERS technique in detecting low concentrations of analyte molecules in solution.[139] Li and co-workers modified gold electrodes with a SAM of benzoquinone to investigate the reaction between quinone rings and L-cysteine molecules, which was monitored by the EC-SERS technique.[140] The reaction was optimal at more positively applied voltages and specific peaks in the resulting SERS spectra marked the presence of the desired final product. The researchers concluded that the results obtained from their experiment showed promise as a possible application in biosensing.[140] EC-SERS has also been used to explore the polymerization

process of molecules on a solid surface.[140] For model membranes, EC-SERS has provided information on conformational changes due to the presence of redox-active biomolecules, configuration of lipid components due to adsorption of species, and intermolecular orientations and conformational changes due to a change in applied voltage.[141] For example, Vezvaie *et al.* used in situ EC-SERS measurements to characterize 1,2-Dimyristoyl-*sn*-glycero-3-phosphocholine (DMPC) lipid bilayers deposited by the Langmuir-Blodgett/Langmuir-Schaefer technique onto highly ordered nanocavity patterned Ag electrodes.[138] The Ag electrodes were modified with a hydrophilic surface (created by a SAM of β-thioglucose) to facilitate deposition of the DMPC lipid bilayers. The results from this study showed that the DMPC lipid bilayer alkyl chains were oriented perpendicular to the modified Ag electrode surface and that the alkyl chains were slightly tilted. In addition, the DMPC lipid bilayers existed in a liquid-crystalline state for the entire potential range (0 V to -1.2 V) with the lower lipid leaflet having more order than the upper lipid leaflet, and at more negative potentials the DMPC lipid bilayer desorbed from the modified Ag electrode.[138] To date, to the best of our knowledge, no research has been completed towards the validation of the pore-hypothesis for AD using EC-SERS to examine aggregate-membrane interactions.

3 Theory

3.1 Introduction

This section provides the background theory for the analytical procedures and methods used to probe the physical and electrical properties of the proposed biomimetic model membrane system.

3.2 Nanoparticle synthesis and characterization

Nanoparticles (NPs) can be thought of as small individual units or particles ranging in size from approximately 1-100 nm. The vast majority of nanoparticles consist of a metal core surrounded by ligands, surfactants, or other molecules.[142] NPs are typically synthesized via two main routes: solution-based and gas/vapour-based. Solution-based techniques are convenient, cost-effective, and thus more commonly used. These techniques include the reduction of a salt, decomposition of a precursor organometallic complex, or colloidal aggregation.[142] The morphology and shape of the nanoparticles is also important e.g. cubes, rods, spheres, triangles or spiked edges.[142] Such diversity in nanoparticle size and composition translates into a wide range of applications such as for use as catalysts, incorporation into existing magnetic materials to improve electrical and magnetic properties, and the development of sensor-based devices.[142]

The relevance of nanoparticles in SERS is to provide a nanoscale roughened surface necessary for the SERS effect to take place. Other factors

crucial for generating the SERS effect are dependent on the optical properties of the individual particles, for instance light absorption or light scattering, and in addition the possession of free electrons to create the necessary localized surface plasmon resonance (LSPR).[142,143] Derived from these conditions is the extensive use of conductive coinage metals such as Cu, Ag, and Au to create effective SERS substrates.[142,143] Ag is the metal of choice because it gives a stronger SERS effect. This is believed to be correlated to the fact that Ag outer electrons can transfer to the conductance band more easily than other metals such as Au giving rise to the LSPR.[142,143] In designing and conducting SERS experiments, the synthesis of Ag substrates can be less costly than Au ones.[144] However, disadvantages of using Ag as a SERS substrate include inherent instability, ease of oxidation, and in addition it has been shown that macrophages, lung cells, and tumor cells exposed to silver nanoparticles (AgNPs) can undergo oxidative stress, cell damage, or cell apoptosis.[145,146]

Although there has been much success associated with the use of nanoparticles in various applications, inconsistent nanoparticle shape and size can affect data quality.[142] In a critical review by Cuenya concerning the catalytic properties of nanoparticles, inconsistencies in the size and shape of nanoparticles used in specific reactions was shown to reduce catalytic activity.[147] It was deduced that more spherical surface morphologies, irregularly shaped, and large NPs reduced substrate binding, resulting in a decrease in the amount of product formed.[147] One of the simplest known procedures that yields very small and relatively uniform colloidal AgNPs occurs via a chemical reduction of a silver salt.[142] The added benefit of using this wet

chemistry synthetic route is the ease of manipulation of the size and growth of the AgNPs which can be simply altered by varying the following experimental conditions: ratio of metal reactant to reducing agent, type of reducing agent, temperature, pH, types of stabilizing reagents, and reaction time.[142] Although the chemical reduction route is simple, the main disadvantage of this method is that over time continued aggregation of the colloids reduces the number of NPs present and increases the overall size of individual NPs.[142] Upon achieving the desired size and shape of AgNPs, the colloidal suspension of AgNPs can be deposited onto a solid substrate to provide a roughened surface that will afford the application of the SERS technique.[56] The uncomplicated synthetic route of synthesizing AgNPs and the quick method of obtaining a roughened metal surface by colloidal deposition unto a solid substrate is one of the rationales for choosing this method for the proposed research project. Another rationale why the use of AgNPs as a SERS substrate is feasible stems from the numerous successful SERS studies already reported on such surfaces for the investigation of biological and non-biological molecules.[148]

3.3 Raman spectroscopy

3.3.1 Basic principles of Raman spectroscopy

Raman spectroscopy involves the study of the vibrational modes of an analyte due to its interaction with monochromatic light.[132] The frequency of the monochromatic light is typically in the visible region of the spectrum (300-780 nm).[149] When a photon interacts with a sample, one of the following can occur: the photon is absorbed, the photon is scattered or the photon is

transmitted.[132,149] Specifically for Raman spectroscopy, the incident photon undergoes inelastic scattering. In this process, there is a net energy transfer between the incident photon and the analyte molecule. The incident photon can either gain or lose energy to the analyte and thus there is a net energy loss or gain in the system. When the analyte gains energy from the incident photon resulting in a scattered photon that has a lower frequency than the incident photon, the process is referred to as Stokes Raman scattering. On the other hand, Anti-Stokes Raman scattering refers to energy passing from the analyte to the incident photon giving a scattered photon of higher frequency. Another type of scattering which is much more common, is Rayleigh scattering. In this type of scattering, there is no net gain or loss of energy.[132,149] Figure 12 is a diagrammatic representation of the types of scattering outlined above. Raman scattering is weak due to its low occurrence; about 1 in every 10^6 incident photons are Raman scattered.[56,132,149] Thus measuring a Raman signal usually entails filtering out stronger signals such as Rayleigh scattering (1 in 10^3). [132,149]
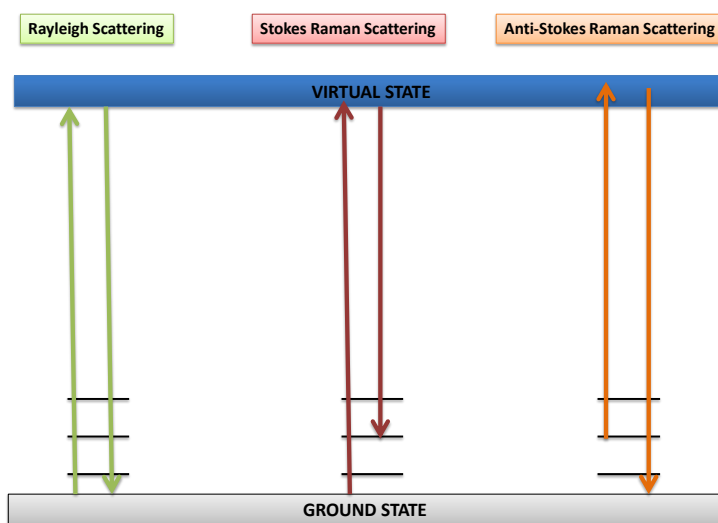
Figure 12: A diagram showing the energy unchanged, gained, or lost due to the vibrations of analyte after the interaction with monochromatic light.

A Raman spectrum is a plot of signal intensity versus wavenumbers, cm^{-1}.[132,149] Each peak in a Raman spectrum corresponds to a different vibrational mode (i.e. stretching, bending etc.) of a specific molecule based on its chemical bonds, atom or ion composition, and symmetry.[132,149] The wavenumber represents the energy difference between the incident photon and the Raman scattered photon. Consequently, Raman spectroscopy can act as a chemical fingerprinting technique for molecules since their particular chemical bonds, atom composition and symmetry translates into a specific layout of peaks in a spectrum. A full range Raman spectrum goes from ~500 cm^{-1} to 3200 cm^{-1}, while the detailed region (referred to as the fingerprint region) ranges from about 400 cm^{-1} to 2000 cm^{-1}.[132,149] Over the years research in the fields of Infrared and Raman spectroscopy has led to the development of the concept of group-frequency where unique wavenumber frequencies are observed for particular functional groups.[149] Table 3 lists some examples of established wavenumber frequency ranges for selected functional groups.

Functional group	Wavenumber region (cm^{-1})	Description
C=O	1550-1870	Esters, ketones, carboxylic acids and amides[134-136]
C=C	1620-1690	Olefin compounds[134-136]
O-H	960-875	Carboxylic acids[134-136]
O-H	3580-3670	Intermolecular hydrogen bonding of hydroxyl groups[134-136]
NH_2	3100-3600	Secondary and tertiary amines[235]
C≡N	2200-2400	Nitriles[231]
C≡C−	2100-2260	Alkynes[231]
$CONH_2$	1640-1720	Amides[231]
R−O−R	1060-1160	Aliphatic ethers[231]

Table 3: Examples of group frequency wavenumber values for specific functional groups and interactions.

3.3.2 Raman spectroscopy: Polarizability and selection rule

When a photon impinges on a molecule it interacts with the electron cloud around the atomic nuclei, causing a change in the polarizability of the molecular electronic cloud.[56] The electron cloud becomes distorted and a dipole moment is induced within the molecule. The formation of such a dipole moment is correlated to how easily the electron cloud can be distorted, i.e. if a molecule is easily polarized, a dipole moment is readily formed.[56] It is this change in shape and size of the electron cloud distortion that is monitored in Raman spectroscopy and also this perturbation dictates how Raman active a molecule is.[56] For example, when homonuclear diatomic molecules such as $O_2(g)$ that are non-polar (no dipole moment) interact with a photon of light of sufficient energy, an induced dipole moment occurs, rendering the molecule Raman active.[150]

The selection rule for Raman spectroscopy dictates that the polarizability of a molecule must change during a vibration.[56] Typically, symmetric molecules, symmetric bonds or large delocalized electron clouds are more polarizable and thus are the greatest Raman scatterers e.g. phenyl rings give strong Raman signals because they possess large delocalized electron clouds that are easily polarized.[132,150,151] Asymmetric molecules and/or asymmetric bonds that already have a dipole moment are generally not Raman active and give little to no signal e.g. weak Raman signals are obtained from the vibrations of the OH bond since it has a dipole moment and is less polarizable.[150,151] A simple explanation for this lack of signal is that the interaction of the photon may not bring about any further polarizability since the molecule already exists in a dipole

state and no overall net change can be detected.[150,151] The selection rules are used to help Ascertain whether vibrational modes might be Raman active or inactive.[56,150]

Dipole moments of highly polar groups are generally infrared (IR) active since IR spectroscopy relies on a change in dipole moment to provide signal.[150] Vibrational modes within a molecule can be either IR active, Raman active, or IR and Raman active.[150] For example, for carbon dioxide the asymmetric stretch of the C-O bond has a dipole moment which renders it IR active. Since this asymmetric stretch of the C-O bond is already in a dipole state, interaction with radiation energy does not bring about a greater dipole moment and therefore no change in its polarizability, hence giving no Raman signal. For the carbon dioxide asymmetric C-O bond it can be said that this bond is IR active and Raman inactive.[150] This characteristic is typically found in molecules that are centrosymmetric and for this reason this feature has been used to identify the symmetry of molecules. In Raman spectroscopy this is called the mutual exclusion principle.[56,150] The mutual exclusion principle has been used to determine if a molecule has a center of symmetry and typically molecules with no center of symmetry possess a vibrational mode that is both Raman and IR active.[56,150]

Since the basis of Raman spectroscopy relies on the polarizability of an analyte, the environment or state of the analyte is important to consider. Whether a solid, dissolved in a liquid, a species in the gas phase, or adsorbed on a substrate, all of these conditions can have an affect on the observed Raman signal.[56,149] Interactions between solvent and analyte, or packing of an analyte into a crystal

lattice can affect bonding environments since this can alter the symmetric or asymmetric nature of bonds.[56,149] These changes in bond environment can lead to shifts in observed wavenumbers, peak broadening, as well as the appearance or disappearance of peaks in the spectrum.[56,149] Such observed changes in the spectra can allow deductions to be made based on possible interactions present in solutions. For example, in experiments investigating the interactions of the amino acid tryptophan (trp) with 1,2-Dimyristoyl-*sn*-glycero-3-phosphocholine (DMPC) lipid bilayers the extent of hydrogen bonding was observed by changes in peak intensity of the three trp marker peaks for hydrogen donation: i) carboxyl OH group, ii) primary amine group, and iii) secondary amine group. In these experiments, Raman spectra of trp only and trp with DMPC lipid bilayer were compared, and it was deduced that increased peak intensities of the trp marker peaks was an indication of the existence of hydrogen-bonding interactions between trp and the DMPC lipid bilayer.[88]

3.3.3 Raman spectroscopy instrumentation

Raman instrumentation is centered around focusing the monochromatic laser radiation onto a sample and the collection of the resulting Raman scattered photons. The basic components of Raman spectrometers include the following: laser source, sample holder, filters, gratings, detector, and data processor.[132,149]

The laser source provides high powered radiation at a chosen wavelength which is directed onto the sample by lenses at a particular focal length. This ensures that the beam of radiation is concentrated onto the sample and scattering of

the incident beam is reduced.[132,149]   The size of the beam on the sample can be adjusted by changes in the diameter of the aperture from which the laser beam emerges.[132,149]   The sample is contained or mounted onto surfaces that have very little to no Raman scattering, easily transmit laser radiation, block external light during measurement, and prevent the laser beam from exiting the holder.[132,152] Sample holders and sample units typically consist of glass, aluminum, and plastic.[149] The sample can be investigated via two methods. Conventional Raman spectrometers have a 90° geometry where the laser beam direction is perpendicular to the direction of the collection axis.[152]   The 90° geometry was designed to reduce laser radiation from reaching the detector. Modern Raman spectrometers have a 180° geometry (back-scattering mode) where the laser beam axis and the collection axis coincide.[152] The radiation from the sample as a result of the interaction with the laser is passed through filters to eliminate all Rayleigh scattering. In the 180° geometry, an optical component (collection lens) is present that both blocks Rayleigh scattering and directs Raman scattered light towards the next instrument component. The filtered light is then passed to the grating which separates the radiation beam into individual wavelengths. The separated wavelengths are then directed onto the detector which transforms the radiant energy into an electrical signal. The electrical signal is then used to generate a Raman spectrum of peak intensity versus wavelength, which is converted to peak intensity versus wavenumber.[152]

3.3.4 Advantages and limitations of Raman spectroscopy

One main advantage of Raman spectroscopy is that water is a weak Raman scatterer. Hence, biological molecules can be studied in an aqueous environment without strong interferences arising from the aqueous medium.[149,152] Another advantage is that Raman spectroscopy is a well-known non-destructive technique because in monitoring the vibrational modes of the analyte no bond breaking or formation occurs. This non-destructive nature of the technique is one of the reasons that Raman spectroscopy is used as a quantitative method since in some cases, an increase in analyte concentration can lead to an increase in signal intensity.[149,151] Other benefits of Raman spectroscopy include the ability to analyze heterogeneous samples, rapid signal acquisition, and complementary information can be gained from Raman spectroscopy to supplement data from other techniques such as IR.[149,152] For example, Raman can be used to study skeletal or backbone vibrations in molecules where IR has reduced capability in this regard.[134]

The numerous advantages of Raman spectroscopy such as excellent fingerprint spectral detail, small required analyte volume, low sensitivity to water, as well as speed of spectral acquisition makes the applications of Raman spectroscopy broad; as such it has been applied to various fields. Some general examples include:[132,149]

-In inorganic chemistry, Raman spectroscopy has been used to study the bonding environment in metal complexes.

-Organic chemists have used Raman spectroscopy to identify the presence of specific functional groups in a final product e.g. the formation of an alkene can be marked by the appearance of the Raman peaks for the C=C bond.

-In material science Raman spectroscopy is used to study the orientation of crystallites in a polycrystalline solid.

-In forensics Raman spectroscopy is used to identify the presence of blood or urine in samples.

To overcome the disadvantage of weak Raman scattering, the following can increase the Raman signal of an analyte: increasing the intensity of the laser power or increasing the concentration of the analyte.[149] Increasing the power of the laser will affect the signal intensity but not the position of the Raman peak (Raman shift).[149] The negative effect of increasing the laser power is that it can cause degradation and fluorescence of the sample. Fluorescence (typically occurs at shorter laser wavelengths) happens when the analyte absorbs the incident light energy and is elevated to an excited electronic state instead of a virtual state.[149] If the chosen wavelength used to obtain a Raman spectrum is in the same wavelength region that causes fluorescence of the sample, then the weak Raman signals can be masked by the much stronger fluorescence signal. However, fluorescence can be reduced by using a wavelength outside of the absorption band of the analyte, and degradation of the sample can be decreased by reducing the laser power and/or exposure time.[149]

3.3.5 Basic principles of Surface Enhanced Raman Spectroscopy (SERS)

To improve upon the sensitivity of Raman spectroscopy a new technique was developed in the late 1970s called surface enhanced Raman spectroscopy (SERS).[56] In this method, the analyte is near to, adsorbed onto, or chemically bonded to a roughened metal surface. Monochromatic radiation is then focused on this surface and an enhanced vibrational signature is obtained. The enhancement leads to signal amplification in the range of $10\text{-}10^{13}$. From the onset there has been a debate as to what factors contribute to this signal enhancement.[56] Since a signal must be generated from energy transfer between the incident photon and the analyte, it was deduced that additional energy must somehow be transferred from the roughened metal surface to the analyte.[56] Investigations into this theory showed that irradiation by the laser caused the creation of a local electromagnetic (EM) field generated by the oscillations of valence or free electrons in the metal. The collective oscillation of these conductive electrons was termed a localized surface plasmon resonance (LSPR). These oscillating electrons have limited area and do not propagate far from their site of origin.[56] The theory used to describe the signal enhancement due to the interaction between the oscillating electrons and adsorbed analyte is called the "EM mechanism". However, the SERS signal contribution was not solely from the presence of this LSPR. It has been argued that chemical effects have some contribution to the SERS signal or enhancement. Chemical effects are said to arise from the interaction of the analyte molecule with the surface of the NPs. This interaction can lead to distortion of the analyte's electron cloud, changes in the analyte's polarizability, and charge transfer between

the metal-analyte complex formed, all of which can contribute to the SERS enhancement. This mechanism of enhancement has been termed the chemical enhancement (CE) mechanism.[56]

SERS and Raman spectra are identical in layout where the signal intensity is plotted against wavenumber (Raman shift). The basic experimental set-up, sample acquisition time, and instrumentation are also equivalent. The main difference arising between Raman and SERS is the presence of a roughened metal surface. The roughened metal NP surface is required to afford the SERS effect and the observed signal enhancement.[56,132]

3.3.6 SERS: chemical and electromagnetic contributions

Understanding the factors that govern the EM and CE theories can lead to better interpretation of spectral data, or manipulation of experimental conditions to yield stronger signals. The EM field enhancement is dependent on the availability of free or valence electrons and the radiation frequency.[56,142] SERS substrates are traditionally made from noble metals because in addition to their great ability to absorb or scatter light, they possess outer-shell electrons that can readily enter the conductance band. The energy required to produce free electrons varies from metal to metal. The absorbed incident energy must match or have a higher energy than that required to generate oscillating electrons. For example, typically the absorbance peak for AgNPs falls around 400-550 nm, and therefore an incident photon with a wavelength within this region would be sufficient to generate conductive electrons for AgNPs.[142] The movement of electrons causes a polarization of the electron cloud and results in a dipole moment. This dipole

moment induces polarization and/or a dipole moment in the adsorbed molecule.[142]

The CE theory of SERS originates from the direct interaction of the metal and SERS substrate, i.e. whether there is physical or chemical adsorption.[56,142] For physisorption, the analyte comes close enough so that its electron cloud interacts with that of the metal, i.e. the molecule can experience the SERS effect. Yet, the analyte does not come close enough to form a chemical bond.[56,142] In chemisorption, the analyte comes close enough to the metal surface so that the overlap of the electron clouds fall within the realm of a chemical bond. If there is enough energy provided to the system during chemisorption there can be transfer of electrons between analyte and metal or vice versa. Regardless of the nature of the interaction, both cases cause a distortion of the analyte electron cloud and contribute to the observed SERS enhancement.[56,142]

3.3.7 Factors affecting SERS signal

Since the metal NPs play a crucial role in the SERS effect, their size, shape, and surrounding environment become important factors. Changing the size of NPs changes their optical properties dramatically.[142] If the NPs are midsized to large (~60-100 nm) or even larger, absorption of the radiation is lowered and reflection is dominant. This reduces the manifestation of LSPR and hence reduces the SERS effect.[142] For very small NPs (<10 nm) transition of electrons to the conductance band becomes more difficult since the energy requirement for this process increases. Thus shorter wavelengths (higher energy) are required to

bring about LSPR.[142] The obvious reason for achieving uniformed NPs of a desired size is evident, since the presence of smaller or larger NPs can reduce the occurrence of the LSPR, resulting in a poor SERS signal.[142] The LSPR can also be reduced by changing the surface morphology of the NPs. The interaction of solvent molecules or the addition of ligands to the surface of NPs can reduce the availability of oscillating electrons and distort the metal's electron cloud, shifting the occurrence of LSPR to higher or lower wavelength.[142]

Classically NPs are spherical, but recent research where the shape of NPs has been modified to include flower-shaped, jagged or pointed morphologies have shown increased LSPR and stronger more uniform SERS enhancements.[142] The enhanced LSPR effect is linked to the increased possibility of forming more dipole moments. Symmetric spheres have one possible dipole moment, while shapes with many edges have multiple dipole moments along each edge or face.[142] An intense SERS signal and strong LSPR have been linked to closely packed NPs. The interpretation for this effect was based on inducing dipole moments in other particles, and consequently creating areas of numerous dipole moments.[142] The term "hot spots" is used in the literature to describe areas on a SERS substrate that have a greatly amplified SERS signal.[56,142] Another significant aspect of the substrate morphology to bring about the SERS effect is the roughness of the metal surface. A roughened metal surface is more likely to absorb radiation energy as opposed to reflecting radiation. Absorbance of radiant energy is needed to create oscillating conductive electrons.[142]

SERS is a distance and coverage dependent technique. For an adsorbed

analyte molecule to experience the SERS effect, it must be close to the roughened metal surface. It has been proven experimentally that molecules with distances greater than 10 nm from the roughened metal surface do not experience the SERS effect. [56,142] It was deduced that the EM field generated from the oscillating electrons at the roughened metal surface dissipates beyond this distance and there is not sufficient energy to induce changes in the polarizability of the analyte molecules. In addition, there is also a reduction in CE effects because at this distance analyte molecules are neither physisorbed or chemisorbed, and an overlap of the electron clouds between analyte molecules and the roughened metal does not occur. The overlap of electron clouds between analyte molecules and the roughened metal surface brings about distortion of the analyte electron cloud and as a result changes in the polarizability of analyte molecules. Since both the CE and EM effects are reduced, the molecules do not experience the SERS effect and very weak or no SERS signal is observed. Therefore, strong SERS signals for analyte molecules are observed when these molecules are directly adsorbed near the roughened metal surface. Strong SERS signal is also observed when the concentration of analyte molecules is high. The high concentration of analyte molecules ensures maximum coverage of the roughened metal surface and an increase in the SERS signal is due to an additive effect.[56,142, 181]

The orientation and strength of interaction of the analyte species on the roughened metal surface determines the signal strength, as well as the presence or absence of peaks in the SERS spectrum.[56,142] Vibrational modes that are perpendicular to the metal surface give a strong SERS signal while vibrational

modes parallel to the metal surface give negligible to no SERS signal.[56] This observation is referred to as the SERS surface selection rule and has been useful in determining the orientation of molecules adsorbed on SERS substrates.[56] An explanation for this phenomenon arises from the polarizability tensor created between the adsorbed analyte and roughened metal surface. Vector quantities described by both size and direction are used to represent dipole moments in SERS theory. Thus if a vibrational mode is parallel to the surface and experiences a dipole moment, it induces a dipole moment of equal magnitude but opposite in direction in the SERS substrate, hence cancelling the analyte's dipole moment resulting in no SERS signal. Vibrational modes that are perpendicular to the SERS substrate induce dipole moments in the SERS substrate that are of the same magnitude and direction, therefore enhancing the analyte's dipole moment and giving a SERS signal. Figure 13 illustrates this point.[56]
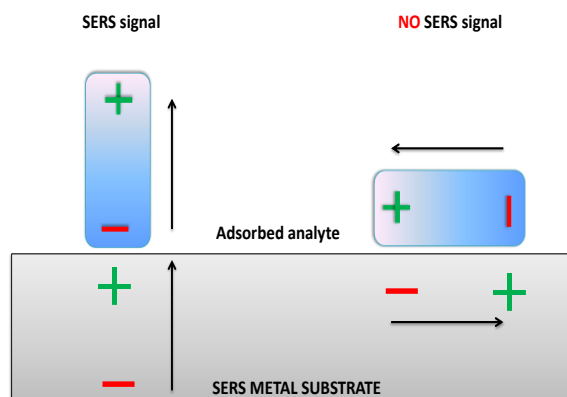
Figure 13: A diagram illustrating how the surface selection rules of SERS based on polarizability tensors dictates the appearance of a SERS signal for adsorbed molecules.

This phenomenon can explain differences in the Raman and SERS spectra of the same analyte since a peak in the SERS spectrum will be greatly reduced or

absent if that vibrational mode is now parallel to the roughened metal surface. For analytes which are strongly adsorbed onto the roughened metal surface, the electron clouds for both parties involved are modified. This modification can make the electron clouds less symmetric or less dipolar generating a weak SERS signal and a strong SERS signal, respectively.[56,142]

The SERS technique offers increased sensitivity for very low analyte concentration, high specificity and selectivity, and additionally there is experimental proof for single molecule detection capability.[56] On the other hand disadvantages include: complex spectra due to heterogeneous systems, signal interference from impurities, degradation of analyte by the laser beam, desorption of analyte molecule from the SERS substrate by the laser beam, non-uniform SERS signal due to differences in NP shape and size, dissimilar SERS spectra of the same analyte due to various orientations of the analyte molecule on the SERS substrate.[56,142] Additionally, the non-uniform enhancement that typically occurs with the SERS technique makes it a poor choice for quantitative analysis.[56]

3.3.8 Biological applications of SERS

SERS applications are prominent in the biological field; for example it has been used for the detection of proteins, DNA, nucleotides, peptide aggregates (i.e. Aβ) and other biological molecules.[141] From time to time, modifications are made to the surface of the SERS substrate in order to bind or attach target analyte species if they cannot adhere to the SERS substrate easily.[141] Negri and his researchers suggested this type of technique facilitated binding in their

experiment.[153] The aim was to detect influenza by attaching a strand of DNA to the metal NP surface that binds specifically to the influenza nucleoprotein. The modified NPs were then placed in a solution containing the influenza strain as well as other species. The experiment proved successful and the manipulated surface was polyvalent in nature i.e. had the ability to bind different strains.[153] Researchers have also used SERS coupled with other techniques to obtain particular biological information. For example, Doering *et al.* coupled SERS and with an immunoassay technique to detect the presence of cancerous tissues in the colon.[154] Immunoassays are used to detect the presence of specific macromolecules via the binding of an antigen present on an analyte molecule to the corresponding antibody present on target molecules. In their article, SERS nanotags were used, which were composed of SERS-active metal cores (Ag or Au) whose surfaces contained strong Raman scattering molecules (referred to as reporter molecules) as well as the specific antigens that bind to the antibodies of interest. Both cancerous and non-cancerous tissues were treated with the antibody and then exposed to the SERS nanotags. The results showed that only the cancerous tissues gave a SERS signal from the reporter molecules.[154] SERS can also be used to characterize and study the interactions of SAMs e.g. molecular orientation of molecules within a SAM at an electrode surface due to specific redox behaviour. Nishiyama *et al.* studied the assembly of anthraquinone derivatives on Au and Ag electrodes based on their redox states using SERS.[155] The results showed that molecular orientation of the anthraquinone derivatives within the SAM was dictated by electrode potential, the nature of the SERS

substrate, redox state, and the functional groups attached to the anthraquinone moiety. For example, 2-anthraquinonylbutylsulfide in its reduced form was tilted so that the ring moieties were almost parallel to the metal surface, while the oxidized form had a perpendicular orientation with respect to the metal surface.[155]

3.3.9 Characterization of alkanethiols, monolayers, and bilayers using SERS

SAMs have been characterized by many methods in order to understand their structure, properties, and defects.[96] These methods include but are not limited to AFM, STM, X-ray Photoelectron Spectroscopy (XPS), CV, contact angle measurements, Raman Spectroscopy, and SERS.[96] Since carboxyl terminated alkanethiol SAMs were employed in this research project, results from the SERS characterization of these types of molecules will be the focus of this section.

The two main SERS signals used to signify the presence of an adsorbed alkanethiol SAM on a metal surface are the *trans* and *gauche* conformation vibrational modes.[110,156] The *trans* and *gauche* conformations are denoted by $v(C-S)_T$ and $v(C-S)_G$, respectively. The intensities of these SERS peaks indicate if the monolayer is well formed. If the $v(C-S)_T$ conformation is much higher than the $v(C-S)_G$ conformation then the monolayer is said to be well organized with relatively few kinked chains.[110,156] Table 4 gives a summary of band assignments for SERS vibrational modes of alkanethiols adsorbed on metal surfaces. This table combines common stretches seen for various chain lengths and carboxyl

terminated chains.

Band Assignment	SERS Wavenumber Approximation (cm^{-1})
Metal-Sulphur bond[110,159]	200-360
CCC/CCS deformations[110,159]	400
COO^- [102]	525
COO^- [157,158]	575
$v(C-S)_G$ [90,101,102,109,110,157,159]	620-650
$v(C-S)_T$ [90,101,102,109,110,157,159]	700-740
CH_2 rocking[90,110]	700-900
$(CH_2)_G$ [159]	848
$(CH_2)_T$, CH_3rock[90,159]	891
C-COOH[102]	896
COOH[104,109]	900
COO^- [102,104,109]	930
$v(C-C)$ [102,110,159]	1000-1100
$(C-C)_T$ [90,159]	1070
$(C-C)_G$ [90]	1080
$(C-C)_T$ [90]	1126
(CH_2) twisting[110,158]	1250
(CH_2) wagging and twisting[90,102,110,159]	1300
COOH[157]	1387
COO^-, COO^-Ag^+ [102,104,157,158]	1395
CH_2 bending[90,102]	1435
COO^- [109]	1570
C=O, hydrogen bonding[109,157,158]	1680
C=O, hydrogen bonding[110,157]	1700
$v(S-H)$ [101]	2577
$v_s(CH_2)$ [90,110,158,159]	2850
$v(C-H)$ [90,110,158,159]	2960

Table 4: Cumulative band assignment for alkanethiols adsorbed unto metal surfaces. *v*, stretching vibrations; G, *gauche*; and T, *trans*.

The relative intensity and absence or presence of SERS peaks can provide information on alkyl chain orientation and SAM formation.[110] The interaction of the SAM with other molecules will cause a change in peak intensity depending on how these molecules interact with the monolayer.[90] For molecules such as ions that penetrate the SAM, more *gauche* defects or bending of the chains is

expected, while in some instances lipid monolayers or bilayers that adsorb onto the terminal groups of the SAM may cause reordering of the alkyl chains within the SAM resulting in more *trans* conformations.[90,103,110] An important peak is the SERS band for the stretching of the sulphur and hydrogen bond, v(S-H), for thiols adsorbed on a metal surface. The presence of this peak, usually appearing at 2577cm^{-1}, is a clear indication that the alkanethiol did form the desired metal-S bond.[101]

Lipid monolayers and bilayers can form ordered layers on a solid surface (similar to SAMs) using techniques such as Langmuir-Blodgettry.[115] The deposition of compact lipid layers onto SERS substrates creates a barrier that prevents direct contact of analyte species in solution with the roughened metal surface.[96] It has been shown experimentally that analyte molecules which do not penetrate inert layers (such as lipid monolayers and bilayers) formed on the surfaces of SERS substrates gave weaker SERS signals due to the increase in distance between analyte molecules and the roughened metal surface.[56] As mentioned previously, an analyte must be close to the roughened metal surface (i.e. within a few nm) in order to experience the CE and EM effects and thus provide a SERS signal. Therefore proof for the formation of a compact well-ordered lipid monolayer or bilayer with complete coverage can be determined by a corresponding decrease in the signal of a SERS-active analyte.[56]

Changes in molecular orientation and polarizability of adsorbed species at a roughened metal surface can also affect SERS signals.[56,142] One example where analyte species adsorbed at a roughened metal surface can change their

orientation and polarizability is by the physical adsorption of molecules onto lipid monolayers and bilayers that are directly adsorbed onto a SERS substrate.[56,142] Adsorbed molecules can cause bending and tilting of lipid alkyl chains, and such alterations in lipid monolayers and bilayers can be observed in the SERS spectra. For example, shifts in wavenumbers of particular peaks, the disappearance or appearance of peaks, and changes in the signal intensities of specific peaks can be observed.[160]

3.4 Electrochemical measurements

3.4.1 Components of an electrochemical cell

Electrochemistry is an analytical method that merges chemical and electrical energy. Modern electrochemical measurements require an electrochemical cell and a potentiostat.[149] The main components of an electrochemical cell are the electrodes and electrolyte. The electrolyte is the conductive liquid medium where ions, both negative and positive, are present due to the partial or complete dissociation of ionic substances.[122] The electrodes are immersed in the electrolyte solution and the material that the electrodes are made from varies depending on the reaction investigated or the electrolyte used. Common electrode materials include solid metals (i.e. Pt, Cu), liquid metals (i.e. Hg or amalgams), carbon (graphite), and semiconductors (Si).[122] The transfer of electrons between electrodes and electrolyte solution generates a current within an electrochemical cell during which redox processes can occur. For oxidation there is a flow of electrons from the solution to the electrode called the oxidation/anodic

current while for reduction there is a flow of electrons from the electrode to the solution called the reduction/cathodic current.[122] Electrochemical cells can be categorized as Galvanic (Voltaic) cells or electrolytic cells. In Galvanic cells, the reactions occurring at the electrodes are spontaneous and generate an electric current. Conversely, in electrolytic cells the reactions are not spontaneous and electrical energy is used to force the reaction to proceed.[122]

A three-electrode system is a special type of electrochemical cell that is applied to voltammetric methods. In voltammetric methods the resulting current is measured at a specific electrode as the potential is varied. The three electrodes are the working electrode (WE), the reference electrode (RE), and the counter electrode (CE).[122] The WE is the site of interest for the analytical species under investigation. At this electrode, the potential is varied and the resultant current is measured. The RE functions to measure the value at the WE. REs are used to determine a potential value at a specific electrode (WE) with respect to specific analyte ions.[122] In some instances the RE and the WE are placed closer together in the same electrolyte in order to reduce the liquid-junction potential that stems from the difference in concentration of two separate electrolyte solutions in contact with each other, and to lower the electrical resistance derived from wires connecting two separate compartments. The potential of the RE is kept constant and has a relatively precise value.[122] The potential value of a RE can be affected by temperature, applied current, and time. A potential value for the WE can be derived from the potential difference between the RE and WE.[122] Examples of REs include the standard hydrogen electrode (SHE) which has a potential value

of 0.000V, and the silver/silver chloride electrode (SSCE, or Ag/AgCl) which has a potential value of 0.199V at 25°C.[149]   Electrical current is prevented from flowing to the RE so that its potential remains stable. This leads to the purpose of the CE, which is typically a solid inert metal such as Au or Pt which has a larger surface area than the WE, which functions to accept and balance the current at the WE, and completes the electrical circuit.[122]   Potentiostats are electrical devices used in a three- electrode system to measure and control the voltage between the working and reference electrode, and to measure the current flow between the WE and CE.[149]

3.4.2 Electrical double-layer structure

The site of interest in an electrochemical reaction is at the WE surface. At the interfacial region of a solid electrode and an electrolyte, a very thin layer exists which is termed the electrical double layer.[122,161] The electrical double layer is used to describe the ordering of positive and negative ions at an electrode surface. The potential and the ordering of species within the double layer are different to that of the bulk solution.[122,161] Several models have been developed to help describe the ordering of species at the electrode and the resulting double layer structure. Two examples of such electrical double layer models are the Grahame model developed in 1947 and the Bockris/Devanathan/Müller model developed in 1963.[162] The Grahame model first defined the area around the electrode surface into three regions. The first region consists of specifically desolvated adsorbed ions that are directly in contact with the electrode surface.

This is the most compact layer and the specifically adsorbed ions can be of any charge. An imaginary vertical line passing through the center of this first compact layer of ions is called the inner Helmholtz plane (IHP). The next layer consists of solvated ions and solvated non-specifically adsorbed ions. This layer is less compact and an imaginary vertical line passing through these ions is called the outer Helmholtz plane (OHP). The final region is called the diffuse region/layer and this exists outside the OHP. The ions are all solvated and widely dispersed among solvent molecules. The concentration of ions is said to exponentially decrease with respect to the distance from the electrode surface and hence the electrical potential also decreases exponentially away from the electrode.[162] The Bockris/Devanathan/Müller model (Figure 14) is similar; however, it takes into consideration the presence of solvent molecules. For this model, within the IHP region are solvent molecules and desolvated, specifically adsorbed ions which are directly attached to the electrode surface. The OHP consists of solvated ions, solvent molecules and solvated non-specifically adsorbed ions while the diffuse layer contains widely spaced solvated species and solvent molecules.[162]
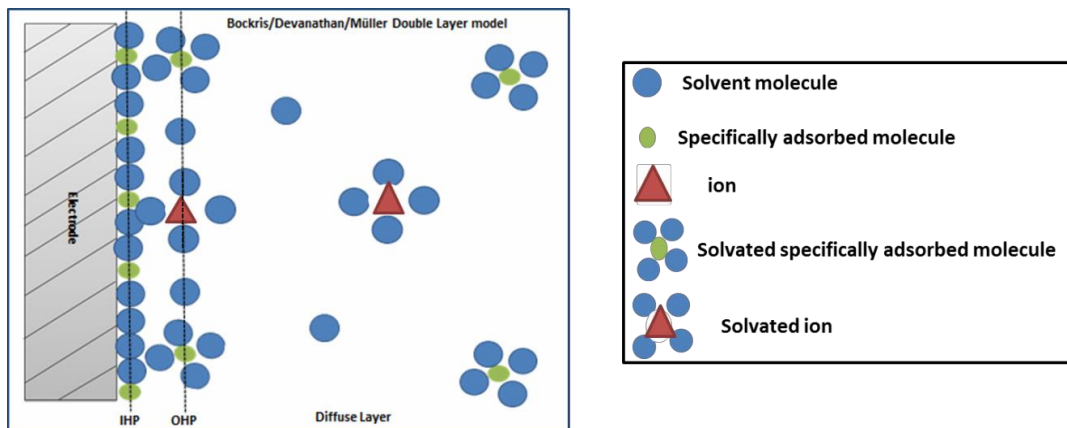
Figure 14: A diagram representing the double layer model proposed by Bockris, Devanathan, and Müller which takes into account solvent molecules.

The electrical double layer is described as having alternating positively and negatively charged layers; for example if the electrode is negative then the overall charge in the IHP is positive and that of the OHP is negative. The alternating arrangement of charge in the electrical double layer is said to be comparable to a parallel plate capacitor.[162] Equation 5 describes the capacitance of such a parallel plate capacitor.[163]

$$C = \frac{k\varepsilon_0 A}{d}$$
[5]

The capacitance for a parallel plate capacitor is determined by the area of the plates (A), the distance between the places (d), the relative permittivity of the material separating the plates (k), and the permittivity of free space (ε_o). The capacitance corresponds to the amount of stored charge an object has based on the voltage applied. Charge is measured in Coulombs, which is defined as the amount of current (I) that flows per unit time.[164] Therefore, the capacitance of an electrical double layer can describe the amount of current

flow within the layer based on the applied voltage.[122,162] Referring to Equation 5, for an electrical double layer with minute areas, assuming relative permittivity and permittivity of free space are constant, capacitance is inversely proportional to the thickness between the plates (d) as shown in Equation 6.

$$C \approx \frac{1}{d} \qquad\qquad [6]$$

The following factors can affect the nature of the electrical double layer: type of material and structure of electrode, concentration of analyte ions in solution, presence and concentration of other ions in solution, applied potential, and the size and charge of ions in solution. If the potential is altered at the electrode, the amount and type of ions adsorbed at its surface changes and the electrical double layer is changed.[162] For electrodes immersed in an electrolyte with solvent molecules only, the applied voltage establishes the charge of the electrode and dictates the number of solvent molecules adsorbed, giving a particular charge density. The potential at which the overall charge density equals zero is called the potential of zero charge (pzc). The pzc is pH dependent and its value is given based on the RE used to determine its value. For example, for polycrystalline Ag electrodes the pzc value versus a saturated calomel electrode (SCE) in 0.1M NaF solution is reported to be -0.914 ± 0.005 V.[55,162,165]

### 3.4.3 Cyclic voltammetry (CV)

Cyclic voltammetry (CV) is a potential sweep method in electrochemistry that measures the resultant current at the WE as the potential is changed linearly with time.[162] The potential is switched between two terminal

values at a constant sweep rate. For instance, a CV can be performed where the initial voltage is +2.0 V and a sweep rate of 1 mVs^{-1} takes it to a final potential of -2.0 V. The reverse scan or sweep occurs when at -2.0 V the potential is swept back to the initial voltage of +2.0 V at a sweep rate of 1 mVs^{-1}.[162] Cyclic voltammograms are plots of current output at the WE verses the change in applied potential. The cycling of the potential yields curves whose characteristic shapes are based on the type of redox reaction occurring and the peaks present in cyclic voltammograms represent specific redox processes.[162] Redox reactions can be reversible, irreversible, or quasi-reversible. For example, reversible redox reactions at a planar electrode can give a cyclic voltammogram that has a peak maximum (cathodic potential) and a peak minimum (anodic potential). Two characteristic features of reversible redox reactions is that i) the separation between the cathodic peak and the anodic peak is approximately equal to 0.0592V/n (where n is the number of electrons transferred per molecule), and ii) the peaks are symmetric (Figure 15).[162]
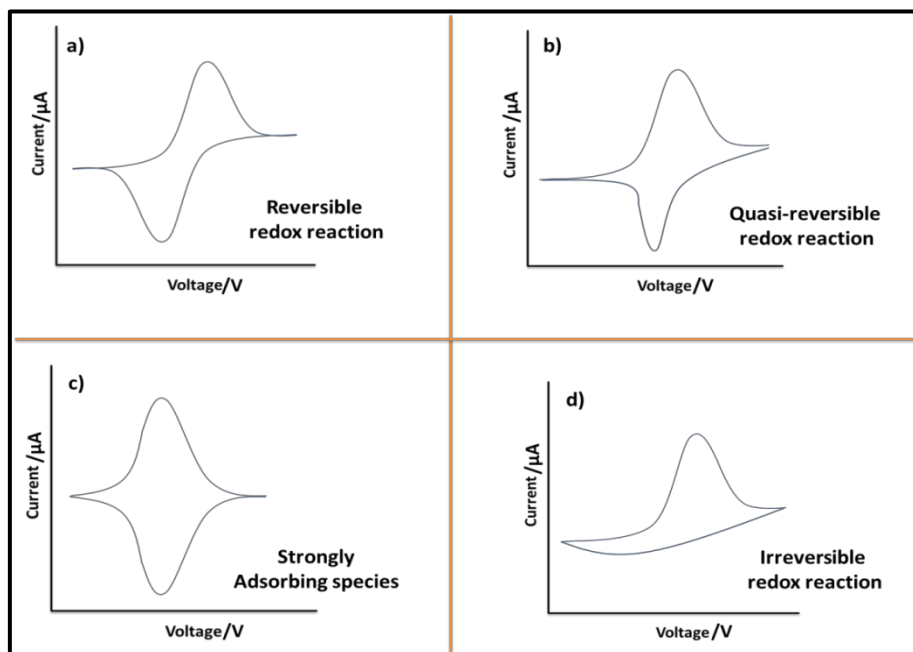
Figure 15: Diagrams adopted from theory used to associate the shape of cyclic voltammograms to identify the type of redox reaction or the strength of adsorbing species on the electrode surface. For a) reversible reactions peaks appear to be symmetric to each other, b) in quasi-reversible reactions the peaks are not identical or symmetric, c) strongly adsorbing species have peaks that are mirror images of each other, and d) irreversible reactions have a diminished peak in one direction showing little to no redox behaviour.[162]

CV can be used to study the oxidation and reduction of electroactive species, to identify species present in solution, and can be used as a semi-quantitative analysis method.[57] CV is also a quick method to indicate the possible formation of a compact layer at the surface. An electrode immersed in an electrolyte with a redox species present will give a distinctive curve obtained from the current generated due to specific redox reactions. If a compact layer is formed on the electrode surface first, redox species are inhibited from reaching the electrode surface, and this results in a reduction in current (Figure 16).[122]
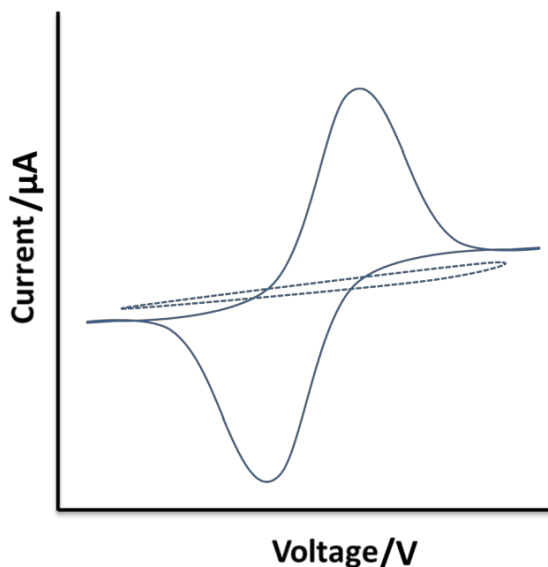
Figure 16: An overlay of cyclic voltammograms representing the drastic reduction in current response due to the presence of a compact monolayer on the electrode surface. In the absence of the monolayer (-) the redox probe is in direct contact with the electrode surface giving rise to a current response. In the presence of the monolayer (---) the redox probe interaction with the electrode surface is limited and the measured current is reduced.

3.4.4 Applications of electrochemical methods

Electrochemical methods are powerful analytical techniques and the interaction of analyte species or ions in solution with electrode surfaces has led to the development of electrochemical sensing devices.[57] The surfaces of electrodes have been modified to increase their selectivity to specific biological and non-biological molecules.[57,122] Zhang *et al.* demonstrated that an electrode surface could be modified to create a "sensor system". In the experiment luminol was polymerized onto an electrode surface by CV. This created an immobile surface which was used to detect flavin in solution by electrochemiluminescence.[166] Highly selective gas sensors have also been developed to detect specific gases in the

atmosphere which can have beneficial application in the environmental or industrial fields.[57]

The combination of electrochemistry with other techniques can provide more than one type of chemical information simultaneously, thus increasing the quality of the data.[122,131] Scanning Electrochemical Microscopy (SECM) for example is an imaging technique that maps an image originating from electrochemical reactions at the tip of a scanning electrode probe.[149] Takahashi and associates used this technique to obtain an image of a boar spermatozoa and to locate the sites of chemically active components within the membrane.[167] Electrochemistry has been coupled to several spectroscopic methods such as Raman, SERS, and Surface Enhanced Infrared Absorption Spectroscopy (SEIRAS) to obtain information on surface adsorption behavior, orientation of molecules at the surface, structure of the electrical double layer, or to gain a better understanding of redox reactions.[57,122,131] Boscheto *et al.* used electrochemical SEIRAS to investigate the electro-oxidation of methanol on a platinum electrode with respect to surface coverage of carbon monoxide. The results revealed the adsorption, desorption, and orientation of molecules during the reaction.[168]

3.4.5 Characterization of monolayers and bilayers by electrochemical techniques

Lipid monolayers and bilayers can be deposited on the surface of electrodes to form compact films that can act as selective barriers, only permitting the passage of particular molecules, or to study membrane associated processes e.g. electron transfer processes.[57,169] The potential

distribution at the interface created by the electrode surface, the lipid layer, and the electrolyte solution can be modified to represent the potential distribution of a biological membrane.[141] As mentioned in Section 2.2.2, the membrane potential for biological cells, with respect to the interior of the cell, falls within -40 mV and -80 mV which means a more negative voltage in the intracellular matrix compared to the extracellular matrix. Thus to mimic a cell membrane, the potential at a lipid modified electrode surface can be adjusted so that the applied electrode potential is more negative to that of the potential of zero charge (pzc; at the electrode/electrolyte interface), Figure 17. Molecules that adsorb, bind, or penetrate model membranes deposited on electrode surfaces can therefore be detected by monitoring changes in the pzc.[141]
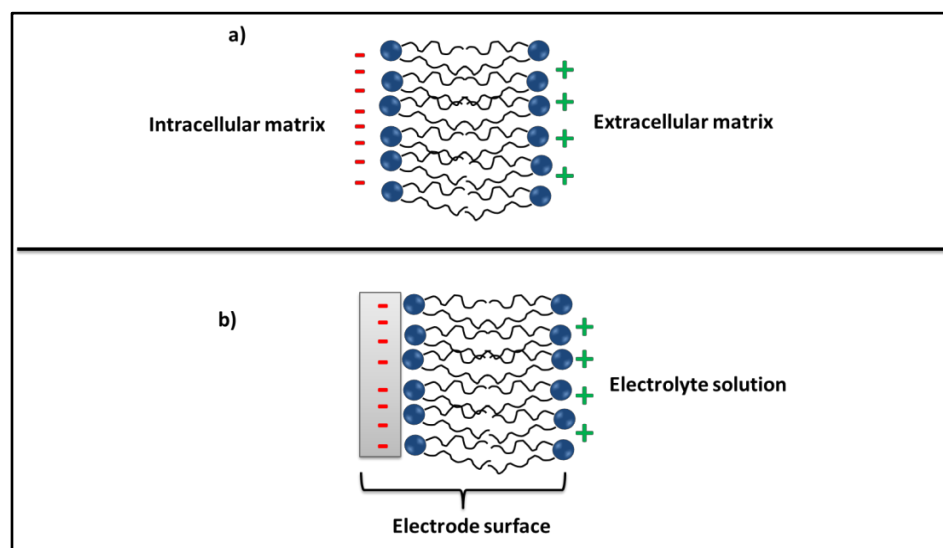
Figure 17: A schematic diagram showing how the a) potential difference across cell membranes can be mimicked by that of the b) potential difference of electrodes modified with lipid bilayers.

The CV technique is used to monitor or investigate electron transfer, flow of ions, or redox processes involving lipid layers.[74,169] When lipid layers are deposited

on electrode surfaces, they restrict electrode access to charged electroactive species in solution and as a result reduce the observed current at the electrode. Cyclic voltammograms of electrodes modified with lipid layers are thinner (lower current) than the cyclic voltammograms of these same electrodes unmodified. Therefore an increase in current at lipid modified electrodes, for example due to the presence of a redox probe in the lipid layer, can be observed by increased current for the cyclic voltammogram, or the appearance of redox peaks.[130] Additionally, for lipid bilayer modified electrodes, an increase in the observed current can also suggest deterioration of the lipid bilayer.[122]

3.5 Lipid bilayer formation by Langmuir-Blodgett/Langmuir-Schaefer (LB-LS) technique

3.5.1 Introduction

The Langmuir-Blodgett/Langmuir-Schaefer (LB-LS) technique transfers compressed lipid monolayers formed at an air-solution interface onto hydrophilic solid substrates, in a sequential fashion, to yield lipid bilayers.[55,115] Advantages of the LB-LS technique over other lipid bilayer forming procedures such as vesicle fusion include the ability to form asymmetric bilayers, high degree of order and uniformity within the bilayer, and mixed monolayer composition formed at the air-water interface is maintained during monolayer transfer.[115,117] This section outlines the general procedure for the LB-LS technique and the experimental conditions needed for the successful deposition of a lipid bilayer.

3.5.2 Compression isotherm of desired monolayer

To achieve the deposition of a lipid bilayer onto a solid substrate using the LB-LS method the following steps are required: 1) monolayer compression, 2) LB transfer of compressed monolayer onto solid substrate to obtain first (inner) leaflet, 3) compression of second monolayer, and 4) LS transfer of second compressed monolayer onto first deposited monolayer leaflet.[55,115,117] To follow the progression of a compressed monolayer at the air-water interface a surface pressure-area isotherm is used. Modern Langmuir instruments equipped with Teflon® troughs, sensitive microbalances, temperature control, and complementary software are used to produce such isotherms.[55,118] At constant controlled temperatures and steady compression, a graph of surface pressure at the interface against the area per molecule is plotted. The shape of the curve can be distinctive for certain molecules and molecular compositions, but the general trend shows the increase in surface pressure as the area per molecule decreases.[55,115] If the measurement is sensitive enough, different monolayer phases can be observed through changes in slopes of the isotherm. If sensitivity is low, a more smooth curve is obtained, e.g. a smooth sigmoidal curve.[55,115] A surface pressure-area isotherm also provides an important property of Langmuir monolayers which is the collapse pressure. When the collapse pressure is reached there is a sharp and sudden drop in surface pressure. Beyond this point a single molecule monolayer no longer exists; instead bilayers and multilayers are present as the monolayer collapses in on itself. Collapse pressures are used as guiding points to determine

the limit of compression for monolayers.[55,115] An example of a collapse pressure value is the compression of an alcohol, octadecanol, on the surface of distilled water. A steady rate compression of an octadecanol film exhibits a collapse pressure of approximately 50 mN/m at 22°C.[170] The value of the collapse pressure is affected by changes in temperature, rate of compression, and the presence of impurities.[55,115]

3.5.3 Langmuir-Blodgett monolayer deposition

In order for the hydrophilic polar head region of lipid molecules to be in contact with the hydrophilic solid substrate, this substrate must be submerged in the subphase prior to monolayer deposition and compression.[55,115,117] This transfer process can be performed and monitored by modern Langmuir instruments. When the monolayer is compressed to a desired pressure where a compact monolayer is known to exist (below that of the collapse pressure) and left for a few minutes to stabilize, the submerged solid substrate is brought slowly through the interface at a steady rate while the surface pressure is held constant (Figure 18 a). The efficiency of the deposition process is measured by the transfer ratio. The transfer ratio is the ratio of the area decrease on the subphase surface to the area of substrate covered by the monolayer. A transfer ratio of 1.0 ± 0.1 represents a successful transfer of a monolayer.[55,115,117]

3.5.4 Langmuir-Schaefer monolayer transfer

The final step in the LB-LS lipid bilayer deposition onto the solid surface involves the Schaefer touch (horizontal touch) technique. A monolayer is

compressed again to a desired surface pressure and left for a few minutes to stabilize. After this time, the solid substrate with the lipid monolayer leaflet is oriented parallel to the subphase surface. In this orientation the hydrophobic region on the solid substrate will be facing the hydrophobic region of the compressed lipid monolayer. This orientation ensures that strong Van der Waals interactions can occur between the lipid alkyl chains. The horizontal solid substrate is lowered slowly until it just touches the surface of the subphase and then it is immediately lifted from the subphase surface at a slow rate (Figure 18 b).[55,115,117]
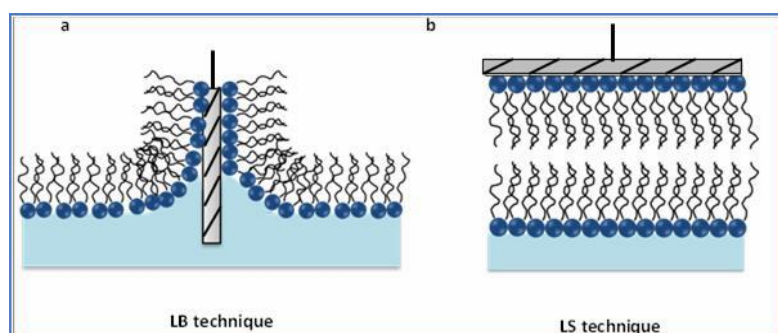
Figure 18: Illustration of lipid bilayer formation by the LB-LS technique. Action **a** is a vertical withdrawl of a solid substrate through a compressed monolayer. Action **b** is a horizontal touch of a solid substrate with an already deposited monolayer onto the surface of a compressed monolayer.

4 Materials and methods

4.1 Introduction

This section outlines the reagents, solvents, instrumentation, and procedures implemented in the fabrication and characterization of the biomimetic model membranes developed in this thesis work. Modifications made to

experimental procedures or conditions were designed to achieve better quality data, optimal signal, and decrease interferences. To reduce impurities or cross contamination all glassware was soaked for ~24 hrs in concentrated sulphuric acid (Fisher Scientific, 95 %, NJ, U.S.A.) and rinsed repeatedly with water ultrapure Milli-Q water before each analysis. All reagents were used without further purification. Purified water used for rinsing and making solutions was obtained from a Milli-Q Direct-Q water system (Millipore, Molsheim, France) with a resistivity of >18.2 MΩ·cm at 25 °C. Experiments were performed at 20 °C ± 2.0 °C. For electrochemical measurements, all potentials reported in this thesis are versus Ag/AgCl unless otherwise indicated.

4.2 Raman spectroscopy instrumentation

Raman and SERS spectra were recorded with a DXR Smart Raman spectrometer equipped with a 180 degree sampling mode, a charged-coupled device (CCD) detector, and laser excitation wavelengths of 532 nm and 780 nm (Thermo Scientific, Madison, WI). Raman control studies were performed at both wavelengths with an aperture slit of 25 μm, laser spot size of 2.1 μm, and a spectral resolution of 2.0 cm^{-1} in order to determine the optimal excitation wavelength. Control studies were performed with solid lipid components used in the experiments. The optimal wavelength was found to be 532 nm since it gave the strongest and clearest signals with the least amount of background. To reduce possible degradation of the biological components and to decrease background noise, the data acquisition time was adjusted and the laser power was kept below 5 mW for the bilayer probe studies. Collection exposure time and sample exposure

time were adjusted to 1s and 30s respectively, where a final spectrum represented the average of 30 spectra. Data were collected at full range (50 cm^{-1} to 3500 cm^{-1}), data points were normalized by dividing each data point by the product of the laser power and data acquisition time, and data points were smoothed by Origin 9.0 software using the Savitzky-Golay method (Origin Lab Corporation, USA).

4.3 Fabrication of silver nanoparticle modified screen-printed electrodes

To obtain relatively uniform silver colloids by a simple and quick synthetic route, a modification of the Lee and Meisel method was used, which involved the reduction of a silver salt.[171] 0.09 g of silver nitrate (AgNO$_3$, 99.9999%, Sigma Aldrich, St. Louis, MO) was added to approximately 500 ml of Millipore water, and the mixture was heated with stirring to a vigorous boil on a hot plate in a darkened fume hood to decrease light interference. 10.0 ml of a 1% w/w sodium citrate solution (Na$_3$C$_6$H$_5$O$_7$.2H$_2$O, ACP, Montreal, Québec) was added to the boiling AgNO$_3$ solution and the mixture was allowed to continue boiling for 30 minutes. The solution was then removed, covered with foil, and topped up with Millipore water to roughly 400 ml. 1.0 ml of the cooled solution was centrifuged at 3600 rpm for 15 minutes and the supernatant was then removed. To the resultant pellet a fresh 1.0 ml aliquot of the colloidal suspension was added and the process was repeated nine more times to obtain sufficient AgNPs to cover the WE surface. After the tenth cycle, the supernatant was discarded and the resulting pellet, consisting of a nanoparticle paste was applied to a carbon screen-printed electrode (Pine Research Instrumentation, CA, U.S.A.).

To facilitate the combination of SERS and electrochemical measurements, the WE surface was modified to accommodate both types of techniques. The electrochemical measurements were carried out using a convenient and modern approach to the three- electrode system. Screen-printed electrodes (SPEs) are very convenient and cost- effective when compared to conventional electrochemical electrodes.[57] The SPEs are based on microchip technology and thus use smaller sampling volumes, less bench top space, require no electrode filling solution, require lower capital cost to manufacture, and demonstrate high sensitivity.[57] The SPE used in this work (Pine Research Instrumentation, CA, U.S.A.) was a flat coated rectangular plastic chip (15 mm x 61 mm x 0.36mm) consisting of a carbon rectangular WE (5mm x 4mm), a Ag/AgCl RE, and a carbon CE all located on one end of the chip (Figure 19). 5 µL of the concentrated citrate reduced NPs was gently spread onto the entire WE surface with a pipette tip. This layer was allowed to dry and NP deposition was repeated two more times to give a total of three layers.
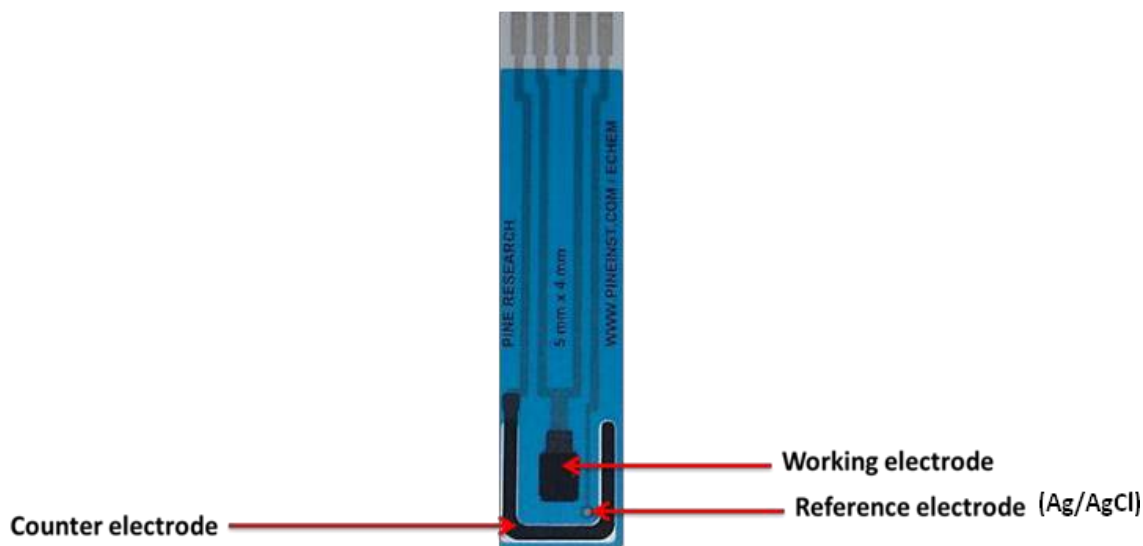
Figure 19: A picture of the screen-printed electrodes used in this thesis project (scaled and resized).

The synthesis of AgNPs via the Lee and Meisel method leaves citrate on the surface of the NPs.[172] To reduce the resulting strong citrate SERS signal, a displacement reaction was performed using potassium chloride (KCl, Fisher Scientific, 99.0 %, NJ, U.S.A.). The strong adsorption of Cl$^-$ onto the Ag surface removes the majority of the surface bound citrate.[173] Citrate removal was done by immersing the modified screen- printed electrodes in a 0.5 M KCl solution. Time studies were conducted to determine the minimum immersion time needed to attain a significant reduction in citrate signal. This minimum time was found to be 30 minutes. After roughly 30 minutes the electrode was removed and rinsed with Millipore water on both sides and left to dry in the dark. Due to the instability of the AgNPs the modified electrodes were used within a week of being made.

4.4 Formation of the alkanethiol self-assembled monolayer

Published literature has shown that millimolar concentrations of alkanethiols dissolved in slightly polar or polar solvents can provide completely

covered surfaces of solid substrates within 12 hr.[96] Ethanol (Commercial Alcohols, 95 %, Brampton, Ontario) was used to make 1 mM alkanethiol solutions from the following: 6-mercaptohexanoic acid, (6-MHA) (Sigma Aldrich, 90 %, St. Louis, MO); 12-mercaptododecanoic acid, (12-MDA) (Sigma Aldrich, 96 %, St. Louis, MO); and 1-octadecanethiol, (1-ODT) (Sigma Aldrich, 98 %, St. Louis, MO). SAMs of each alkanethiol were formed by the immersion of the AgNP modified screen-printed electrodes into the alkanethiol solution for approximately 18 hr. After the incubation period, the electrodes were rinsed with ethanol, dried in the fumehood, and used within 20 minutes for other experimental procedures or analyses.

4.5 Lipid bilayer formation

The cell membrane is a complex structure comprising many components. To mimic a neuron membrane which has a high lipid percentage, and to achieve the desired research goal, a simple model membrane that eliminates most variables must be established so that the desired detection of a probe molecule is the focal point. The membrane components chosen for this project were 1,2-Dimyristoyl-*sn*-glycero-3-phosphocholine, DMPC (Avanti Polar Lipids, 99 %, Alabaster, Alabama) and cholesterol (Avanti Polar Lipids, 98 %, Alabaster, Alabama). Figure 20 shows the structures of DMPC and cholesterol.
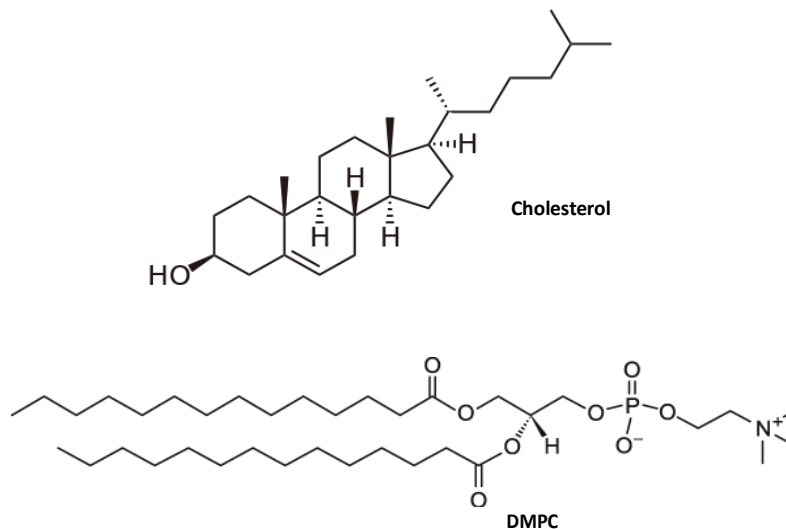
Figure 20: Structures of the two membrane components used in the formation of the biomimetic model membrane studied in this work.

DMPC was chosen because it is a zwitterionic lipid, it possesses no double bonds that are susceptible to oxidation, it is well studied and characterized, and it has shown success in other research work involving the formation of model monolayers and bilayers.[174-176] The purpose of cholesterol in this work was to provide fluidity and reduce membrane defects.[58,59,62] Raman spectra were recorded for solid samples of DMPC and cholesterol as control studies to aid in peak assessment for future SERS spectra. Previous research work done on model lipid bilayers used a 70:30 mole % ratio of DMPC and cholesterol, respectively.[177,178] This research reported stable formation of monolayers and bilayers, and since this mole ratio is comparable to lipid/cholesterol content of cells in the myelin sheath[58]; it was used in the current research.

The formation of lipid monolayers at the air-water interface was accomplished using a KSV NIMA Langmuir-Blodgett Trough, and its accompanying software (Biolin Scientific, Finland). This instrument is positioned

on top of a 6.50 cm thick marble slab in order to reduce vibrations and to improve the quality of measurements. Surface pressure measurements were obtained using a 10 mm wide (20.6 mm perimeter) Whatman #1 filter paper Wilhelmy plate hung from the microbalance area, and subphase temperatures were controlled by a Lauda K-2/R circulating water bath (Brinkmann Instruments, NJ, U.S.A.) attached to the trough. Solid substrates were manipulated by a dipping arm, and subphase temperature readings were measured continuously with a temperature probe. To afford an easy deposition of the 70:30 DMPC/cholesterol mixture, a 2 mg/mL lipid mixture was prepared using chloroform as the solvent (Caledon, HPLC grade, Georgetown, Ontario). The calculated mass values for each lipid component was used to accurately weigh and transfer the masses of the lipid components to the same volumetric flask. The Teflon® trough and Delrin® hydrophilic barriers were cleaned with ethanol and rinsed thoroughly with Millipore water. The trough was then filled with Millipore water, the Wilhelmy plate was hung, and the temperature probe was inserted below the water surface avoiding contact with the trough. The surface was cleaned by gentle vacuum suction and 40 μL of lipid solution was carefully deposited dropwise via a glass syringe randomly over the water surface. After 30 minutes (allotted time for chloroform evapouration) the lipid components were compressed at the air-water interface at a rate of 5 mm/min until a surface pressure of 40 mN/m was attained. This value was derived from the predetermined collapse pressure (50 mN/m) of the DMPC/cholesterol 70:30 mixture from a surface-pressure isotherm. The lipid monolayer leaflet that will be in

contact with the AgNP modified screen-printed electrode was formed first by the LB technique where a compressed DMPC/cholesterol 70:30 monolayer was transferred by a vertical withdrawl of the substrate. The outer monolayer leaflet was then transferred by the LS horizontal touch method to the AgNP modified screen-printed electrode containing the LB lipid monolayer leaflet. This gave the desirable lipid bilayer structure of a hydrophobic region sandwiched by the hydrophilic polar head region. Refer to Figure 18 in Section 3.5.4 for a schematic representation of the LB-LS technique.

Compressed monolayer transfers onto solid substrates (LB and LS) were completed within one day of each other, i.e. LB vertical deposition on one day followed by LS horizontal touch the next day. This was done to ensure complete drying of each layer. For lipid monolayers, SERS and CV measurements were performed the following day, while for lipid bilayers measurements were completed the day after the formation of the second monolayer leaflet.

During increased subphase temperature studies, the subphase water was allowed to reach the desired temperature before submerging the modified screen-printed electrodes and before lipid deposition. The T_m for pure DMPC is approximately 23°C and for a DMPC bilayer containing 30 % cholesterol, T_m <20°C.[62] To ensure that these temperatures were surpassed, the temperature of the circulating water bath was set to 32°C. For the humidity experiments, attempts were made to maintain similar conditions from day to day, > 70 % relative humidity (RH). A 250 ml beaker containing boiled Millipore water filled to about the 250 ml mark was placed inside the housing for the Langmuir

instrument after lipid deposition. The beaker was left for the duration of the experiment with the lid closed. The RH and temperature within the closed housing for the Langmuir instrument were monitored by an indoor thermometer and hygrometer (Bios Weather, Markham, Canada). In addition, for the humidity experiments each monolayer leaflet was dried overnight in a closed chromatography glass chamber containing about 200 mL of boiled Millipore water. This was done in order to ensure slow drying of the monolayer.

4.6 Preparation of probe molecule solutions

The probes selected to evaluate the quality of the model membrane were chosen to test the following objectives: 1) to determine if there were gaps present and the potential size of these gaps, 2) what size or charge of molecules penetrate the lipid bilayer, and 3) which molecules were prohibited from crossing the lipid bilayer. Efforts were made to ensure variation in probe size and polarity, but most importantly potential probes had to be Raman active, SERS active, and water soluble.

The electrolyte used was 0.1 M sodium fluoride, NaF (Sigma Aldrich, 99.99 %, St. Louis, MO). NaF is a well-known non-interfering electrolyte because the ions will not react with species in solution but merely form ionic interactions. In addition, the fluoride anion binds weakly to the AgNP surface thus reducing spectral interference.[179,180] A probe concentration of 1 mM was chosen as an upper-range concentration value. This probe concentration ensures that the presence of the probe will give a distinct signal.
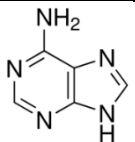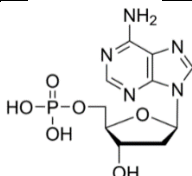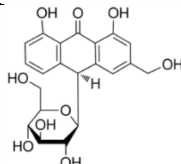
The rationale for the selection of each probe is outlined below and Table 5 shows the molecular structure, some important features of the chosen probes, and categorization. The sizes of the molecules provided in the table are calculated estimations derived from accumulated material from theory, experimental data, and bond length tables. These values are meant to be a rough estimation of the size of possible gaps that may exist in the model membrane if the molecule is able to freely traverse the lipid bilayer. The probe molecules chosen for this work were as follows:

i) 2′-Deoxyadenosine 5′-phosphate, dAMP (Sigma Aldrich, 98 %, St. Louis, MO) is an analog of the neurotransmitter adenosine. It is Raman and SERS active, giving two strong spectral peaks around 730 cm^{-1} and 1320 cm^{-1}.[182] The presence of the phosphate group gives some polarity to the molecule allowing for good solubility in water.[59]

ii) The adenine (Sigma Aldrich, 99 %, St. Louis, MO) molecule is simply dAMP without the sugar and phosphate group. Like dAMP it also gives strong peaks around 730 cm^{-1} and 1326 cm^{-1},[183] but it is less polar and has a lower solubility in water (0.05 g/100 ml).[184]

iii) 1,8-Dihydroxy-10-(β-D-glucopyranosyl)-3-(hydroxymethyl)-9(10H)-anthracenone, also known as aloin (Sigma Aldrich, 97 %, St. Louis, MO), is an anthraquinone derivative. Anthraquinones give very intense Raman and SERS signals.[134] Aloin is also larger than adenine and dAMP, and less polar. The non-polar nature of Aloin is evident

in its slight solubility in water (1 mg/1 ml).[185]

iv) Potassium thiocyanate, KSCN, (Fisher Scientific, A.C.S. grade, NJ, U.S.A.) in solution provides the thiocyanate anion (SCN⁻) which has a distinct SERS peak in the 2000 cm⁻¹ region which is a spectral area usually devoid of peaks.[132,134] This eliminated the ambiguity for discerning probe peaks from other peaks within the spectra. The SCN⁻ anion is fairly small and can help determine if the model membranes allow passage of small ions.

Probe name	Structure	Categorization	Lateral size estimation	Solubility in water
Adenine		Small probe Non-polar probe	0.62 nm[193]	fair
dAMP		Medium probe Polar probe	1.152 nm[191,192,193]	good
Aloin		Large probe Non-polar probe	2.51nm[186-191]	poor
Thiocyanate		ion	0.296 nm[192]	good

Table 5: A list of the probe molecules used in the experiments and their categorization based on size, polarity, and type.

The Raman spectra of solid dAMP, adenine, aloin, and potassium thiocyanate and were recorded as a reference. Peak assignment values were taken from literature Raman experiments of these probes or their derivatives.

4.7 Electrochemical Surface Enhanced Raman spectroscopy (EC-SERS) measurements

A WaveNow potentiostat (Pine Research Instrumentation, CA, U.S.A.) was used to adjust the potential at the WE. The potentiostat was connected to the electrochemical cell via a mini USB adapter. Figure 21 shows the set-up used for EC-SERS experiments. Before the addition of any electrolyte/probe solution to the glass vial electrochemical cell, a SERS measurement was taken of the modified screen-printed electrode in air.
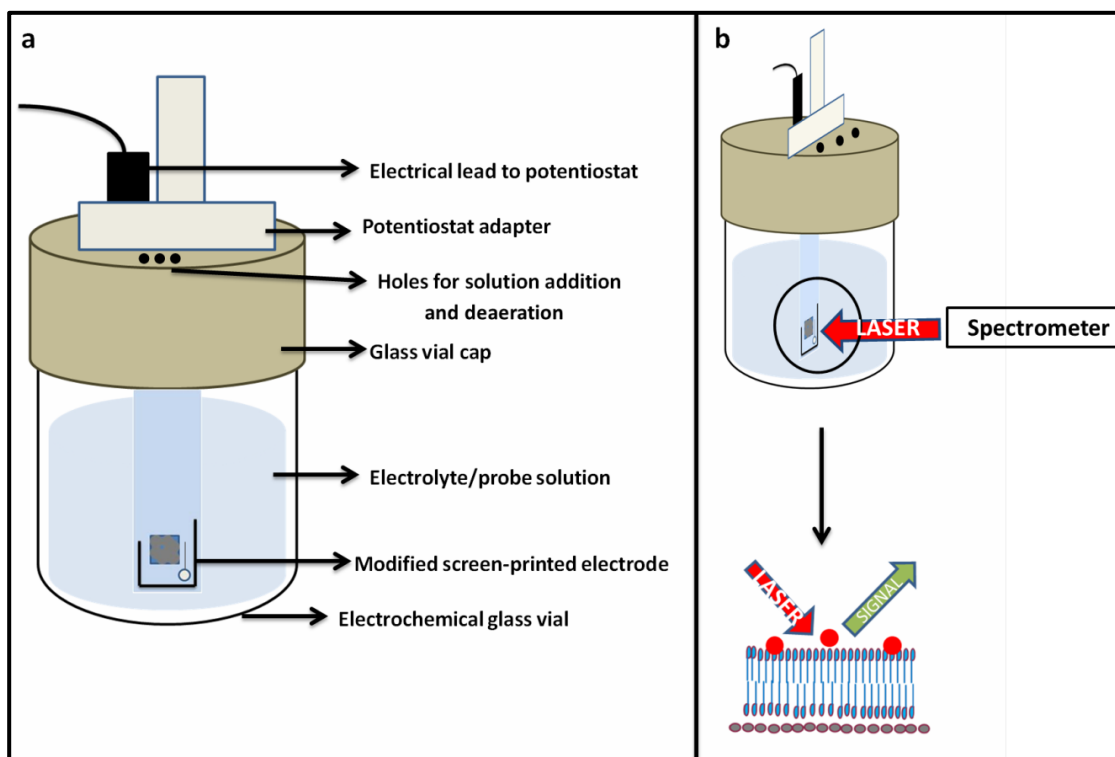
Figure 21: EC-SERS set-up for the analysis of biomimetic model membranes: a) shows the main components, and b) shows the orientation of the glass vial with respect to the incident laser beam.

All electrolyte/probe solutions were purged with Argon (Praxair Canada Inc., 99.999 %, Mississauga, Ontario) for approximately 40 minutes prior to

measurement. This eliminated the presence of oxygen in the electrochemical cell which can cause interference.[96] After purging, approximately 4.5 ml of solution was added to the EC- SERS cell and a SERS spectrum was recorded with no applied potential. This type of measurement is called the open circuit potential (OCP) measurement.[122] The OCP spectrum represents the spectrum for the system at its resting potential, in the absence of applied potential. The applied potential range for the proposed experiments was 0 V to -1.0 V vs Ag/AgCl. This potential range was selected for the following reasons:

- Potentials more positive than 0V will cause oxidation of the silver surface, which will reduce the SERS effect, and possibly lead to the detachment of the bilayer.[139]

- Potentials more negative than -1.0 V will cause the reduction of water and lead to an increase in the current. At this point the evolution of H_2 gas is possible which can destroy the AgNP layer. There is also a strong likelihood of electroporation (artificially induced pores in cell membranes by change in electrical signal) at negative applied voltages.[58,194]

After the OCP measurement, the potential was stepped from 0 V to -1.0 V (cathodic direction) in 0.1 V increments and each potential step was held for 30 s. At each potential step, a SERS spectrum was recorded. At the end of the cathodic sequence, the potential was stepped in the anodic direction, i.e. -1.0 V to 0 V in 0.1 V increments, and a SERS spectrum was also recorded for each stabilized potential increment. The final step in the EC-SERS study was the collection of a

cyclic voltammogram at a sweep rate of 50 mVs^{-1} between 0 V and -1.0 V to obtain a current response.

5 Results and discussion

5.1 Introduction

In this section the main experimental data are presented. Experiment were conducted at Saint Mary's University in the Chemistry Department between September 2012 to March 2014. Control studies were performed to determine the useful marker spectral peaks for each probe molecule, to identify peaks for each component in the bilayer system, to provide cyclic voltammograms of 0.1 M NaF electrolyte solutions with AgNP electrodes for comparison with other cyclic voltammograms of AgNP electrodes modified with lipid layers or SAMs, as well as to determine optimal experimental conditions for the formation of a lipid bilayer by the LB-LS technique and the formation of a SAM. Peak assignment was done for all experiments to assist in ascertaining probe or lipid presence. Peak assignments were completed with the aid of reference tables or experimental data from journal articles. For data analysis, both the cathodic and anodic pathway data will be presented in an overlay fashion. The overlay highlights the main spectral features and easily allows for the determination of changes due to the varying applied potential.

5.2 Raman spectra of lipid components and probe molecules

The Raman spectra of solid DMPC and cholesterol were recorded at 6 mW for 30 s at 532 nm. Vibrational modes assigned for peaks in both spectra

were based on literature values found in Raman reference tables and journal articles.[134-136,195] The strongest peaks for cholesterol were the CH_2 alkyl stretching vibrations at 2868 cm^{-1} and 2932 cm^{-1} (Figure 22). The characteristic ring alkene stretching vibration clearly observed at 1672 cm^{-1} was used as an identifier for the presence of cholesterol. Please refer to Table A-1 in the Appendix for full peak assignment of solid cholesterol. For the DMPC Raman spectrum, shown in Figure 23, the alkyl chain stretching peaks between 2880 cm^{-1} and 2960 cm^{-1} were observed to be the strongest. Other important spectral peaks were those belonging to the polar head region of the lipid. The presence of these peaks in future SERS bilayer studies is an indication that the lipid polar head region is located near the AgNP surface. The peaks for the polar head region were 712 cm^{-1}, 873 cm^{-1}, 953 cm^{-1}, 1061 cm^{-1}, 1090 cm^{-1}, and 3032 cm^{-1}. Please refer to Table A-2 in the Appendix for full peak assignment of solid DMPC.
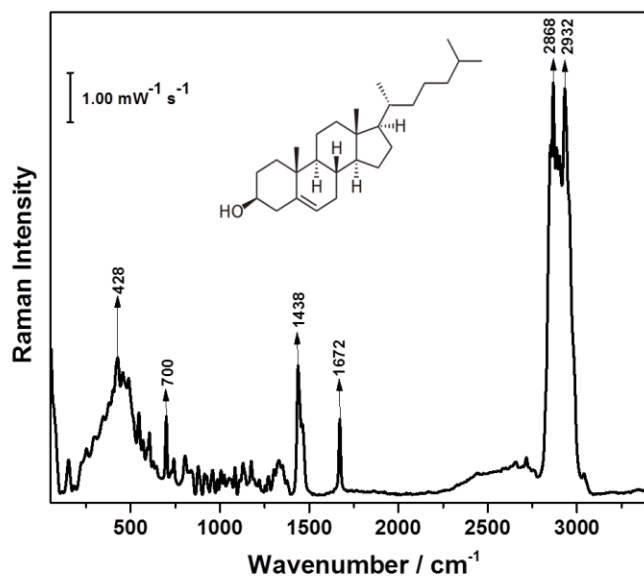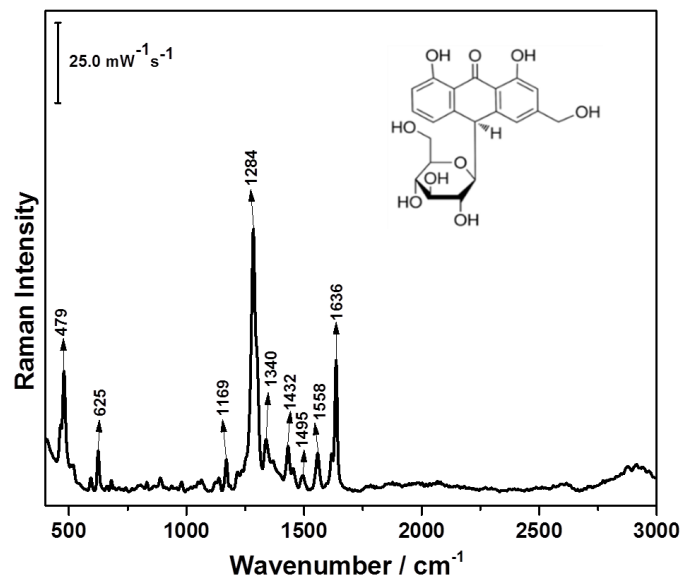
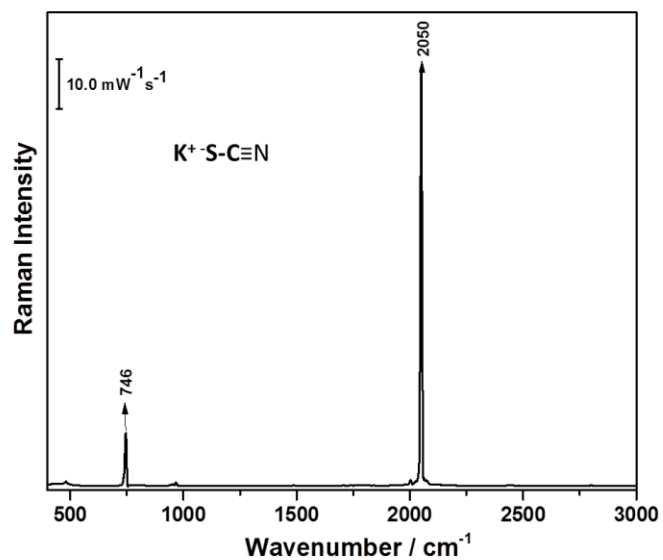**Figure 22**: Raman spectra of solid cholesterol collected for 30 s at a laser power of 6 mW at 532 nm.
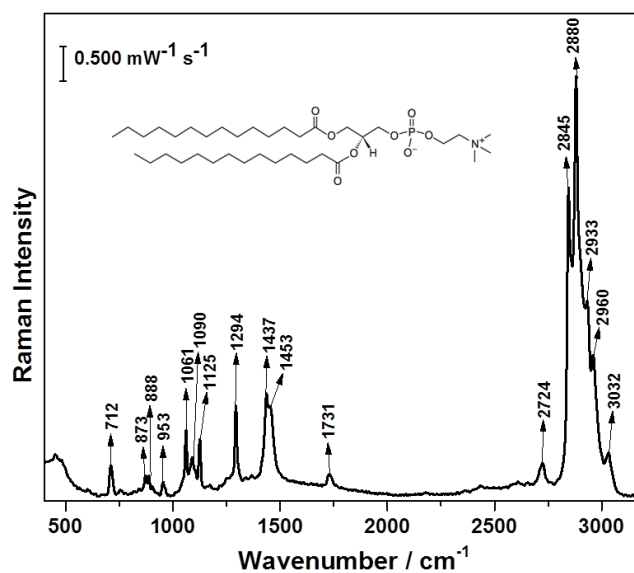
Figure 23: Raman spectra of solid DMPC collected for 30 s at a laser power of 6 mW at 532 nm.

For the Raman spectrum of adenine, shown in Figure 24, the strongest peaks were the purine ring breathing mode at 721 cm^{-1}, and the imidazole ring stretch at 1331 cm^{-1}. All other peaks in the spectrum represented either ring stretches, ring deformations, ring breathing modes, or rocking vibrations of the adenine ring moiety (Table A-3).[136,183,196] The Raman spectrum of solid dAMP, shown in Figure 25, also had strong peaks at 732 cm^{-1} and 1331 cm^{-1} representing the ring breathing mode of the purine, and the imidazole stretch respectively. Other distinct peaks in the dAMP Raman spectra included C-H and v_{as}(CH$_2$) stretches in the 2900 cm^{-1} region , the N-deoxyribose stretch at 1037 cm^{-1}, and the phosphate O-P-O stretch at 813 cm^{-1}. Please refer to Table A-4 for full peak assignment of dAMP. [182,197]
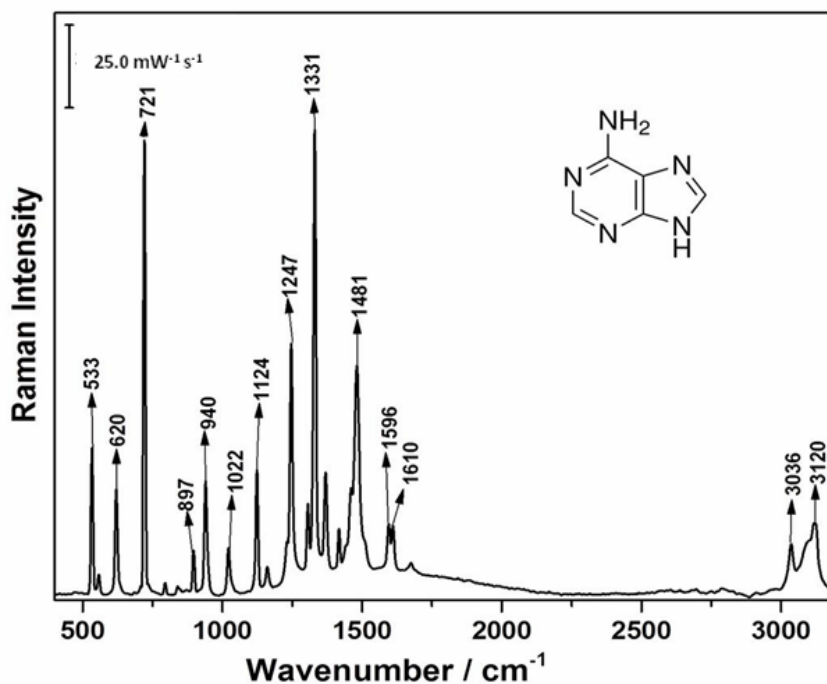
Figure 24: Raman spectra of solid adenine collected for 30 s at a laser power of 7 mW at 532 nm.
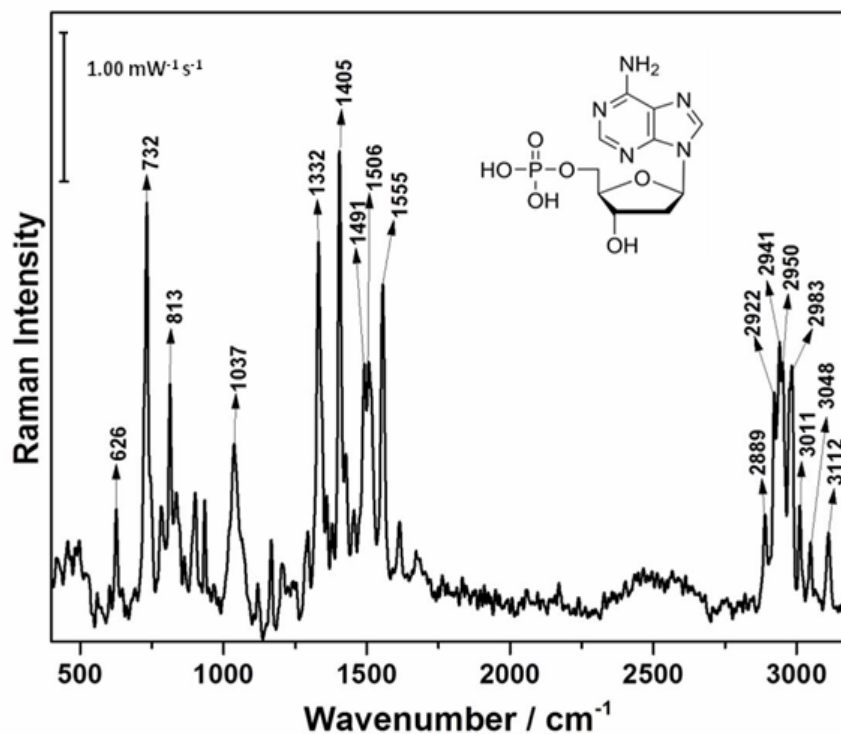
Figure 25: Raman spectra of solid dAMP collected for 30 s at a laser power of 7 mW at 532 nm.

The most distinctive spectral peaks for aloin (Figure 26) are for the ring alcoholic deformation, 1284 cm^{-1}; ring deformation, 479 cm^{-1}; and the carbonyl stretch, 1636 cm^{-1}. The full peak assignment for aloin can be found in Appendix Table A-5.[198-200] The Raman spectrum of solid KSCN (Figure 27) was straightforward and two discernible peaks were observed: i) one peak at 746 cm^{-1} for the C-S stretch and ii) another peak at 2050 cm^{-1} for the asymmetric stretch of the C≡N bond.[134]

Figure 26: Raman spectra of solid aloin collected for 30 s at a laser power of 6 mW at 532 nm.

Figure 27: Raman spectra of solid potassium thiocyanate collected for 30 s at a laser power of 7 mW at 532 nm.

In some instances specific functional groups present in both lipid components and probe molecules gave Raman peaks within the same region. However, as a consequence of different bonding environments the values can vary, making it possible to discern one molecule from the other. For example, C=O groups are present in both DMPC and aloin, but the carbonyl stretch for DMPC at 1731 cm^{-1} occurs at a much higher wavenumber than that for aloin at 1636 cm^{-1}, allowing them to be discerned from one another.

5.3 Citrate removal and OCP bilayer studies

The synthesis of AgNPs by the modified Lee and Meisel method leaves citrate on the surface of the Ag colloids.[172] Citrate gives a strong SERS signal in the region from 600–1700 cm^{-1} which can interfere with SERS studies of other molecules.[134] Citrate removal treatment was performed by immersing the AgNP modified screen-printed electrode into a 0.5 M KCl solution for 30 minutes, after which the electrode was rinsed with Millipore water and used for further analyses. Chloride binds strongly to the silver surface, displacing surface bound citrate molecules. Figure 28 shows how drastically the citrate signal had decreased within the fingerprint region after treatment with 0.5M KCl solution. This confirmed that the deposition of a lipid bilayer onto the chloride-treated AgNP surface should have minimal peak interference from citrate.
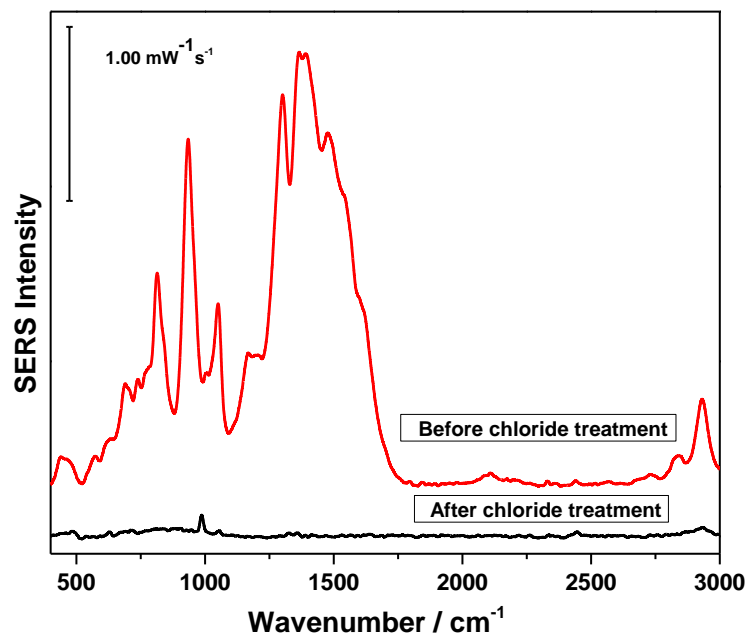
Figure 28: A spectral overlay showing the decrease in citrate peak intensity after a 30 minutes immersion in 0.5M KCl solution. The spectra were collected for 30 s at a laser power of 10 mW at 532 nm.

To determine the stability of the model membrane fabricated in this research in terms of possible degradation by continuous use of the laser, or due to spontaneous desorption from the AgNP modified screen-printed electrode over time, a lipid bilayer stability study was performed. The LB-LS technique was used to deposit a DMPC/cholesterol (70:30) lipid bilayer onto a chloride treated AgNP screen-printed electrode. An OCP spectrum was recorded for 30 seconds at 5 minute intervals for a total of an hour at maximum power (10 mW) with the EC-SERS set-up containing purged 0.1 M NaF. The first spectrum recorded at 0 min had peaks indicating the presence of DMPC, cholesterol, and citrate (Appendix Table A-7). The strong peak at 690 cm^{-1} fell within the region for cholesterol methylene deformations and also citrate carboxylic deformations.

114

However, the presence of the lipid carbonyl peak around 1763 cm^{-1} and the lipid CH$_2$ asymmetric stretches substantiated possible lipid bilayer formation. Figure 29 shows that over time the peaks for the lipid components decreased significantly, and furthermore peaks such as the lipid carbonyl peak at 1763 cm^{-1} had disappeared completely. The carbonyl peak was barely visible after 25 minutes in the spectral overlay. It was deduced that over time the laser power degraded the lipid bilayer or possibly desorption of the lipid bilayer occurred. However, photodegradation of lipid components would lead to lipid degradation products such as ketones, aldehydes, or alcohols.[205] The presence of these new molecules at the AgNP surface would yield new spectral peaks since products such as these contain functional groups that exhibit distinctive SERS signal e.g. ketones and aldehydes contain carbonyl groups which give rise to a SERS peak between 1600 cm^{-1} and 1760 cm^{-1}, while alcohols have OH SERS peaks between 800 cm^{-1} and 1440 cm^{-1}. Since there were no decomposition peaks in the spectra and most of the lipid component peaks present at the first timed reading disappeared around 40 minutes, it was concluded that around 40 minutes the lipid bilayer quality decreased and spontaneous desorption of lipid bilayer structure possibly occurred. Hence, for future experiments the laser power was kept below 10 mW and EC-SERS measurements were recorded for no more than a total of 30 minutes.
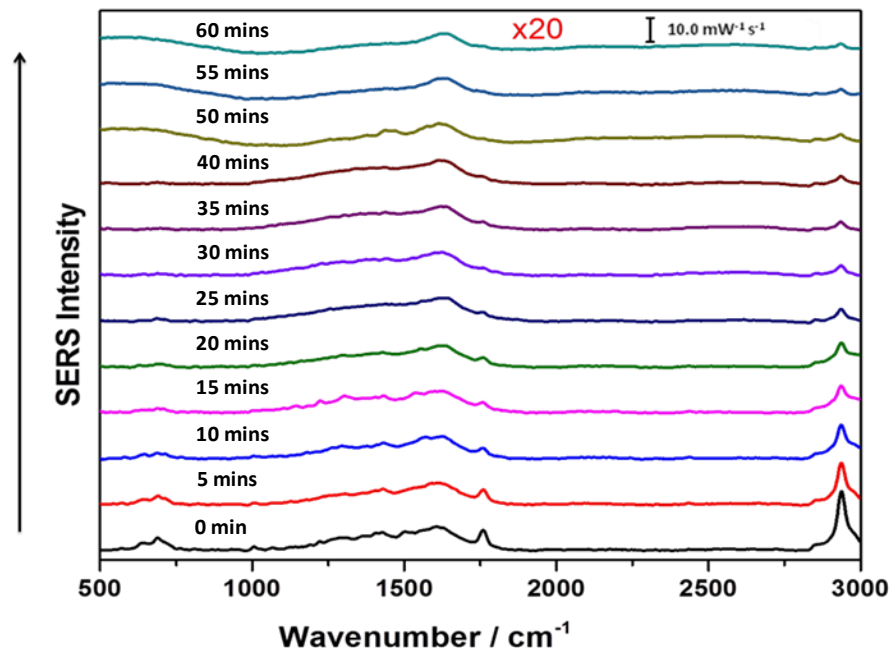
Figure 29: Spectral overlay of the lipid bilayer time studies on a chloride treated AgNP modified electrode. Overtime the stability of the lipid bilayer decreased. Spectra were recorded for 30 s at a laser power of 10 mW at 532 nm.

5.4 Lipid monolayer studies with dAMP

A deposited lipid monolayer on the surface of a AgNP modified electrode can act as a barrier and reduce the SERS effect of other molecules present. To determine the extent to which the chosen lipid monolayer reduced the SERS effect on analyte molecules a control study was performed with a DMPC/cholesterol (70:30) monolayer deposited on a AgNP modified electrode in the presence of 1mM dAMP/0.1 M NaF solution. This probe molecule was chosen for this study because its spectral peaks are strong and distinct (Figure 25).[203] Thus, a decrease in signal intensity of the dAMP peaks can be an indication that the lipid monolayer is an effective barrier and that the dAMP molecules are not close enough to the SERS substrate to experience the full SERS effect. In

116

application to this research project, using dAMP in the presence of a model membrane can help infer the following: i) decrease in signal intensity of dAMP peaks can indicate a lipid monolayer/bilayer is present which blocks access to the AgNP surface, and ii) strong dAMP peak intensities may indicate that there are gaps or defects within the lipid bilayer. A DMPC/cholesterol (70:30) monolayer was deposited onto a modified screen-printed electrode using the LB technique as described in Chapter 4. A SERS spectrum of the monolayer-covered electrode in air was collected and peak assignment showed the presence of both lipid components and residual citrate molecules (Table 6).[134-136,195,203] This electrode was then used in an EC-SERS experiment with an electrolyte composition of 0.1 M NaF/1 mM dAMP.

Wavenumber (cm^{-1})	Assignment	Description	Molecule
641	O-C-O	Bending or out of plane deformation	Citrate
683	σ(COO)	carboxylic group deformation	Citrate
833	O-P-O	Stretch vibration	DMPC
1003	v(O-CH$_2$-C)	Ester group stretch	citrate
1176	v_{as}(CO-O-C) γ_w(CH$_2$)	Ester C-O asymmetric stretch Wagging of lipid tail	DMPC DMPC
1210	o (COO)	carboxylic group deformation	Citrate
1293	CH CH$_2$	Bending Wagging and twisting deformation	DMPC DMPC
1372	σ_s(CH$_3$) COO$^-$	Symmetric bending Binding of carboxylic group to surface	DMPC Citrate
1588	v_{as}(COO$_2^-$)	Asymmetric stretch of vibration	citrate
2936	v_{as} (CH$_2$)	Asymmetric stretch	DMPC/cholesterol

Table 6: SERS peak assignment of the in air SERS spectrum of a DMPC/cholesterol (70:30) monolayer deposited on a AgNP modified electrode. The spectrum was collected for 30 s at a laser power of 10 mW at 532 nm.

At OCP, as shown in Figure 30a, the probe peaks relative to the lipid peaks were intense. This observation indicated that in the presence of a lipid monolayer a probe signal was easily obtainable. The cathodic overlay (Figure 30 b) showed the persistence of the probe peaks with a gradual signal increase then decrease going towards more negative potentials. The increased intensity demonstrated that dAMP molecules were getting closer to the AgNPs, and/or the amount of dAMP molecules reaching the surface had increased. The decreased intensity at more negative potentials suggests possible potential-induced desorption or molecular reorientation.
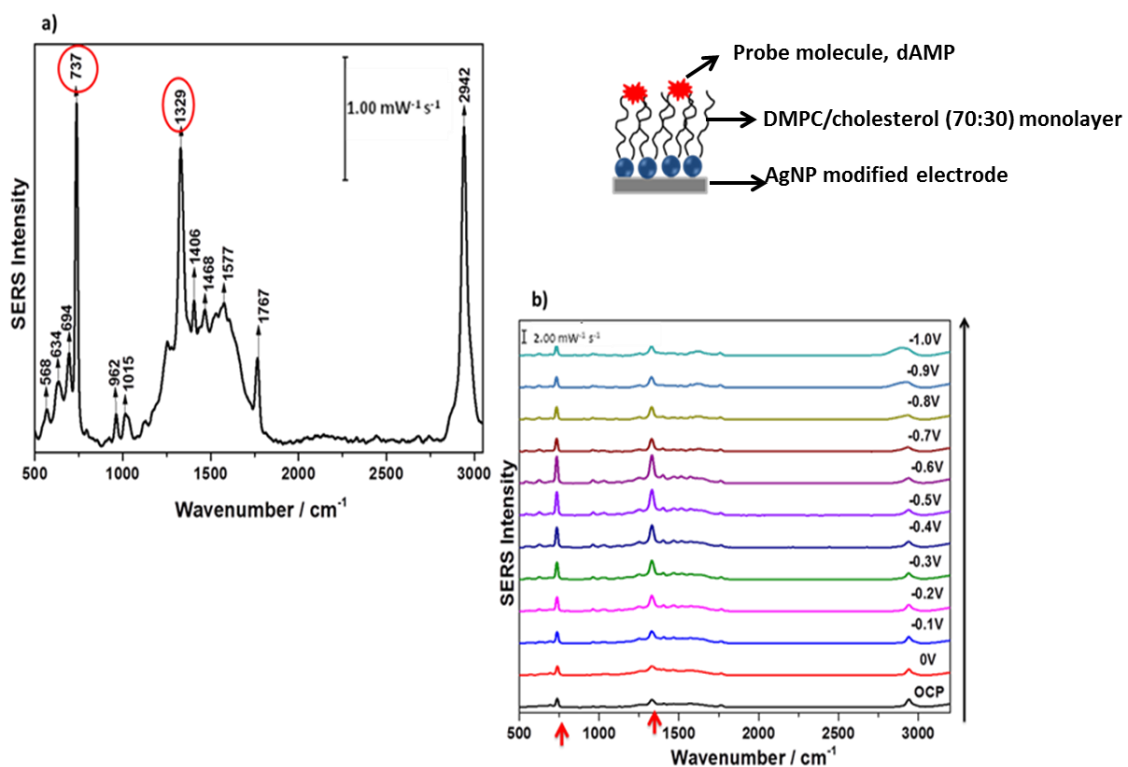
Figure 30: DMPC/cholesterol (70:30) monolayer probe studies with 1mM dAMP/0.1 M NaF solution. Spectrum **a)** shows peaks present at OCP and overlay spectra in **b)** shows increased dAMP peak intensities with more negative potentials for the cathodic scan.

An example where changes in SERS signal intensities indicated reorientation of dAMP molecules near a metal surface was pointed out by Papadopoulou *et al.* The studies demonstrated that dAMP reorients at Ag surfaces between pH 7-11 due to changing concentration of molecules at the metal surface.[204] At concentrations $<10^{-4}$ M the ring moiety of dAMP is parallel to the metal surface (weaker SERS signal), while at concentrations $\geq$ $^{-4}$ M, the ring moiety of dAMP is perpendicular to the metal surface (stronger SERS signal).[204] At more negatively applied potentials, the WE surface charge will become less positive since the pzc of Ag is approximately -0.9 V.[165] Around this value and at more negative voltages the AgNP surface would be negatively charged. The presence of the negatively charged phosphate group may direct rearrangement of the dAMP molecules as a result of electrostatic repulsion. The probe peaks still persisted in the anodic pathway (Appendix Figure A-9) with a signal increase then decrease going towards less negative potentials. The persistence of the probe peak signals in the anodic pathway demonstrated that dAMP remained near the AgNP surface. The CV obtained from the monolayer studies was significantly thinner (reduced current) to that of the control, which was 0.1 M NaF only (Figure 31). The conclusion was made that monolayer formation on the WE was plausible, however probe signal was readily observed, indicating the monlayer quality was poor.
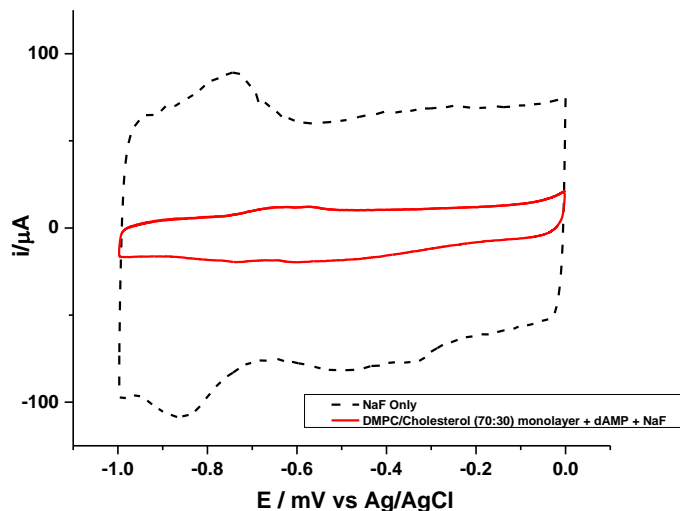
Figure 31: CV comparison between: (-) deposited DMPC/cholesterol (70:30) monolayer on the surface of a AgNP modified electrode in the presence of 1 mM dAMP/0.1M NaF solution, and (---) a AgNP modified electrode in the presence of a 0.1 M NaF solution. The CVs were performed at a scan rate of 50 mV s^{-1} between 0 V and -0.1V.

5.5 Initial lipid bilayer and dAMP EC-SERS studies

A DMPC/cholesterol bilayer was formed by the LB-LS technique and the quality of the bilayer was assessed using 0.1 M NaF/1 mM dAMP solution. The existence of lipid components at the electrode surface in air was corroborated by peak assignment (Appendix Table A-10). Additional proof for lipid bilayer formation was given by the reduction in the size of the cyclic voltammogram compared to the control (Appendix Figure A-11). At OCP (Figure 32) the probe peaks were discrete, though their intensities relative to the other peaks in the spectra were not as distinct as compared to the monolayer studies (Figure 33). The assumption was made that the presence of the bilayer, being thicker than the monolayer, provided a greater distance from the AgNP surface and hence a weaker probe signal. Moreover, peak assignment completed for the OCP spectrum

120

(Appendix Table A-12) indicated the presence of lipid components on the AgNP surface.[134-136,195,203]

The cathodic pathway showed an increase and then slight decrease of the probe peak intensities going towards more negative potentials. The presence of the probe peaks throughout the entire anodic pathway (Appendix Figure A-13) revealed the close proximity of the probe molecules to the AgNP surface.
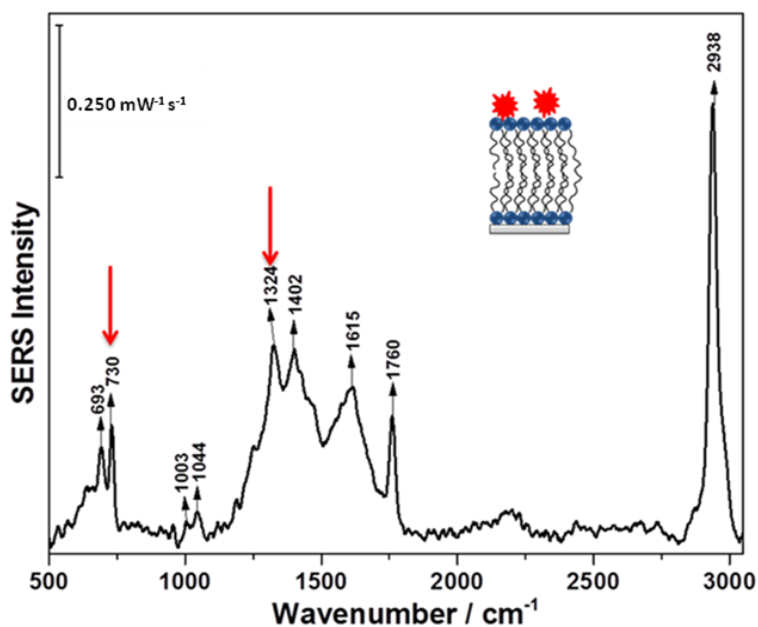
Figure 32: OCP spectrum of DMPC/cholesterol (70:30) bilayer in the presence of 1mM dAMP/0.1 M NaF solution. Probe peaks at 730 cm^{-1} and 1324 cm^{-1} were clearly detectable. The spectrum was collected for 30 s with a laser power of 7 mW at 532 nm.

Since the dAMP probe peaks were present at OCP, it was then postulated that bilayer formation was likely and that defects in the lipid bilayer accounted for the presence of these peaks in the spectra. The presence of probe peaks at more negative potentials in the cathodic and anodic pathway (Appendix Figure A-13) can be explained by results reported in literature. It has been proven that at more negative potentials biomimetic membranes directly

121

adsorbed onto metal surfaces desorb from the electrode surface and create a gap that can be filled by other species in solution.[138] Another important fact to consider is the occurrence of electroporation where the deviation from a normal membrane potential range leads to electrical instability and the formation of pores.[58,194] Thus it was construed that at more negative applied potentials the presence of a probe molecule could be due to possible voltage-induced pore-formation within the model membrane.
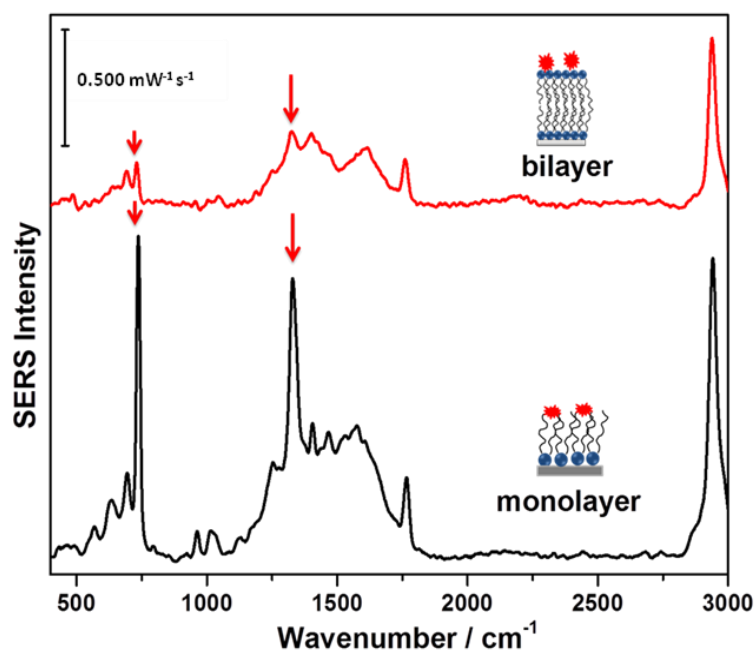
Figure 33: A comparison between the OCP spectra of DMPC/cholesterol (70:30) monolayer and bilayer dAMP probe studies showing the reduction of the probe peaks. The spectra were collected for 30 s with a laser power of 7 mW at 532 nm.

5.6 Improving fabrication conditions of bilayer system

5.6.1 Increased subphase temperature and humidity studies

Clearly the quality of the model membrane employed thus far was not suitable for further studies since the dAMP probe peaks were evident at OCP and

research indicates dAMP molecules do not permeate cell membranes. Polar surface area values, in units of $Å^2$, are used in the medical field to define the cell membrane permeating capabilities of a drug. Values greater than 140 $Å^2$ suggest poorly permeating species[206], and because dAMP has a polar surface area of 165.84 $Å^2$ it should not penetrate a lipid bilayer and hence no dAMP peaks at OCP should be observed in the SERS spectra.[207] Literature studies emphasize that lipid bilayers in the L_d state were of better quality, and to achieve the L_d state monolayers must be formed above the T_m temperature.[60] Likewise the improvement of model membrane quality can further be enhanced by forming the lipid bilayer in an elevated humidity environment. High humidity increases the fluidity of membranes and rounds the edges of bilayers to shield hydrophobic regions from contact with the aqueous environment.[208-210] Steps were then taken to repeat lipid bilayer formation at a subphase temperature of roughly 30°C and a relative humidity (RH) of above 60 %. Under these new conditions, a spectrum was collected for a DMPC/cholesterol (70:30) bilayer deposited on a AgNP modified electrode in the absence of the probe/electrolyte solution (Figure 34). The spectrum consisted of more peaks when compared to previous experiments (Appendix Table A-14) and peaks observed were indicative of lipid components on the AgNP surface.
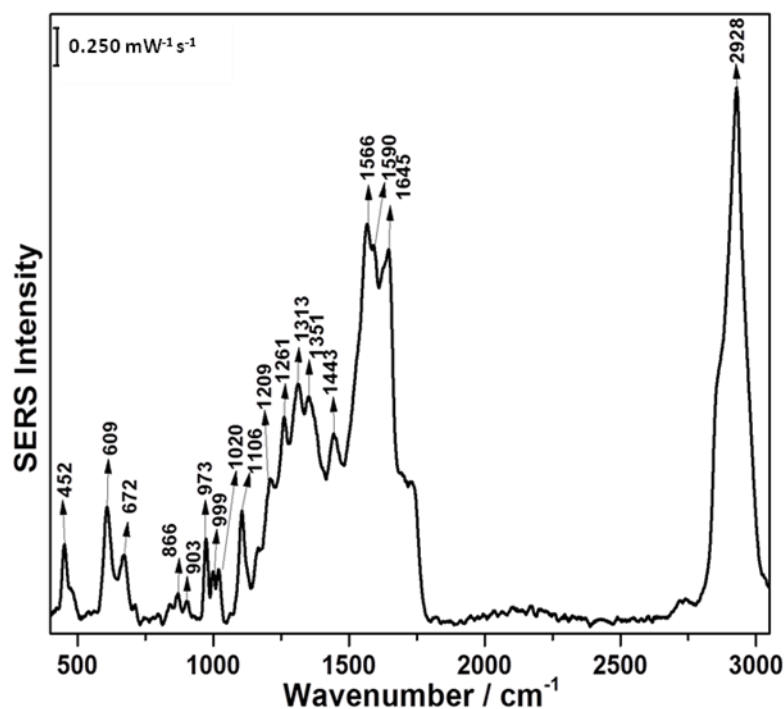
Figure 34: The spectrum of DMPC/cholesterol bilayer deposited on a chloride treated AgNP modified electrode formed at high humidity and elevated subphase temperature. The spectrum was collected for 30 s with a laser power of 2 mW at 532 nm.

At OCP the dAMP peak at 729 cm^{-1} was observed but relative to the other lipid component peak intensities, its intensity was not dominant (Figure 35). This reduced signal intensity of the 729 cm^{-1} peak indicated an improvement in membrane quality. However, the presence of the other dAMP peak was unclear. Before the addition of the electrolyte solution a peak was observed at 1313 cm^{-1} and then at OCP a strong peak was observed at 1317 cm^{-1}. The peak at 1317 cm^{-1} could represent the ring breathing mode of dAMP (which typically falls around 1320 cm^{-1}) or a shift of the peak at 1313 cm^{-1}.
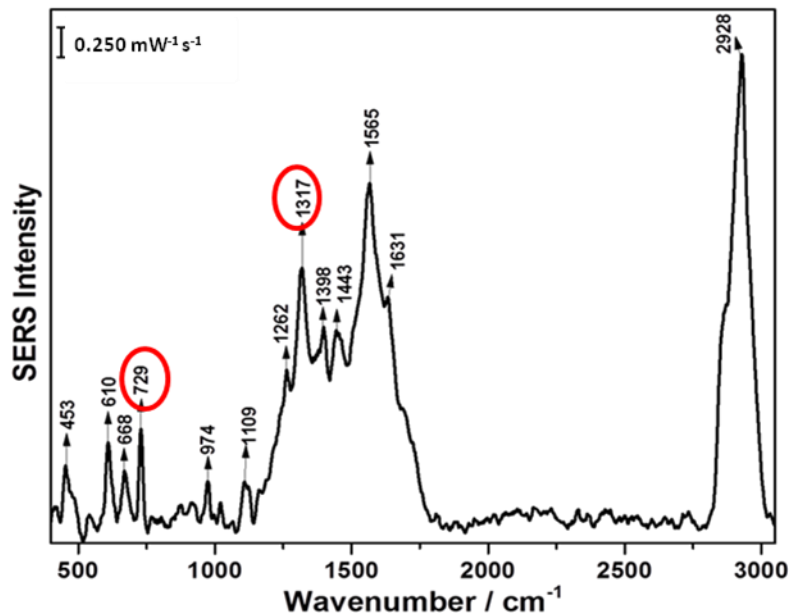
Figure 35: The OCP spectrum of DMPC/cholesterol bilayer deposited on a chloride treated AgNP modified electrode formed at high humidity and subphase temperature in the presence of 1 mM dAMP/0.1 M NaF solution. The spectrum was collected for 30 s with a laser power of 10 mW at 532 nm.

The cathodic and anodic data sets (Appendix FigureA-15) showed the same general trend for probe peak intensities but the main differences were the stronger intensities of the lipid components and the emergence of new peaks. Literature research for the assignment of these new peaks pointed towards hydrogen bonding among water molecules and interactions between water molecules and lipid components (Appendix Table A-16). The adjusted temperature and humidity conditions provided some improvement to the membrane quality, based on the relative peak intensities between the probe molecule and lipid components, which showed decreased probe signal intensities with respect to lipid component intensities. An example of this change in relative intensities is shown in Figure 36.
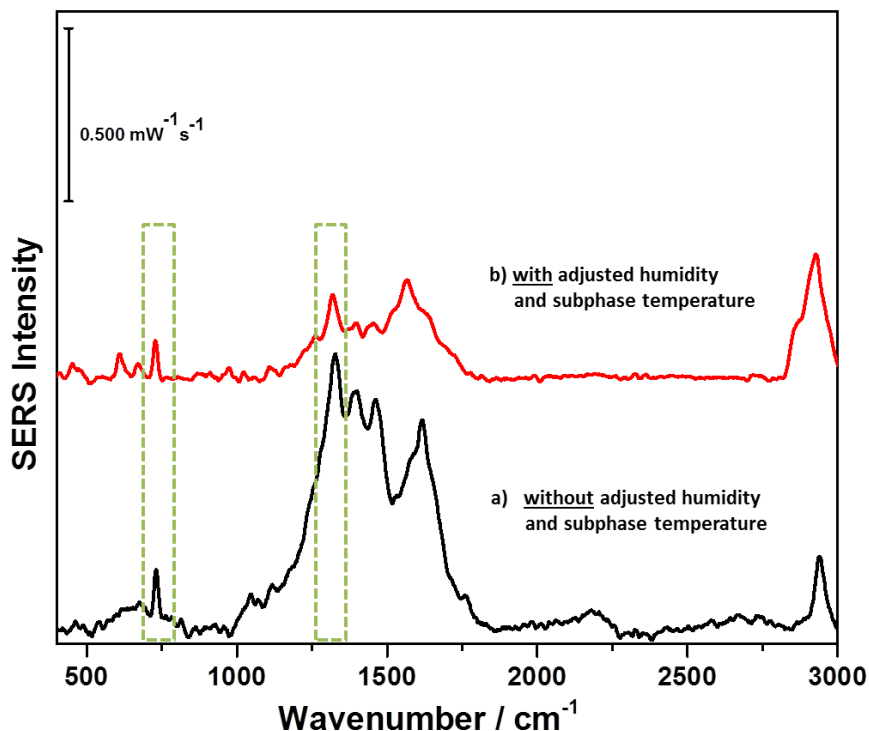
Figure 36: An overlay of -0.1 V spectra of a) DMPC/cholesterol bilayer in the presence of 1mM dAMP/0.1 M NaF solution without adjustment of experimental conditions, and b) DMPC/cholesterol bilayer in the presence of 1mM dAMP/0.1 M NaF solution at increased subphase temperature and elevated humidity. Both spectra were collected for 30 s at 532 nm with a laser power of 7 mW for a) and 10 mW for b).

5.6.2 Increased cholesterol content, temperature and humidity studies

The percent mole ratio of DMPC/cholesterol was changed to 50:50 mol % in order to determine what effect cholesterol content had on decreasing defects in the lipid bilayer. Although this alteration gave a cholesterol/lipid ratio that was outside the range of a normal human neuron membrane[58] the aim was to determine possible ways that the lipid bilayer quality could be improved. In this study the dAMP probe molecule peaks were visible at OCP but the peaks were not dominant. The peaks still remained throughout the cathodic and anodic pathways

126

but their intensities were weak and fairly consistent (Refer to Figure 37).
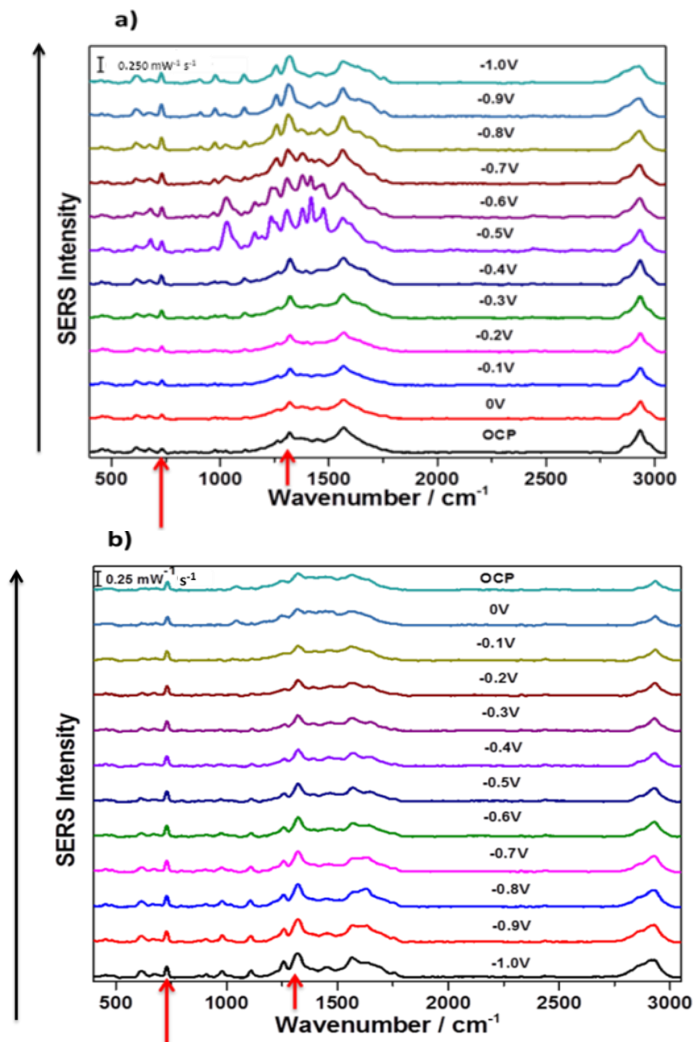
Figure 37: a) Cathodic and b) anodic spectra for DMPC/cholesterol (50:50) bilayer in the presence of 1mM dAMP/0.1 M NaF solution. The spectra were collected for 30 s with a laser power of 10 mW at 532 nm.

The observation made from the increased cholesterol content based on the weak probe peak intensities was that cholesterol either both increased the stiffness of the model membrane, or cholesterol increased the thickness of the bilayer, which pushed dAMP molecules further from the AgNPs surface whereby giving a weaker SERS signal. It was concluded that increasing the cholesterol content decreased

the fluidity of the lipid bilayer and dAMP molecules permeated the lipid bilayers to a lesser extent. However, since the cholesterol/lipid content was not comparable to that of a typical human neuron cell membrane, the decision was made to continue all other lipid bilayer studies using a lipid/cholesterol mole percent ratio of 70:30.

5.6.3 Surface coverage studies of silver nanoparticles by various self-assembled alkanethiol molecules

Although increased subphase temperatures and elevated humidity improved the quality of the model membrane, the dAMP probe peaks were still observed at OCP. This led to two deductions about the appearance of dAMP peaks: 1) dAMP molecules were adsorbing onto uncovered AgNPs due to the rounding of the lipid bilayer at the edges, or 2) if dAMP molecules are partially embedded in the upper leaflet of the model membrane then they may be close enough to provide a SERS signal. A modified support was used to explore these deductions. Alkanethiols were the ideal molecules to act as a lipid support since they form a completely compact monolayer with a fairly smooth surface and in addition, alkanethiols can have a hydrophilic terminal which can be used to aid in the adsorption of a lipid bilayer.[96] In choosing the correct alkanethiol SAM to use, two important aspects were considered:

1) the probe molecule must give a discernible signal to that of the SAM or cause a distinct signal change of the SAM

2) to observe and detect changes of the lipid components within the model

membrane, the length of the alkyl chains within the alkanethiol SAM must not be too long so as to put the lipid bilayer outside the range of the SERS effect.

The alkanethiol 1-octadecanethiol (1-ODT) which has 18 carbon atoms forms a SAM giving an approximately 2 nm distance from the AgNP surface.[211] The results from the experiment forming a 1-ODT monolayer for nearly 12 hr showed no SERS probe signal for dAMP. The characteristic ring breathing peaks for dAMP around 730 cm^{-1} and 1320 cm^{-1} were not observed at OCP or during the cathodic and anodic pathways (Appendix Table A-22). To determine if the absence of the probe signal was due to the sizable distance from the AgNP surface or a completely compact SAM, studies were performed to explore these factors. The 1-ODT SAM was formed using various incubation times and the probe signal was observed when the shorter incubation times were used. Figure 38 shows how the incubation time for the formation of the 1-ODT SAM affected the detection of the dAMP probe molecule. At 1 minute incubation, the dAMP characteristic peaks were clearly seen. However, after only 15 minutes incubation the dAMP probe peaks were absent. This suggested that a very compact monolayer had formed which would restrict the size of probe molecules used in the study since only molecules that could permeate the SAM would be detected. Moreover, a distance of 2 nm (approximate length of 1-ODT) formed by a SAM may be too far away from the AgNP surface to give a strong SERS enhancement for probe molecules. For these reasons, 1-ODT was rejected as a possible SAM material for these studies.
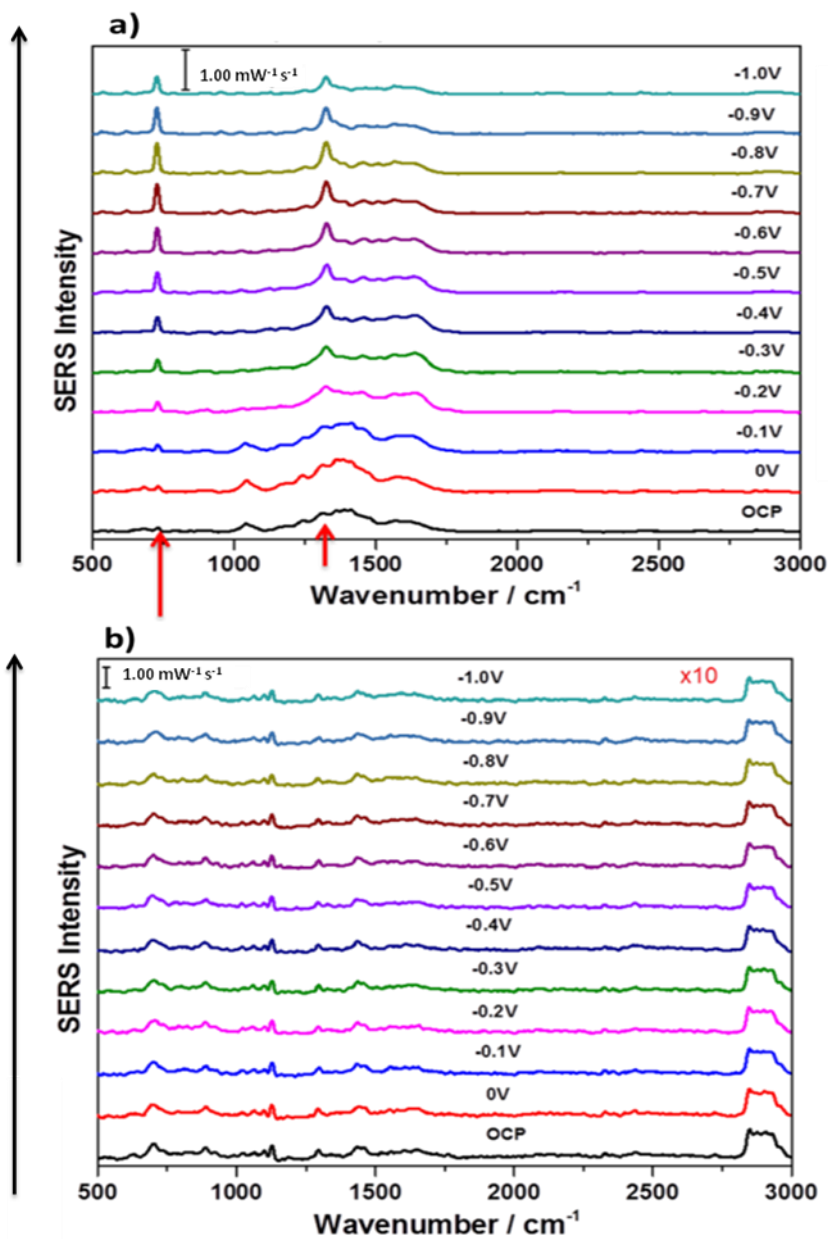
Figure 38: a) Cathodic spectra of 1 minute incubation for th formation of a 1-ODT SAM where 730 cm^{-1} and 1320 cm^{-1} dAMP peaks were observed at 1 mM dAMP. b) Cathodic spectra of 15 minutes incubation for th formation of a 1-ODT SAM where 730 cm^{-1} and 1320 cm^{-1} dAMP peaks were absent at 1 mM dAMP. The spectra were collected for 30 s with a laser power of 10 mW at 532 nm.

To decrease the distance from the AgNP surface and to reduce the compact nature of the SAM, 12-mercaptododecanoic acid (12-MDA) was viewed as an ideal

130

candidate. 12-MDA would give a distance of approximately 1.5 nm from the metal surface.[213] Unlike 1-ODT, which possesses a hydrophobic terminal group (CH_3), 12-MDA possesses a carboxyl terminal group which when deprotonated will give a negatively charged surface that can facilitate lipid bilayer adsorption. The pKa of 12-MDA[213] lies around 4.80 and laboratory prepared 0.1 M NaF gave a pH approximately between 7 and 8. Thus, the expectation was that the introduction of a 0.1 M NaF solution would give the deprotonated form of 12-MDA. The peaks obtained in any SERS spectra recorded for an adsorbed 12-MDA monolayer can verify such an assumption since deprotonated and protonated carboxyl groups give different spectral peaks (Section 3.3.9, Table 4). In this study, the peaks indicated the presence of deprotonated carboxyl groups (Appendix Figure A-24). The dAMP probe study involving a 12-MDA SAM for a 12 hr incubation time showed the probe peaks distinctly at OCP (Appendix Figure A-24). At more negative potentials however the probe peak signal intensity decreased and only the peak around 1320 cm^{-1} persisted while the peak at 730 cm^{-1} disappeared or appeared as a shoulder on the v(C-S)$_{trans}$ stretching vibration for the alkanethiol. It was deduced that at negative potentials the negatively charged metal surface likely caused molecular reorientation of the dAMP molecules. Additionally, the v(C-S)$_{trans}$ alkanethiol stretching at more negative potentials became intense and may have masked the signal for the dAMP molecule (Figure 39).
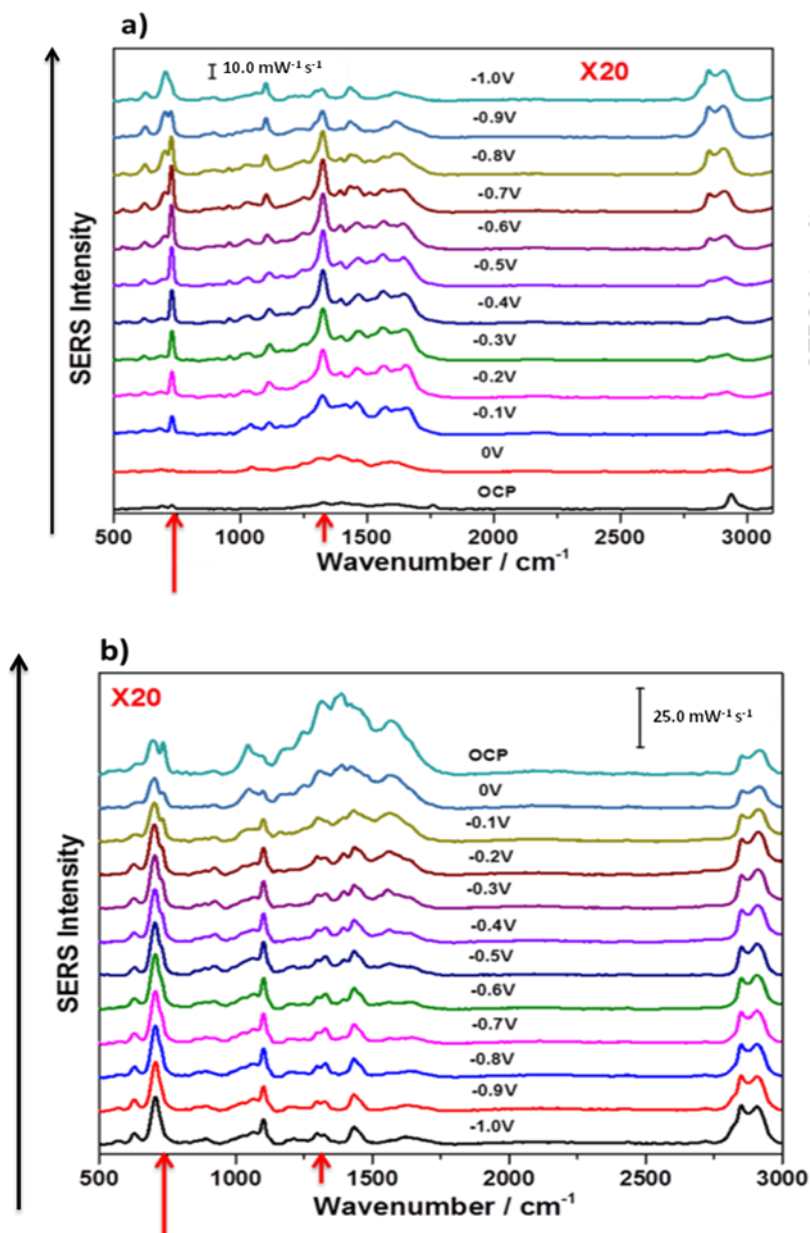
Figure 39: a) Cathodic and b) anodic spectra for dAMP probe study of 12-MDA SAM which demonstrated that the probe molecule can be detected in the presence of the alkanethiol SAM. The spectra were collected for 30 s with a laser power of 10 mW at 532 nm.

To ensure the closest possible distance to the AgNP surface while still exploiting a carboxylated terminal group, a shorter chained alkanethiol was explored, 6-mercaptohexanoic acid (6-MHA). If 12-MDA has an approximate length of 1.5 nm then it was deemed that half the chain length would give a

length of approximately 0.75 nm, which would allow for lipid component detection for the LB leaflet. Shorter chained alkanethiols with terminal carboxylic groups have Ag-COO$^-$ interactions during the formation of a SAM on a roughened Ag surface.[102] These Ag-COO$^-$ interactions are not sustained, but if present they can lead to a disordered monolayer.[102] Therefore, to ensure the 6-MHA is completely formed with no Ag-COO$^-$ interactions the incubation time was increased to a minimum of 18 hr.

To better ascertain peaks within such rich spectral data, triplicate EC-SERS measurements of the 6-MHA SAM on the AgNP surface in 0.1 M NaF were completed. The formation of the SAM was confirmed by the v(C-S)$_{trans}$ and v(C-S)$_{gauche}$ stretches around 700 cm^{-1} and 630 cm^{-1} respectively, the alkyl chain stretches around 2930 cm^{-1}, and the absence of the SH peak around 2570 cm^{-1}. Characteristic peaks around 1500 cm^{-1} indicated the presence of deprotonated carboxyl groups.[102,104,109,157] Figure 40 shows the OCP spectrum of a 6-MHA SAM formed on the AgNP modified screen-printed electrode. Peak assignment was done for each trial (Appendix Table-A: 27, 29, 33, 35, 39, and 40) and was used as a reference point for comparisons of future experiments employing a lipid bilayer.
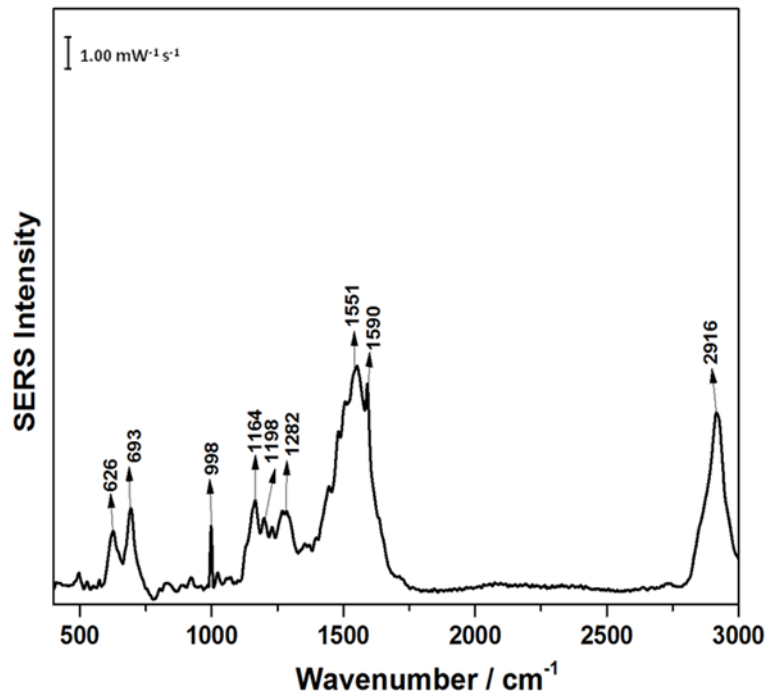
Figure 40: In air spectrum of a 6-MHA SAM formed on AgNP modified electrode. The spectrum was collected for 30 s with a laser power of 5 mW at 532 nm.

At more negatively applied potentials the following general trends were observed in the EC-SERS spectra: increased 630 cm^{-1} v(C-S)$_{gauche}$ intensity compared to the v(C-S)$_{trans}$ stretch, slight broadening of peaks in the 1500 cm^{-1} region, increased intensity of CH$_2$ deformations around 1430 cm^{-1}, and increased intensity of CH$_2$ stretching vibrations around 2920 cm^{-1}. These observations indicate that at more negative potentials the alkyl chains became more tilted and disordered. Figure 41 displays the cathodic and anodic spectra for the 6-MHA SAM on the AgNP electrode in 0.1 M NaF.
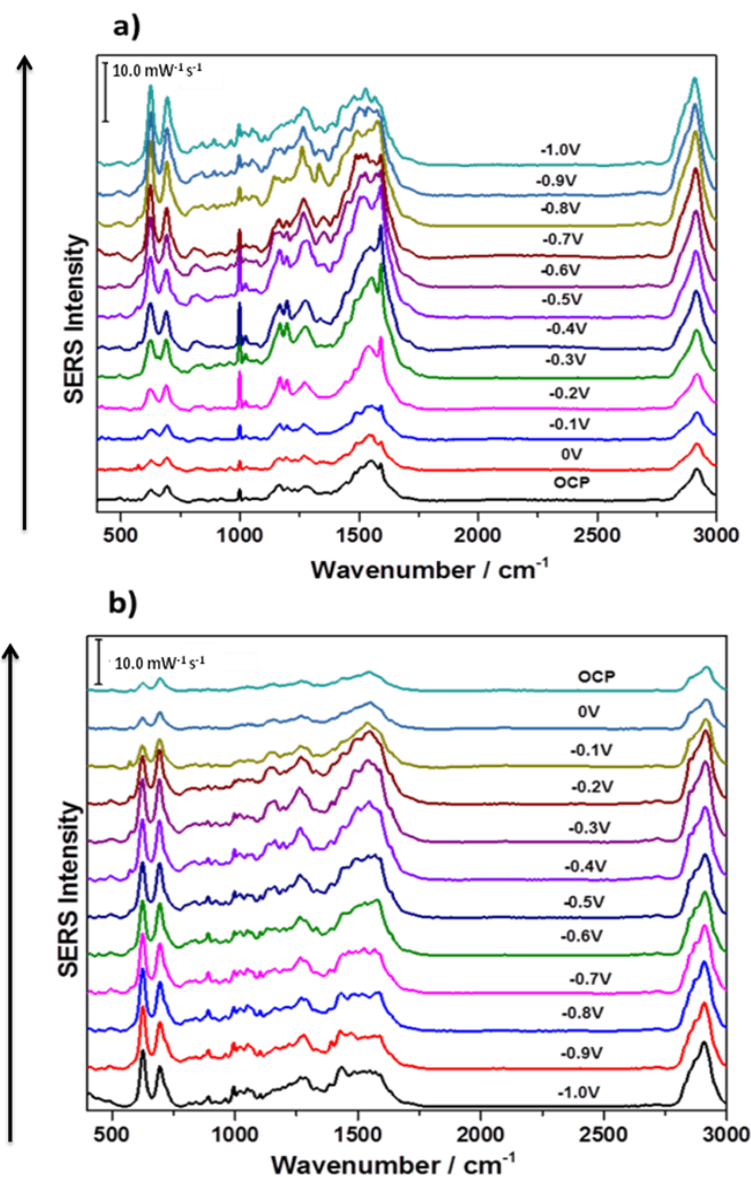
Figure 41: a) Cathodic and b) anodic spectra of 6-MHA SAM on the AgNP modified electrode in the presence of 0.1 M NaF solution. The spectra were collected for 30 s with a laser power of 5 mW at 532 nm.

In the literature for methyl terminated alkanethiol monolayers the distance between individual chains was found to be roughly 0.3 nm which restricted the passage of solvated ions or molecules with diameters greater than 0.3 nm.[103] Therefore for 6-MHA the distance between individual chains would be slightly greater than 0.3 nm to accommodate electrostatic repulsion between neighbouring

deprotonated carboxyl groups. Thus, it was hypothesized that solvated ions and large molecules would still be restricted from penetrating the SAM and reaching the electrode surface. It was concluded from the 6-MHA studies that a well-formed compact monolayer was formed on the AgNP modified screen-printed electrode surface since there were no peaks indicating Ag-COO⁻ interactions, and the peaks observed in the studies corroborated with those in literature indicating well-formed SAMs. Based on the alkanethiol SAM studies, the 1-ODT and 12-MDA SAMs formed on the surfaces of the AgNP modified electrodes created barriers that restricted analyte molecules from coming into direct contact with the metal surface since the dAMP SERS signals were absent and reduced, respectively. At distances beyond 2 nm (based on the 1-ODT studies), a SERS signal from analyte molecules would most likely be obtained through penetration of the SAM by the analyte molecule. Thus, for the purpose of this research it was concluded that the use of 6-MHA SAM as a lipid bilayer support was appropriate because: i) it provided the hydrophilic surface that will accommodate the adsorption of a lipid bilayer, and ii) the shorter alkyl chain gave a distance (< 1 nm) close enough to the SERS substrate that if probe molecules traversed the lipid bilayer a SERS probe signal could be observed whether the probe molecule was adsorbed onto the surface of the SAM or the probe molecule had penetrated the SAM.

5.7 Investigation of the quality of the LB-LS lipid bilayer system using various probes

5.7.1 Introduction

With the improved conditions (e.g. using the lipid bilayer support 6-MHA SAM and using chloride treatment for AgNP modified electrodes) the quality of the model membranes were investigated using different probes. Control studies (in the absence of the lipid bilayer) were performed in order to determine distinguishable SERS signals from probe molecules that traverse the lipid bilayer, these studies are outlined in the next sections.

5.7.2 dAMP studies

5.7.2.1 EC-SERS of dAMP on silver nanoparticles

EC-SERS spectra collected in the cathodic direction for dAMP on the bare AgNP surface gave strong spectral peaks around 730 cm^{-1} and 1320 cm^{-1} (See Figure 42). This indicated that dAMP molecules were directly adsorbed onto the metal surface. Since these two peaks were present at OCP and were consistently strong throughout both the cathodic and anodic scans (Figure 42 and Appendix Figure A-43), they were deemed the marker peaks for dAMP.
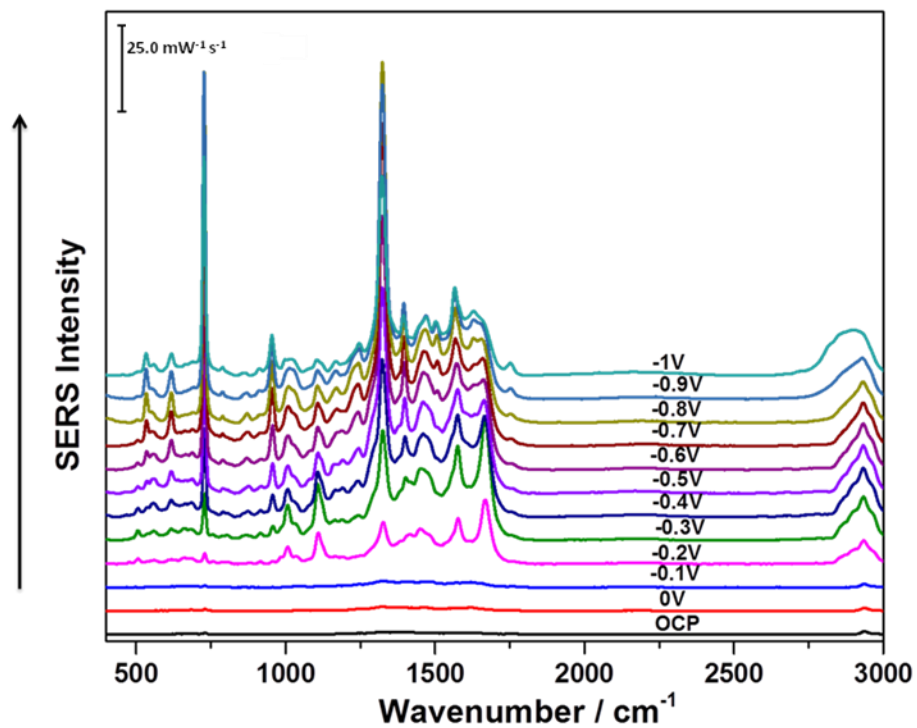
Figure 42: Cathodic spectra of 1 mMm dAMP on AgNP surface showing strong spectral peaks around 730 cm^{-1} and 1320 cm^{-1}. Intense signal intensities at more negative potentials diminished the appearance of peaks at less negative potentials in the overlay, however dAMP probe peaks were present at OCP. The spectra were collected for 30 s with a laser power of 5 mW at 532 nm.

These results showed that in spite of the negative applied potentials the dAMP molecules were not repelled from the surface. Repeat analysis of this experiment provided very reproducible results (Appendix Figure A: 45-47).

5.7.2.2 EC-SERS of dAMP in the presence of alkanethiol

Since the model membrane support was chosen to be a 6-MHA SAM, dAMP probe molecules were exposed to AgNP electrodes modified with 6-MHA SAMs in order to determine if a SERS signal from dAMP could be observed. At OCP the probe peaks for dAMP were not observed. During the cathodic pathway (Figure 43 a) at more negative potentials the probe peaks appeared. The probe peak at 730 cm^{-1} was found to overlap that of the v(C-S)$_{trans}$ stretching peak. In the anodic pathway (Figure 43 b) the peak at 1320 cm^{-1} became even more difficult to distinguish as the characteristic peak broadening previously shown for 6-MHA SAM indeed occurred. On the other hand, the peak at 730 cm^{-1} became more distinct and now existed as a nearly separate peak. This same trend was also observed in repeat trials of the experiment (Appendix Figure A: 51-58). This inferred that the potential induced disordering of the SAM alkyl chains permitted the penetration of dAMP molecules into the SAM.
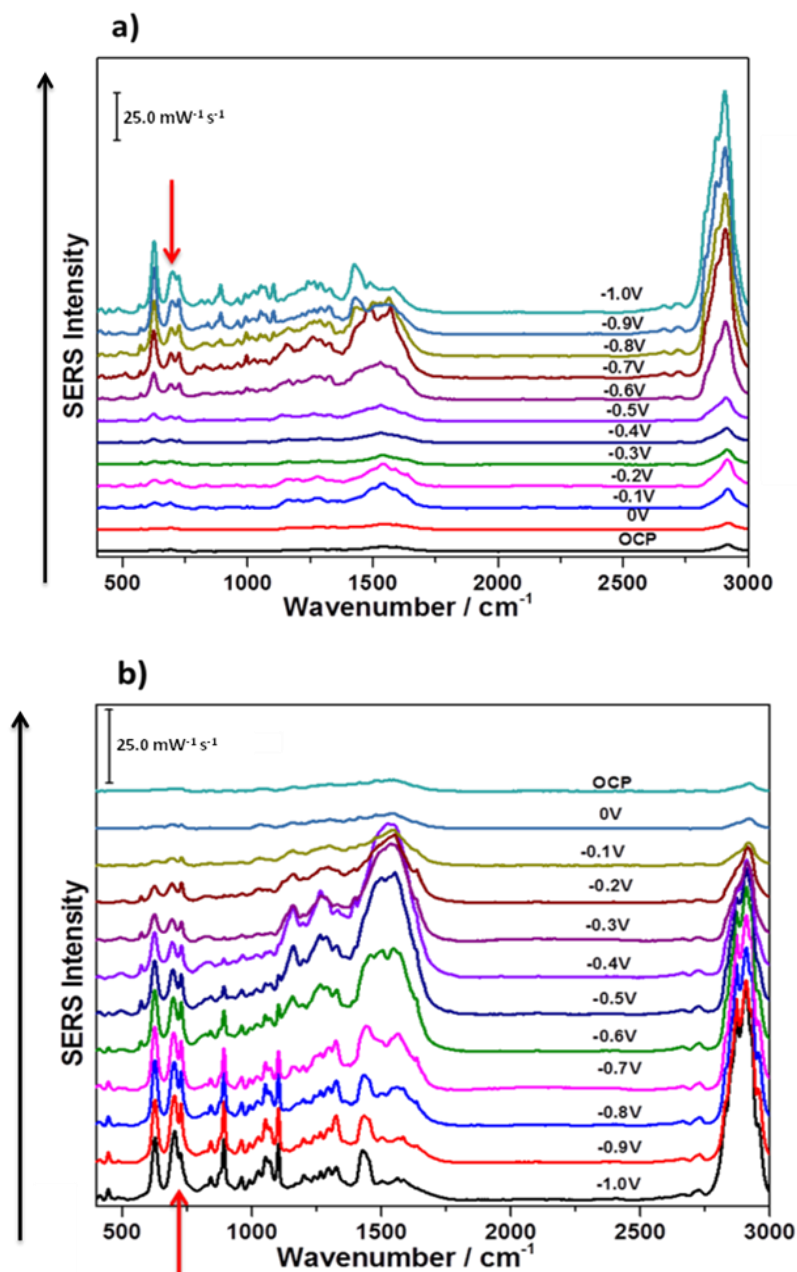
Figure 43: a) Cathodic and b) anodic spectra of 1mM dAMP/0.1 M NaF solution in the presence of 6-MHA SAM AgNP modified electrode. Probe peaks are observed after more negative potentials in the cathodic direction and increased presence in the anodic scan. The spectra were collected for 30 s with a laser power of 5 mW at 532 nm.

It was concluded that at OCP, dAMP molecules cannot penetrate the SAM and that disruption of the ordering of the SAM alkyl chains would allow for the penetration of the probe molecules into the SAM. Thus, for future experiments investigating pore-formation using 6-MHA as a lipid bilayer support and dAMP as the probe molecule, the distruption of the akyl chains within this model can be indicated by the presence of the dAMP SERS peaks.

5.7.2.3 EC-SERS of dAMP and lipid bilayer system

Based on the dAMP and 6-MHA SAM studies, the appearance of the dAMP ring breathing mode at 730 cm^{-1} will be used to indicate dAMP molecules permeating the lipid bilayer and coming into contact with the 6-MHA SAM. Unlike the other dAMP ring breathing mode at 1320 cm^{-1}, this peak was easier to discern and had no spectral overlap with lipid components and SAM molecules.

At OCP two of the trials showed a very small shoulder on the v(C-S)$_{trans}$ stretching peak around 700 cm^{-1}(Figure 44 b) of the alkanethiol but comparison to the electrode spectrum in air (before the addition of electrolyte/probe solution, Figure 44 a) showed that this shoulder was present as well. Therefore this shoulder was most likely a v(C-S)$_{trans}$ stretching mode and not the SERS signal indicating the permeation of the lipid bilayers by dAMP molecules.
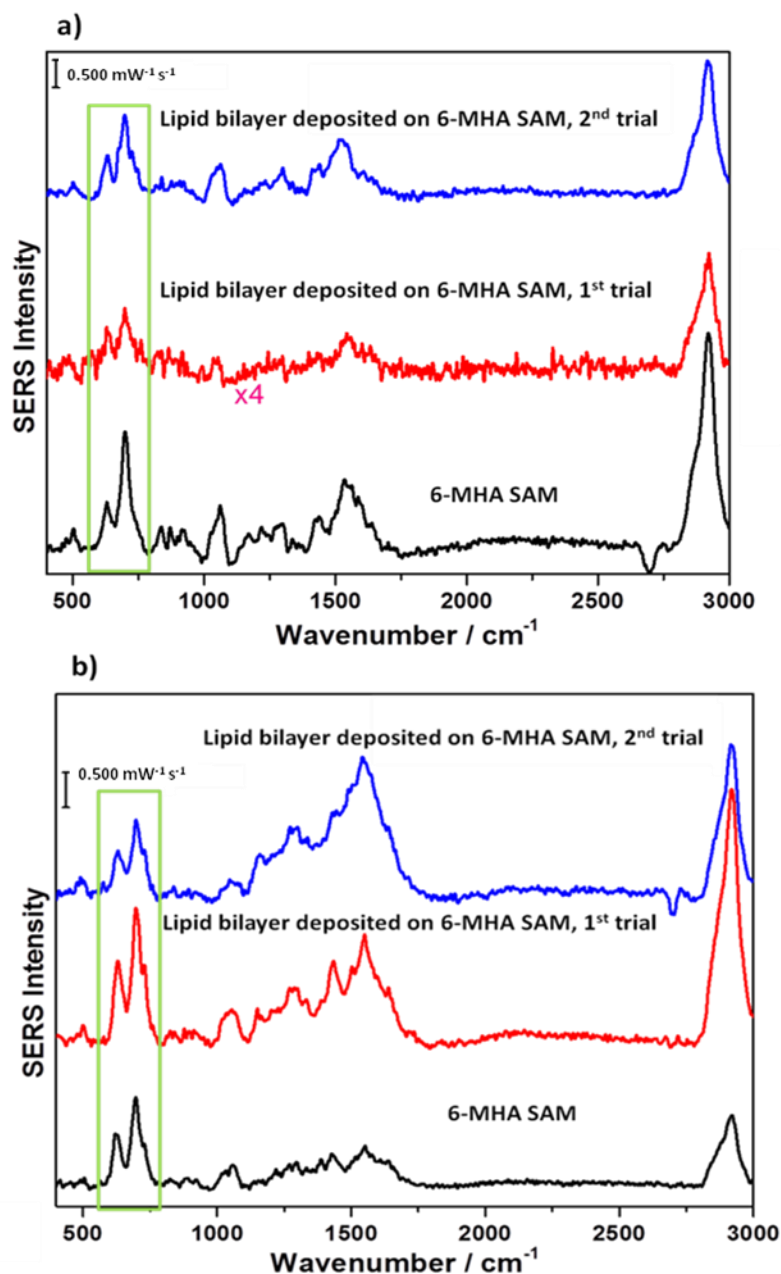
Figure 44: Overlay spectra of a) before and b) OCP (after the addition of 1 mM dAMP/ 0.1 M NaF solution). Shoulders were present before and after solution addition and hence affiliated with v(C-S)$_{trans}$ stretching of the alkanethiols. The spectra were collected for 30 s with a laser power of 5 mW at 532 nm.

During the cathodic and anodic scans the shoulder on the v(C-S)$_{trans}$ alkanethiol peak became more pronounced and in one case peak splitting was observed at

more negative potentials (Refer to Figure 45). It was deduced that the peak splitting could either indicate changes in the orientation of the C-C-S bond at the silver surface, or possibly dAMP molecules partially permeating the lipid bilayer system. Since in the control studies of 6-MHA SAM with 0.1M NaF solution there was no splitting of the v(C-S)$_{trans}$ peak at more negative potentials, it was concluded that dAMP molecules penetrating the lipid bilayer was more probable. It has been established previously in the dAMP probe study with a DMPC/cholesterol (70:30) bilayer directly deposited onto a AgNP modified electrode that at more negative potentials and during the anodic sequence the lipid bilayer is compromised. Thus, based on this assumption it was presumed that in this present study (lipid bilayer deposited onto a 6-MHA SAM AgNP electrode) that initially at OCP the dAMP molecules were adsorbed onto or were partially embedded into the top leaflet of the lipid bilayer. The applied negative potentials decreased the quality of the lipid bilayer likely due to electroporation. This potential-induced damage caused the dAMP molecules to penetrate further into the lipid bilayer eventually reaching the top of the 6-MHA SAM at which point the SERS signal for the probe was observed.

Peak assignment was done for the lipid bilayer studies (Appendix Table A: 6, 62, 65, 67, 71, and 73) and there was significant overlap of peaks for both lipid components and the 6-MHA SAM. Although it was difficult to authenticate the presence of the lipid bilayer based solely on this fact, the difference in spectral behaviour between experiments with and without a bilayer indicated the lipid bilayer was likely present.
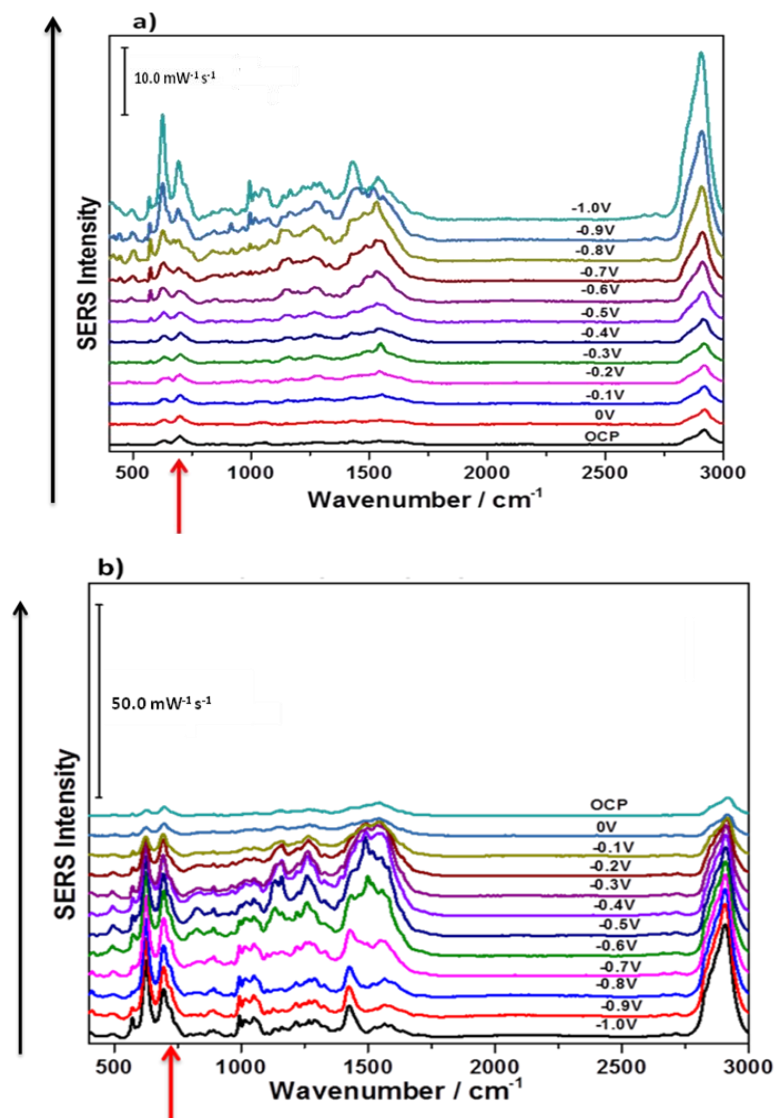
Figure 45: a) Cathodic and b) anodic spectra for DMPC/cholesterol (70:30) lipid bilayer deposited on 6-MHA SAM AgNP modified electrode in the presence of 1 mM dAMP/ 0.1 M NaF solution. The spectra were collected for 30 s with a laser power of 5 mW at 532 nm.

5.7.3 Adenine studies

5.7.3.1 EC-SERS of adenine on silver nanoparticles

Adenine was chosen to determine if a less polar, less hydrophobic, and smaller molecule (compared to dAMP) could penetrate the proposed model membrane. The first step in the investigation involved exposing the bare AgNP

modified screen-printed electrodes to adenine in order to determine the strongest SERS peaks. The strongest spectral peaks for adenine shown in Figure 46, representing the ring vibrations at 730 cm^{-1} and 1320 cm^{-1}, confirmed the adsorption of adenine onto the AgNP surface. The adenine molecules remained on the AgNP surface during the anodic pathway; the ring breathing vibrations were still clearly observable (Appendix Figure A-78). Replicate trials of this experiment indicated that these peaks were unmistakeably the marker peaks for adenine (Appendix Figure A: 80-85).
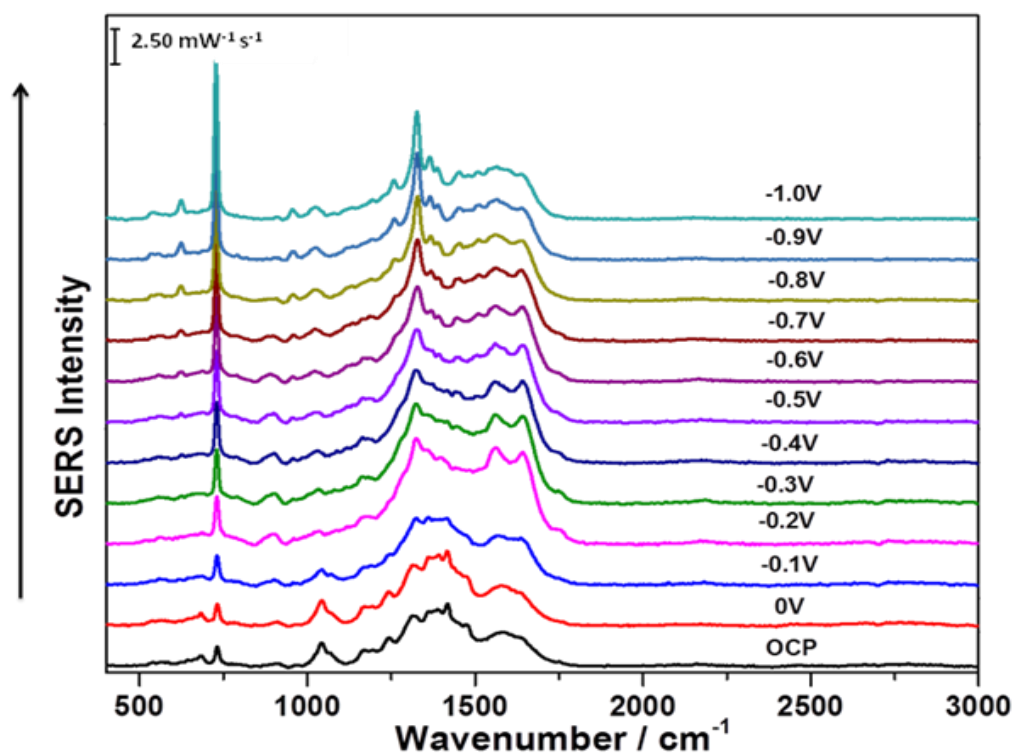
Figure 46: Cathodic spectra of 1 mM adenine adsorbed onto the AgNP modified electrode surface showed strong spectral peaks around 730 cm^{-1} and 1320 cm^{-1}. The spectra were collected for 30 s with a laser power of 5 mW at 532 nm.

5.7.3.2 EC-SERS of adenine in the presence of alkanethiol

In the presence of a 6-MHA SAM, the adenine peaks were observed from OCP and became much stronger as the experiment progressed. The peaks were the strongest in the anodic pathway, even surpassing that of the thiol C-S stretches at 630 cm^{-1} and 700 cm^{-1} and the alkyl chain stretching around 2920 cm^{-1} (See Figure 47). Repeat trials of this experiment showed consistently that the adenine peaks overpowered the C-S thiol stretches (Appendix Figure A: 86-96). This strong signal intensity indicated that the adenine molecules penetrated the 6-MHA SAM very easily and likely adsorbed onto the AgNP surface. Unlike the experiment with dAMP molecules in the presence of a 6-MHA SAM, the ring breathing modes at 730 cm^{-1} and 1320 cm^{-1} were very distinguishable at OCP. Thus it was likely that the presence of the negatively charged phosphate group may have prevented the penetration of the dAMP molecules into the alkanethiol SAM at OCP in the precvious study.
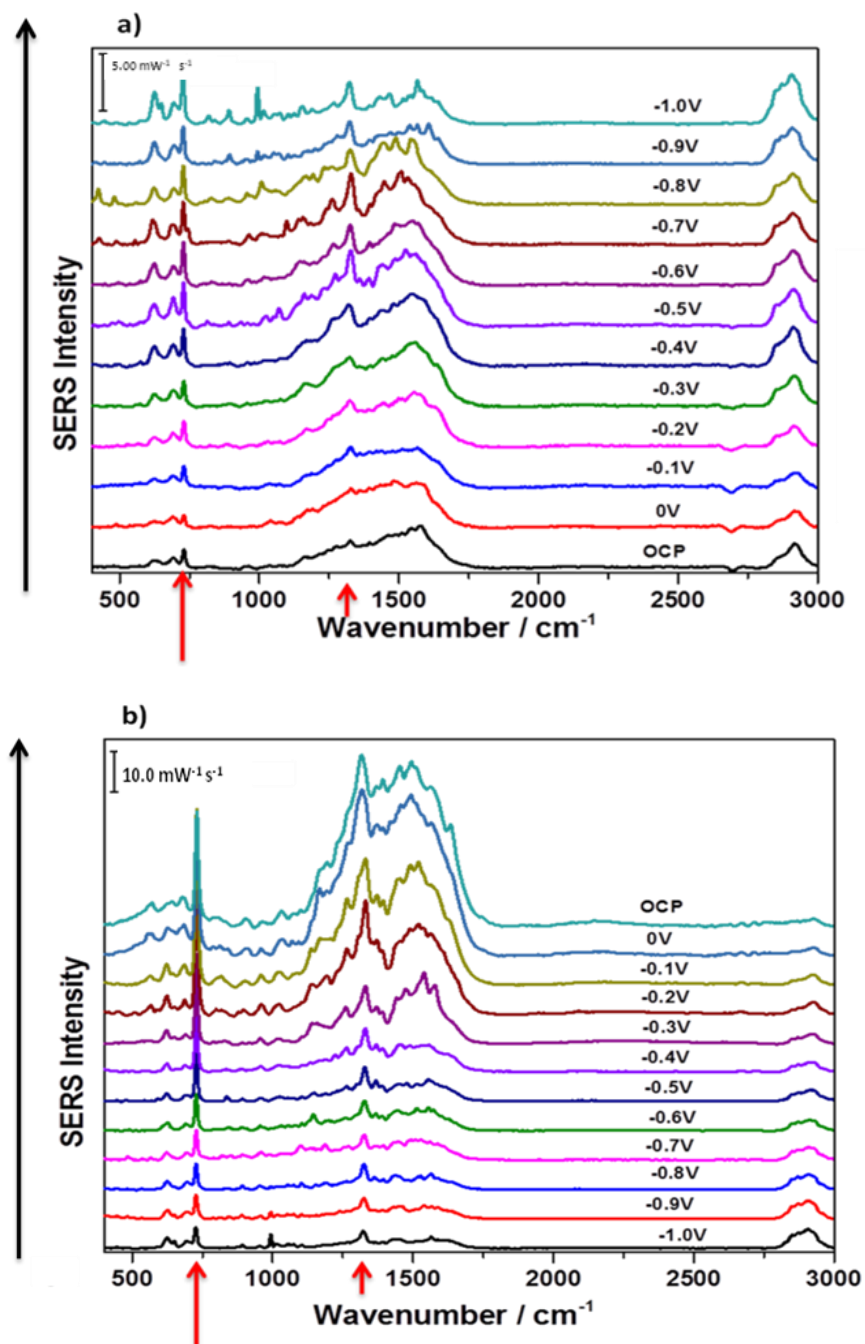
Figure 47: a) Cathodic and b) anodic spectra of 1mM adenine/0.1 M NaF solution in the presence of a 6-MHA SAM AgNP modified electrode. Probe peaks become significantly intense during the anodic direction. The spectra were collected for 30 s with a laser power of 5 mW at 532 nm.

5.7.3.3 EC-SERS of adenine and lipid bilayer system

The next step in the adenine studies involved the introduction of the probe molecule to the DMPC/cholesterol (70:30) lipid bilayer supported on a 6-MHA SAM. At OCP the adenine peaks were distinguishable (Appendix Figure A-99), which indicated that the adenine molecules permeated through both the lipid bilayer and the 6-MHA monolayer. The permeation of the adenine molecules could be due to its smaller size or the increased hydrophobic nature of the adenine moiety compared to dAMP. Repeat trials of this experiment were very consistent with each trial showing the adenine signal distinctly from OCP onwards (Appendix Figure A: 102-113). As illustrated in Figure 48, the probe signal intensities, both at 730 cm^{-1} and 1320 cm^{-1}, continued to increase throughout the cathodic and anodic sequences. Another intriguing observation is the broadening of peaks and increased signal intensity between 1000 cm^{-1} and 1700 cm^{-1} during the anodic pathway. Comparisons made with previous results showed that for experiments involving a 6-MHA SAM, or a lipid bilayer deposited on the alkanethiol, peak broadening and increased signal intensities always occurred within this same region. The peak broadening may be an indicator for a flawed lipid bilayer containing gaps or defects. This statement is supported by Richard Foucault *et al.* who showed that multilayers can be formed on a Ag metal surface by lipid molecules and surfactants.[175] At negative applied potentials, multilayers become more stable and well formed, giving broad peaks at 1530 cm^{-1} and 1130 cm^{-1}.[175] An even more obvious deduction was the possibility of photodegradation of the lipid bilayer by the laser. Thus, it was

concluded that during the anodic pathway the lipid bilayer structure was compromised and its double leaflet structure likely no longer existed.
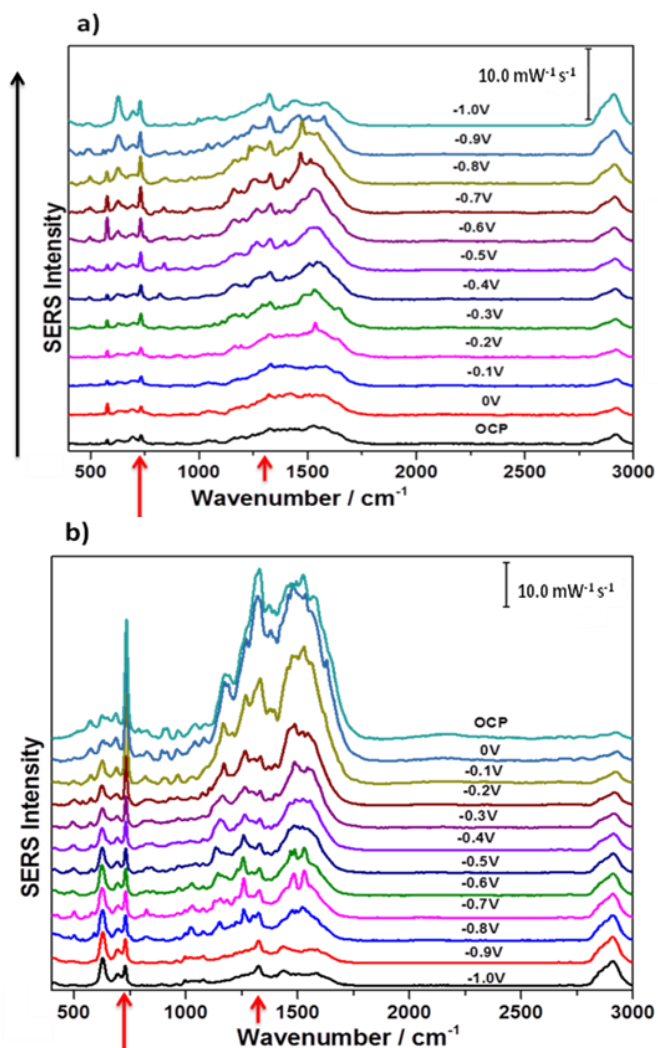
Figure 48: a) Cathodic and b) anodic spectra for DMPC/cholesterol (70:30) lipid bilayer deposited on 6-MHA SAM AgNP modified electrode in the presence of 1 mM adenine/0.1 M NaF solution. The spectra were collected for 30 s with a laser power of 5 mW at 532 nm.

5.7.4 Aloin studies at micromolar and nanomolar concentrations

5.7.4.1 Initial EC-SERS of aloin at millimolar concentration

The probe molecule aloin was chosen based on its size (the largest probe in this research project). In this thesis research project, all probe concentrations

were set to 1 mM, however in the initial studies using aloin at this concentration the peaks for aloin overwhelmed the spectra. Examples of this overwhelming SERS signal is provided in Figure 49 a and b, showing the OCP spectra of 0.1M NaF/1 mM aloin in the presence of 6-MHA SAM, and in the presence of a DMPC/cholesterol (70:30) lipid bilayer deposited on 6-MHA SAM, respectively. In previous lipid bilayer and SAMs studies the data suggested that both lipid bilayers and SAMs were stable at OCP in the presence of probe/electrolyte solutions, and additionally the SERS signals for both lipid components and SAM molecules could be observed in the presence of probe molecules (e.g. dAMP, adenine). It was deduced that the strong Raman scattering effect of the anthraquinone moiety overwhelmed the other peaks in the spectra. In both cases for mM aloin (Figure 49 a, b), intense peaks were seen around: 460 cm^{-1}, 1228 cm^{-1}, 1290 cm^{-1}, 1370 cm^{-1}, 1390 cm^{-1}, and 1561 cm^{-1}. The most intense peaks, all with similar peak intensities, were within the 1220 cm^{-1}-1560 cm^{-1} region but the peak around 1290 cm^{-1} was always the most intense. Similar SERS peaks were found in the literature in both Raman and SERS experiments of anthraquinone derivatives[155,198-200] and hence these peaks were deemed the marker peaks for aloin.
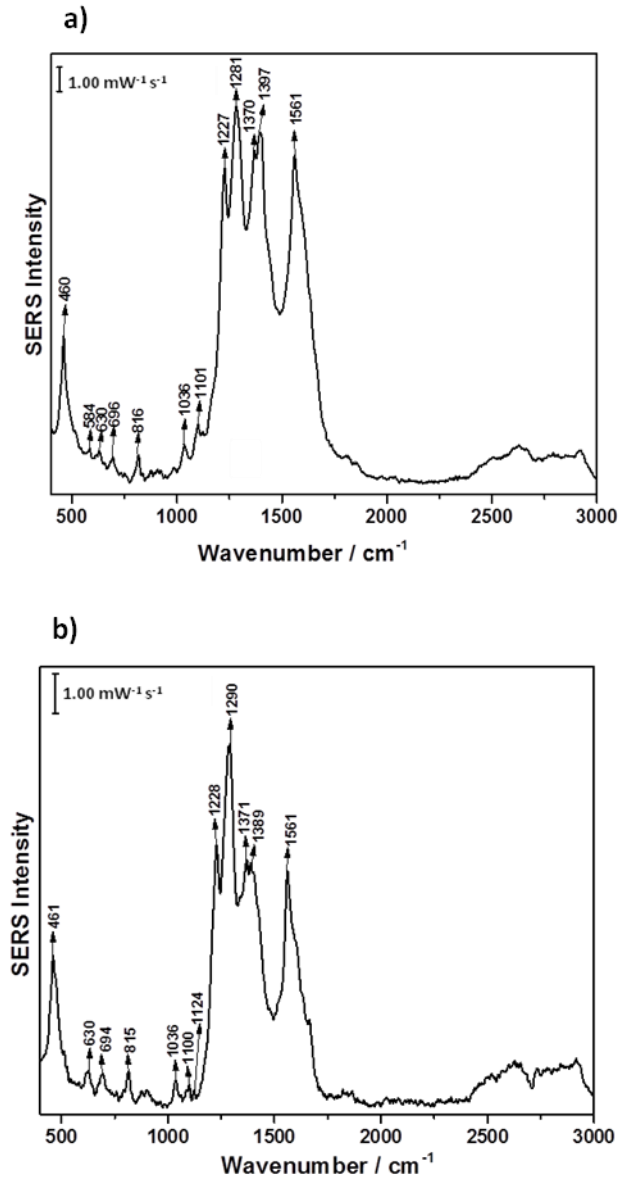
Figure 49: a) OCP spectrum of 1 mM aloin/0.1 M NaF solution in the presence of a 6-MHA SAM AgNP modified electrode, b) OCP spectrum of 1 mM aloin/0.1M NaF solution in the presence of a deposited DMPC/cholesterol (70:30) lipid bilayer on a 6-MHA SAM AgNP modified electrode. The spectra were collected for 30 s with a laser power of 5 mW at 532 nm.

It was decided that since 1 mM concentration was too high, a lower concentration value would be used for future probe studies. Both µM and nM concentrations were explored.

5.7.4.2 Aloin nanomolar concentration studies

5.7.4.2.1 EC-SERS of aloin on silver nanoparticles, nanomolar concentration

SERS has the capability of detecting very low analyte concentration and in addition, detecting analytes down to the single molecule level in some cases. Nanomolar concentrations of aloin were exposed to AgNP modified screen-printed electrodes, and repeat trials gave different spectra (Appendix Figure A: 115-124). This came as no surprise since the probability of acquiring a SERS signal with aloin molecules present on the surface would be drastically reduced at such a low concentration. Peaks obtained from the cathodic scan of nM aloin with AgNP modified electrodes showed none of the aloin marker peaks but rather correlated to citrate peaks found on colloidal Ag surfaces. Therefore it was deduced that aloin did not adsorb onto the AgNP surface during the cathodic sequence. The anodic data shown in Figure 50 a) represented the adsorption of aloin onto the AgNP surface since the following peaks corroborated with SERS peaks found in literature where anthraquinone derivative studies[155,198-200] showed the ring moiety interacting with a metal surface: 856 cm^{-1}, 1001 cm^{-1}, 1129 cm^{-1}, 1401 cm^{-1}, and 1605 cm^{-1}.
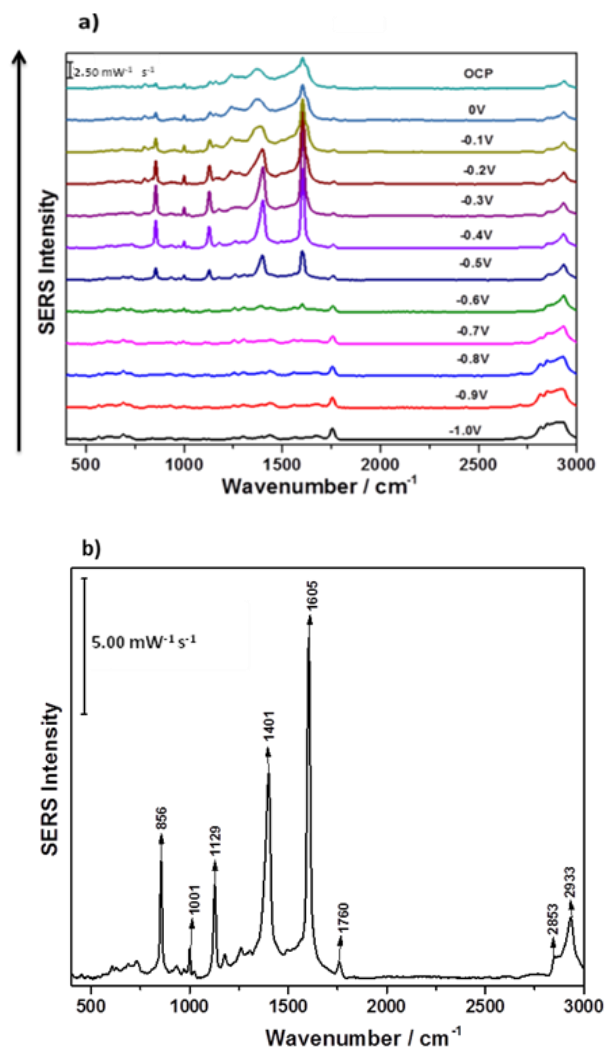
Figure 50: a) Anodic spectra of 1 nM aloin/0.1 M NaF solution with AgNP modified electrode. b) -0.4V spectrum of the anodic scan showing the distinct aloin peaks indicating adsorption onto the AgNP surface. The spectra were collected for 30 s with a laser power of 5 mW at 532 nm.

5.7.4.2.2 EC-SERS of aloin in the presence of alkanethiol, nanomolar concentration

A 0.1 M NaF/1 nM aloin solution was introduced to a 6-MHA SAM AgNP modified electrode to determine if very low concentration aloin could be detected in the presence of the SAM. The strong peaks observed in the previous study of aloin with AgNP modified electrode were not present at OCP in this

study. Peak assignment showed that peaks possibly indicating the presence of aloin overlapped with peaks already obtained for the control study of 6-MHA (Appendix Table A: 126, 129, and 133). Furthermore, two out of the three trials of this experiment showed similar cathodic trends to that observed in the control study of 6-MHA, where at more negative potentials both C-S stretches were almost equal in intensity (Figure 51). Such similarity can be correlated to that fact that in the presence of such low aloin concentration the alkyl chains of 6-MHA SAM were oriented in a very similar manner to previous studies. Additionally, the peak broadening in the anodic pathway of the aloin nM studies was not analogous to that observed for the aloin mM studies, but was more comparable to the dAMP and adenine studies for 6-MHA SAM. Therefore, it was concluded that aloin at nM concentration could not give a distinct signal in the presence of a 6-MHA SAM and that the similarities observed in the dAMP and adenine studies indicated similar alkyl chain movements of the molecules within the 6-MHA SAM.
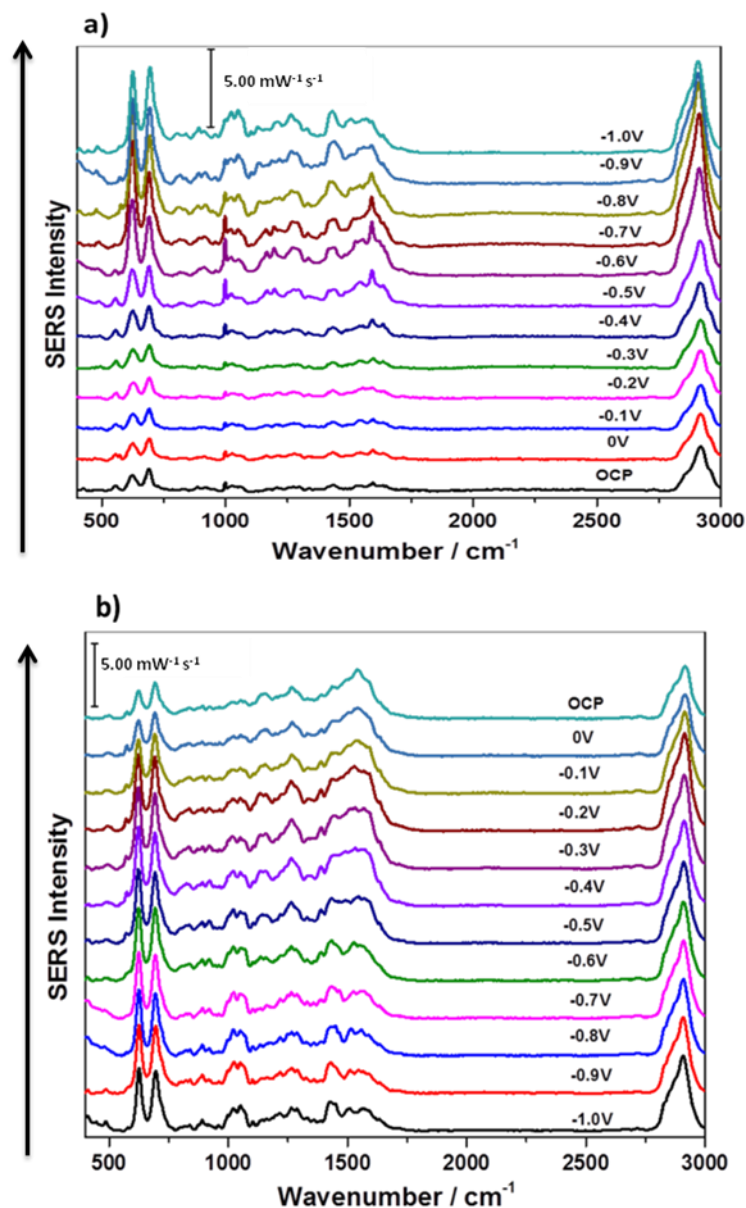
Figure 51: a) Cathodic and b) anodic spectra of 1 nM aloin/0.1 M NaF solution in the presence of 6-MHA SAM AgNP modified electrode. The spectra were collected for 30 s with a laser power of 5 mW at 532 nm.

5.7.4.2.3 EC-SERS of aloin and lipid bilayer system, nanomolar concentration

Nanomolar concentrations of aloin were introduced to DMPC/cholesterol (70:30) lipid bilayers deposited on 6-MHA SAM AgNP modified screen-printed electrodes. At OCP, typical peaks seen for 6-MHA SAM lipid bilayer studies

were observed but no marker peaks for aloin were seen. The peaks at the more negative potentials of the cathodic pathway were observed to increase in intensity and become broader. The regions for peak broadening were once more in the three main regions around 1550 cm^{-1}, 1270 cm^{-1}, and 1150 cm^{-1}, with the strongest signal intensities appearing at more negatively applied potentials (Figure 52). Also in one trial the v(C-S)$_{trans}$ 700 cm^{-1} alkanethiol stretching vibration was split into two peaks (Appendix Figure A-151) indicating reorientation of the C-S bond at the metal surface. Peak assignment for this study revealed peaks present in the spectra which could indicate the presence of aloin based on literature research peak values (Appendix Table A: 137, 139, 142, 144, 148, and 150). However, these peaks were also observed in other lipid bilayer studies where aloin was not present and this fact diminished the probability that such low aloin concentrations can give a significant SERS signal in this case. Owing to the lack of other specific aloin marker peaks and the observation that other studies gave peak broadening in the same regions in the absence of aloin, the peak broadening may be explained as penetration of other electrolyte constituents (e.g. water molecules) causing rearrangement of alkyl chains of 6-MHA SAM or lipid components. Results from repeat trials of this experiment were fairly consistent and it was concluded that nM concentrations of aloin in the presence of a DMPC/cholesterol (70:30) lipid bilayer deposited on 6-MHA SAM cannot give a distinct SERS signal and would therefore not be useful as a probe under these conditions.
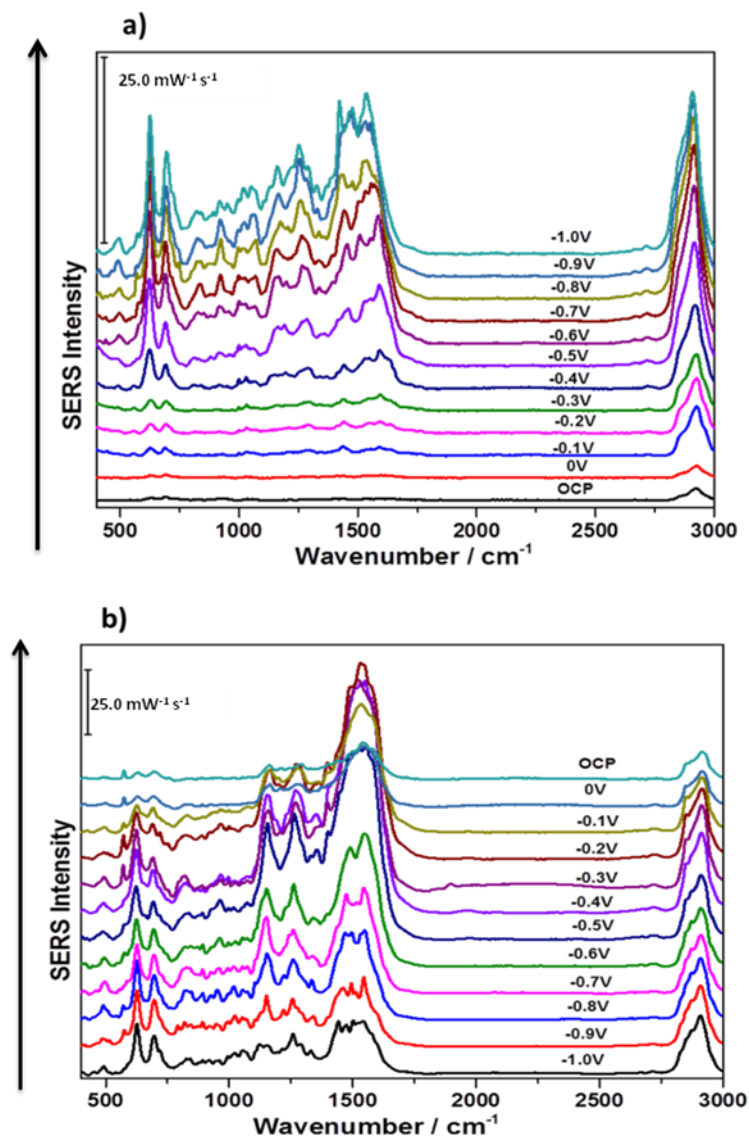
Figure 52: a) Cathodic and b) anodic spectra for DMPC/cholesterol (70:30) lipid bilayer deposited on 6-MHA SAM AgNP modified electrode in the presence of 1 nM aloin /0.1 M NaF solution. The spectra were collected for 30 s with a laser power of 5 mW at 532 nm.

5.7.5 Aloin micromolar concentration studies

5.7.5.1 EC-SERS of aloin on silver nanoparticles, micromolar concentration

For 1 μM aloin/0.1 M NaF solutions, the cathodic pathways again were comparable to citrate peaks found on colloidal Ag surfaces. The citrate peaks

persisted throughout the cathodic scan but during the anodic pathway these peaks disappeared and the peaks previously seen in the 1 mM Aloin studies were now present: 460 cm^{-1}, 1000 cm^{-1}, 1283 cm^{-1}, 1371 cm^{-1}, and 1575 cm^{-1}. This verified the previous observation made for the aloin 1 nM studies; residual citrate on the AgNP surface prevented the adsorption of aloin until the anodic scan. In repeat trials of this experiment similar peaks were observed (Appendix Figure A: 153-163). The general trend in all the experiments was that the aloin marker peak signal intensities were comparable. Figure 53 shows the cathodic and anodic pathway data for a µM aloin study.
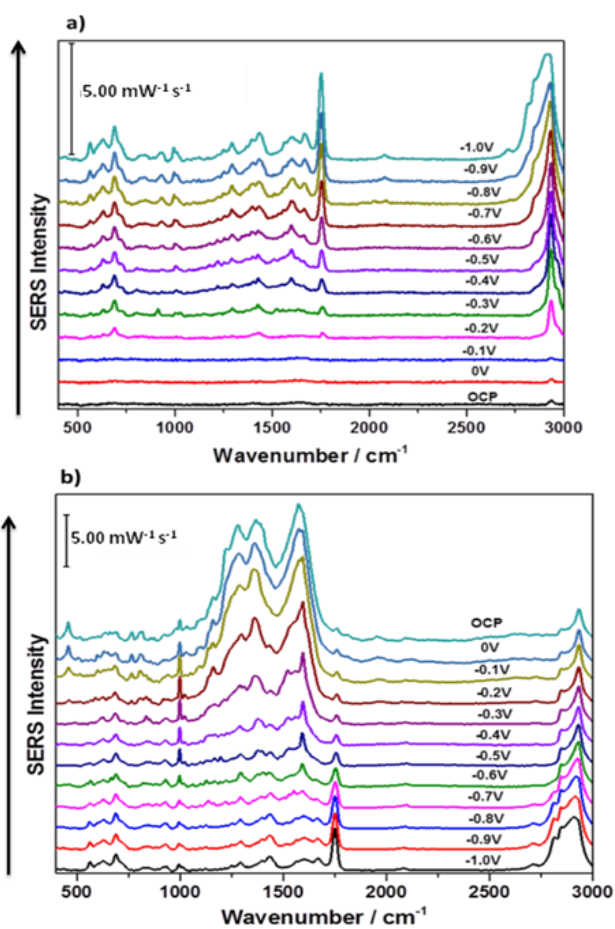
Figure 53: a) Cathodic and b) anodic spectra of 1 µM aloin/0.1 M NaF solution with AgNP modified electrode. The spectra were collected for 30 s with a laser power of 5 mW at 532 nm.

5.7.5.2 EC-SERS of aloin in the presence of alkanethiol, micromolar concentration

For 1 μM aloin in the presence of the 6-MHA SAM at OCP, no aloin marker peaks were seen and no distinctive aloin peak broadening was observed. However, at negative potentials during the cathodic measurements and during the anodic measurements some marker peaks for aloin (which overlapped with 6-MHA SAM peaks) were observed (Appendix Figure A: 164-70). For one trial of the aloin μM solution in the presence of 6-MHA SAM, peak splitting of the v(C-S)$_{trans}$ stretching peak of 6-MHA at 700 cm^{-1} was observed (Figure 54 a,b), and this same trend was found in the previous dAMP probe study with the 6-MHA SAM. It was deduced that the peak splitting of the v(C-S)$_{trans}$ peak could be an indication of changes in the alkyl chains due to different terminal group interactions from absorption of molecules onto the 6-MHA surface. This point can be substantiated by Matulaitienė *et al.* who characterized lipoic acid histamide derivative SAMs on roughened Ag electrodes surfaces in buffered (pH 8) salt solutions.[214] The study showed that for the v(C-S) stretching region around 600 cm^{-1}, applied 0 V potentials gave only one SERS peak at 606 cm^{-1}, while at more negative applied potentials a shoulder appeared at 640 cm^{-1}. Based on their SERS observations and theoretical calculations, the peaks were assigned to be the in-phase 606 cm^{-1} and out-of- phase 640 cm^{-1} displacements of the C-S bond. They further concluded that due to SERS surface selection rules the presence of the out-of-phase v(C-S) stretching mode at more negatively applied potentials was as a result of the reorientation of the molecule

at the roughened metal surface, whereby bringing the out-of-phase mode perpendicular to the metal surface.[214] Therefore, the splitting of v(C-S) stretching observed for all future probe studies, whether *gauche* or *trans*, can be attributed to reorientation of the C-C-S bond at the metal surface and not penetration of the SAM by probe molecules.

Again, the anodic pathway peak broadening (Figure 54 a) was observed but it was not equivalent to that of previous aloin studies (μM aloin with bare AgNPs or mM aloin with 6-MHA SAM). Instead there were three main regions in the spectra which had strong signal intensities: 1) around 1550 cm^{-1} which had the strongest signal, 2) at 1270 cm^{-1} whose signal intensity was almost half of the signal intensity at 1550 cm^{-1}, and 3) in the region of 1150 cm^{-1} which had similar signal intensity to the 1270 cm^{-1} peak. The peak broadening in these three wavenumber regions was similar to that observed in the studies of dAMP in the presence of 6-MHA SAM and since it was deduced that dAMP only partially penetrated the 6-MHA SAM at more negative potentials, it is likely that aloin behaved in a comparable manner. Thus it was concluded that aloin at the μM concentration did not penetrate the 6-MHA SAM at OCP since no aloin peaks were observed and at more negative applied potentials based on peak broadening that was comparable to dAMP studies, aloin likely partially penetrated the 6-MHA SAM.
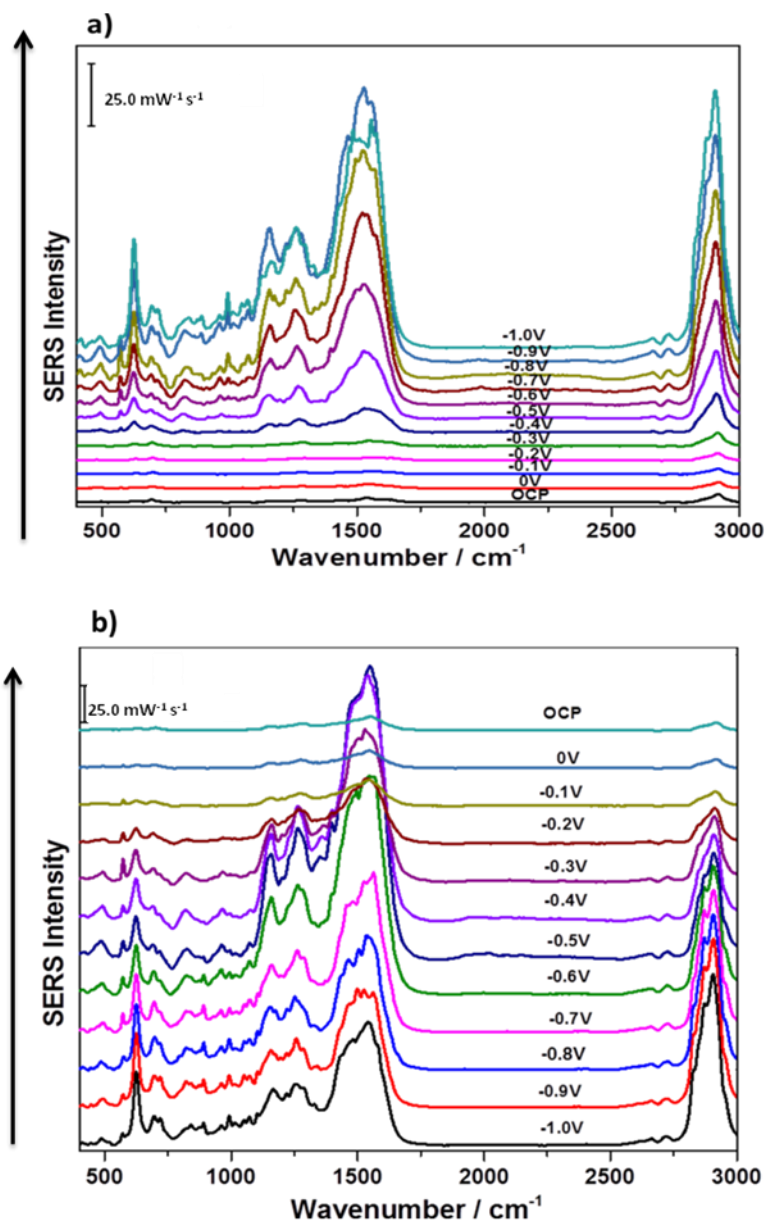
Figure 54: a) Cathodic and b) anodic spectra of 1 μM aloin/0.1 M NaF solution in the presence of 6-MHA SAM AgNP modified electrode. The spectra were collected for 30 s with a laser power of 5 mW at 532 nm.

5.7.5.3 EC-SERS of aloin and lipid bilayer system, micromolar concentration

Triplicate trials of the 1 μM aloin/0.1 M NaF with lipid bilayers were inconsistent (Appendix F i g u r e A : 171-186). Two trials showed parallel

results to the nM aloin lipid bilayer studies where at OCP peaks were more indicative of the presence of lipid components and 6-MHA molecules and no aloin marker peaks were observed, splitting of the 700 cm^{-1} v(C-S)$_{trans}$ peak, peak broadening at more negatively applied potentials, and no characteristic aloin peak broadening observed. The third trial shown in Figure 55 had no significant peak broadening or enhanced signal intensity, and rather than the splitting of the 700 cm^{-1} v(C-S)$_{trans}$ peak, the 630 cm^{-1} v(C-S)$_{gauche}$ peak separated at more negative potentials. Although the third trial was different, it still did not indicate that aloin was close to the AgNP surface. The third trial brought to light the variability that must exist on the surface of the WE. There might be areas that are more defective where molecules easily penetrate, or spots where the SERS signal is weak. Thus it was concluded that μM concentrations of aloin cannot permeate the lipid bilayer and the 6-MHA SAM and provide a SERS signal.
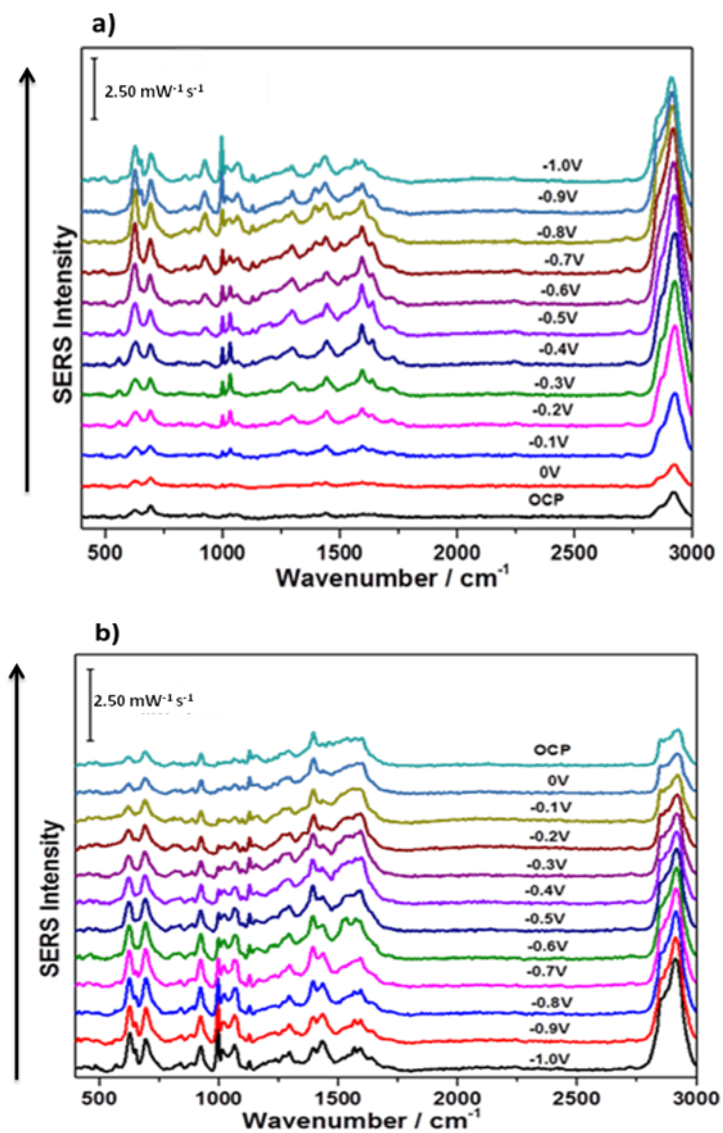
Figure 55: a) Cathodic and b) anodic spectra for DMPC/cholesterol (70:30) lipid bilayer deposited on 6-MHA SAM AgNP modified electrode in the presence of 1 μM aloin /0.1 M NaF solution. The spectra were collected for 30 s with a laser power of 5 mW at 532 nm.

5.7.6 Potassium thiocyanate studies

5.7.6.1 EC-SERS of KSCN on silver nanoparticles

The SCN⁻ probe was used to determine if the proposed model membrane was impermeable to the anion. The added benefit of the SCN⁻ probe was that its

characteristic SERS signal falls mostly outside the fingerprint region (400 cm^{-1}-2000 cm^{-1}).[134] The adsorption of the SCN^{-} anion on the bare AgNP surface in all three trials (Appendix Figure A: 187-195) was marked by the following strong peaks at OCP: 2120 cm^{-1} and 2140 cm^{-1} for the v(C≡N) stretching vibration, 440 cm^{-1} for the δ(N-C-S) bend, and 730 cm^{-1} for the v(C-S) stretching. At more negative potentials the intensity of the peaks in the 2000 cm^{-1} region decreased drastically but the signal for the other two peaks at 440 cm^{-1} and 730 cm^{-1} increased, signifying possible molecular reorientation at the AgNP surface. SERS surface selection rules dictate that vibrational modes perpendicular to the metal surface give stronger SERS signals than modes which are parallel to the metal surface.[56,142] Since the v(C≡N) stretching vibration around 2000 cm^{-1} decreased significantly it was deduced that the stretching mode was parallel to the surface or that the triple bond no longer existed and possibly that the more negative AgNP surface stabilized the resonance structure of SCN^{-}. In the literature, electrochemical surface enhanced Raman spectroscopy (EC-SERS) experiments of SCN^{-} indicated that reorientation occurred at the electrode surface where for negatively applied potentials SCN^{-} anions interact via the N atom (dominance of the N-bond vibration around 2050 cm^{-1}) while at more positively applied potentials, the anion interacts with the metal surface through the S atom (dominance of the S-bond vibration around 2130 cm^{-1}).[215] In addition, the most stable form of the SCN^{-} ion, as its resonance structure S=C=N^{-} (isothiocyanate), can co-exist at the metal surface with the and –S-C≡N structure.[216] The SERS peak for a mixture of the isothiocyanate and thiocyanate structures can occur as a

164

broad band or two separate peaks where the isothiocyanate structure is observed at lower wavenumbers ($\sim$ $<$ 2100 cm^{-1}).[216]   However, at high concentrations of SCN$^-$ ($\sim$70 µM and above), it is suggested that adsorption at the metal surface mainly occurs via the –S-C≡N structure.[216]   Furthermore, the literature proposes that increasing the concentration of SCN$^-$ can possibly cause shift in peaks to higher wavenumbers pointing towards S=C=N$^-$ structures dominating at the metal surface, while no changes or slight shifts of peaks to higher wavenumbers indicates –S-C≡N structures dominating at the metal surface.[216]   For the present study, the cathodic and anodic spectra for the SCN$^-$ anion on the AgNP surface are given in Figure 56. It was concluded based on literature findings that the SCN$^-$ forms a strong interaction with the AgNP surface and provides a strong distinct SERS signal. Moreover, since the concentration of the SCN$^-$ ion was kept constant throughout   the   experiments   the   more   reasonable   explanation   for   the disappearance of the SCN$^-$ peak at more negative potentials is due to reorientation of the ion at the metal surface rather than a shift to its resonances structure.
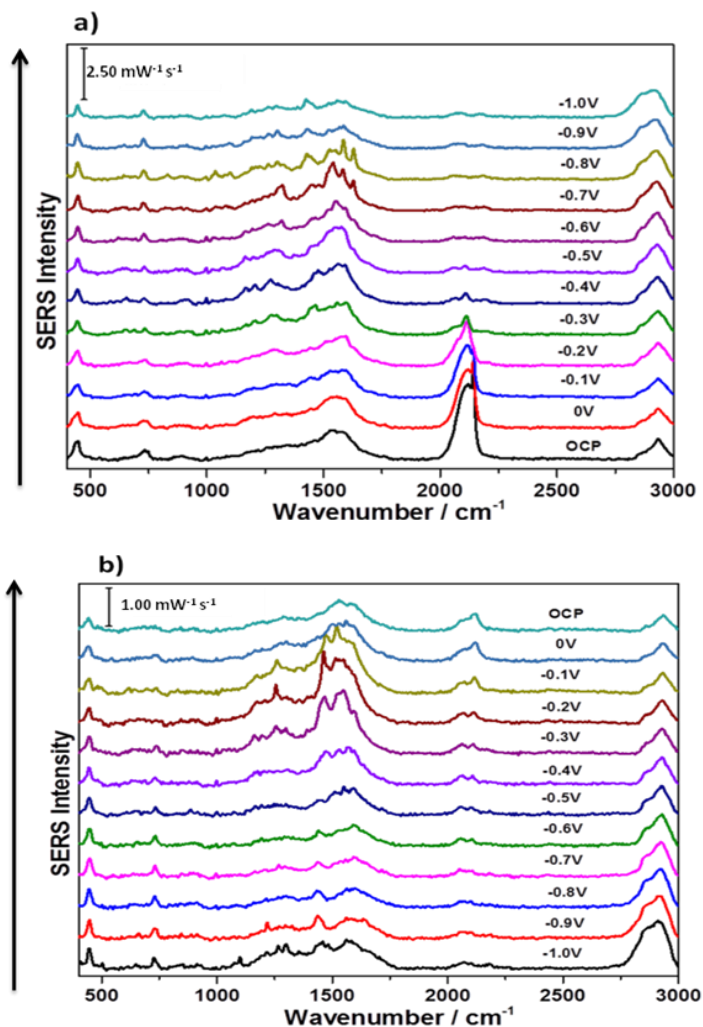
Figure 56: a) Cathodic and b) anodic spectra illustrating the SCN$^-$ peaks (2120 cm^{-1}, 2140 cm^{-1}, 440 cm^{-1}, and 730 cm^{-1}) observed when 1 mM KSCN/0.1 M NaF solution is exposed to a AgNP modified electrode. The spectra were collected for 30 s with a laser power of 5 mW at 532 nm.

5.7.6.2 EC-SERS KSCN in the presence of alkanethiol

In the presence of a 6-MHA SAM the SCN$^-$ peaks in the 2000 cm^{-1} region are very distinct at OCP in repeat trials (Appendix Figure A: 196-199). Two trials showed peak broadening in several regions (1550 cm^{-1}, 1270 cm^{-1}, and 1150 cm^{-1}) as also seen for other probe studies with the 6-MHA SAM (e.g. dAMP, and aloin μM studies) while in the other trial peak broadening was

minimal as demonstrated in Figure 57. Given that peak broadening was observed for two out of the three trials, again this observation pointed towards a non-uniform SAM or variable SERS signal. Despite this fact, in all three trials the peaks around 2000 cm^{-1} behaved as in the AgNP studies where the peaks were more intense at less negative potentials. Moreover the thiocyanate peaks at OCP were generally the most intense peaks in the spectra and thus it was concluded that the thiocyanate can easily penetrate the SAM and adsorb directly onto the AgNP surface.
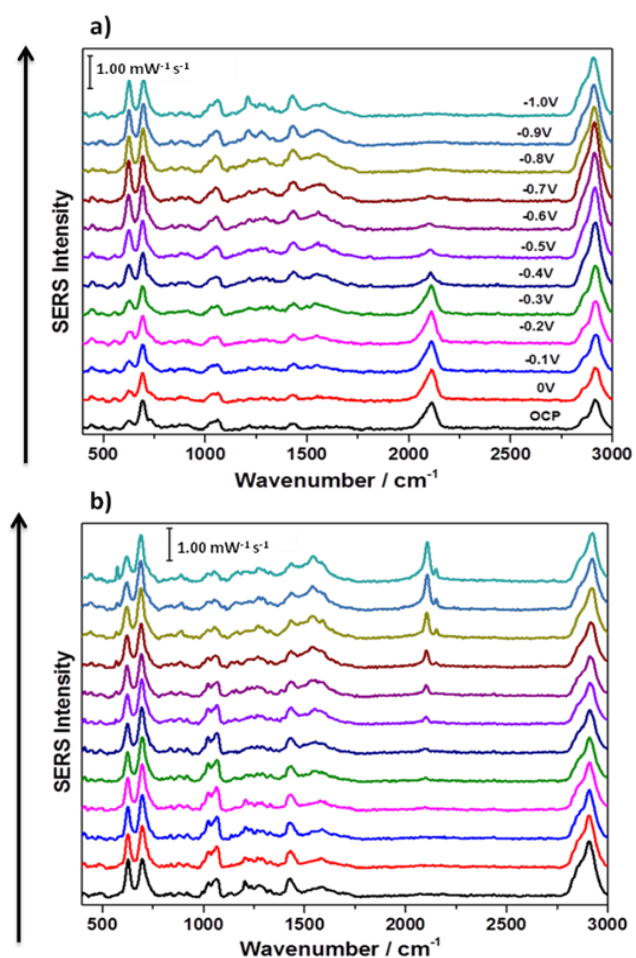
Figure 57: a) Cathodic and b) anodic spectra of 1 mM KSCN/0.1 M NaF solution in the presence of 6-MHA SAM AgNP modified electrode. The spectra were collected for 30 s with a laser power of 5 mW at 532 nm.

5.7.6.3 EC-SERS of KSCN and lipid bilayer system

Solutions of 1 mM KSCN/0.1 M NaF were added to EC-SERS glass vials containing DMPC/cholesterol (70:30) bilayers deposited on 6-MHA SAM AgNP modified electrodes. Results obtained from all three trials in the experiment of SCN⁻ in the presence of the lipid bilayer system solidified previous assumptions regarding peak broadening (Appendix Figure A: 200-216). An example of data from such an experiment is given in Figure 58. The OCP spectrum exhibited strong signal intensity from the SCN⁻, indicating that this ion freely penetrated both the lipid bilayer and 6-MHA SAM, and adsorbed onto the AgNP surface. Band broadening and increased signal intensity continued throughout the cathodic sequence for the lipid and 6-MHA components, and the v(C≡N) stretching vibration peak around 2000 cm^{-1} diminished as expected. At OCP, peak broadening in several regions (~1550 cm^{-1}, ~1270 cm^{-1}, and ~1150 cm^{-1}) was observed and compared to other earlier probe studies typically the band broadening in these regions occurred at negative applied potentials. Earlier in this thesis, it was concluded that at negative potentials the alkyl chains were more disordered and that peak broadening could infer permeation by the electrolyte solution. Thus, it was concluded for this study that SCN⁻ penetrated the lipid bilayer and possibly brought about alkyl chain disorder within the lipid bilayer, thereby promoting easy penetration of other electrolyte constituents to enter, giving rise to the observed peak broadening.
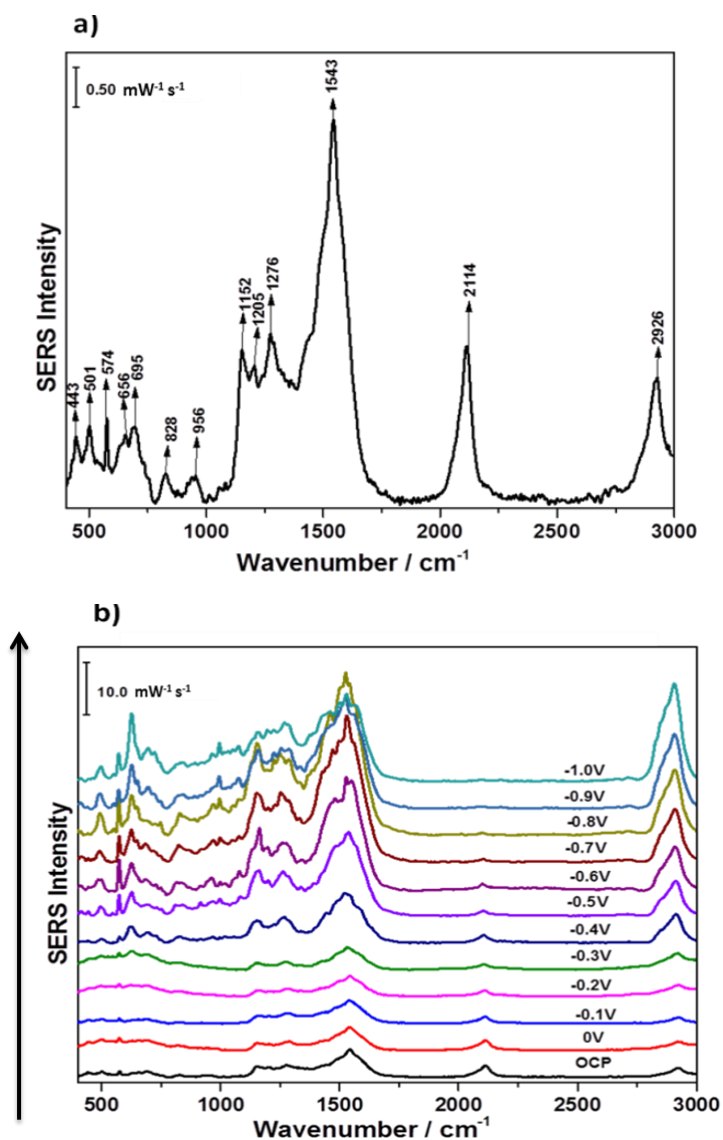
Figure 58: a) Cathodic and b) anodic spectra for DMPC/cholesterol (70:30) lipid bilayer deposited on 6-MHA SAM AgNP modified electrode in the presence of 1 mM KSCN/0.1 M NaF solution. The spectra were collected for 30 s with a laser power of 5 mW at 532 nm.

The SCN$^-$ anion was the smallest probe used in this research project. If this probe easily traversed the lipid bilayer due to its size, then smaller ions, such as Ca^{2+}, would likely do so as well. Another consideration was the charge on the ion. There is an electrical potential difference between the exterior of the lipid bilayer system (electrolyte/probe solution) and the underside of the lipid bilayer

system (surface near to the AgNP surface) and this could be a driving force for fast ion permeation. This led to two main questions in the current research project: 1) is SCN$^-$ penetration of the proposed model membrane derived from a particular property of the anion, and 2) is the proposed model membrane penetrable by all small ions regardless of their properties. To commence designing experiments to examine these questions, a literature search was performed in order to ascertain the properties of the SCN$^-$ anion. Background theory stated that the SCN$^-$ anion is classified as a chaotropic ion because of its weak interaction with water molecules. Introduction of SCN$^-$ into aqueous solutions disrupts the hydrogen bonding of water molecules.[217] This weak water interaction and destabilization of water hydrogen bonding by SCN$^-$ are explanations for its poor hydration shell.[218] As a result, SCN$^-$ ions are said to be repelled from highly hydrated surfaces and instead are found embedded into hydrophobic regions where water interactions are minimized. This trait of the SCN$^-$ anion is one of the suggestions made as to why this anion is a protein denaturant. Mason *et al.* relates SCN$^-$ poor hydration shell (approximately 3 water molecules) to its role as a protein denaturant.[218] In their studies it states that the SCN$^-$ anion embeds itself into the hydrophobic regions of proteins, disrupting water hydrogen bonding and other electrostatic interactions that stabilize the protein's native structure, and as a result the protein loses its particular three-dimensional shape.[218] Another crucial literature finding was a journal article by Zimmermann and associates who investigated ion mobility in model membranes by various techniques such as Fluorescence Recovery After Photobleaching (FRAP). These studies demonstrated that ions with weak hydration

shells permeated lipid bilayers more readily.[219] This finding can help explain the results observed in this research project where SCN$^-$ readily penetrated the proposed lipid bilayer system. To eliminate this possibility, the pH of the probe/electrolyte solution was adjusted to basic conditions to improve the interaction between water molecules and the SCN$^-$ anions, i.e. strengthen the SCN$^-$ hydration shell.

In alkaline conditions the SCN$^-$ anion adsorbed onto the AgNP surface and unlike previous experiments the peak around 2000 cm^{-1} persisted throughout the cathodic and anodic measurements (Appendix Figure A: 217-222). This difference indicated that the change in pH was altering the anion's interaction with the metal surface and in addition, possibly its orientation with respect to the metal surface or stabilizing its triple bond structure. For example, it was mentioned earlier in this thesis that SCN$^-$ peaks around 2000 cm^{-1} indicated metal interaction via the S atom and the presence of the v(C≡N) stretching vibration. The persistence of the 2000 cm^{-1} peak suggested interactions via the S atoms and the triple bond structure were dominant and stabilized in basic conditions in spite of the applied potential range used in this experiment (0 V to -1.0 V).

In alkaline conditions, in the presence of a 6-MHA SAM or a lipid bilayer deposited onto a 6-MHA SAM, repeat trials (Appendix Figure A: 223-234) had a common trend where the SCN$^-$ peak around 2000 cm^{-1} was not detectable at OCP or its peak intensity was considerably reduced (Figure 59). In cases where the peaks were detectable at OCP, the pH was found to be closer to pH 7.
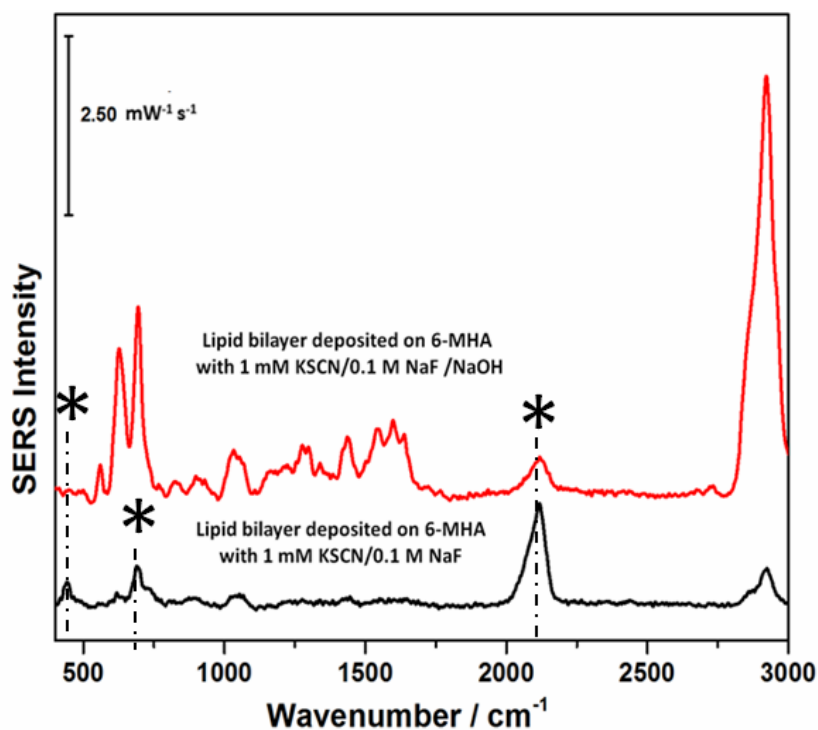
Figure 59: Basic conditions reduced mM SCN⁻ penetration of DMPC/cholesterol (70:30) lipid bilayers deposited on 6-MHA SAM AgNP modified electrodes. This was evident in OCP overlay spectra where SCN⁻ $v(C\equiv N)$ stretching vibration at 2120 cm⁻¹ had lower signal intensities. The spectra were collected for 30 s with a laser power of 5 mW at 532 nm.

Towards the end of the anodic sequence for the studies using basic solutions of the SCN⁻ probe the $v(C\equiv N)$ stretching vibration at 2120 cm⁻¹ did appear but with a lower signal intensity relative to the other peaks in the spectrum. This indicated that a portion of the SCN⁻ molecules were still able to adsorb onto the AgNP surface. The conclusion drawn from this experiment was that the stronger hydration shell of the SCN⁻ brought about by the more alkaline electrolyte solution hindered penetration of the anion into the lipid bilayer system.

5.7.7 Calcium ion detection

The intention of the proposed model membrane is for future investigations of pore-forming diseases such as AD. In the neurons of an AD patient an influx of Ca^{2+} ions into the intracellular matrix of the cells is said to occur.[20] With respect to the proposed model membranes fabricated in this thesis project, the detection of Ca^{2+} may be pivotal. Most complexes used to detect the presence of Ca^{2+} ions or extract these ions from solution possess a carboxyl or a phosphate group that binds to the cation.[222-224] Studies have shown that analytical techniques have designed or studied ways to identify specific carboxylate-positive ion interactions in solution e.g. distinguishable SERS shift of COO^- peak in mercaptobenzoate upon co-ordination to various cations such as Cu^{2+}, Ag^+, and Hg^{2+}.[225,226] Since the support layer (6-MHA SAM) of the proposed model membrane consisted of carboxyl terminal groups it would be plausible to investigate whether a distinguishable SERS signal for a Ca^{2+}/COO^- interaction could be observed if Ca^{2+} ions were to traverse the lipid bilayer (Figure 60).
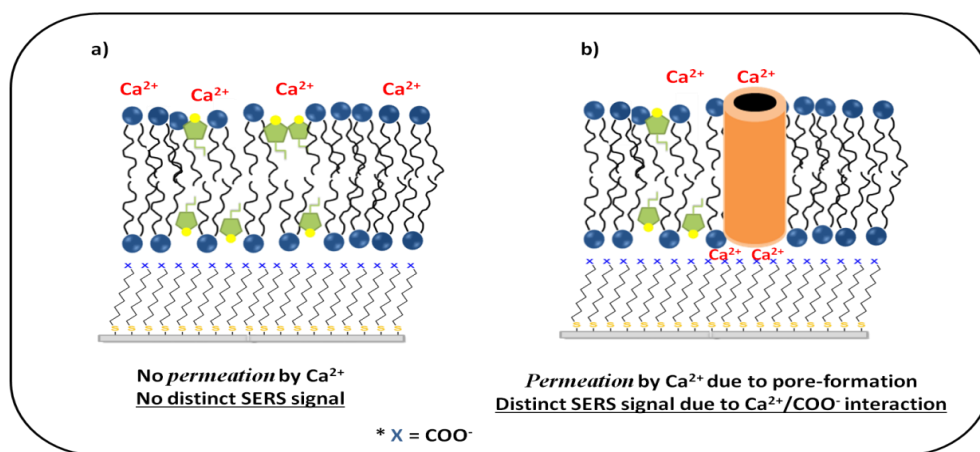
Figure 60: A cartoon diagram (not drawn to scale) illustrating that pore-formation would lead to Ca^{2+}/COO^- interactions that would provide a distinct SERS signal.

The wavenumber region of interest for Ca^{2+}/COO^- interactions was focused around 1500 cm^{-1} since one of the most distinct vibrations for deprotonated carboxylic groups arise within this region.[109,226] In an attempt to identify discrete SERS signals for the Ca^{2+}/COO^- interaction EC-SERS experiments were carried out with carboxyl terminated SAMs derived from 6-MHA, and electrolyte solutions containing Ca^{2+} ions. Control studies were also performed with another cation, Na^+, to determine if the SERS signal obtained for the Ca^{2+}/COO^- interaction was indeed characteristic of this particular interaction and not just a COO^- interaction with a positive species. Table 7 gives examples of peak values observed within the 1500 cm^{-1} region from the EC-SERS experiments. Peak values around 1500 cm^{-1} were monitored at OCP and through the cathodic and anodic scans. Examples for these SERS spectra can be found in the Appendix, Figure A: 235-238. The values in Table 7 represented peak values that were dominant at one point in the experiment (e.g. at OCP or at -1.0V cathodic), or showed persistence throughout the EC-SERS experiment.

EC-SERS study	Deprotonated carboxyl group wavenumber/ cm^{-1}
0.1 M CaSO$_4$ + 6-MHA	1526, 1596
0.1M NaCl + 6-MHA	1541, 1597
0.1 M NaF + 6-MHA	1528, 1543, 1561, 1598

Table 7: Peak values within the deprotonated carboxyl region for the interaction between 6-MHA and various electrolyte solutions.

The results from Table 7 showed that deprotonated carboxylic peak values within the 1500 cm^{-1} region had similar values for both the presence of Ca^{2+} ions and the presence of Na^+ ions. For that reason, the conclusion made was no discrete

signal for the Ca^{2+}/COO^- interaction can be observed. In addition, it was deduced that other interactions and not a Ca^{2+}/COO^- interaction can account for the values observed around 1500 cm^{-1} e.g. hydrogen bonding of COO^- with water molecules in solution, or electrostatic interactions between the charged polar head region of a deposited lipid bilayer and the COO^- groups of 6-MHA. Therefore, it was concluded that for the Ca^{2+} detection studies a distinguishable SERS signal for the presence of the cation at the carboxyl terminal surface of the 6-MHA SAM could not be obtained.

6 Conclusions and future directions

6.1 Conclusions

The use of a hydrophilic solid support (6-MHA), increased subphase temperature and high humidity conditions improved the quality of the LB-LS lipid bilayer. For future studies, the model membrane developed in this thesis work will be used to detect the presence of new species or detect increased concentration of specific ions. From the foregoing results it can be concluded that only analyte species with strong distinctive SERS signals can be easily distinguished from other SERS signals derived from lipid components or the SAM. Additionally, the aloin nM concentration studies demonstrated that very low concentrations of a SERS-active analyte cannot provide distinct SERS signals in the presence of a SAM or a lipid bilayer supported by a SAM.

The probe studies performed with the proposed model membrane revealed a selective permeability to molecules based on size, charge, hydration shell

175

strength, and hydrophobicity. Large or medium sized molecules carrying a charge would not traverse the lipid bilayer easily. This resistance can be attributed to the possible gaps/sizes that exist within the lipid bilayer and that the lipid bilayer was well-formed with minimal defects. Since the estimated size of the medium probe, dAMP, was approximately 1.152 nm then it was concluded that the sizes of gaps/spaces within the lipid bilayer were less than 1.152 nm. If this indeed was the approximate size of gaps within the model membrane, then dehydrated ions will be able to diffuse easily across the membrane if there was a drastic electrochemical difference across the membrane. Also, the probe molecule dAMP provided proof that there were structural similarities between the proposed model membranes and biological cell membranes (e.g. hydrophobic region sandwiched by hydrophilic polar heads) since dAMP cannot permeate biological membranes and did not permeate the proposed model membrane in this thesis project.

The model membrane system was susceptible to penetration by molecules that are fairly hydrophobic (adenine) or have poor hydrogen bonding with water molecules (SCN$^-$). This demonstrated that the model membrane was not rigid and most likely will facilitate the penetration of amyloid beta fragments to form pores.

The EC-SERS method allowed for simultaneous monitoring and detection of components within the lipid bilayer and SAM in response to applied voltages. In this thesis project, it was deduced that spectral features such as peak broadening in specific regions and peak splitting of the alkanethiol C-S stretches were indications of reorientation of alkyl chains within the lipid bilayer and SAM. In future applications of the proposed model membrane to the

investigation of pore-forming species such as the amyloid beta (Aβ) aggregates for AD, these characteristic spectral features can be used to deduce the possible penetration of Aβ aggregates at OCP into the model membranes. Another characteristic of the model membrane observed during these studies was its stability in the solution and during the EC-SERS measurements. The lipid bilayer stability time studies and control studies used to optimize the laser power suggested that the proposed model membranes provide better SERS signal at lower laser power (less likelihood of photodegradation) and that desorption of the lipid bilayer from a hydrophilic surface might occur after specific times (in this study around an hour). Knowledge of these model membrane characteristics is important because it aids in better experimental designs for future investigations of pore-forming diseases. For example, to ensure that spectral changes are indicative of decreased membrane quality due to Aβ aggregate insertion into the lipid bilayer and not due to desorption of the lipid bilayer from the membrane support, incubation times of Aβ aggregates with model membranes, along with EC-SERS measurements, should be kept under 40 minutes.

Although the data offered sufficient evidence from which plausible conclusions could be made, there were limitations of the experimental design that accounted for the variability observed in the experiments. EC-SERS spectra are recorded at one spot on the WE surface and this selected area may not be a true representation of the vast majority of the lipid bilayer surface. Poor mass transport of molecules in a solution could alter the results of the experiment. If analyte molecules were not near to the lipid bilayer surface within the time frame of the

experiment, then the ability of the analyte molecules to permeate the lipid bilayer would not be fully established.

However, the benefits of the proposed model membrane system, which incorporated the EC-SERS technique, include the ability to determine the orientation of molecules near the roughened metal surface, the manipulation of the WE surface to achieve a desired potential, the capability for determining and proving the existence of an intact film on the WE surface, and a sensitive model that can detect molecules which permeate the model membrane system reaching close to the roughened metal surface. The use of such a model can add to the understanding of the mechanism of diseases, provide a way to determine membrane integrity after interactions with specific molecules, monitor drug interactions with lipid bilayers, or to comprehend redox processes of specific membrane associated molecules. Thus this model membrane system shows promise since there is versatility in its biological applications.

6.2 Future directions

The absence of the dAMP SERS peaks in the presence of the lipid bilayer system authenticated lipid bilayer formation by the LB-LS technique onto modified AgNP electrodes. Further justification could be attained by using other techniques such as atomic force microscopy (AFM) to give a visual mapping of the lipid bilayer surface and also determine its thickness through force-distance measurements. AFM could also shed light on whether the surface was uniform or not. Another avenue for scrutinizing the homogeneity of the lipid bilayer surface could be explored by using a Variable Dynamic Point Sample

(VDPS) component for Raman instruments. This separate sampling component records an area of about 5 mm^2 and provides an overlay of about 25 spectra. This increases efficiency, and variability across the surface is easily monitored.[227]

Adjustments to particular experimental conditions, set-up, or modification of analyte molecules can afford better quality or novel data and the following sentences are examples of steps that can be taken to improve the quality of the data. For the formation of the SAM, degassing the alkanethiol solution with an inert gas (e.g. Argon) before the incubation of the AgNP modified electrode can reduce the likelihood of thiol oxidation and afford a more defect free SAM. Another adjustment to the experimental condition that can possibly reduce errors is stirring the electrolyte/probe solutions during purging prior to performing the EC-SERS measurements. Thus the addition of the electrolyte/probe solution to an EC-SERS vial containing modified AgNP electrodes would afford a more homogenous solution and aid in reducing mass transport concerns. In this thesis project, the EC-SERS spectra recorded for repeat trials of the same study where signal intensities varied from one trial to another e.g. dAMP on bare AgNP modified electrodes gave signal intensities of 25.0 mW^{-1} s^{-1} in one trial and 5.00 mW^{-1} s^{-1} in another trial. Such fluctuating signals could be linked to the non-uniform shape and size of the AgNPs. New methods of synthesizing AgNPs have shown great success in producing relatively small uniform particles and these new synthetic routes can be used instead of the Lee and Meisel method.[142] With the introduction of a solution to lipid bilayers or biological cell membranes

the movement of ions or molecules across these structures is determined by an electrochemical potential.[58,59] Sequential addition of an electrolyte solution followed by an analyte solution at a timed interval would afford an electrochemical potential to be established across the model membrane before the introduction of the analyte molecules. This reduces the probability that analyte molecules will diffuse rapidly due to a drastic electrochemical difference. For the proposed model membrane system if analyte molecules diffuse across the lipid bilayer due to an electrochemical potential, or through pores formed in the lipid bilayer, a distinct discernible SERS signal of the analyte molecule is required.

Since the proposed model membranes will be used in future studies to investigate the pore hypothesis theory of AD with respect to Ca^{2+} ion influx, detecting Ca^{2+} ions is important. The results from the Ca^{2+} ion detection studies performed in this project showed that Ca^{2+} ions could not give a discernible SERS signal in the presence of 6-MHA SAM. To make the presence of Ca^{2+} ions more prominent, surfactants or ligands can be used to form stable ion complexes. This ion complex must be able to: i) give a strong SERS signal when near the surface of modified AgNP, ii) be smaller than 2 nm in order to pass through the Aβ pores, possess a positive charge so that the ion complex can traverse the negative core of the Aβ pore more easily, and iv) the ligands or surfactants must not be lipophilic (compounds that dissolve in lipids)[59] so as to drive permeation of the complex into the lipid bilayer. Additionally, the SAM can be modified to increase its efficiency for detecting analyte molecules that permeate the lipid bilayers or

traverse the model membrane due to defects. Such modifications can include a different hydrophilic terminal group other than COOH or an entirely different lipid bilayer membrane support such as a polymer cushion.

Observing a SERS signal for specific analyte species is one way of indicating possible pore-formation in the model membrane. Another method that can be used to support possible pore-formation is employing electrochemical techniques such as CV. For the bilayer studies performed in this experiment, the resultant current response compared to the control electrolyte solution was smaller, indicating that a compact film was formed on the WE surface whereby creating a barrier to the electrolyte solution. It has been proven experimentally that defective membranes on an electrode surface have increased current responses due to contact with electrolyte solution and the exposed electrode surface.[130] Thus for the application of these biomimetic model membranes in the investigation of pore-formation the current response can be monitored whereby increases in current response signifies pore-formation or a defective membrane.

Finally, to make the proposed biomimetic model membranes more comparable to biological cell membranes the following modifications can be performed: i) altering the lipid composition and varying the types of lipids such as incorporating unsaturated lipids into the DMPC/cholesterol composition, ii) using lipids with a charged polar head e.g. using the negatively charged phospholipid, phosphatidylserine, or iii) using lipids with a modified polar head containing a protein or carbohydrate.

References

1. "Alzheimer's Disease", *Alz.org®/Alzheimer's Association®*, Alzheimer's Association®, 2013, Web Sept 2012.

2. "Alzheimer's Disease Info", *Alzheimer's Drug Discovery Foundation*, Alzheimer's Drug Discovery Foundation, 2010, Web Sept 2012.

3. Nunan, J., Small, D. H., *FEBS Lett.* 483 (2000) 6.

4. Dahm, R., *Curr. Biol.* 16 (2006) R906.

5. Uversky, V. N., Fink, A. L., eds., "Protein Misfolding, Aggregation, and Conformational Diseases, Part A: Protein Aggregation and Conformational Diseases", Volume 4. Springer Science + Business Media Inc., New York, (2006).

6. "World Alzheimer Report 2010, The Global Economic Impact of Dementia", *Alzheimer's Disease International*, Alzheimer's Disease International, 2010, Web Feb 2013.

7. "Dementia in Canada", *Alzheimer Society Canada*, Alzheimer Society of Canada, 2013, Web Mar 2013.

8. "2013 Alzheimer's Disease Facts and Figures", *Alz.org®/Alzheimer's Association®*, Alzheimer's Association®, 2012, Web Mar 2014.

9. "Rising Tide: The Impact of Dementia on Canadian Society, Execute Summary", *Alzheimer Society Canada*, Alzheimer Society of Canada, 2010, Web Feb 2013.

10. "Facts: Alzheimer's Disease and other dementias", *Alzheimer Society Ontario*, Alzheimer Society of Canada, 2012, Web Feb 2013.

11. "2012 Alzheimer's Disease Facts and Figures", *Alz.org®/Alzheimer's Association®*, Alzheimer's Association®, 2012, Web Feb 2013.

12. Hensley, K., Hall, N., Subramaniam, R., Cole, P., Harris, M., Aksenov, M., Aksenova, M., Gabbita, S. P., Wu, J. F., Carney, J. M., Lovell, M., Markesberry, W. R., Butterfield, D. A., *J. Neurochem.*, 65 (1995) 2146.

13. Stefani, M., Dobson, C. M., *J. Mol. Med.*, 81 (2003) 678.

14. Shafrir, Y., Durell, S., Arispe, N., Guy, H. R., *Proteins*, 78 (2010) 3473.

15. Selkoe, D. J., *Nature*, 426 (2003) 900.

16. Kagan, B. L., Hirakura, Y., Azimov, R., Azimova, R., Lin, M., *Peptides*, 23 (2002) 1311.

17. Lin, H., Bhatia, R., Lal, R., *FASEB J.*, 15 (2001) 2433.

18. Mirzabekov, T., Lin, M., Yuan, W., Marshal, P. J., Carman, M., Tomaselli, K., Lieberburg, I., Kagan, B. L., B*iochem. and Biophys. Res. Commun.*, 202 (1994) 1142.

19. Arispe, N., Rojas, E., Pollard, H. B., *Proc. Natl. Acad. Sci. USA*, 90 (1993) 567.

20. Kawahara, M., Kuroda, Y., *Brain Res. Bull.*, 53 (2000) 389.

21. Connelly, L., Jang, H., Arce, F. T., Capone, R., Kotler, S. A., Ramachandran, S., Kagan, B. L., Nussinov, R., Lal. R., *J. Phys. Chem. B.*, 116 (2012) 1728.

22. Bucciantini, M., Giannoni, E., Chiti, F., Baroni, F., Formigil, L., Zurdo, J., Taddei, N., Ramponi, G., Dobson, C. M., Stefani, M., *Nature*, 416 (2002) 507.

23. Zako, T., Sakono, M., Hashimoto, N., Ihara, M., Maeda, M., *Biophys. J.*, 96 (2009) 3331.

24. Celej, M., Sarroukh, R., Goormaghtigh, E., Fidelio, G. D., Ruysschaert, J., Raussens, V., *Biochem. J.*, 443 (2012) 719.

25. Yoshiike, Y., Kayed, R., Milton, S. C., Takashima, A., Glabe, C. G., *NeuroMol. Med.*, 9 (2007) 270.

26. Lashuel, H., Hartley, D., Petre, B. M., Waltz, T., Lansbury, P. T. Jr., *Nature*, 418 (2002) 291.

27. Green, J. D., Kreplak, L., Goldsbury, C., Blatter, X. L., Stolz, M., Cooper, G. S., Seelig, A., Kistler, J., Aebi, U., *J. Mol. Biol.*, 342 (2004) 877.

28. Dobson, C. M., *Nature*, 426 (2003) 884.

29. Jang, H., Connelly, L., Arce, F. T., Ramachandran, S., Kagan, B. L., Lal, R., Nussinov, R., *J. Chem. Theory Comput.*, 9 (2013) 822.

30. Munoz, V., ed., "Protein Folding, Misfolding and Aggregation (RSC Biomolecular Sciences), *Classical Themes and Novel Approaches", Royal Chemistry Society, Cambridge, (2008).*

31. Cohen, F., Kelly, J. W., *Nature*, 426 (2003) 905.

32. Voiciuk, V., Valincius, G., Budvytyte, R., Matijoska, A., Matulaitiene, I., Niaura, G., *Spectrochim. Acta Part A*, 95 (2012) 526 .

33. Thakur, G., Micic, M., LeBlanc, R.M., *Colloids Surf. B.*, 74 (2009) 436.

34. Kremer, J. J., Murphy, R. M., *J. Biochem. Biophys. Methods*, 57 (2003) 15.

35. Terzi, E., Hölzemann, G., Seelig, J., *Biochemistry*, 33 (1994) 7434.

36. Lau, T., Ambroggio, E. E., Tew, D. J., Cappai, R., Masters, C. L., Fidelio, G. D., Barnham, K. J., Separovic, F., *J. Mol. Biol.*, 356 (2006) 759.

37. Ionov, M., Klajnert, B., Gardikis, K., Hatziantoniou, S., Palcez, B., Salakhutdinov, B., Cladera, J., Zamaraeva, M., Demetzos, C., Bryszewska, M., *J. Therm. Anal. Calorim.*, 99 (2010) 741.

38. Choi, I., Huh, Y. S., Erickson, D., *Microfluid Nanofluid*, 12 (2012) 663.

39. Kagan, B. L., Azimov, R., Azimova, R., *J. Membr. Biol.*, 202 (2004) 1.

40. Prangkio, P., Yusko, E. C., Sept, D., Yang, J., Mayer, M., *PLOS ONE*, 7: e47261 (2012) 1.

41. Jang, H., Ma, B., Lal, R., Nussinov, R., *Biophys. J.*, 95 (2008) 4631.

42. Capone, R., Jang, H., Kotler, S. A., Kagan, B. L., Nussinov, R., Lal, R., *Biochemistry*, 51 (2012) 776.

43. Connnelly, L., Jang, H., Arce, F. T., Ramachandran, S., Kagan, B. L., Nussinov, R., Lal, R., *Biochemistry*, 51 (2012) 3031.

44. Jang, H., Arce, F. T., Capone, R., Ramachandran, S., Nussinov, R., *Biophys. J.*, 97 (2009) 3029.

45. Thakur, G., Pao, C., Micic, M., Johnson, S., Leblanc, R. M., *Colloids Surf., B*, 87 (2011) 369.

46. Jang, H., Arce, F. T., Ramachandran, S., Capone, R., Azimova, R., Kagan, B. L., Nussinov, R., Lal, R., *Proc. Natl. Acad. Sci. USA.* 107 (2010) 6538.

47. Goodison, W. V., Frisardi, V., Kehoe, P. G., *J. Alzheimers Dis.*, 30 (2012) S269.

48. Nimmrich, V., Eckert, A., *Br. J. Pharmacol.*, 169 (2013) 1203.

49. Hermann, D., Mezler, M., Müller, M., Wicke, K., Gross, G., Draguhn, A., Bruehl, C., Nimmrich, V., *Eur. J. Pharmacol.*, 702 (2013) 44.

50. Scarpini, E., Scheltens, P., Feldman, H., *Lancet Neurol.*, 2 (2003) 539.

51. Nicolli, J. A. R., Wilkinson, D., Holmes, C., Steart, P., Markham, H., Weller, R.O., *Nature*, 9 (2003) 448.

52. Golde, T. E., Eriksen, J. L., Weggen, S., Sagi, S. A., Koo, E. H., *Drug Deliv. Rev.*, 56 (2002) 415.

53. Cohen, N. C., ed., "Guidebook on Molecular Modelling in Drug Design", Academic Press Inc., California, (1996): 1-5.

54. Petty, M. C., "Langmuir Blodgett films, an introduction", Cambridge University Press, Britain, (1996).

55. Barnes, G. T., Gentle, I. R., "Interfacial science: an introduction, 2nd Edition", Oxford University Press, New York, (2011).

56. Aroca, R., "Surface-Enhanced Vibrational Spectroscopy", John Wiley & Sons Ltd., England, (2006).

57. Wang, J., "Analytical Electrochemistry Second Edition", Wiley-VCH, Canada,(2000).

58. Karp, G., "Cell and Molecular Biology, Concepts and Experiments", John Wiley & Sons Inc., England, (1996).

59. Garrett, R. H., Grisham, C. M., "Biochemistry, 5th Edition", Brooks/Cole Cengage Learning, California,(2013).

60. Garcia-Manyes, S., Oncins, G., Sanz, F., *Biophys. J.*, 89 (2005) 4261.

61. Kalyanasundaram, K., "Photochemistry in Microheterogeneous Systems", Academic Press Inc., London, (1987).

62. Meyer de F., Smit, B., *Proc. Natl. Acad. Sci. USA*, 106 (2009) 3654.

63. Léonard, A., Escrive, C., Laguerre, M., Pebay-Peyroula, E., Néri, W., Pott, T., Katsaras, J., Dufourc, E. J., *Langmuir*, 17 (2001) 2019.

64. Marsan, M. P., Muller, I., Ramos, C., Rodriguez, F., Dufourc, E. J., Czaplicki, J., Milon, A., *Biophys. J.*, 76 (1999) 351.

65. Harroun, T.A., Katsaras, J., Wassall, S.R., *Biochemistry*, 45 (2006) 1227.

66. Hung, W. C., Lee, M. T., Chen, F. Y., Huang, H. W., *Biophys. J.*, 92 (2007) 3960.

67. Levine, Y. K., Wilkins, M. H., *Nat. New Biol.*, 230 (1971) 69.

68. "Biomimetic definition, Oxford Dictionaries Language Matters", *Oxford Dictionaries Language Matters*, Oxford University Press, 2013, Web Oct 2013.

69. Esfand, R., Tomalia, D. A., *Drug Discov. Today*, 6 (2001) 427.

70. Hud, D., Torisawa, Y., Hamilton, G. A., Kim, H. J., Ingber, D. E., *Lab Chip*, 12 (2012) 2156.

71. Yang, T., Juang, S., Mao, H., Cremer, P. S., *Anal. Chem.*, 73 (2001) 165.

72. Xu, L., Frederik, P., Pirollo, K. F., Tang, W., Rait, A., Xiang, L., Huang, W., Cruz, I., Yin, Y., Chang, E. H., *Hum. Gene Ther.*, 13 (2002) 469.

73. Naumann, R. L. C., Nowak, C., Knoll, W., *Soft Matter*, 7 (2011) 9535.

74. Castellana, E. T., Cremer, P. S., *Surf. Sci.*, 61 (2006) 429.

75. Tatur, S., Maccarini, M., Barker, R., Nelson, A., Fragneto, G., *Langmuir*, 29 (2013) 6606.

76. Laouini, A, Jaafar-Maalej, C., Limayem-Blouza, I., Sfar, S., Charcosset, C., Fessi, H., *J. Colloid Sci. Biotechnol.*, 1 (2012) 147.

77. Prasad, K. U., Alonso-Romanowski, S., Venkatachalam, C. M., Trapane, T. L., Urry, D. W., *Biochemistry*, 25 (1986) 456.

78. "Fluorescence Recovery After Photobleaching (FRAP), Biology department", *Davidson*, Davidson College, 2010, Web Oct 2013.

79. Picas, L., Milihiet, P., Hernández-Borrell, J., *Chem. Phys. Lipids*, 165 (2012) 845.

80. Meyer, E., Hug, H., Bennewitz, R., "Scanning Probe Microscopy: A Lab on a Tip", Springer, Berlin, (2004).

81. Kaupp, G., "Atomic Force Microscopy, Scanning Near Field, Optical Microscopy and Nanoscratching, Application to Rough and Natural Surfaces", Springer, Berlin,(2006).

82. Mulligan, K., Jakubek, Z. J., Johnston, L. J., *Langmuir*, 27 (2011) 14352.

83. Mayer, D., Ataka, K., Heberle, J., Offenhäusser, A., *Langmuir*, 21 (2005) 8580.

84. Mendelsohn R., Flach, C. R., "Infrared Reflection-Absorption Spectrometry of Monolayer Films at the Air-Water Interface, Handbook of Vibrational Spectroscopy", John Wiley & Sons Ltd., England, (2002).

85. Lyubartsev, A. P., Rabinovich, A. L., *Soft Matter*, 7 (2011) 25.

86. Róg, T., Pasenkiewicz-Gierula, M., *FEBS Lett.*, 502 (2001) 68.

87. Arsov, Z., Rappolt, M., Grdadolnik, J., *Chem. Phys. Chem.*, 10 (2009) 1438.

88. Petersen, F. N. R., Nielsen, C. H., *Spectrosc.*, 24 (2009) 26.

89. Pemberton, J. E., Chamberlain, J. R., *Biopolymers*, 57 (2000) 103.

90. Leverette, C. L., Dluhy, R. A., *Colloids Surf. A*, 243 (2004) 157.

91. Ianoul, A., Westwick, H., Nowacka, L., Quan, B., *J. Raman Spectrosc.*, 38 (2007) 200.

92. Campos, R., Kataky, R., *J. Phys. Chem. B*, 116 (2012) 3909.

93. Nielsen, C. H., *Anal. Bioanal. Chem.*, 395 (2009) 697.

94. Zeng, X., Ruckenstein, E., *Biotechnol. Prog.*, 15 (1999) 1003.

95. Caldwell, G. W., Masucci, J. A., Evangelisto, M., White, R., *J. Chromatogr. A*, 800 (1998) 161.

96. Love, C. J., Estroff, L. A., Kriebel, J. K., Nuzzo, R. G., Whitesides, G. M., *Chem. Rev.*, 105 (2005) 1103.

97. Hasan, M., Bethell, D., Brust, M., *J. Am. Chem. Soc.*, 124 (2002) 1132.

98. Askerka, M., Pichugina, D., Kuz'menko, N., Shestakov, A., *J. Phys. Chem.*, 116 (2012) 7686.

99. Gan, W., Xu, B., Dai, H., *Angew. Chem. Int. Ed.*, 50 (2011) 6622.

100. Desikan, R., Armel, S., Meyer III, H. M., Thundat, T., *Nanotechnology*, 18 (2007) 424028.

101. Kudelski, A., *J. Raman Spectrosc.*, 34 (2003) 853.

102. Ma, C., Harris, J. M., *Langmuir*, 28 (2012) 2628.

103. Dai, J., Li, Z., Jin, J., Shi., Y., Cheng, J., Kong, J., Bi, S., *Biosens. Bioelectron.*, 24 (2009) 1074.

104. Kudelski, A., Michota, A., Bukowska, J., *J. Raman Spectrosc.*, 36 (2005) 709.

105. Kellar, J. J., Cross, W. M., Yalamanchili, M. R., Young, C.A., Miller, J.D., *Miner. Metall. Process*, 10 (1993) 75.

106. Grimm, R. L., Tobias, D. J**,** Hemminger, J. C., *J. Phys. Chem. C*, 114 (2010) 1570.

107. Jenkins, A. T. A., Hu., J., Wang, Y. Z., Schiller, S., Foerch R., Knoll, W., *Langmuir*, 16 (2000) 6381.

108. Zhang, H., Grim, P. C. M., Liu, D., Vosch, T., De Feyter, S., Wisesler, U. M., Berresheim, A. J., Müllen, K., Haesendonck, C. V., Vandamme, N., De Schryver, F. C., *Langmuir*, 18 (2002) 1801.

109. Królikowska, A., Bukowska, J., *J. Raman Spectrosc.*, 38 (2007) 936.

110. Kudelski, A., *J. Vib. Spectro.*, 39 (2005) 200.

111. Li, Z., Niu, T., Zhang, Z, Bia, S., *Electrochim. Acta*, 55 (2010) 6907.

112. Madueño, R., García-Raya, D., Viudez, A. J., Sevilla, J. M., Pineda, T., Blázquez, M., *Langmuir*, 23 (2007) 11027.

113. Zugle, R., Kambo-Dorsa, J., Gadzekpo, V. P. Y., *Talanta*, 61 (2003) 837.

114. Schmid, G., ed., "Nanoparticles, From Theory to Application", Wiley-VCH GmbH & Co., Berlin, (2004).

115. Gaines, G. L. Jr., "Insoluble Monolayers at Liquid-Gas Interfaces", John Wiley & Sons Inc., England, 1966.

116. Norde, W., "Colloids and Interfaces in Life Sciences and Bionanotechnology", Taylor & Francis Group, LLC, Florida, (2011): 105-107.

117. Martin, D., "Nanobiotechnology of Biomimetic Membranes", Volume 1. Springer Science + Business Media Inc., New York, (2006): 23-74.

118. KSV NIMA, "Software Manual, Langmuir and Langmuir-Blodgett devices", KSV NIMA Biolin Scientific, Finland, 2010.

119. Malgorzata, J., *J. Phys. Chem. B*, 117 (2013) 1190.

120. Capone, S., Manera, M. G., Taurino, A., Siciliano, P., Rella, R., Luby, S., Benkovicova, M., Siffalovic, P., Majkova, E., *Langmuir*, 30 (2014) 1190.

121. Eftekhari, A., ed., "Nanostructured Materials in Electrochemistry", Wiley-VCH GmbH & Co., Berlin, (2008).

122. Bard, A. J., Faulkner, L. R., "Electrochemical Methods, Fundamentals and Applications, 2nd Edition", John Wiley & Sons Inc., England, (2001).

123. Becucci, L., Guidelli, R., *Pharmaceuticals*, 7 (2014) 136.

124. Nieciecka, D., Królikowska, A., Joniec, A., Krysinski, P., *J. Electroanal. Chem.*, 710 (2013) 59.

125. Naumann, Schmidt, E. K., Jonczyk, A., Fendler, K., Kadenbach, B., Liebermann, T., Offenhäusser, A., Knoll, W., *Bionsens. Bioelectron.*, 14 (1999) 651.

126. He, L., Robertson, J. W. F., Li, J., Kärcher, I., Schiller, S. M., Knoll, W., Naumann, R., *Langmuir*, 21 (2005) 11666.

127. Schasfoort, R. B. M., Tudos, A. J., "Handbook of Surface Plasmon Resonance", The Royal Society of Chemistry, UK, (2008): 368-369.

128. Brosseau, C. L., Leitch, J., Bin, X., Chen, M., Roscoe, S. G., Lipkowski, J., *Langmuir*, 24 (2008) 13058.

129. Nelson, A., *J. Chem. Soc., Faraday Trans.*, 89 (1993) 3081.

130. Wilkop, T., Danke, X., Cheng, Q., *Langmuir*, 24 (2008) 5615.

131. Lipkowski, J., Ross, P. N., eds., "Adsorption of Molecules at Metal Electrodes", VCH Publishers Inc., New York, (1992): 285.

132. Turrell, G., Corset, J., eds., "Raman Spectroscopy, Developments and Applications", Academic Press Ltd., London, (1996).

133. Baia, M., Astilean, S., Lliescu, T., "Raman and SERS Investigations of Pharmaceuticals", Springer, Berlin, (2008): 61-65.

134. Socrates, G., "Infrared and Raman Characteristic Group Frequencies, 3rd Edition", John Wiley & Sons Ltd., England, (2001).

135. Waltz, D., Teissié, J., Milazzo, G., "Bioelectrochemistry of Membranes, Volume 6", Birkhäuser, Switzerland, (2004): pg 116, Table 4.

136. Movasaghi, Z., Rehman, S., Rehman, I., *Appl. Spectrosc. Rev.*, 42 (2007) 493.

137. Caldwell, W. B., Campbell, D. J., Chen, K., Herr, B. R., Mirkin, C. A., Malik, A., Durbin, M. K., Dutta, P., Huang, K. G., *J. Am. Chem. Soc.*, 117 (1995) 6071.

138. Vezvaie, M., Brosseau, C. L., Lipkowski, J., *Electrochim. Acta*, 110 (2013) 120.

139. Wu, D., Li, J., Ren, B., Tian, Z., *Chem. Soc. Rev.*, 37 (2008) 1025.

140. Li, J., Sun, C., Tan, L., Xie, Y., Zhang, H., *Langmuir*, 29 (2013) 5199.

141. Schlücker, S., ed., "Surface Enhanced Raman Spectroscopy, Analytical, Biophysical and Life Science Application", Wiley-VCH, Berlin, (2011).

142. Zhang, J. Z., "Optical Properties and Spectroscopy of Nanomaterials", World Scientific Publishing Co. Pte. Ltd., Singapore, (2009).

143. Rotello, V., ed., "Nanoparticles Building Blocks for Nanotechnology", Kluwer Academic/Plenum Publishers, New York, (2004).

144. Peplow, M., "Easy route to stable silver nanoparticles", *Nature International Weekly Journal*, Nature Publishing Group, 04 Sept 2013, Web May 2014.

145. AshaRani, P. V., Mun, G. L. K., Hande, M. P., Valiyaveettil, S., *ACS Nano.*, 3 (2009) 280.

146. Martínez-Gutierrez, F., Thi, E. P., Silverman, J. M., Camargo de Oliveira, C., Svensson, S. L., Hoek, A. V., Sánchez, E. P., Reiner, N. E., Gaynor, E. C., Pryzdial, E. L. G., Conway, E. M., Orrantia, E., Ruiz, F., Av-Gay, Y., Bach, H., *Nanomed. Nanotechnol.*, 8 (2012) 328.

147. Cuenya, B. R., *Thin Solid Films*, 518 (2010) 3127.

148. Sharma, B., Frontiera, R. R., Henry, A., Ringe, E., Van Duyne, R. P., *Mater. Today*, 15 (2012) 17.

149. Skoog, D. A., Holler, F. J., Crouch, S. R., "Principles of Instrumental Analysis, 6th Edition", Thomson Brooks/Cole, California, (2007).

150. Reddy, K. V., "Symmetry and Spectroscopy of Molecules", New Age International (P) Ltd., New Dehli, (1998): 338-340.

151. Vadgama, P., Peteu, S., Thompson, M., "Detection Challenges in Clinical Diagnostics", Royal Society of Chemistry, UK, (2013): 205-206.

152. Agarwal, U. P., Atalla, R. H., "Surface Analysis of Paper: Chapter 8 Raman Spectroscopy", CRC Press, Florida, (1995): 152-181.

153. Negri, P., Chen, G., Kage, A., Nitsche, A., Naumann, D., Xu, B., Dluhy, R. A., *Anal. Chem.*, 84 (2012) 5501.

154. Doering, W. E., Piottic, M. E., Natan, M. J., Freeman, R. G., *Adv. Mater.*, 19 (2007) 3100.

155. Nishiyama, K., Tahara, S., Uchida, Y., Tanoue, S., Taniguchi, I., *J. Electroanal. Chem.*, 478 (1999) 83.

156. Kudelski, A., *Langmuir*, 18 (2002) 4741.

157. Królikowska, A., Kudelski, A., Michota, A., Bukowska, J., *Surf. Sci.*, 532-535 (2003) 227.

158. Castro, J. L., López-Ramírez, M. R., Centeno, S. P., Otero, J. C., *Biopolymers*, 74 (2004) 141.

159. Sandhyarani, N., Pradeep, T., *Vacuum*, 49 (1998) 279.

160. Kudelski, A., *Vibrat. Spec.*, 33 (2003) 197.

161. Shaw, D. J., "Colloid & Surface Chemistry, 4th Edition", Reed Educational and Professional Publishing Ltd., London, (1992).

162. Brett, C. M. A., Brett, A. M. O., "Electrochemistry: Principles, Methods and Applications", Oxford University Press Inc., UK, (1993).

163. "Parallel Plate Capacitor", *HyperPhysics*, C. R. Nave, 2012, Web Apr 2014.

164. Knight, P. D., "Physics For Scientists and Engineers, 2nd Edition, A Strategic Approach", Pearson Education Inc., USA, (2008).

165. Jin-Hua, C., Shi-Hui, S., Li-Hua, N., Shou-Zhuo, Y., *Electrochimica Acta*, 42 (1997) 689.

166. Zhang, G., Chen, H., *Anal. Chim. Acta*, 419 (2000) 25.

167. Takahaski, Y., Shevchuk, A. I., Novak, P., Babakinejad, B., Macpherson, J., Unwin, P. R., Shiku, H., Gorelik, J., Klenerman, D., Korchev, Y. E., Matsue, T., *Proc. Natl. Acad. Sci. USA*, 109 (2012) 11540.

168. Boscheto, E., Batista, B. C., Lima, R. B., Varela, H., *J. Electroanal. Chem.*, 642 (2010) 17.

169. Salamon, Z., Hazzard, J. T., Tollin, G., *Proc. Natl. Acad. Sci. USA*, 90 (1993) 6420.

170. Kwok, D. Y., Tadros, B., Deol, H., Vollhardt, D., Miller, R., Cabrerizo-Vílchez, M. A., Neumann, A. W., *Langmuir*, 12 (1996) 1851.

171. Lee, P. C., Meisel, D., *J. Phys. Chem.*, 86 (1982) 3391.

172. Munro, C. H., Smith, W. E., Garner, M., Clarkson, J., White, P. C., *Langmuir*, 11 (1995) 3712.

173. Bell, S. E. J., Sirimuthu, M. S., *J. Phys. Chem. A*, 109 (2005) 7405.

174. Garcia-Araez, N., Brosseau, C. L., Rodriguez, P., Lipkowski, J., *Langmuir*, 22 (2006) 10365.

175. Foucault, R., Birke, R. L., Lombardi, J. R., *Langmuir*, 19 (2003) 8818.

176. Zawisza, I., Bin, X., Lipkowski, J., *Langmuir*, 23 (2007) 5180.

177. Chen, M., Li, M., Brosseau, C. L., Lipkowski, J., *Langmuir*, 25 (2009) 1028.

178. Brosseau, C. L., Bin, X., Roscoe, S. G., Lipkowski, J., *J. Electroanal. Chem.*, 621 (2008) 222.

179. Silva, A. F., "Trends in Interfacial Electrochemistry", D. Reidel Publishing Company, Holland, (1986).

180. Aveyard, R., Haydon, D. A., "An Introduction to The Principles of Surface Chemistry", Cambridge University Press, UK, 1973.

181. Skoog, D. A., West, D. M., Holler, F. J., "Fundamentals of Analytical Chemistry, 7th Edition", Saunders College Publishing, Florida, (1996).

182. Primera-Pedrozo, O. M., Rodríguez, G. D. M., Castellanos, J., Felix-Rivera, H., Resto, O., Hernández-Rivera, S. P., *Spectrochim. Acta A*, 87 (2012) 77.

183. Lopes, R. P., Valero, R., Tomkinson, J., Marques, M . P. M., Batista de Carvalho, L. A. E., *New J. Chem.*, 37 (2013) 2691.

184. Milne, G. W. A., ed., "Gardner`s Commercially Important Chemicals, Synonyms, Trade names, and Properties", John Wiley & Sons Inc., England, (2005): 13.

185. "Aloin (CAS 1415-73-2)", *Santa Cruz Biotechnology*, Santa Cruz Biotechnology Inc., 2014, Web May 2014.

186. Marsh, H., Rodríguez-Reinoso, R., "Activated Carbon", Elsevier Ltd., UK, (2006): 218.

187. Yampolskii, Y., Pinnau, I., Freeman, B. D., eds., "Materials Science of Membranes for Gas and Vapour Separation", John Wiley & Sons Ltd., England, (2006) 352.

188. Unger, K. K., Kreysa, G., Baselt, J. P., eds., "Characterization of Porous Solids, V", Elsevier Science BV, Holland, (2000): 327.

189. Schaefer, H., "Nanoscience, The Science of the Small in Physics, Engineering, Chemistry, Biology, and Medicine", Springer, Berlin, (2010): 146.

190. Papazoglou, E. S., Parthasarathy, A., "BioNanotechnology", Morgan & Claypool, USA, (2007): 4.

191. Srivastava, P. K., "Elemental Biophysics, An Introduction", Alpha Science International Ltd., UK, (2005): 141.

192. Moore, J., Stanitski, C., Jurs, P., "Principles of Chemistry, The Molecular Science", Brooks/Cole Cengage Learning, USA, (2010): 283-284.

193. Cserháti, T., Valkó, K., "Chromatographic Determination of Molecular Interactions, Applications in Biochemistry, Chemistry, and Biophysics", CRC Press Inc., USA, (1994): 149.

194. Neumann, E., Schaefer-Ridder, M., Wang, Y., Hofschneider, P.H., *Embo J.*, 1 (1984) 841.

195. Tantipolphan, R., Rades, T., Strachan, C. J., Gordon, K. C., Medlicott, N. J., *J. Pharmaceut.Biomed.*, 41 (2006) 576.

196. Anizelli, P. R., Bau, J. P. T., Nabeshima, H. S., Costa, M. F., Santana, H., Zaia, D. A. M., *Spectrochim. Acta A*, 126 (2014) 184.

197. Benevides, J. M., Overman, S. A., Thomas, G. G. Jr., *J. Raman Spectrosc.*, 36 (2005) 279.

198. Cañamares, M. V., Garcia-Ramos, J. V., Domingo, C., Sanchez-Cortes, S., *Vib. Spectrosc.*, 40 (2006) 161.

199. Cañamares, M. V., Garcia-Ramos, J. V., Domingo, C., Sanchez-Cortes, *J. Raman Spectrosc.*, 35 (2004) 921.

200. Whitney, A. V., Van Duyne, R. P., Casadio, F., *J. Raman Spectrosc.*, 37 (2006) 993.

201. Rajkumar, B. J. M., Ramakrishnan, V., Rajaram, R. K., *Spectrochim. Acta A*, 54 (1998) 1527.

202. Mary, M. B., Ramakrishnan, V., *Spectrochim. Acta A*, 62 (2005) 164.

203. Munro, C. H., Smith, W. E., Garner, M., Clarkson, J., White, P. C., *Langmuir*, 11 (1995) 3712

204. Papadopoulou, E., Bell, E. J., *J. Phys. Chem. C.*, 115 (2011) 14228.

205. Plummer, B. F., "Selected Principles of Organic Chemistry", Litton Educational Publishing Inc., New York, (1972).

206. Clarke, D. E., *J. Pharm. Sci.*, 88 (1999) 807.

207. Wishart, D. S., Jewison, T., Guo, A. C., Wilson, M., Knox, C., Liu, Y., Djoumbou, Y., Mandal, R., Aziat, F., Dong, E., Bouatra, S., Sinelnikov, I., Arndt, D., Xia, J., Liu, P., Yallou, F., Bjorndahl, T., Perez-Pineiro, R., Eisner, R., Allen, F., Neveu, V., Greiner, R., Scalbert, A., *Nucleic Acids Res.*, 41 (2013) D801.

208. Mansour, H. M., Zografi, G., *J. Pharm. Sci.*, 96 (2007) 377.

209. Baumgart, T., Offenhäusser, A., *Biophys. J.*, 83 (2002) 1489.

210. Kasson, P. M., Pande, V. S., *Biophys. J.*, 86 (2004) 3744.

211. Mancheno-Posso, P., Muscat, A. J., *ECS Trans.*, 58 (2013) 289.

212. Kim, D. J., Koo, K. K., *Nanotech.*, 1 (2005) 438.

213. Preston, C. T., Nuruzzaman, M., Jones, N.D., Mittler, S., *J. Phys. Chem. C*, 113 (2009) 14236.

214. Matulaitienė, I., Kuodis, Z., Eicher-Lorka, O., Niaura, G., *J. Electroanal.Chem.*, 700 (2013) 77.

215. Tian, Z. Q., Ren, B., Mao, B.W., *J. Phys. Chem. B*, 101 (1997) 1338.

216. Pienpinijtham, P., Han, X. X., Ekgasit, S., Ozaki, Y., *Anal. Chem.*, 83 (2011) 3655.

217. Chaplin, M., "Kosmotropes and Chaotropes", *Water Structure and Science*, Creative Commons Attribution, 2013, Web Oct 2013.

218. Mason, P. E., Neilson, G. W., Dempsey, C. E., Barnes, A. C., Cruickshan, J. M., *Proc. Natl. Acad. Sci. USA*, 100 (2003) 4557.

219. Zimmermann, R., K., Küttner, D., Renner, L., Kaufmann, M., Werner, C., *J. Phys. Chem. A*, 116 (2012) 6519.

220. Haynes, W. M., ed., "CRC Handbook of Chemistry and Physics, 93rd Edition", Taylor & Francis Group LLC, Florida, (2012): 7-1.

221. Arenas, J. F., Castro, J. L., Otero, J.C., Marcos, J. I., *Biopolymers*, 62 (2001) 241.

222. Shin, D. W., Ma, J., Kim, D. H., *FEBS Lett.*, 486 (2000) 178.

223. Vogel, H. J., ed., "Methods in Molecular Biology Volume 173: Calcium-Binding Protein Protocols, Volume 2", Humana Press Inc., New Jersey, (2002): 15-17.

224. Changa, D. M., *J. Am. Oil Chem. Soc.*, 60 (1983) 618.

225. Alvarez-Pueblo, R. A., Liz-Marzán, L. M., *Angew. Chem. Int. Ed.*, 51 (2012) 11214.

226. Nara, M., Torii, H., Tasumi, M., *J. Phys. Chem.*, 100 (1996) 19812.

227. "DXR[TM] Smart Raman Spectrometer: The Use of Variable Dynamic Point Sampling to Analyze Non-Homogenous Samples Using Raman Spectroscopy", Thermo Scientific, Thermo Fisher Scientific Inc., 2014, Web Apr 2014.

228. Levin, C. S., Kundu, J., Janesko, B. G., Scuseria, G. E., Raphael, R. M., Halas, N. J., *J. Phys. Chem. B*, 112 (2008) 14168.

229. Zimmermann, F., Wokaun, A., *Progr. Colloid Polym. Sci.*, 81 (1990) 242.

230. Chung, Y., Chen, I., Chen, C., Biomaterials, 29 (2008) 1807.

231. Skoog, D. A., West, D. M., Holler, F. J., Crouch, S. R., "Fundamentals of Analytical Chemistry, 8th edition", Brooks/Cole, California (2004).

Appendix

Table A-1: Solid cholesterol Raman peak assignment

Wavenumber (cm^{-1})	Assignment	Description
428		Ring deformation
700	$\delta_r(-CH_2)$	Rocking vibration
1438	$\delta_d(-CH_2)$	Deformation
1672	$v(C=C)$	Stretch vibration of the alkene
2868	$v_{sym}(-CH_3)$	Symmetric stretch vibration
2932	$v_{sym}(-CH_2)$	Symmetric stretch vibration

Table A-2: Solid DMPC Raman peak assignment

Wavenumber (cm^{-1})	Assignment	Description
712	$C-N^+(CH_3)$	Symmetric choline group stretch vibration
873	$C-N^+(CH_3)$	Antisymmetric choline stretch vibration
888	CH_2	Methylene rocking
953	$N^+(CH_3)$	Antisymmetric choline stretch vibration
1061	$v(C-O-PO_2^-)$ C-C	Phosphate ester stretch Skeletal stretch vibration
1090	$v_s(CO-O-C)$ PO_2^-	Ester C-O symmetric stretch Stretch in the phosphate group
1125	C-C	Skeletal transconformation stretch of lipids
1294	CH_2	Wagging and twisting methylene vibration
1437	CH_2	methylene deformation
1453	CH_2	methylene deformation
1731	$v(C=O)$	Ester carbonyl stretch
2724	C-H	Stretch vibration
2845	$v_s(CH_2)$	Symmetric stretch
2880	$v_{as}(CH_2)$	Asymmetric stretch
2933	$v_{as}(CH_2)$	Asymmetric stretch
2960	$v_{as}(CH_3)$	Out-of-plane chain end antisymmetric stretch
3032	$v_{as}(CH_3)_3N^+$	CH_3 asymmetric stretch in the choline group

Table A-3: Solid adenine Raman peak assignment

Wavenumber (cm^{-1})	Assignment	Description	Molecule
533		In-plane ring deformation	adenine
620		In-plane ring deformation	adenine
721		Pyrimidine and imidazole ring breathing	adenine
897	δ(C-N-C)$_{py}$	Pyrimidine ring deformation	adenine
940	δ(N-C=N)	Imidazole ring deformation	adenine
1022	ρ(NH$_2$)	Amine rocking	adenine
1124	δ(C-H)	Imidazole ring deformation	adenine
1247	v(C-NH$_2$)	Stretch	adenine
1331	v(C-N)$_{im}$	Imidazole ring stretch	adenine
1481	v(C=N)$_{im}$	Imidazole ring stretch	adenine
1596	v(C=C)	Alkene stretch	adenine
1610	v(C=N)	Nitrile stretch	adenine
3036	v(N-H)im	Imidazole ring stretch	adenine
3120	v_{as}((NH$_2$)	Amine asymmetric stretch	adenine

Table A-4: Solid dAMP Raman peak assignment

Wavenumber (cm^{-1})	Assignment	Description	Molecule
626		In-plane ring deformation	dAMP
732		Pyrimidine and imidazole ring breathing	dAMP
813	O-P-O	Phosphate group stretch	dAMP
1037	N-sugar	Stretch between purine and deoxyribose	dAMP
1332	v(C-N)$_{im}$	Imidazole ring stretch	dAMP
1405	N-H	In-plane deformation	dAMP
1491		Ring breathing mode	dAMP
1506	v(C=N)	Nitrile stretch	dAMP
1555		Ring stretching	dAMP
2889	v_{as}(CH$_2$)	Asymmetric stretch	dAMP
2922	(CH)	Stretch	dAMP
2941	C-H v_{as}(CH$_2$)	Vibrations Asymmetric stretch	dAMP
2950	C-H	Stretch	dAMP
2983	C-H	Stretch	dAMP
3011	=CH	stretch	dAMP
3048	=C-H	Stretch	dAMP
3112	=C-H	Stretch	dAMP

Table A-5: Solid aloin Raman peak assignment

Wavenumber (cm^{-1})	Assignment	Description	Molecule
481		Skeletal vibration	aloin
626	C-OH	Possible alcohol deformation	aloin/glucose
1169	CC,CH	Ring deformation	aloin
1284	COH, CC	Alcohol deformation from ring	aloin
1338		Presence of glucose	glucose
1431	CC, CH	Ring deformation	aloin
1496	CC	Ring deformation	aloin
1558	CC, COH, CH	Ring deformation	aloin
1636	C=O	Ring deformation and carbonyl stretches	aloin

Table A-6: Solid KSCN Raman peak assignment

Wavenumber (cm^{-1})	Assignment	Description	Molecule
746	C-S	Stretch vibration	thiocyanate
2050	$v_{as}(C≡N)$	Asymmetric stretch	thiocyanate

Table A-7: Peak assignment for OCP spectrum of DMPC/cholesterol (70:30) bilayer time study (0 minute) in the presence of 0.1 M NaF solution

Wavenumber (cm^{-1})	Assignment	Description	Molecule
690	$\delta_r(-CH_2)$ COO$^-$	Rocking vibration Presence of a carboxylic group	cholesterol citrate
1435	CH$_2$	Methylene deformation	DMPC/cholesterol
1555	COO$^-$	Presence of a carboxylic group	citrate
1763	$v(C=O)$	Ester carbonyl stretch	DMPC
2937	$v_{as}(CH_2)$	Asymmetric stretch	DMPC/cholesterol

Table A-8: SERS peak assignment for OCP spectrum of DMPC/cholesterol (70:30) monolayer in the presence of 1 mM dAMP/0.1 M NaF solution

Wavenumber (cm⁻¹)	Assignment	Description	Molecule
568	O-C-O	Ester group bending Ring bending	citrate dAMP
634	O-C-O	Ester group bending Ring bending	citrate dAMP
694		Steroid ring stretch	cholesterol
737	CH_2	Rocking vibration Ring breathing	DMPC dAMP
962	$v_{as}(C\text{-}N^+C)$	Choline asymmetric stretch	DMPC
1015	C-O	Choline asymmetric stretch	DMPC
1329		H bending + ring stretch phospholipids	dAMP DMPC
1406	$-N(CH_3)_3^+$	Symmetric deformation vibration	DMPC
1468	CH_2	Scissoring and asymmetric bending vibration	DMPC
1577		Ring breathing	dAMP
1767	C=O	Stretch of lipids	DMPC
2942	$v_{as}(CH_2)$ $v(CH)$	Asymmetric and symmetric stretch Stretch vibration	DMPC/cholesterol

Figure A-9: Anodic overlay spectra of DMPC/cholesterol (70:30) monolayer in the presence of 1 mM dAMP/0.1 M NaF solution
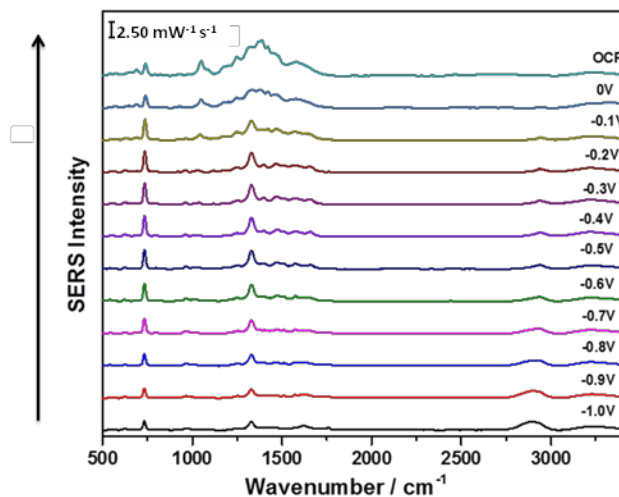
Table A-10: Peak assignment for in air spectrum of DMPC/cholesterol (70:30) bilayer

Wavenumber (cm^{-1})	Assignment	Description	Molecule
634	O-C-O	Bending or out of plane deformation	citrate
686	σ(COO)	carboxylic group deformation	citrate
1000	v(O-CH$_2$-C) v(C-C)	Ester group stretch Skeletal backbone	citrate DMPC
1293	CH CH$_2$	Bending Wagging and twisting deformation	DMPC DMPC
1439	CH$_2$ CH	Scissoring and deformation CH	DMPC cholesterol
1590	v_{as}(COO$_2^-$)	Asymmetric stretch of vibration	citrate
1765	v(C=O)	Ester carbonyl stretch	DMPC
2935	v_{as}(CH$_2$)	Asymmetric stretch	DMPC/cholesterol

Figure A-11: CV comparison between DMPC/cholesterol (70:30) bilayer in the presence of 1 mM dAMP/0.1 M NaF solution and 0.1 M NaF solution

5
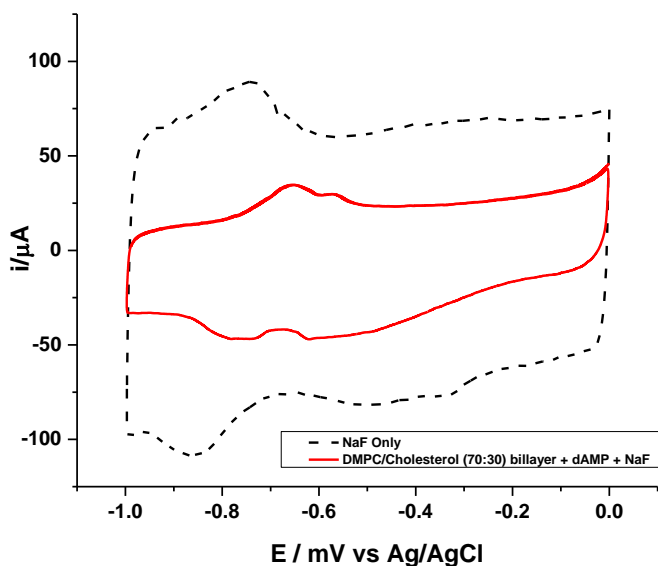
Table A-12: Peak assignment for OCP spectrum of DMPC/cholesterol (70:30) bilayer in the presence of 1 mM dAMP/0.1 M NaF solution

| Wavenumber (cm^{-1})	Assignment	Description	Molecule
693	σ(COO)	Steroid ring stretch carboxylic group deformation	cholesterol citrate
730	CH$_2$	Rocking vibration Ring breathing	DMP C
1003	v(O-CH$_2$-C)	Ester group stretch	citrate
1044	C-O-P	Stretch of lipid	DMPC
1324		H bending + ring stretch phospholipids	dAMP DMPC
1402	-N(CH$_3$)$_3^+$	Symmetric deformation vibration	DMPC
1615	C-NH$_2$	Ring deformation of	dAMP
1760	C=O	Stretch of lipids	DMPC
2938	v_{as}(CH$_2$) v(CH$_3$)	Asymmetric and symmetric stretch	DMPC/cholesterol

Figure A-13: a) cathodic and b) anodic overlay spectra of DMPC/cholesterol (70:30) bilayer in the presence of 1 mM dAMP/0.1 M NaF solution
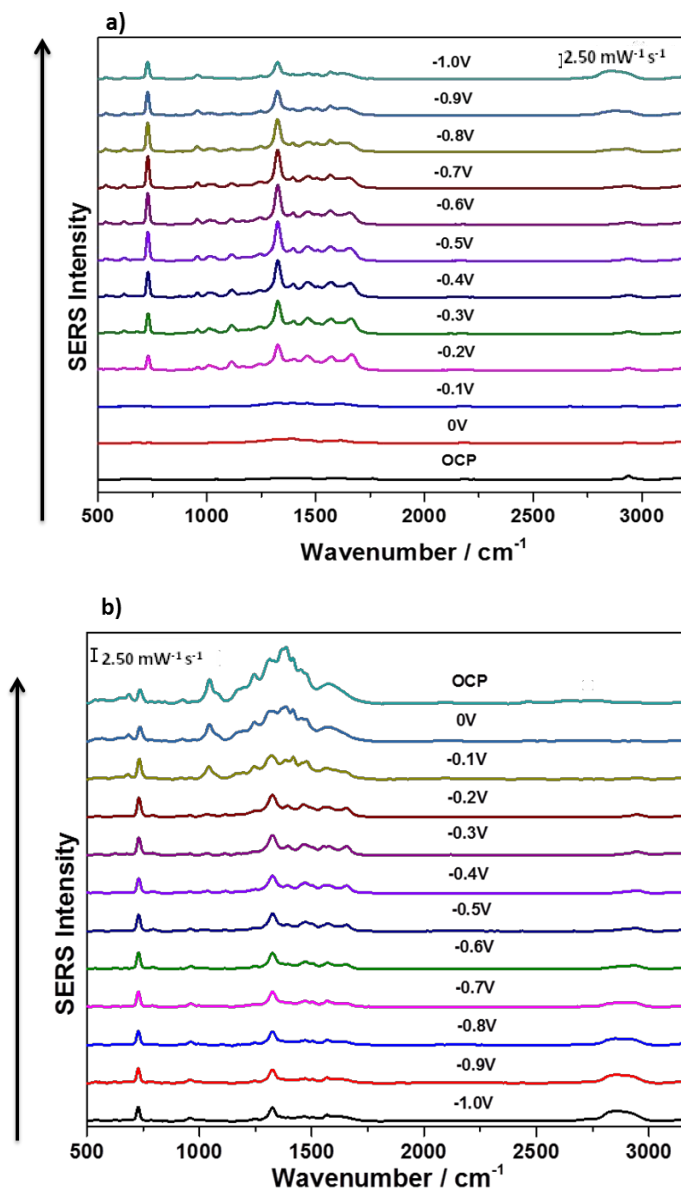
Table A-14: Peak assignment for in air spectrum of DMPC/cholesterol (70:30) bilayer, increased humidity and subphase temperature studies

Wavenumber (cm^{-1})	Assignment	Description	Molecule
452		water interactions with lipids	DMPC/water
609		Presence of cholesterol	cholesterol
672	$\delta(COO^-)$	citrate carboxylic group	citrate
866	C-C PO_4^-	Stretch Presence of a phosphate group	DMPC DMPC
903	$v(C\text{-}COO^-)$	citrate carboxylic Presence of phosphodiester	citrate DMPC
973	$v_{as}(C\text{-}N^+C)$	Choline asymmetric stretch	DMPC
999	$v(O\text{-}CH_2\text{-}C)$	Ester group stretch	citrate
1020	CH_2CH_3	Bending modes of phospholipids	DMPC
1106	$v(C\text{-}C)$	Lipids	DMPC
1209	$\delta(COO^-)$	citrate carboxylic group	citrate
1261	$v_{as}(PO_2^-)$	Phosphate diester asymmetric stretch	DMPC
1313	$\gamma_w(CH_2)$	CH_2 wagging, twisting or bending vibration of lipid	DMPC
1351	COO^-	carboxylate vibration	citrate
1443	$\delta_d(\text{-}CH_2)$	deformation for cholesterol	cholesterol
1566	$v_{as}(COO_2^-)$	Asymmetric stretch of vibration	citrate
1590	$v_{as}(COO_2^-)$	Asymmetric stretch of vibration	citrate
1645	O-H	Intermolecular bending mode	water
2928	$v_{as}(CH_2)$	Asymmetric stretch	DMPC/cholesterol

Figure A-15: a) cathodic and b) anodic overlay spectra of DMPC/cholesterol (70:30) bilayer in the presence of 1 mM dAMP/0.1 M NaF solution at increased humidity and subphase temperature
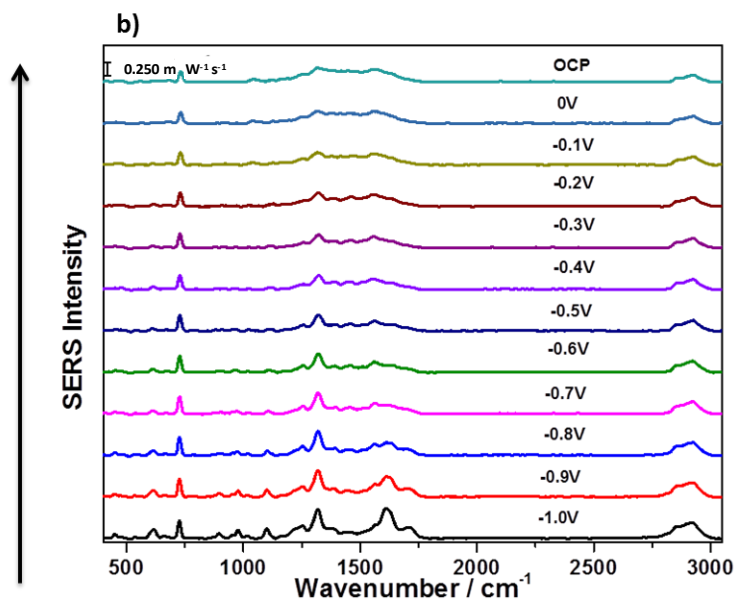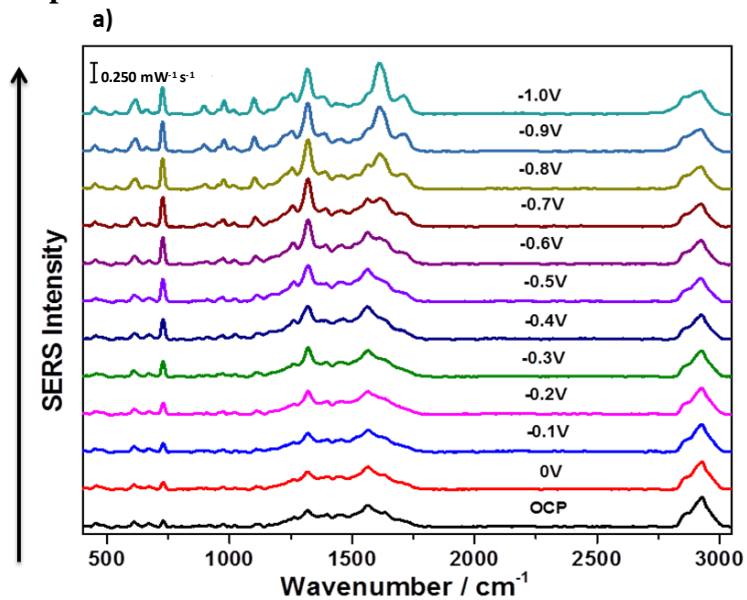
Table A-16: Peak assignment for OCP spectrum of DMPC/cholesterol (70:30) bilayer in the presence of 1 mM dAMP/0.1 M NaF solution at increased humidity and subphase temperature

Wavenumber (cm^{-1})	Assignment	Description	Molecule
453		water interactions with lipids	DMPC/water
610		Presence of cholesterol	cholesterol
668	$\delta(COO^-)$	citrate carboxylic group	citrate
729	CH$_2$	Rocking vibration	DMPC
		Ring breathing	dAMP
974	v_{as} (C-N$^+$C)	Choline asymmetric stretch	DMPC
1109	v(C-C)	Lipids	DMPC
1262	v_a (PO$_2^-$)	Phosphate diester asymmetric stretch	DMPC
1317	γ_w(CH$_2$)	Wagging, twisting or bending vibration of lipid	DMPC
		Possible ring breathing	dAMP
1398	-N(CH$_3$)$_3^+$	Symmetric deformation vibration of a choline group	DMPC
1443	δ_d(-CH$_2$)	deformation for cholesterol	cholesterol
1565	v_{as}(COO$_2^-$)	Asymmetric stretch of vibration	citrate
1631	O-H	Intermolecular bending mode	water
2928	v_{as}(CH$_2$)	Asymmetric stretch	DMPC/cholesterol

Figure A-17: CV comparison between DMPC/cholesterol (70:30) bilayer in the presence of 1 mM dAMP/0.1 M NaF solution (increased humidity and subphase temperature) and 0.1M NaF solution
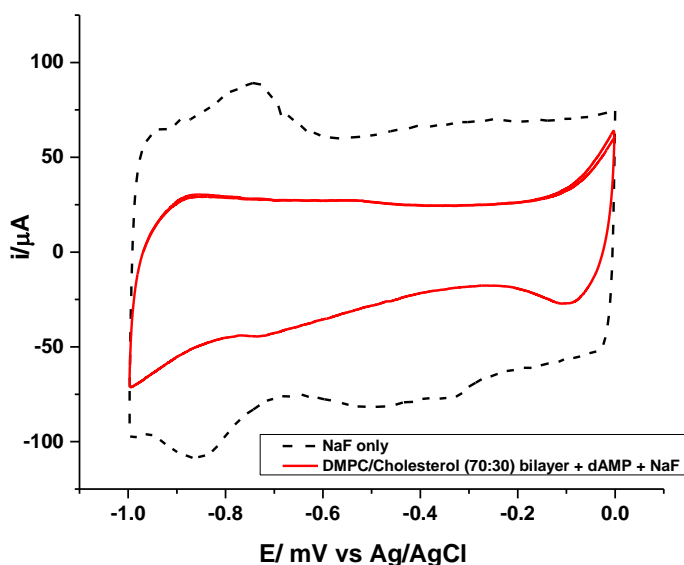
Table A-18: Peak assignment for in air spectrum of DMPC/cholesterol (50:50) bilayer, increased humidity and subphase temperature studies

Wavenumber (cm^{-1})	Assignment	Description	Molecule
457		water interactions with lipids	DMPC/water
611		Presence of cholesterol	cholesterol
676	$\delta(COO^-)$	citrate carboxylic group	citrate
869	C-C PO_4^-	Stretch Presence of a phosphate group	DMPC DMPC
976	$v_{as}(C-N^+C)$	Choline asymmetric stretch	DMPC
1002	$v(O-CH_2-C)$	Ester group stretch	citrate
1027	CH_2CH_3	Bending modes of phospholipids	DMPC
1110	$v(C-C)$	Lipids	DMPC
1266	$v_{as}(PO_2^-)$	Phosphate diester asymmetric stretch	DMPC
1317	$\gamma_w(CH_2)$	Wagging, twisting or bending vibration	DMPC
1442	$\delta_d(-CH_2)$	deformation for cholesterol	cholesterol
1568	$v_{as}(COO_2^-)$	Asymmetric stretch of vibration	citrate
2935	$v_{as}(CH_2)$	Asymmetric stretch	DMPC/cholesterol

Table A-19: Peak assignment for OCP spectrum of DMPC/cholesterol (50:50) bilayer in the presence of 1 mM dAMP/0.1 M NaF solution at increased humidity and subphase temperature

Wavenumber (cm^{-1})	Assignment	Description	Molecule
455		water interactions with lipids	DMPC/water
613		Presence of cholesterol	cholesterol
671	$\delta(COO^-)$	citrate carboxylic group	citrate
733	CH_2	Rocking vibration Ring breathing	DMPC dAMP
976	$v_{as}(C-N^+C)$	Choline asymmetric stretch	DMPC
1003	$v(O-CH_2-C)$	Ester group stretch	citrate
1027	CH_2CH_3	Bending modes of phospholipids	DMPC
1116	$v(C-C)$	Lipids	DMPC
1264	$v_{as}(PO_2^-)$	Phosphate diester asymmetric stretch	DMPC
1320	$\gamma_w(CH_2)$	H bending + ring stretch Wagging, twisting or bending vibration of lipid	dAMP DMPC
1448	$\delta_d(-CH_2)$	deformation for cholesterol	cholesterol
1565	$v_{as}(COO_2^-)$	Asymmetric stretch of vibration	citrate
2932	$v_{as}(CH_2)$	Asymmetric stretch	DMPC/cholesterol

Figure A-20: CV comparison between DMPC/cholesterol (50:50) bilayer in the presence of 1 mM dAMP/0.1 M NaF solution (increased humidity and subphase temperature) and 0.1 M NaF solution
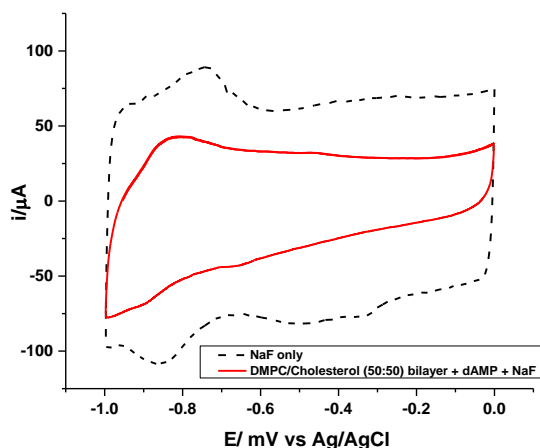
Figure A-21: OCP spectrum of 1-ODT SAM formed from approximately 12 hrs incubation in the presence of 1 mM dAMP/0.1 M NaF solution
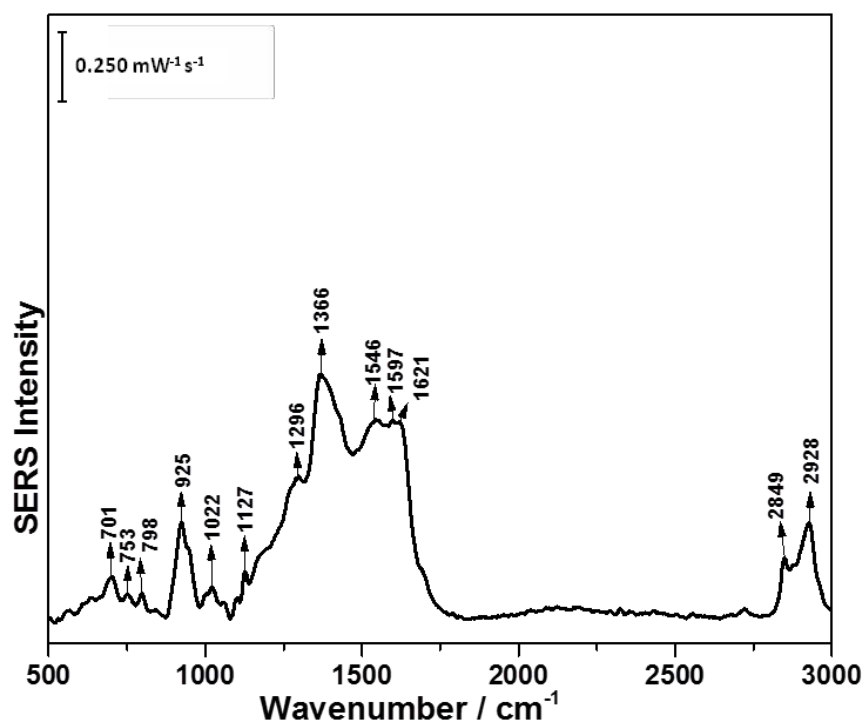
Figure A-22: a) cathodic and b) anodic overlay spectra of 1-ODT SAM formed from approximately 12 hrs incubation in the presence of 1 mM dAMP/0.1 M NaF solution
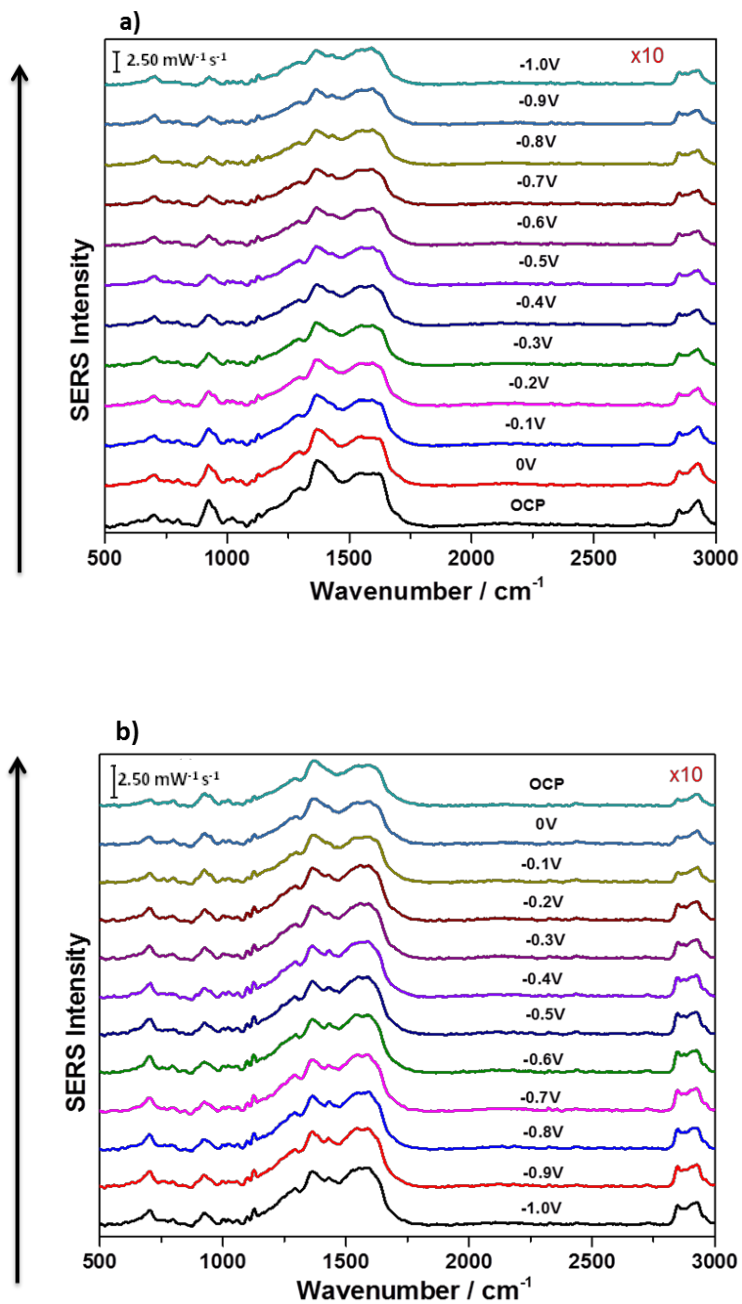
Figure A-23: CV comparison between 1-ODT SAM formed from approximately 12 hrs incubation in the presence of 1 mM dAMP/0.1 M NaF solution, and 0.1M NaF solution
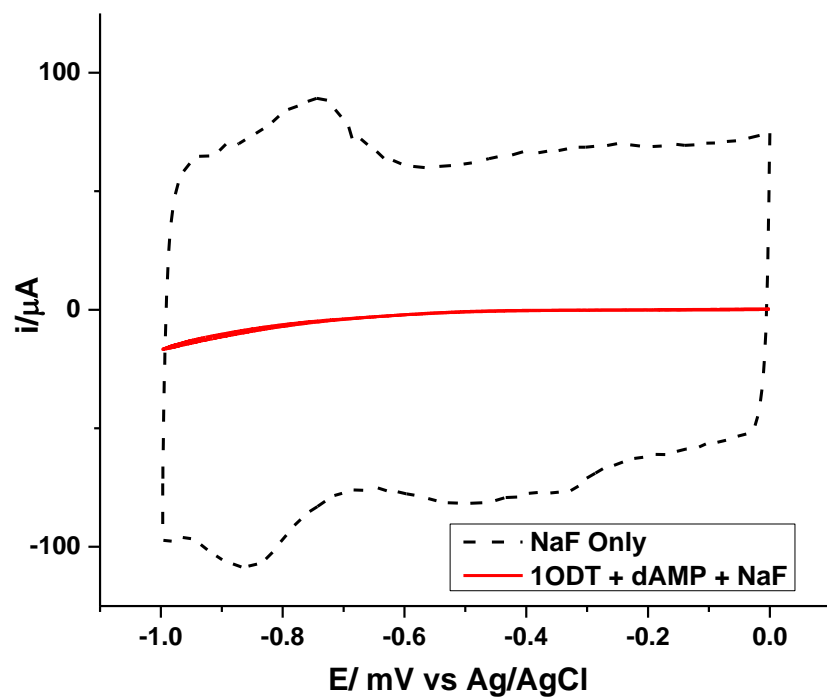
Figure A-24: OCP spectrum of 12-MDA SAM formed from approximately 12 hrs incubation in the presence of 1 mM dAMP/0.1 M NaF solution
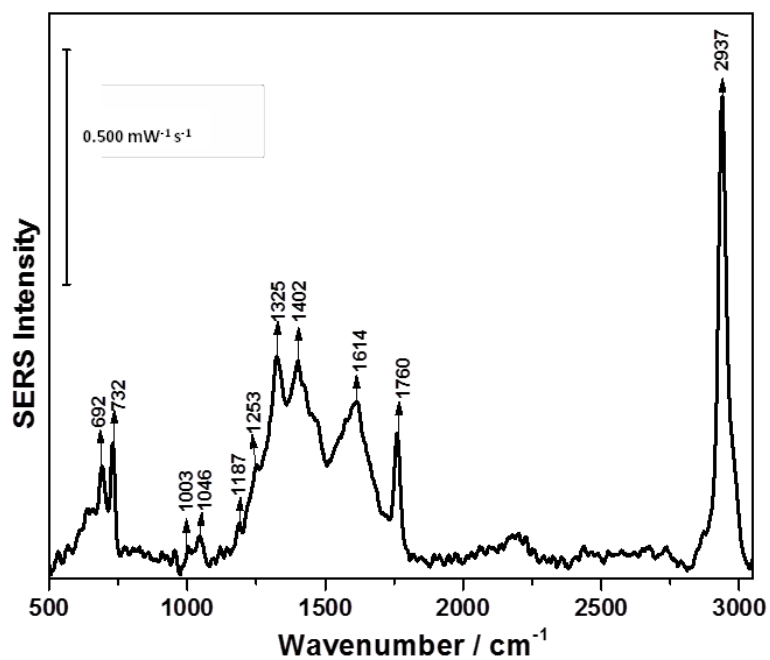
Figure A-25: CV comparison between 12-MDA SAM formed from approximately 12 hrs incubation in the presence of 1 mM dAMP/0.1 M NaF solution and 0.1 M NaF solution
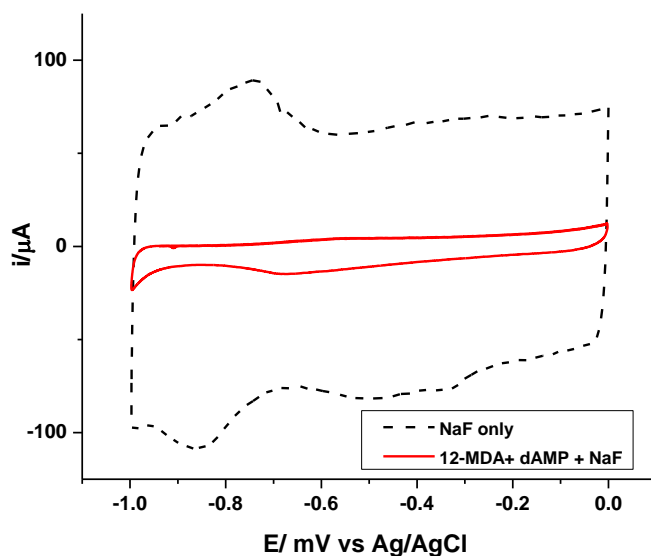
Figure A-26: In air spectrum of 6-MHA SAM, 1st trial
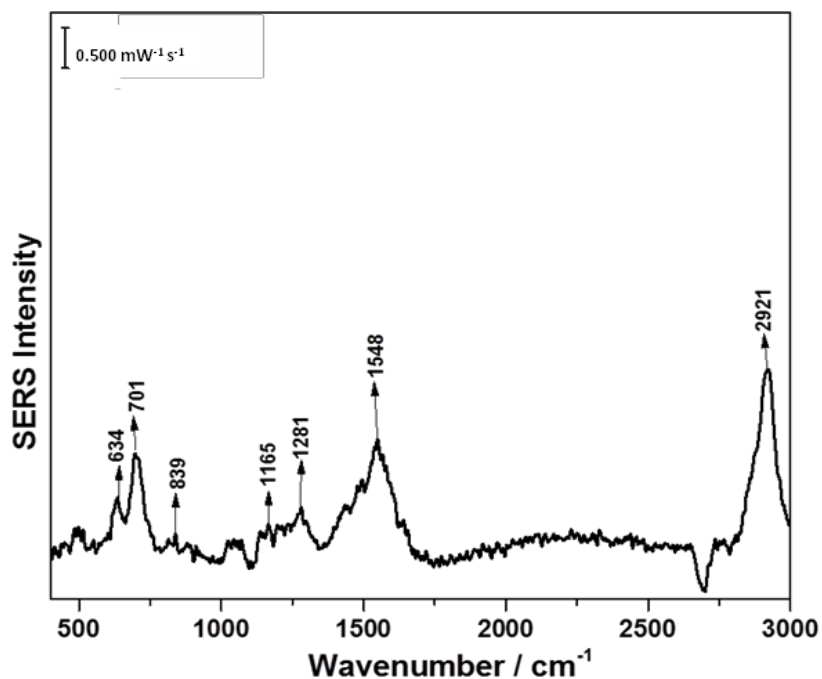
Table A-27: Peak assignment for in air spectrum of 6-MHA SAM, 1st trial

Wavenumber (cm^{-1})	Assignment	Description	Molecule
634	v(C-S)$_G$	Gauche carbon and sulphur deformation	6-MHA
701	v(C-S)$_T$	Trans carbon and sulphur deformation	6-MHA
839	(CH$_2$)$_G$	Methylene rocking	6-MHA
1165	C-C	Skeletal straight chain vibration	6-MHA
1281	ω(CH$_2$)	Wagging vibration	6-MHA
1548	v_{as}(COO$_2^-$)	Asymmetric stretch of vibration	6-MHA
2921	v_{as}(CH$_2$)	Asymmetric stretch alkyl chain	6-MHA

Figure A-28: OCP spectrum of 6-MHA SAM in the presence of 0.1M NaF solution, 1st trial
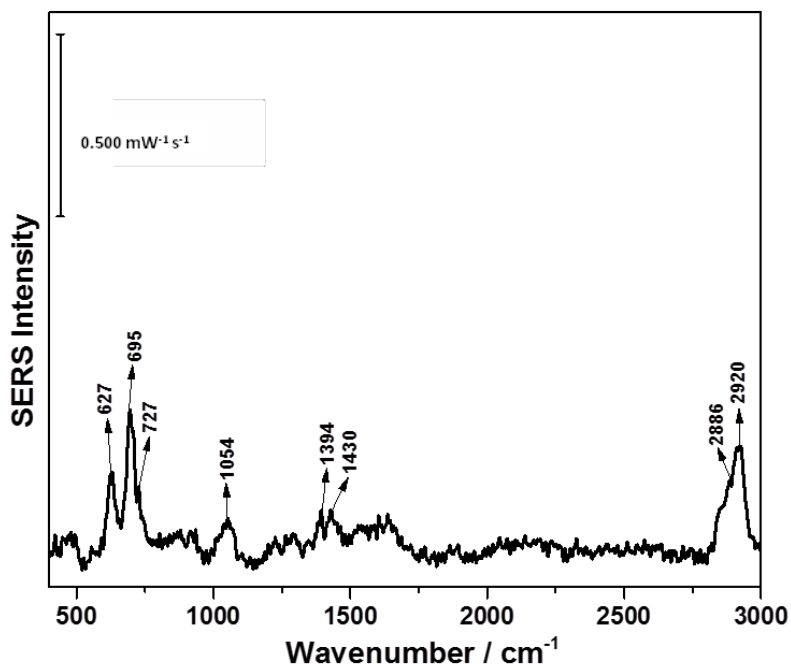
Table A-29: Peak assignment for OCP spectrum of 6-MHA SAM in the presence of 0.1 M NaF solution 1st trial

Wavenumber (cm^{-1})	Assignment	Description	Molecule
627	v(C-S)$_G$	Gauche carbon and sulphur deformation	6-MHA
695	v(C-S)$_T$	Trans carbon and sulphur deformation	6-MHA
727	v(C-S)$_T$	Trans carbon and sulphur deformation	6-MHA
1054	(C-C)$_T$	Trans alkyl chain stretch	6-MHA
1394	v(CO$^-$) v(COO-Ag)	Deprotonated carboxylic group Carboxylic group coordinated to metal	6-MHA 6-MHA
1430	(CH$_2$) COO$^-$	Symmetric deformation Deprotonated carboxylic group	6-MHA 6-MHA
2886	v_s(CH$_2$)	Symmetric stretch alkyl chain	6-MHA
2920	v_{as}(CH$_2$)	Asymmetric stretch alkyl chain	6-MHA

Figure A-30: a) cathodic and b) anodic overlay spectra of 6-MHA SAM in the presence of 0.1M NaF solution, 1st trial

a)

2.50 mW^{-1} s^{-1}

-1.0V
-0.9V
-0.8V
-0.7V
-0.6V
-0.5V
-0.4V
-0.3V
-0.2V
-0.1V
0V
OCP

SERS Intensity

500   1000   1500   2000   2500   3000
Wavenumber / cm^{-1}

b)

2.50 mW^{-1} s^{-1}

OCP
0V
-0.1V
-0.2V
-0.3V
-0.4V
-0.5V
-0.6V
-0.7V
-0.8V
-0.9V
-1.0V

SERS Intensity

500   1000   1500   2000   2500   3000
Wavenumber / cm^{-1}
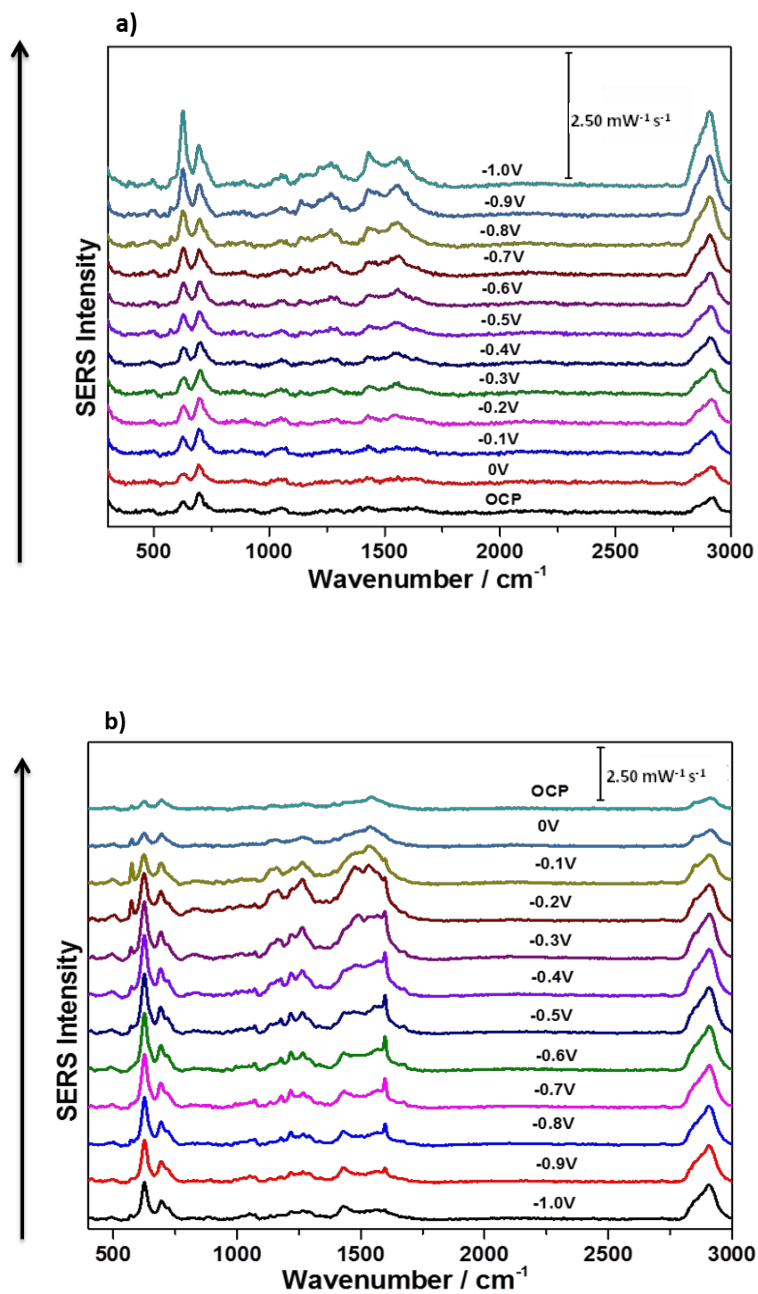
Figure A-31: CV comparison between 6-MHA SAM in the presence of 0.1 M NaF and 0.1 M NaF solution, 1st trial
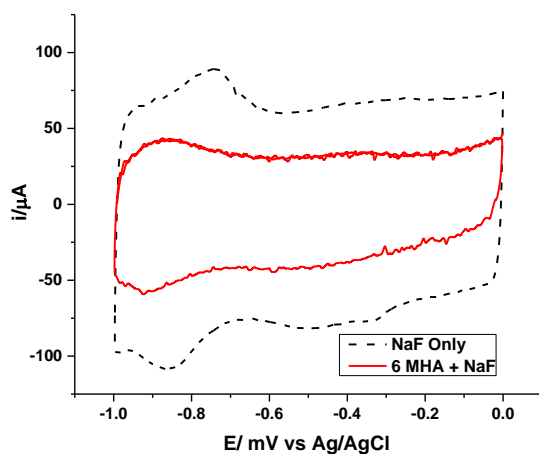
Figure A-32: In air spectrum of 6-MHA SAM, 2nd trial
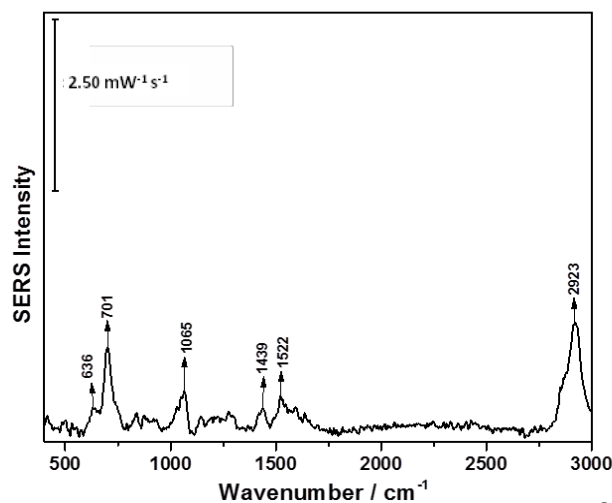
Table A-33: Peak assignment for in air spectrum of 6-MHA, 2nd trial

Wavenumber (cm^{-1})	Assignment	Description	Molecule
636	v(C-S)$_G$	Gauche carbon and sulphur deformation	6-MHA
701	v(C-S)$_T$	Trans carbon and sulphur deformation	6-MHA
1065	v_a(C-C)$_T$	Asymmetric trans alkyl chain stretch	6-MHA
1439	(CH$_2$) COO$^-$	Symmetric deformation Deprotonated carboxylic group	6-MHA 6-MHA
1522	v_{as}(COO$_2^-$)	Asymmetric stretch of vibration	6-MHA
2923	v_{as}(CH$_2$)	Asymmetric stretch alkyl chain	6-MHA

Figure A-34: OCP spectrum of 6-MHA SAM in the presence of 0.1M NaF solution, 2nd trial
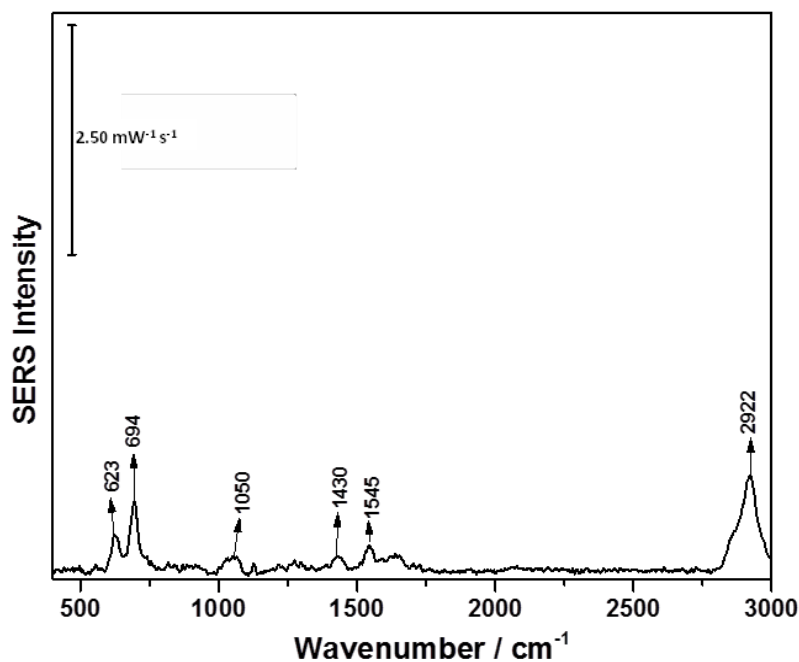
Table A-35: Peak assignment for OCP spectrum of 6-MHA SAM in the presence of 0.1M NaF solution, 2nd trial

Wavenumber (cm^{-1})	Assignment	Description	Molecule
623	v(C-S)$_G$	Gauche carbon and sulphur deformation	6-MHA
694	v(C-S)$_T$	Trans carbon and sulphur deformation	6-MHA
1050	(C-C)$_T$	Trans alkyl chain stretch	6-MHA
1430	(CH$_2$) COO$^-$	Symmetric deformation Deprotonated carboxylic group interacting with positive species	6-MHA 6-MHA
1545	v_{as}(COO$_2^-$)	Asymmetric stretch of vibration	6-MHA
2922	v_{as}(CH$_2$)	Asymmetric stretch alkyl chain	6-MHA

Figure A-36: a) cathodic and b) anodic overlay spectra of 6-MHA SAM in the presence of 0.1M NaF solution, 2nd trial
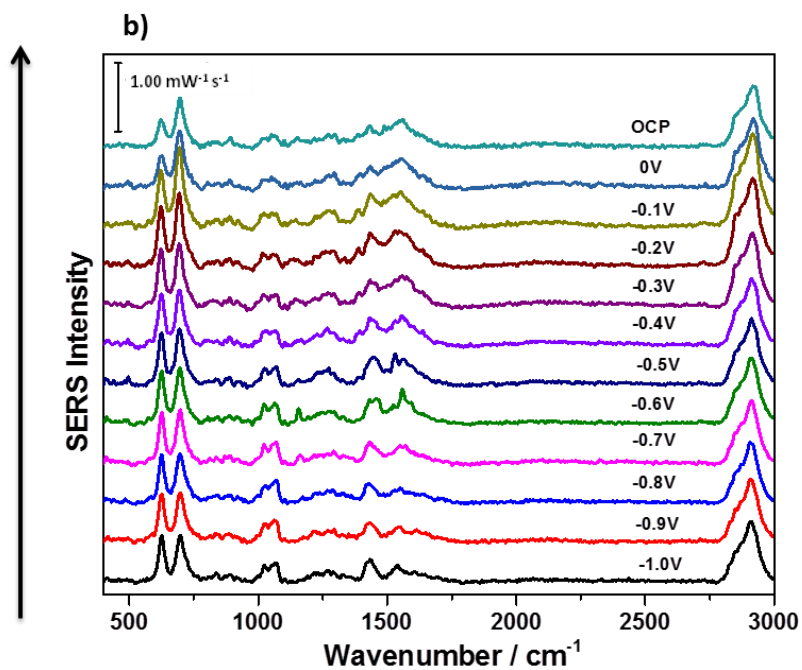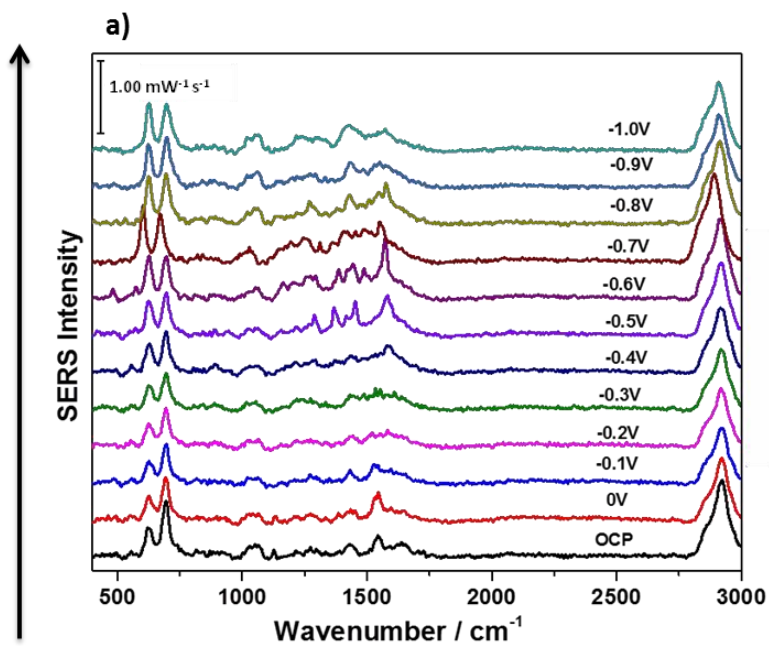
Figure A-37: CV comparison between 6-MHA SAM in the presence of 0.1M NaF solution and 0.1M NaF solution, 2nd trial
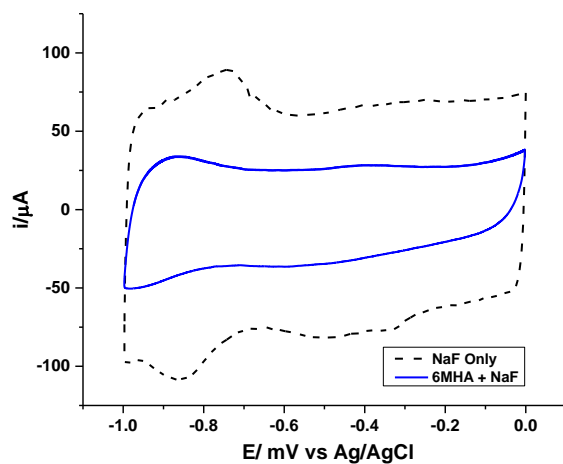
Figure A-38: In air spectrum of 6-MHA SAM, 3rd trial
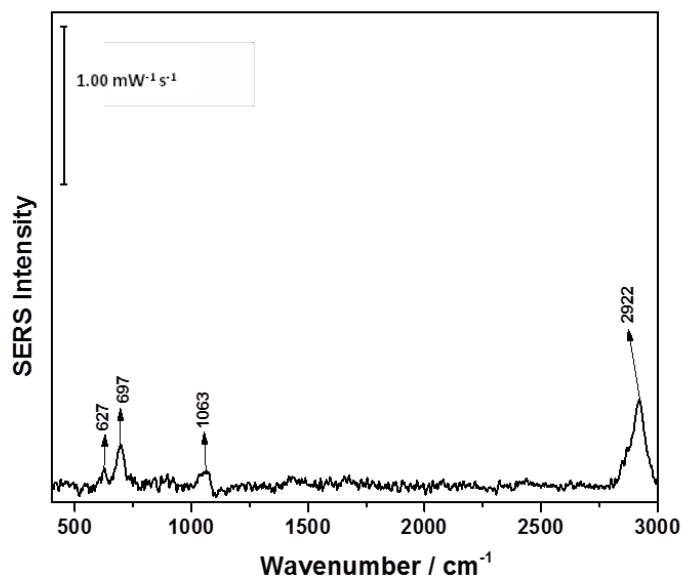
Table A-39: Peak assignment for in air spectrum of 6-MHA SAM, 3rd trial

Wavenumber (cm^{-1})	Assignment	Description	Molecule
626	v(C-S)$_G$	Gauche carbon and sulphur deformation	6-MHA
697	v(C-S)$_T$	Trans carbon and sulphur deformation	6-MHA
1063	v_a(C-C)$_T$	Asymmetric trans alkyl chain stretch	6-MHA
2922	v_{as}(CH$_2$)	Asymmetric stretch alkyl chain	6-MHA

Table A-40: Peak assignment for OCP spectrum of 6-MHA SAM in the presence of 0.1M NaF solution, 3rd trial

Wavenumber (cm^{-1})	Assignment	Description	Molecule
626	v(C-S)$_G$	Gauche carbon and sulphur deformation	6-MHA
693	v(C-S)$_T$	trans carbon and sulphur deformation	6-MHA
998		Deprotonated carboxylic vibration	6-MHA
1164	C-C	Skeletal straight chain vibration	6-MHA
1198	CH$_2$	wagging	6-MHA
1282	ω(CH$_2$)	Wagging vibration	6-MHA
1551	v_{as}(COO$_2^-$)	Asymmetric stretch of vibration	6-MHA
1590	COO$^-$ C=O	Deprotonated carboxylic group Presence of a carbonyl	6-MHA 6-MHA
2916	v_{as}(CH$_2$)	Asymmetric stretch alkyl chain	6-MHA

Figure A-41: CV comparison between 6-MHA SAM in the presence of 0.1M NaF solution and 0.1M NaF solution 3rd trial
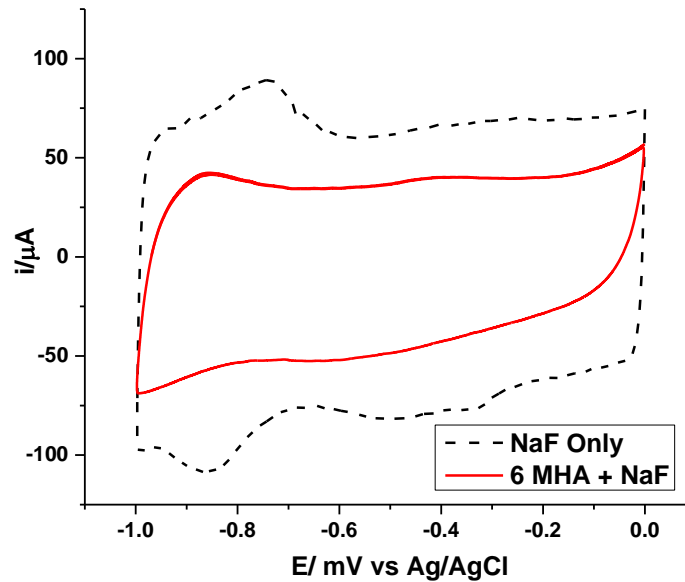
Figure A-42: OCP spectrum of 1mM dAMP/0.1 M NaF solution with AgNP modified electrode, 1st trial
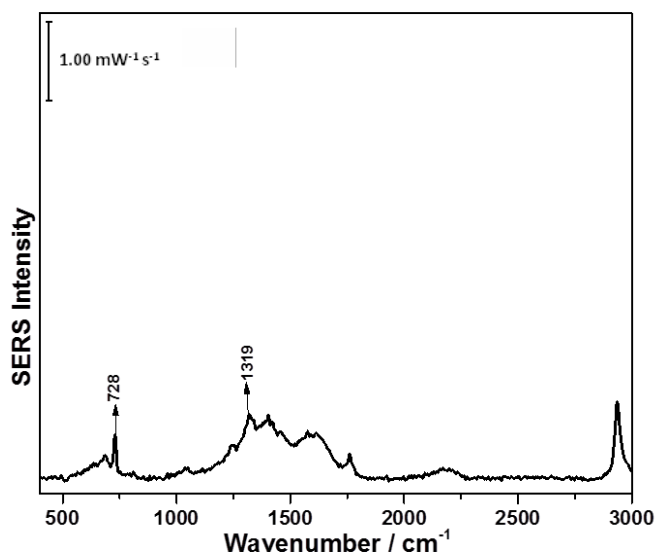
Figure A-43: Anodic overlay spectra of 1mM dAMP/0.1 M NaF solution with AgNP modified electrode, 1st trial
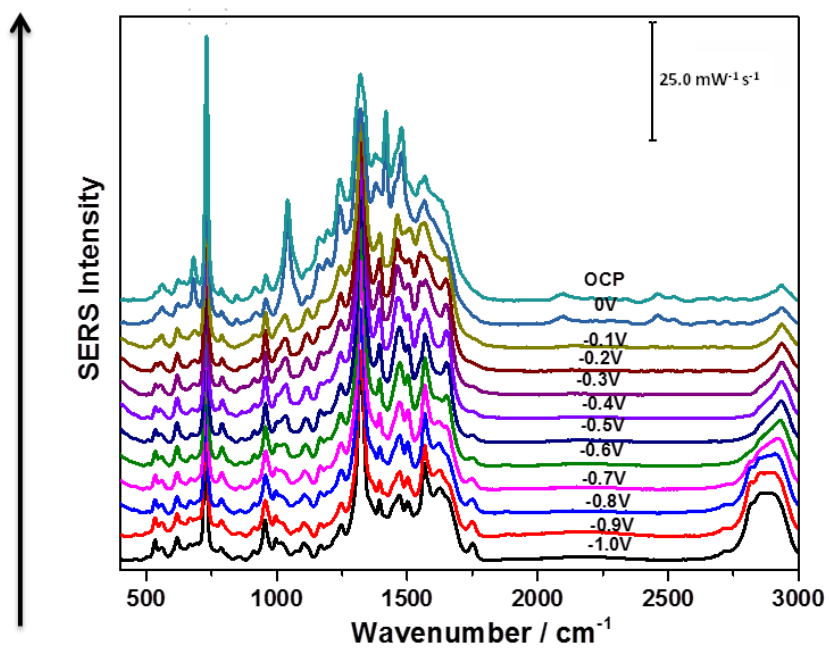
Figure A-44: CV comparison between 1mM dAMP/0.1 M NaF solution and 0.1M NaF solution, 1st trial
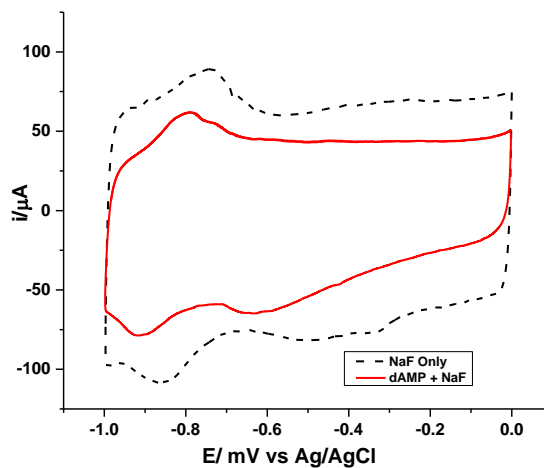
Figure A-45: OCP spectrum of 1mM dAMP/0.1 M NaF solution with AgNP modified electrode, 2nd trial
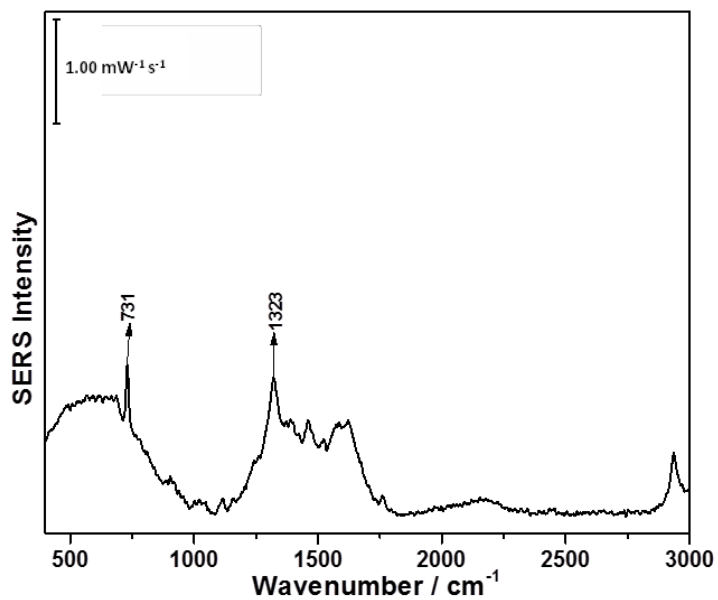
Figure A-46: a) cathodic and b) anodic overlay spectra of 1mM dAMP/0.1 M NaF solution with AgNP modified electrode, 2nd trial
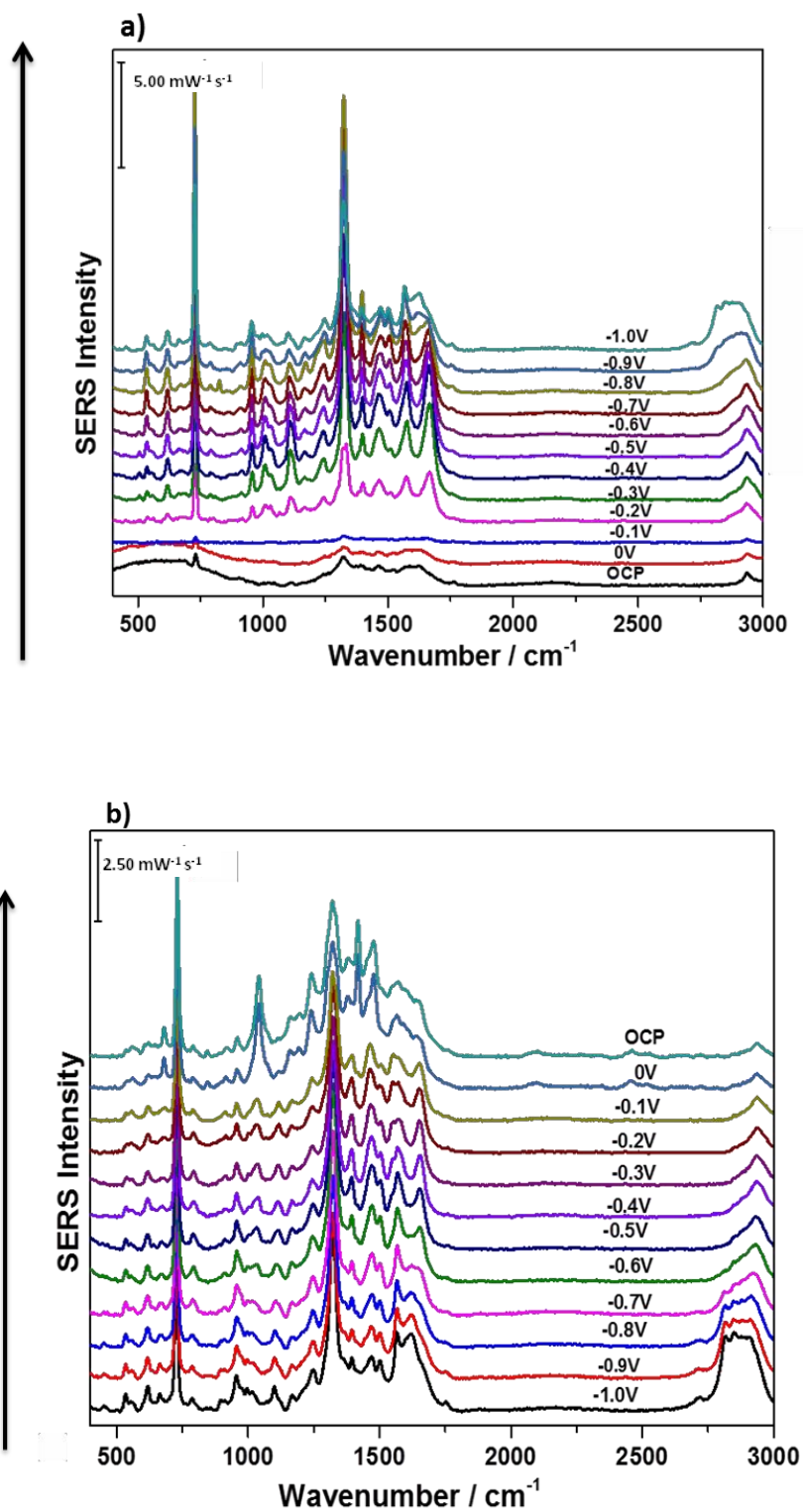
Figure A-47: CV comparison between 1mM dAMP/0.1 M NaF solution and 0.1 M NaF solution, 2nd trial
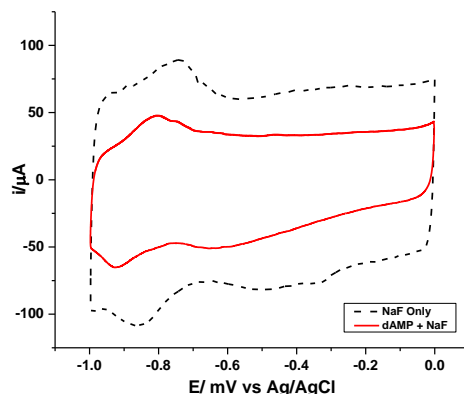
Figure A-48: OCP spectrum of 1mM dAMP/0.1 M NaF solution in the presence of 6-MHA SAM, 1st trial
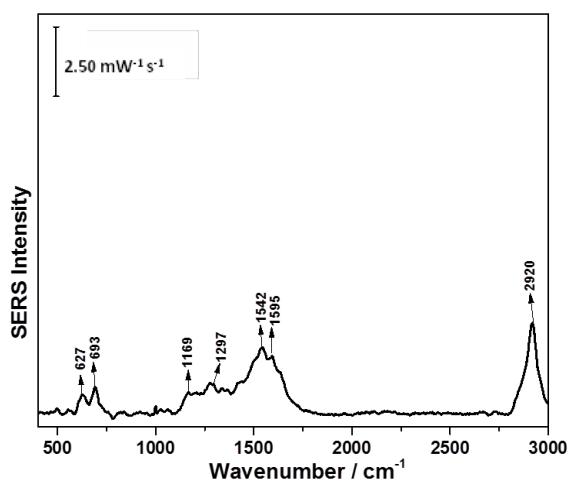
Table A-49: Peak assignment for OCP spectrum of 1mM dAMP/0.1 M NaF solution in the presence of 6-MHA SAM, 1st trial

Wavenumber (cm^{-1})	Assignment	Description	Molecule
627	v(C-S)$_G$	Gauche carbon and sulphur deformation	6-MHA
693	v(C-S)$_T$	trans carbon and sulphur deformation	6-MHA
1169	C-C	Skeletal straight chain vibration	6-MHA
1297	CH$_2$	Methylene bending	6-MHA
1542	v_{as}(COO$_2^-$)	Asymmetric stretch of vibration	6-MHA
1595	COO$^-$	Deprotonated carboxylic group	6-MHA
	C=O	Presence of a carbonyl	6-MHA
2920	v_{as}(CH$_2$)	Asymmetric stretch alkyl chain	6-MHA

Figure A-50: CV comparison between 1mM dAMP/0.1 M NaF solution in the presence of 6-MHA SAM and 0.1 M NaF solution, 1st trial
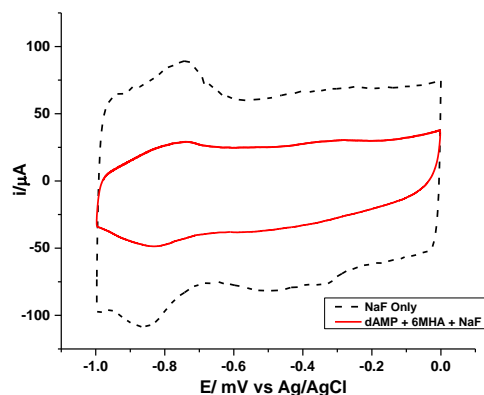
Figure A-51: OCP spectrum of 1mM dAMP/0.1 M NaF solution in the presence of 6-MHA SAM, 2nd trial
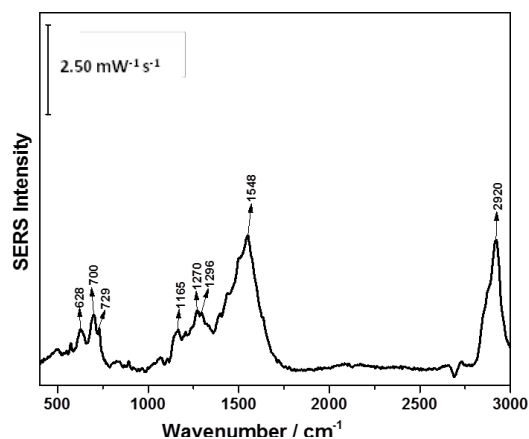
Table A-52: Peak assignment for OCP spectrum of 1mM dAMP/0.1 M NaF solution in the presence of 6-MHA SAM, 2nd trial

Wavenumber (cm^{-1})	Assignment	Description	Molecule
628	v(C-S)$_G$	Gauche carbon and sulphur deformation	6-MHA
700	v(C-S)$_T$	trans carbon and sulphur deformation	6-MHA
729		Ring breathing	dAMP
1165	C-C	Skeletal straight chain vibration	6-MHA
1270		Unassigned peak	6-MHA
1296	CH$_2$	Methylene bending	6-MHA
1548	v_{as}(COO$_2^-$)	Asymmetric stretch of vibration	6-MHA
2920	v_{as}(CH$_2$)	Asymmetric stretch alkyl chain	6-MHA

Figure A-53: a) cathodic and b) anodic overlay spectra of 1mM dAMP/0.1 M NaF solution in the presence of 6-MHA SAM, 2nd trial
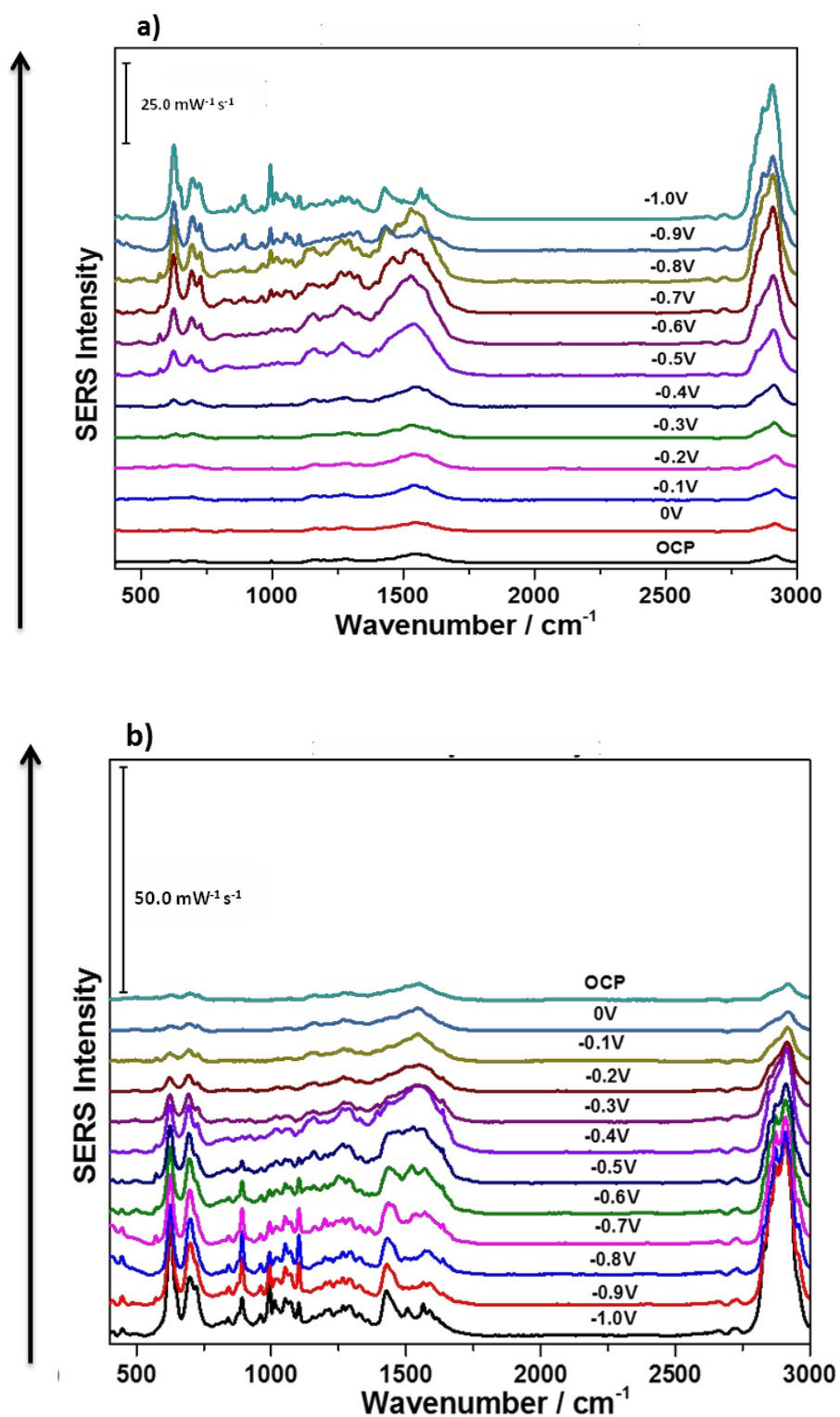
Figure A-54: CV comparison between 1mM dAMP/0.1 M NaF solution in the presence of 6-MHA SAM and 0.1 M NaF solution, 2nd trial
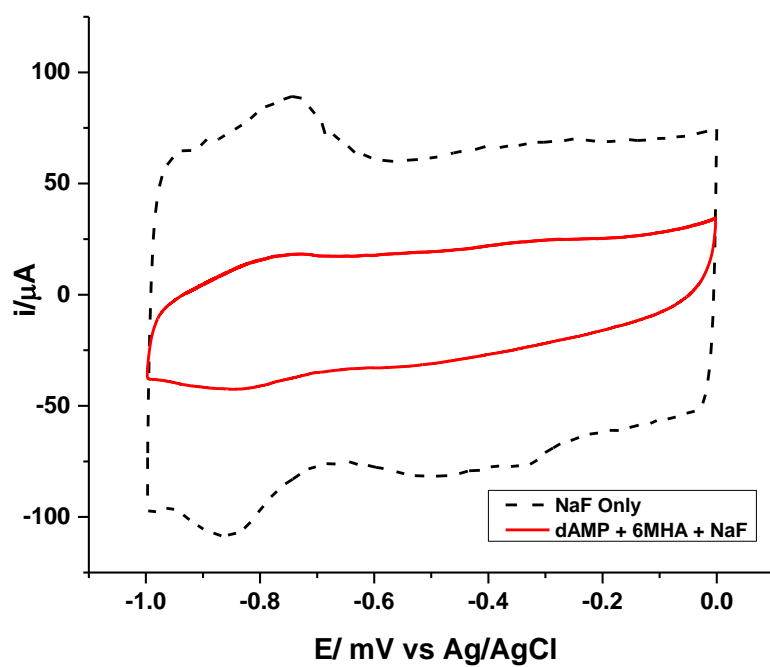
Figure A-55: OCP spectrum of 1mM dAMP/0.1 M NaF solution in the presence of 6-MHA SAM, 3rd trial
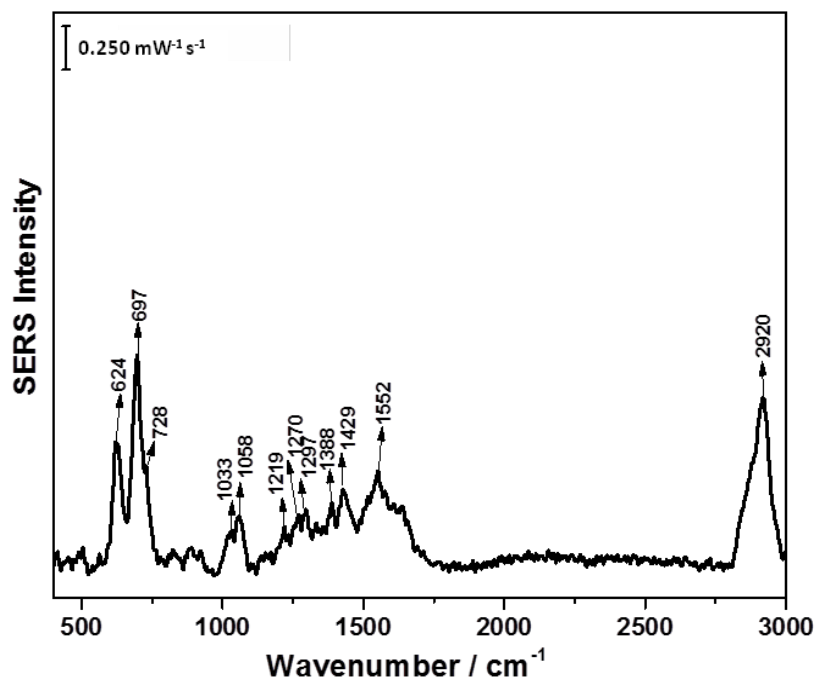
Table A-56: Peak assignment for OCP spectrum of 1mM dAMP/0.1 M NaF solution in the presence of 6-MHA SAM, 3rd trial

| Wavenumber (cm^{-1})	Assignment	Description	Molecule
624	v(C-S)$_G$	Gauche carbon and sulphur deformation	6-MHA
697	v(C-S)$_T$	trans carbon and sulphur deformation	6-MHA
728	P-O-C	Ring breathing vibration	dAMP
1033	C-C	Straight chain alkane stretch	6-MHA
1058	(C-C)$_T$	Trans alkyl chain stretch	6-MHA
1219	ω(CH$_2$)	Wagging vibration	6-MHA
1270		Unassigned 6-MHA SAM peak	6-MHA
1297	ω(CH$_2$)	Wagging vibration	6-MHA
1388	COOH	Non-dissociated carboxylic group vibration	6-MHA
1429	(CH$_2$) COO$^-$	Symmetric deformation Deprotonated carboxylic group vibration	6-MHA 6-MHA
1552	v_{as}(COO$_2^-$)	Asymmetric stretch of vibration	6-MHA
2920	v_{as}(CH$_2$)	Asymmetric stretch alkyl chain	6-MHA

Figure A-57: a) cathodic and b) anodic overlay spectra of 1mM dAMP/0.1 M NaF solution in the presence of 6-MHA SAM, 3rd trial
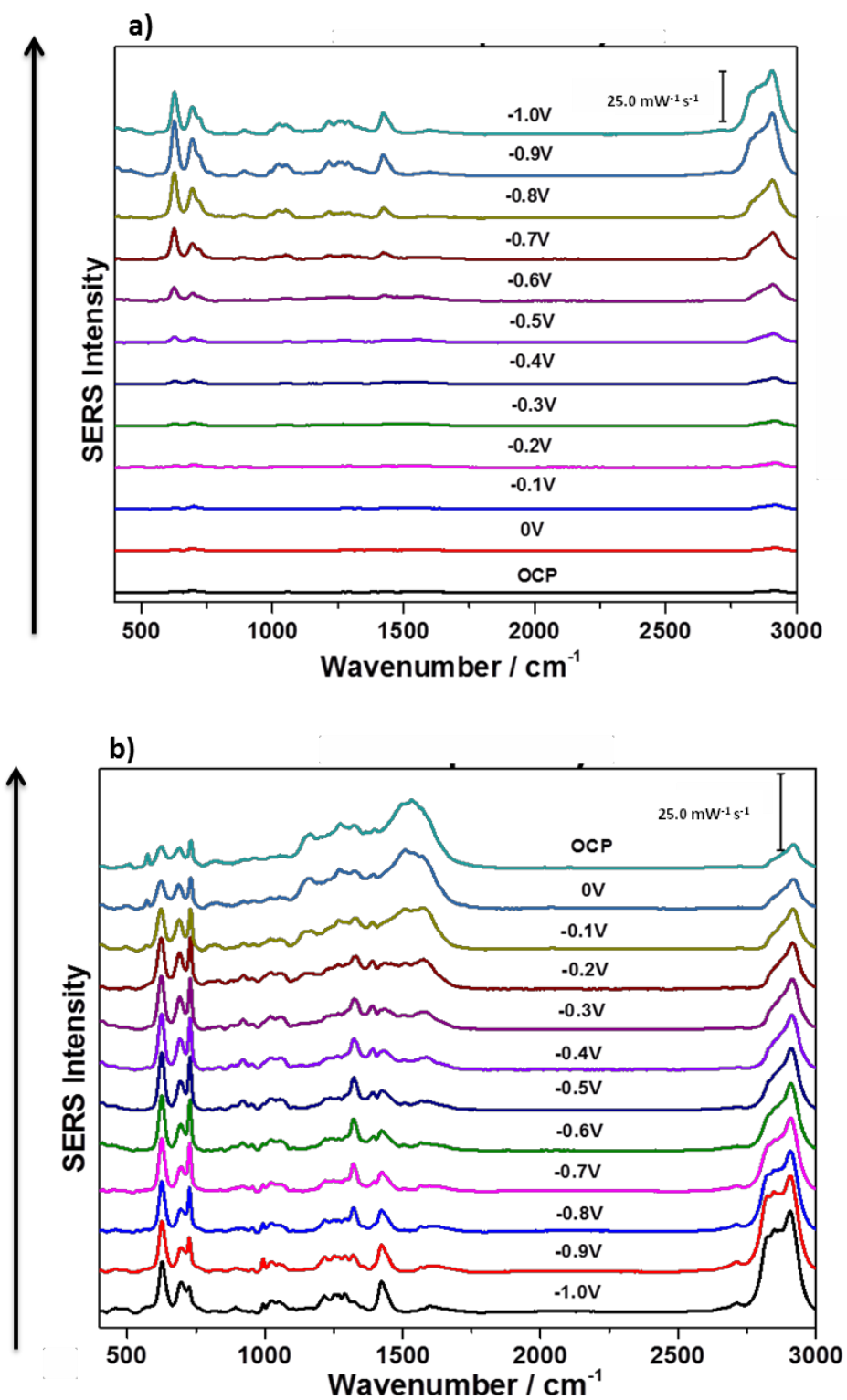
Figure A-58: CV comparison between 1mM dAMP/0.1 M NaF solution in the presence of 6-MHA SAM and 0.1 M NaF solution, 3rd trial
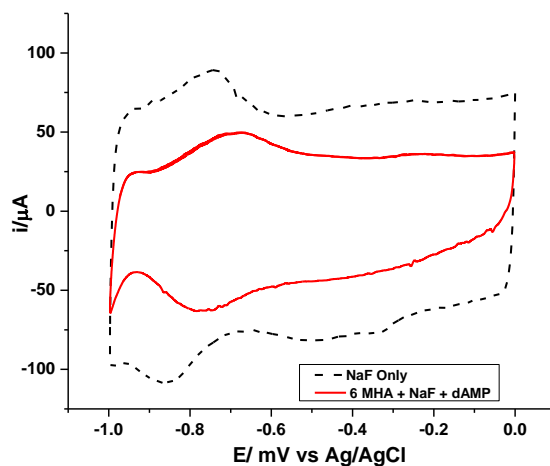
Figure A-59: In air spectrum of deposited DMPC/cholesterol (70:30) bilayer onto 6-MHA SAM, 1st trial
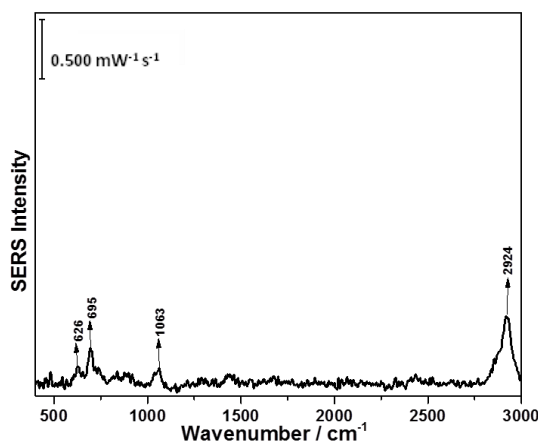
Table A-60: Peak assignment for in air spectrum of deposited DMPC/cholesterol (70:30) bilayer on 6-MHA SAM AgNP modified electrode, 1st trial

Wavenumber (cm^{-1})	Assignment	Description	Molecule
626	v(C-S)$_G$	Gauche carbon and sulphur deformation	6-MHA
695	v(C-S)$_T$	trans carbon and sulphur deformation	6-MHA
1063	v_{as}(PO$_2^-$)	Phosphate diester asymmetric stretch	DMPC
	(C-C)$_T$	Alkyl chain stretch	6-MHA
2924	v_{as}(CH$_2$)	Asymmetric stretch of alkyl chain	6- MHA/DMPC

Figure A-61: OCP spectrum of deposited DMPC/cholesterol (70:30) bilayer onto 6-MHA SAM in the presence of 1mM dAMP/0.1 M NaF solution, 1st trial
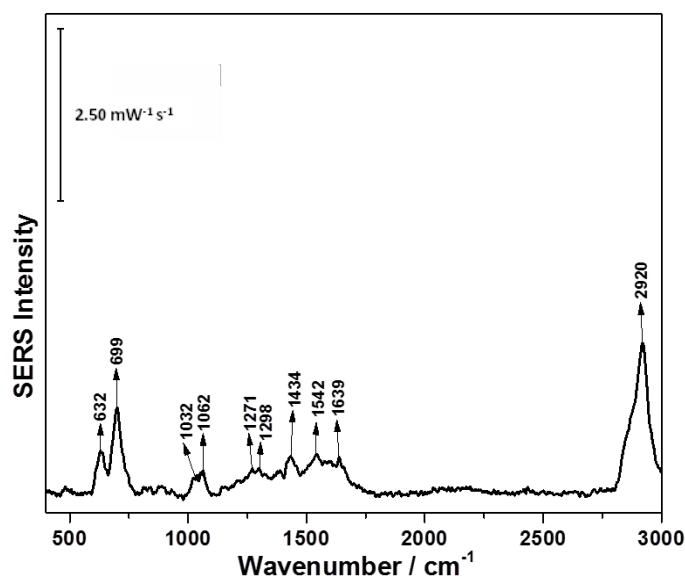
Table A-62: Peak assignment for OCP spectrum of deposited DMPC/cholesterol (70:30) bilayer on 6-MHA SAM AgNP modified electrode in the presence of 1mM dAMP/0.1 M NaF solution, 1st trial

Wavenumber (cm^{-1})	Assignment	Description	Molecule
632	v(C-S)$_G$	Gauche carbon and sulphur deformation	6-MHA
699	v(C-S)$_T$	trans carbon and sulphur deformation	6-MHA
1032	C-C CH$_2$CH$_3$	Alkyl chain stretch Bending of lipids	6-MHA DMPC
1062	v_{as}(PO$_2^-$) (C-C)$_T$	Phosphate diester asymmetric stretch Alkyl chain stretch	DMPC 6-MHA
1271		Presence of a phospholipid Unassigned 6-MHA monolayer peak	DMPC 6-MHA
1298	ω(CH$_2$)	Wagging vibration	6-MHA
1434	(CH$_2$) COO$^-$ δ$_d$(-CH$_2$)	Symmetric deformation Deprotonated carboxylic deformation for cholesterol	6-MHA/DMPC 6-MHA cholesterol
1542	v_{as}(COO$_2^-$)	Asymmetric stretch of vibration	6-MHA
1639	O-H C=O	Intermolecular bending mode Presence of a carbonyl	water 6-MHA
2920	v_{as}(CH$_2$)	Asymmetric stretch alkyl chain	6-MHA/DMPC

Figure A-63: CV comparison between DMPC/cholesterol (70:30) bilayer deposited on 6-MHA SAM AgNP modified electrode in the presence of 1mM dAMP/ 0.1 M NaF solution and 0.1 M NaF solution, 1st trial
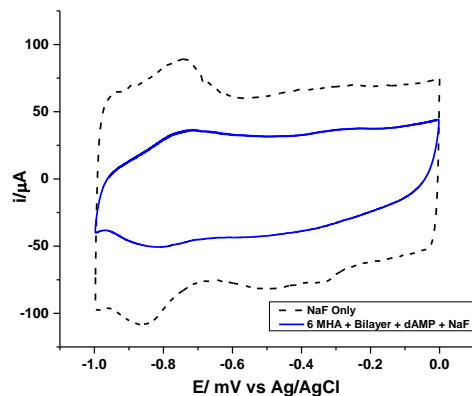
Figure A-64: In air spectrum of deposited DMPC/cholesterol (70:30) bilayer onto 6-MHA SAM, 2nd trial
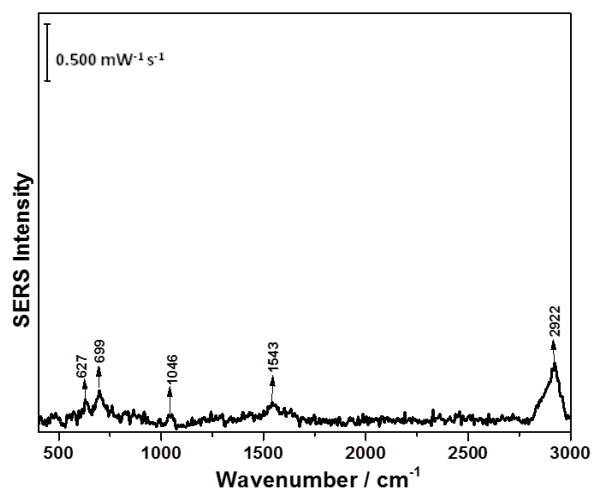
Table A-65: Peak assignment for in air spectrum of deposited DMPC/cholesterol (70:30) lipid bilayer on 6-MHA SAM AgNP modified, 2nd trial

Wavenumber (cm^{-1})	Assignment	Description	Molecule
627	v(C-S)$_G$	Gauche carbon and sulphur deformation	6-MHA
699	v(C-S)$_T$	trans carbon and sulphur deformation	6-MHA
1046	(C-C)$_T$	Trans alkyl chain stretch	6-MHA
1543	v_{as}(COO$^-$)	Asymmetric stretch of a carboxylic group	6-MHA
2922	v_{as}(CH$_2$)	Asymmetric stretch of alkyl chain	6-MHA/DMPC

Figure A-66: OCP spectrum of deposited DMPC/cholesterol (70:30) bilayer onto 6-MHA SAM in the presence of 1mM dAMP/0.1 M NaF solution, 2nd trial
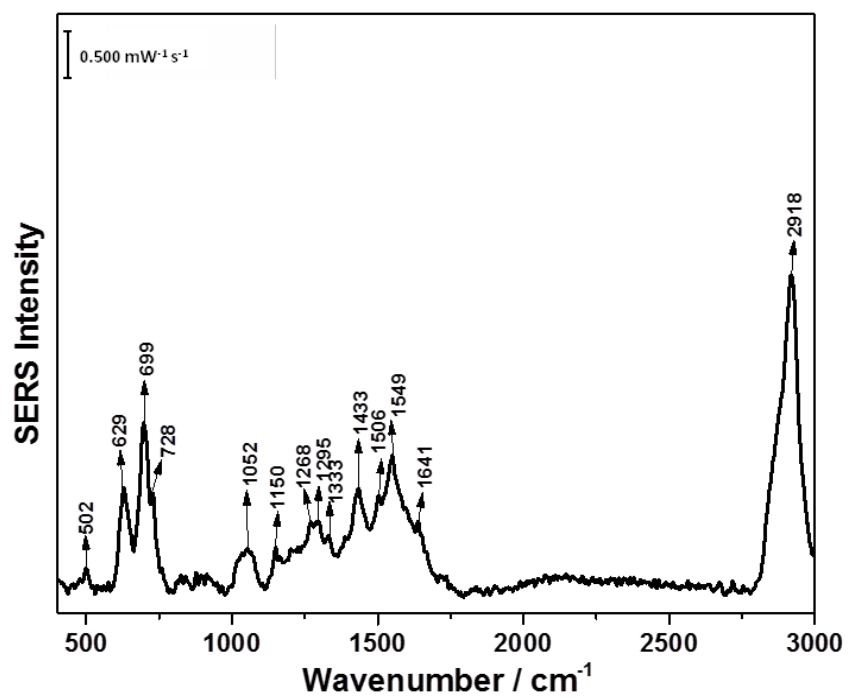
Table A-67: Peak assignment for OCP spectrum of deposited DMPC/cholesterol (70:30) lipid bilayer on 6-MHA SAM AgNP modified electrode in the presence of 1mM dAMP/0.1 M NaF solution, 2nd trial

Wavenumber (cm^{-1})	Assignment	Description	Molecule
502	-C-C-C-	Straight chain alkyl vibration	6-MHA
629	vC-S)$_G$	Gauche stretch vibration	6-MHA
699	v(C-S)$_T$	Trans carbon and sulphur deformation	6-MHA
728	v(C-S)$_T$	Possible trans carbon and sulphur deformation	6-MHA
1052	v_{as}(PO$_2^-$) (C-C)$_T$	Phosphate diester asymmetric stretch Alkyl chain stretch	DMPC 6-MHA
1150	C-C	Skeletal straight chain vibration for alkanes	6-MHA
1268		Presence of a phospholipid Unassigned 6-MHA monolayer peak	DMPC 6-MHA
1295	ω(CH$_2$)	Wagging vibration	6-MHA
1333	ω(CH$_2$)	Wagging for phospholipids or 6-MHA	6-MHA/DMPC
1433	(CH$_2$) COO$^-$ δ$_d$(-CH$_2$)	Symmetric deformation Deprotonated carboxylic deformation for cholesterol	6-MHA/DMPC 6-MHA cholesterol
1506	COO$^-$	deformation of a carboxylic group,	6-MHA
1549	v_{as}(COO$_2^-$)	Asymmetric stretch vibration	6-MHA
1641	O-H C=O	Intermolecular bending mode Presence of a carbonyl	water 6-MHA
2918	v_{as}(CH$_2$)	Asymmetric stretch alkyl chain	6-MHA/DMPC

Figure A-68: a) cathodic and b) anodic overlay spectra of deposited DMPC/cholesterol (70:30) bilayer on 6-MHA SAM AgNP modified electrode in the presence of 1mM dAMP/0.1 M NaF solution, 2nd trial
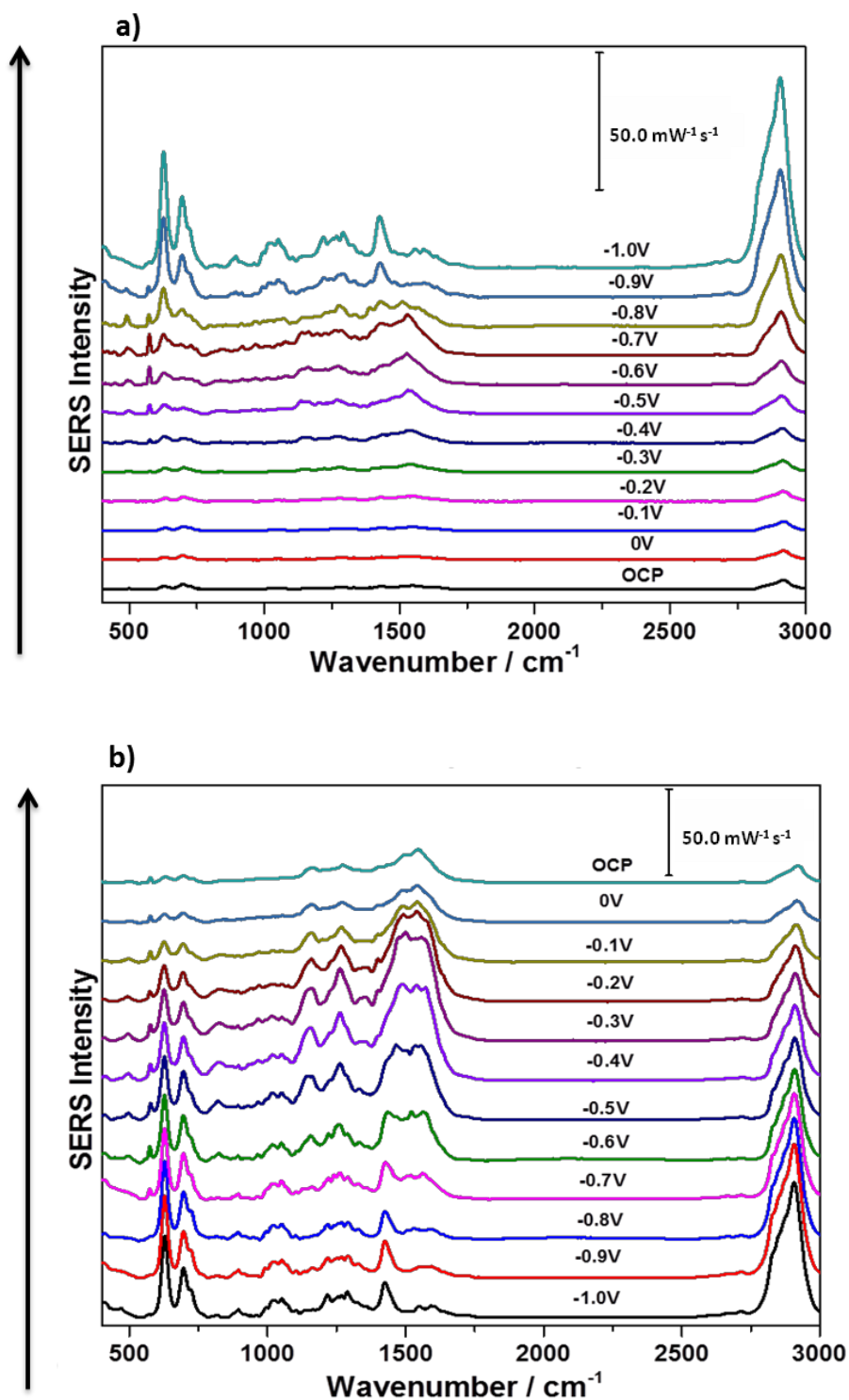
Figure A-69: CV comparison between deposited DMPC/cholesterol (70:30) bilayer on 6-MHA SAM AgNP modified electrode in the presence of 1mM dAMP/ 0.1 M NaF solution and 0.1M NaF solution, 2nd trial
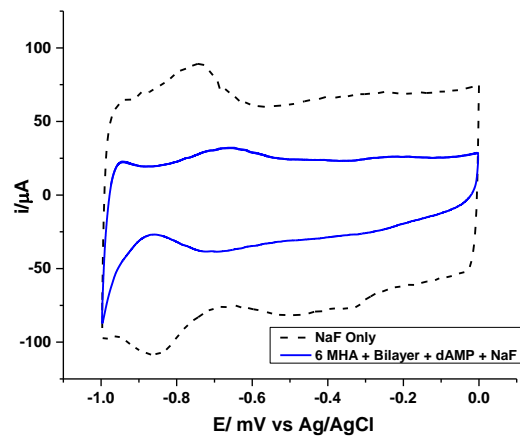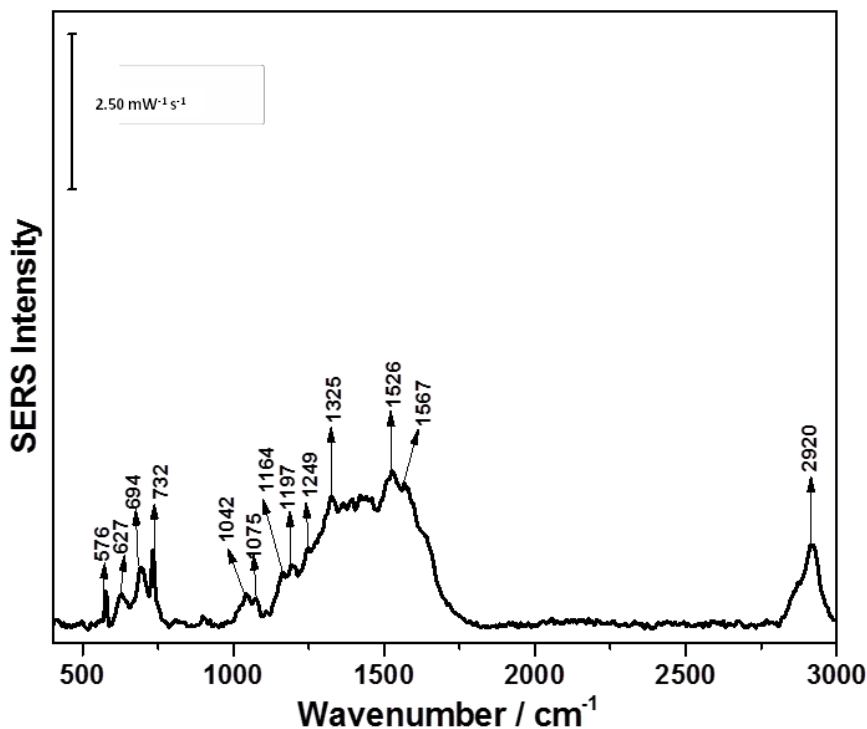

Figure A-70: In air spectrum of deposited DMPC/cholesterol (70:30) bilayer onto 6-MHA SAM, 3rd trial
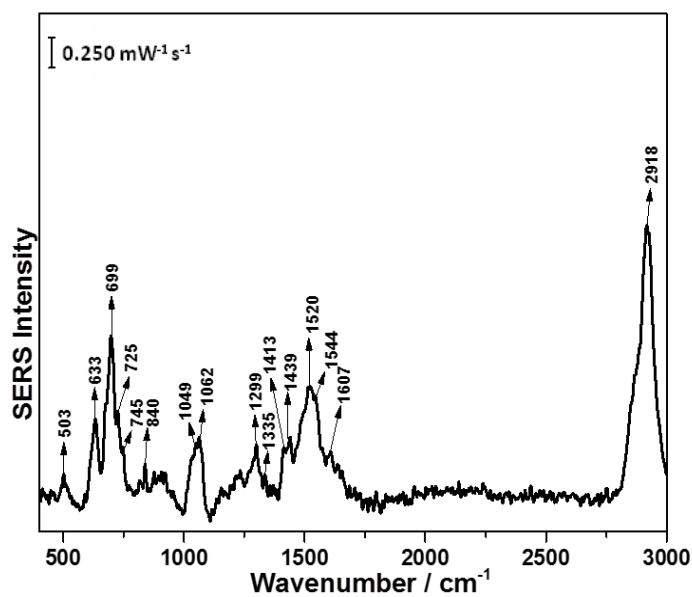
Table A-71: Peak assignment for in air spectrum of deposited DMPC/cholesterol (70:30) bilayer on 6-MHA SAM AgNP modified, 3rd trial

Wavenumber (cm^{-1})	Assignment	Description	Molecule
503	-C-C-C-	Straight chain alkyl vibration	6-MHA
633	v C-S)$_G$	Gauche stretch vibration	6-MHA
699	v(C-S)$_T$	trans carbon and sulphur deformation	6-MHA
725	v(C-S)$_T$	trans carbon and sulphur deformation	6-MHA
745	v(C-S)$_T$	trans carbon and sulphur deformation	6-MHA
840	-C-C-C-	Straight chain alkyl vibration	6-MHA
1049	(C-C)$_T$	Trans alkyl chain stretch	6-MHA/DMPC
1062	v_{as}(PO$_2^-$)	Phosphate diester asymmetric stretch	DMPC
	(C-C)$_T$	Alkyl chain stretch	6-MHA
1299	ω(CH$_2$)	Wagging vibration	6-MHA
1335	ω(CH$_2$)	Wagging for lipids or 6-MHA	6-MHA/DMPC
		Presences of phospholipids	DMPC
1413	(CH$_2$)	Stretch of lipids	DMPC
1439	(CH$_2$)	Symmetric deformation	6-MHA/DMPC
	COO$^-$	Carboxylic group vibration	6-MHA
	δ_d(-CH$_2$)	Deformation for cholesterol	cholesterol
1520	v_{as}(COO$_2^-$)	Asymmetric stretch of vibration	6-MHA
1544	v_{as} (COO$_2^-$)	Asymmetric stretch of vibration	6-MHA
1607	C=C	Presence of a double bond	cholesterol
	C=O	Presence of a carbonyl group	6-MHA
2920	v_{as}(CH$_2$)	Asymmetric stretch alkyl chain	6-MHA/DMPC

Figure A-72: OCP spectrum of deposited DMPC/cholesterol (70:30) bilayer onto 6-MHA SAM in the presence of 1mM dAMP/0.1 M NaF solution, 3rd trial
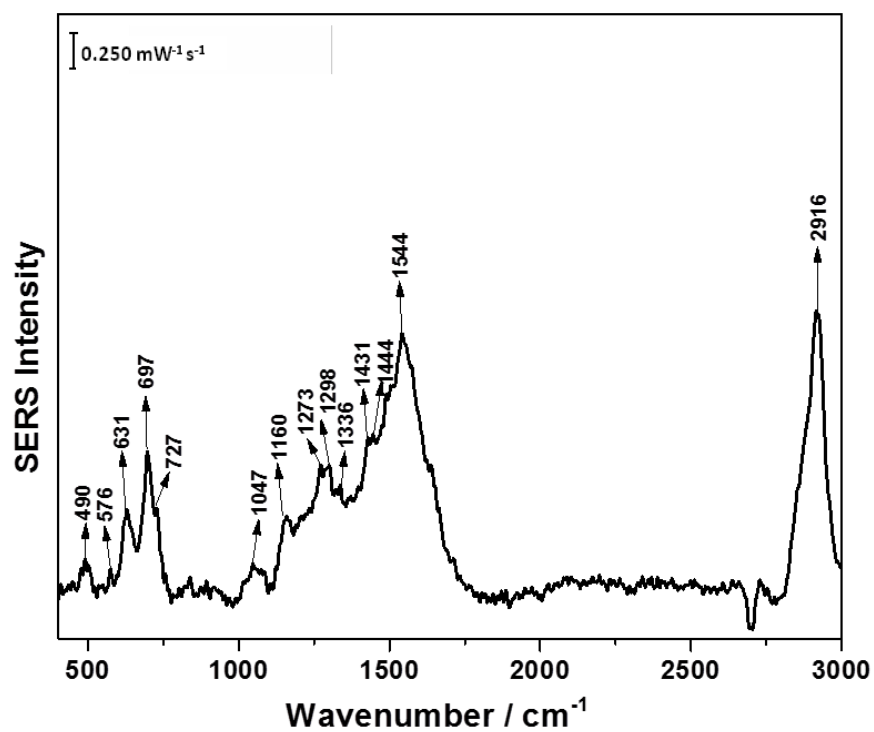
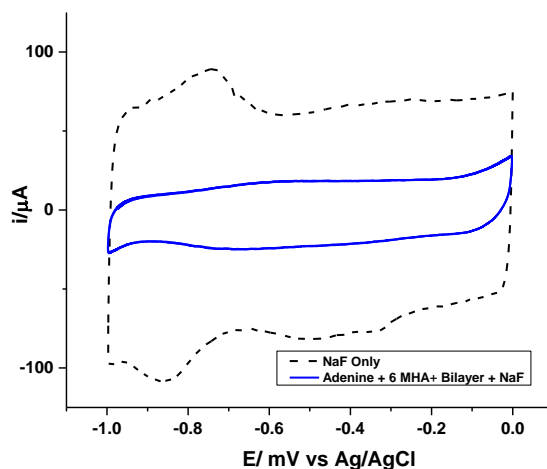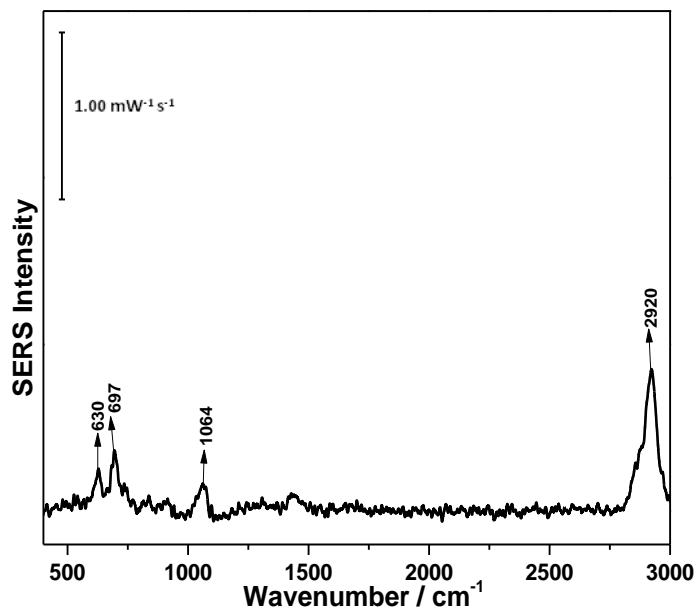**Table A-73: Peak assignment for OCP spectrum of deposited DMPC/cholesterol (70:30) bilayer on 6-MHA SAM AgNP modified electrode in the presence of 1mM dAMP/0.1 M NaF solution, 3rd trial**

Wavenumber (cm^{-1})	Assignment	Description	Molecule
490	-C-C-C-	Straight chain alkyl vibration	6-MHA
576	COO$^-$	Carboxylic deformation	6-MHA
631	v (C-S)$_G$	Gauche vibration stretch of alkanethiol	6-MHA
697	v(C-S)$_T$	trans carbon and sulphur deformation	6-MHA
727	v(C-S)$_T$	Possible trans carbon and sulphur deformation	6-MHA
1047	(C-C)$_T$	Trans alkyl chain stretch	6-MHA/DMPC
1160	C-O C-C	Ester asymmetric stretch Skeletal straight chain vibration	DMPC 6-MHA
1273		Unassigned peak in 6-MHA	6-MHA
1298	ω(CH$_2$)	Wagging vibration	6-MHA
1336	ω(CH$_2$)	Possible H bending + ring stretch Wagging for lipids or 6-MHA Presences of phospholipids	dAMP 6-MHA/DMPC DMPC
1431	(CH$_2$) COO$^-$ δ$_d$(-CH$_2$)	Symmetric deformation Deprotonated carboxylic vibration deformation for cholesterol	6-MHA/DMPC 6-MHA cholesterol
1444	(CH$_2$) δ$_d$(-CH$_2$)	Symmetric deformation deformation for cholesterol	6-MHA/DMPC cholesterol
1544	v_{as} (COO$_2^-$)	Asymmetric stretch vibration	6-MHA
2920	v_{as}(CH$_2$)	Asymmetric stretch alkyl chain	6-MHA/DMPC

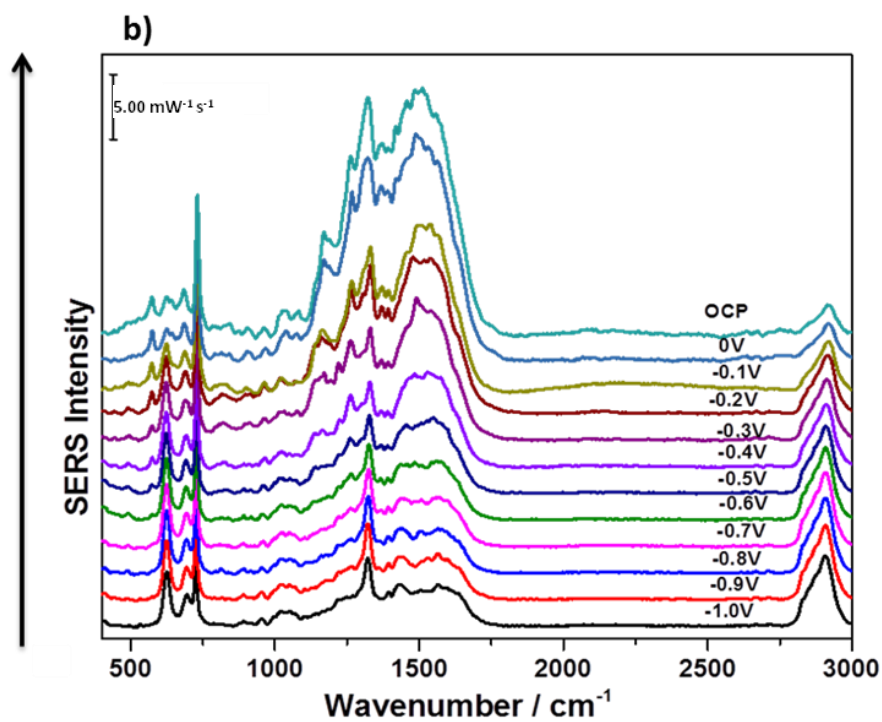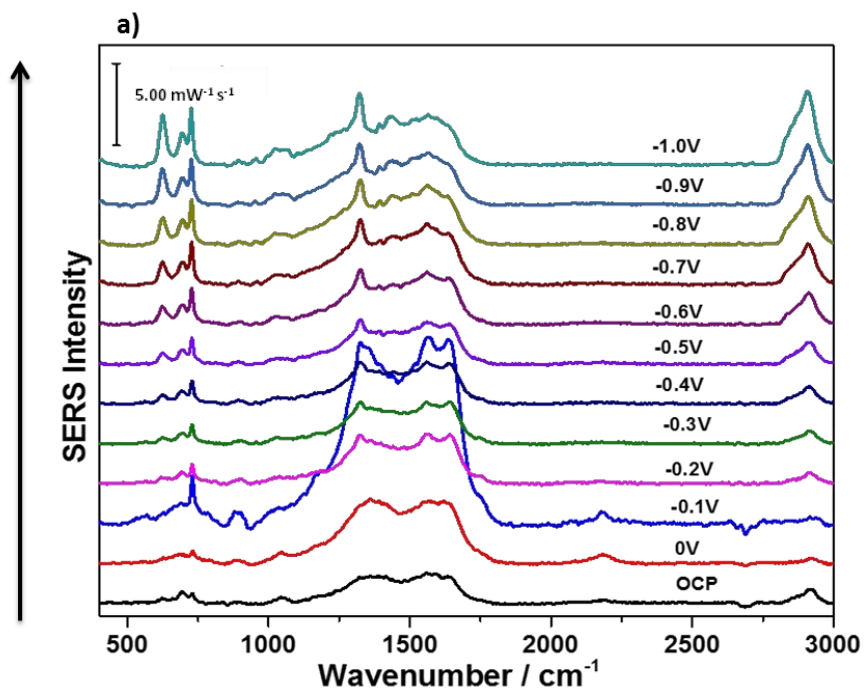**Figure A-74: a) cathodic and b) anodic overlay spectra of deposited DMPC/cholesterol (70:30) bilayer on 6-MHA SAM AgNP modified electrode in the presence of 1mM dAMP/0.1 M NaF solution, 3rd trial**
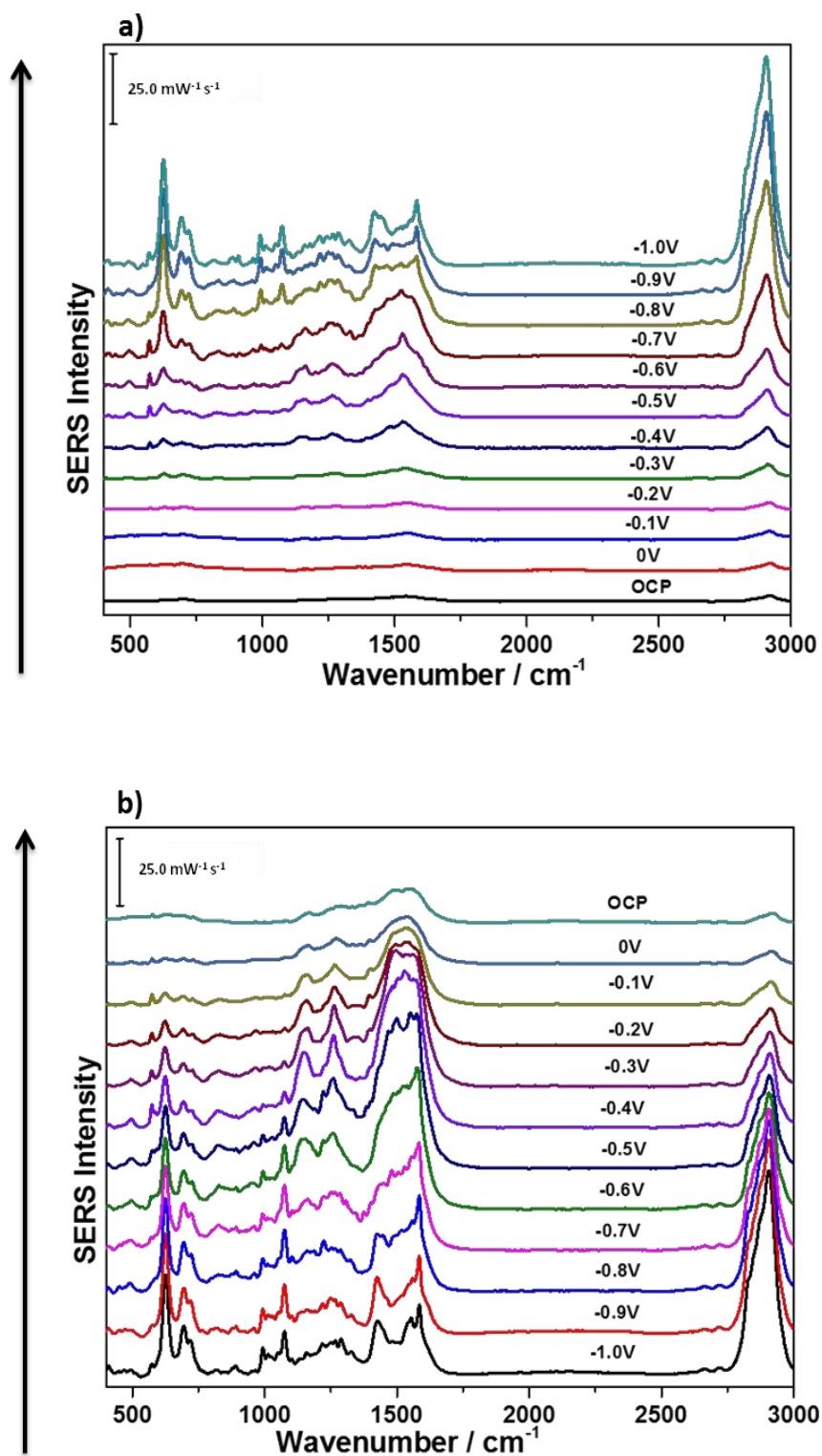
Figure A-75: CV comparison between deposited DMPC/cholesterol (70:30) bilayer onto 6-MHA in the presence of 1mM dAMP/0.1 M NaF solution and 0.1 M NaF solution, 3rd trial
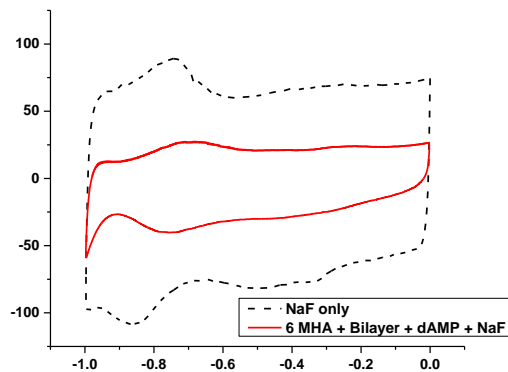
Figure A-76: OCP spectrum of 1mM adenine/0.1 M NaF solution with AgNP modified electrode, 1st trial
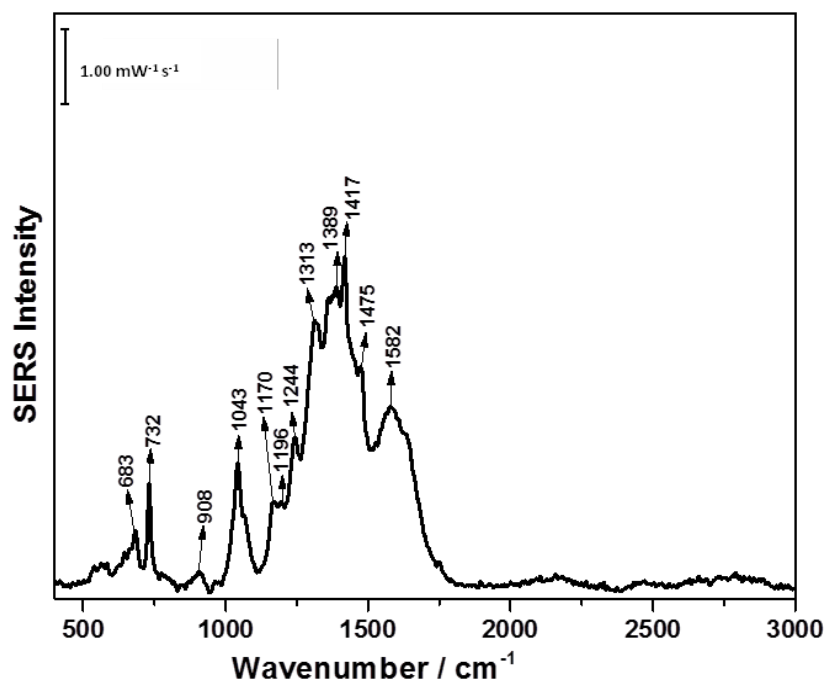
Table A-77: Peak assignment for OCP spectrum of 1mM adenine/0.1 M NaF solution with AgNP modified electrode, 1st trial

Wavenumber (cm⁻¹)	Assignment	Description	Molecule
683		Ring deformation	adenine
732		Ring breathing	adenine
908	COO⁻	Carboxyl deformation	citrate
1043	COO⁻	Carboxyl deformation	citrate
1170	COO⁻	Carboxyl deformation	citrate
1196		Presence of citrate decomposition products	citrate
1244		Ring breathing	adenine
1313		Ring stretch	adenine
1389		Ring bending	adenine
1417	C=C	Ring alkene stretch	adenine
1475		Ring stretch	adenine
1582	COO⁻	Carboxyl deformation	citrate

Figure A-78: Anodic overlay spectra of 1mM adenine/0.1 M NaF solution with AgNP modified electrode, 1st trial
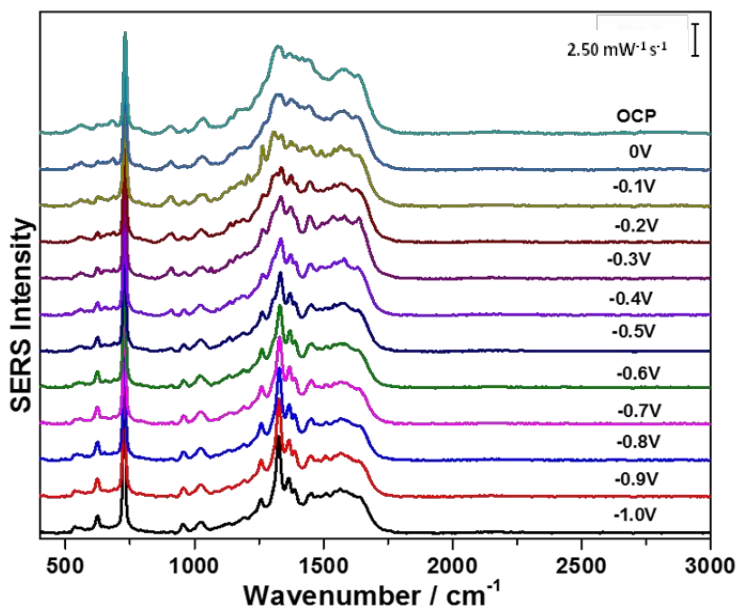
Figure A-79: CV comparison between 1mM adenine/0.1 M NaF solution and 0.1 M NaF solution, 1st trial
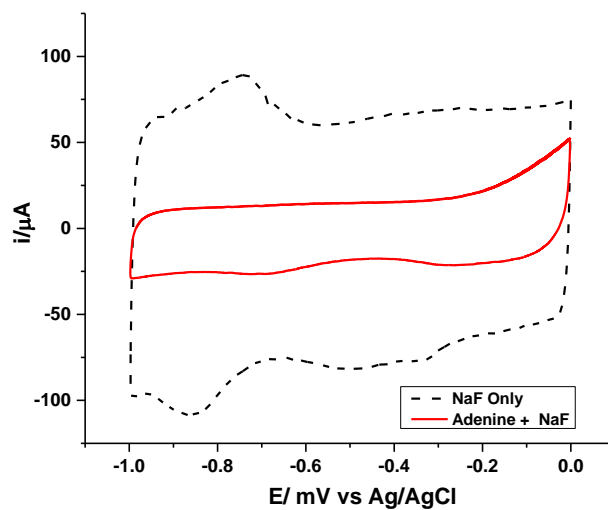
Figure A-80: OCP spectrum of 1mM adenine/0.1 M NaF solution with AgNP modified electrode, 2nd trial
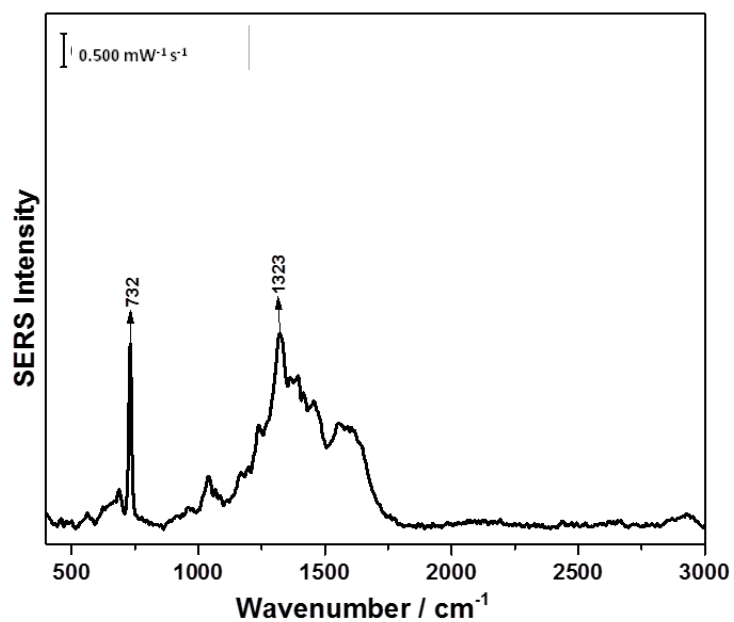
Figure A-81: a) cathodic and b) anodic overlay spectra of 1mM adenine/0.1 M NaF solution with AgNP modified electrode, 2nd trial
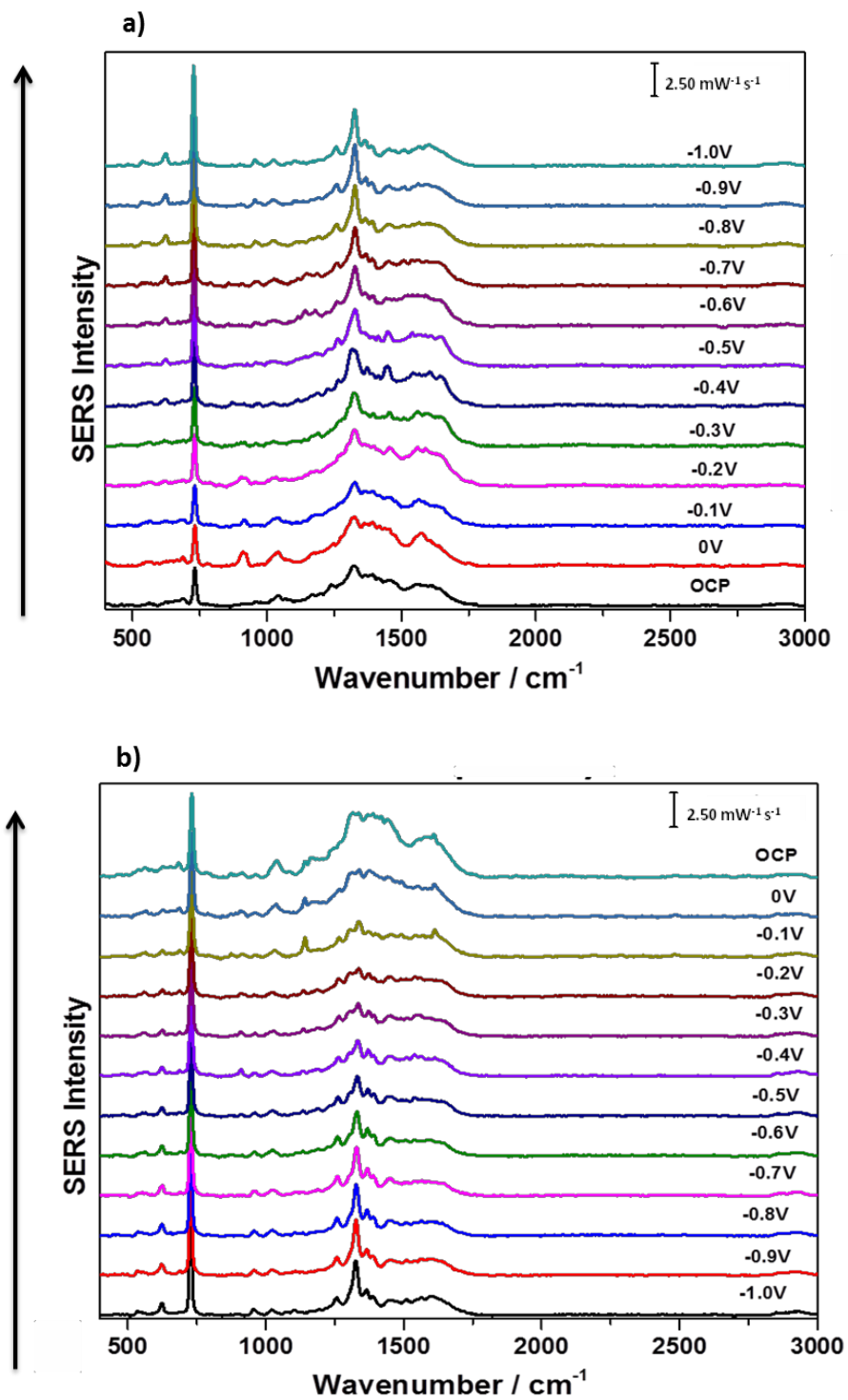
Figure A-82: CV comparison between 1mM adenine/0.1 M NaF solution with AgNP modified electrode and 0.1 M NaF solution, 2nd trial
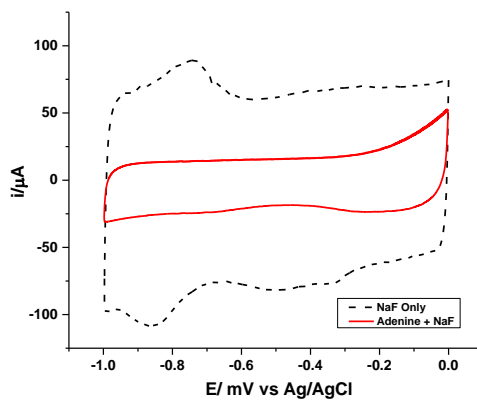
Figure A-83: OCP spectrum of 1mM adenine/0.1 M NaF solution with AgNP modified electrode, 3rd trial
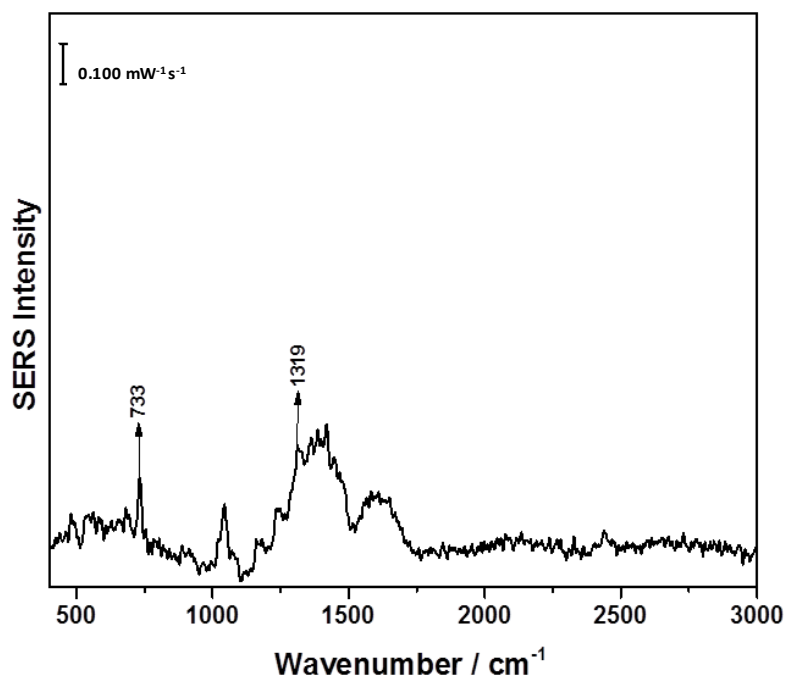
Figure A-84: a) cathodic and b) anodic overlay spectra of 1mM adenine/0.1 M NaF solution with AgNP modified electrode, 3rd trial
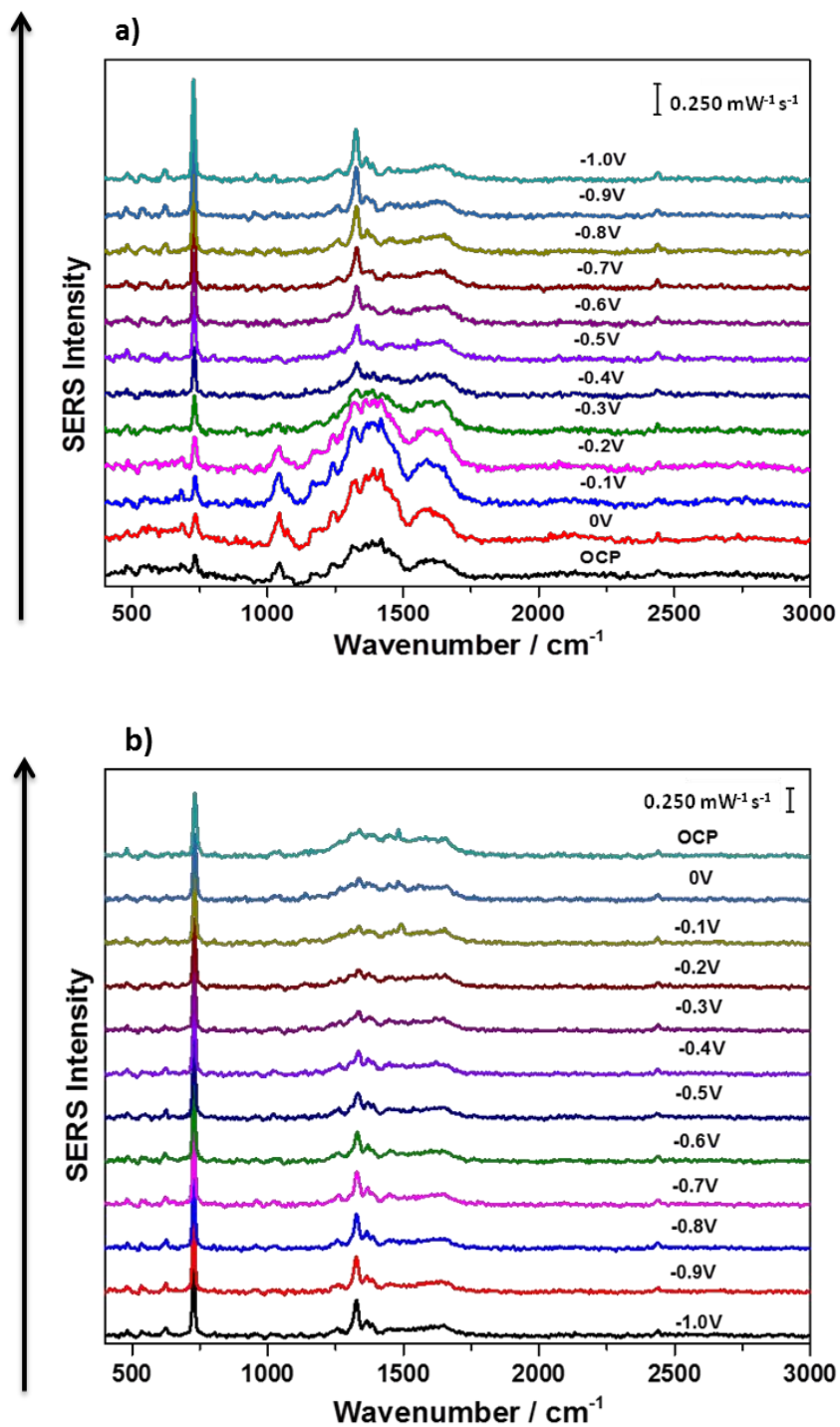
Figure A-85: CV comparison between 1mM adenine/0.1 M NaF solution and 0.1 M NaF solution, 3rd trial
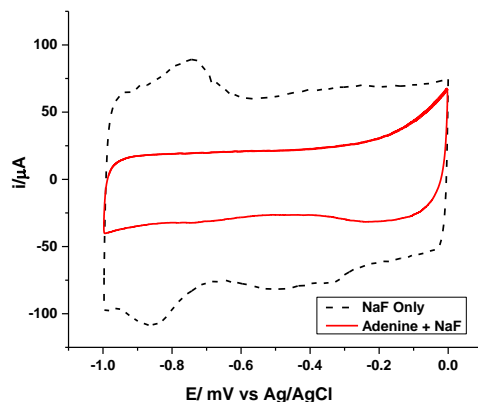
Figure A-86: OCP spectrum of 1mM adenine/0.1 M NaF solution in the presence of 6-MHA SAM, 1st trial
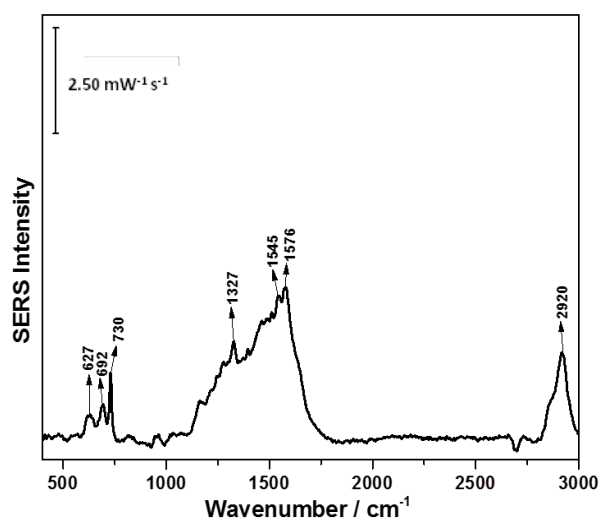
Table A-87: Peak assignment of OCP spectrum of 1mM adenine/0.1 M NaF solution in the presence of 6-MHA SAM, 1st trial

Wavenumber (cm^{-1})	Assignment	Description	Molecule
627	$v(C\text{-}S)_G$	Gauche carbon and sulphur deformation	6-MHA
692	$v(C\text{-}S)_T$	trans carbon and sulphur deformation	6-MHA
730		Ring breathing	adenine
1327		H bending + ring stretch	dAMP
1545	$v_{as}(COO_2^-)$	Asymmetric stretch of vibration	6-MHA
1576		Ring breathing	dAMP
2920	$v_{as}(CH_2)$	Asymmetric stretch alkyl chain	6-MHA

Figure A-88: CV comparison between 1mM adenine/0.1 M NaF solution in the presence of 6-MHA SAM and 0.1 M NaF solution, 1st trial
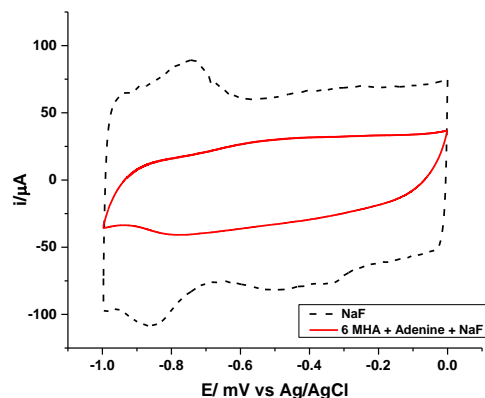
Figure A-89: OCP spectrum 1mM adenine/0.1 M NaF solution in the presence of 6-MHA SAM, 2nd trial
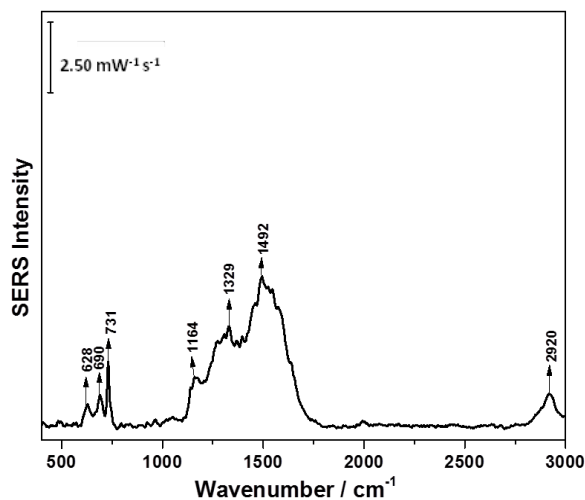
Table A-90: Peak assignment of OCP spectrum of 1mM adenine/0.1 M NaF solution in the presence of 6-MHA SAM, 2nd trial

Wavenumber (cm^{-1})	Assignment	Description	Molecule
628	v(C-S)$_G$	Gauche carbon and sulphur deformation	6-MHA
690	v(C-S)$_T$	trans carbon and sulphur deformation	6-MHA
731		Ring breathing	adenine
1164	C-C	Skeletal straight chain vibration	6-MHA
1329		Ring stretch	adenine
1492	COO$^-$ NH$_2$	Presence of a carboxylic group Scissoring	6-MHA adenine
2920	v_{as}(CH$_2$)	Asymmetric stretch alkyl chain	6-MHA

52

Figure A-91: a) cathodic and b) anodic overlay spectra of 1mM adenine/0.1 M NaF solution in the presence of 6-MHA SAM, 2ⁿᵈ trial

Figure A-92: CV comparison between a1mM adenine/0.1 M NaF solution in the presence of 6-MHA SAM and 0.1 M NaF solution, 2nd trial
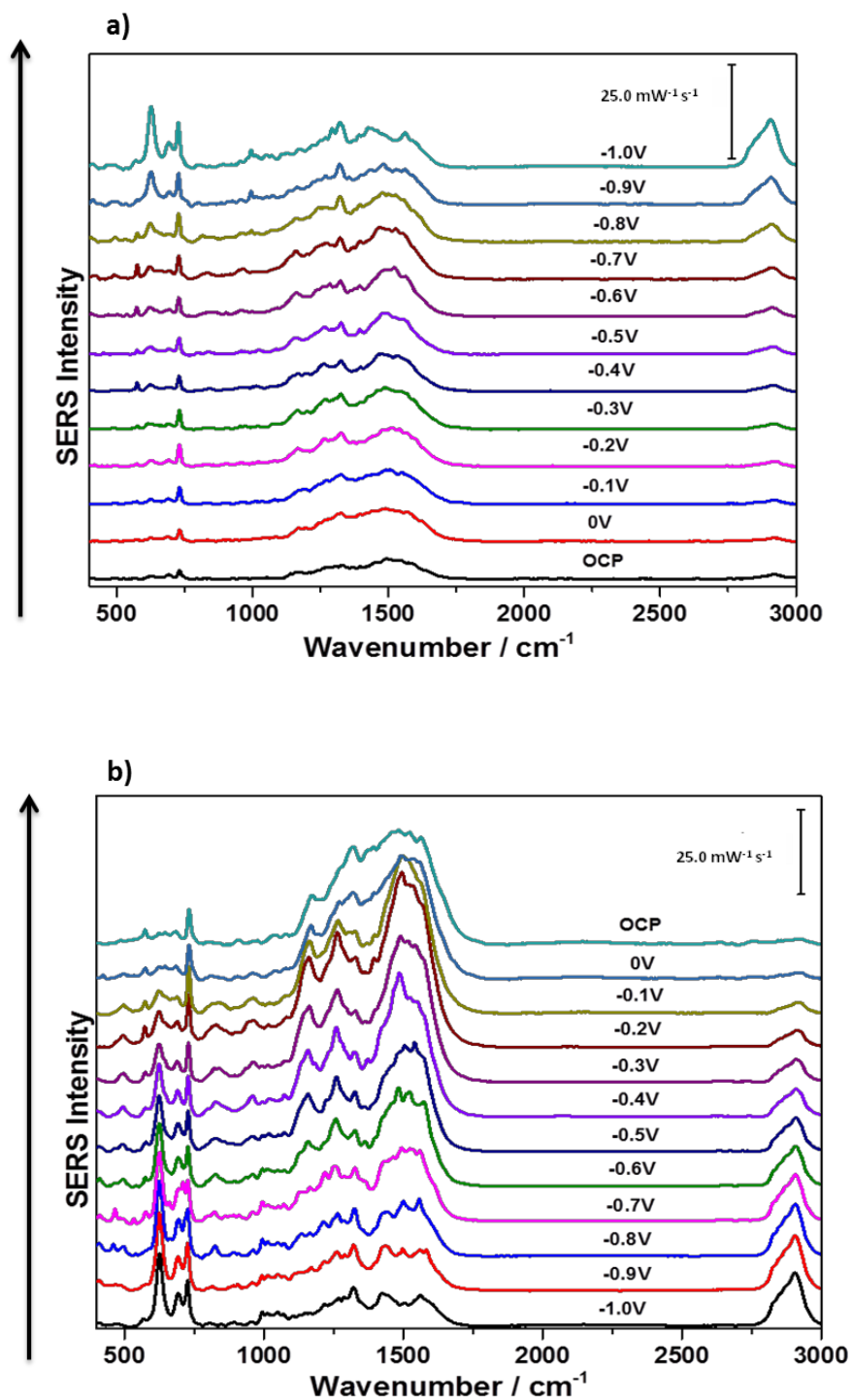
Figure A-92: **CV comparison between a1mM adenine/0.1 M NaF solution in the presence of 6-MHA SAM and 0.1 M NaF solution, 2nd trial**
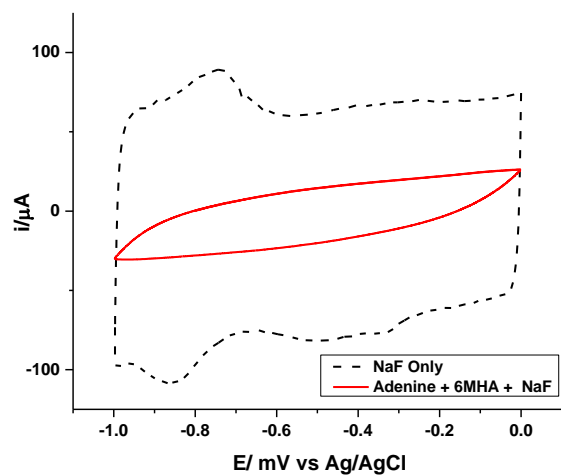
Figure A-93: OCP spectrum of 1mM adenine/0.1 M NaF solution in the presence of 6-MHA SAM, 3rd trial
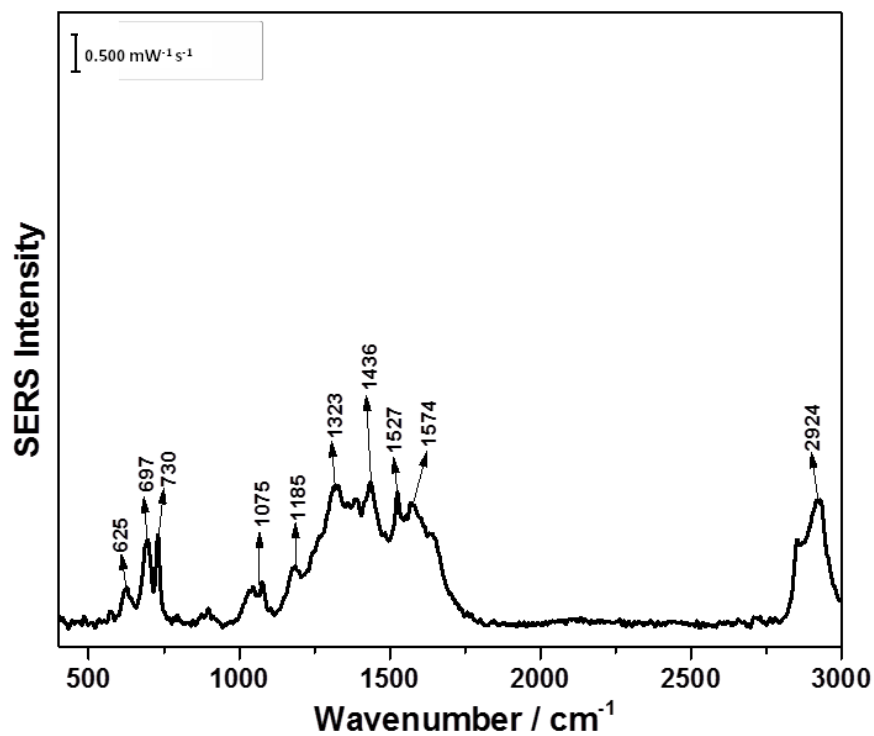
Table A-94: Peak assignment of OCP spectrum of 1mM adenine/0.1 M NaF solution in the presence of 6-MHA SAM, 3rd trial

Wavenumber (cm^{-1})	Assignment	Description	Molecule
625	v(C-S)$_G$	Gauche carbon and sulphur deformation	6-MHA
697	v(C-S)$_T$	trans carbon and sulphur deformation	6-MHA
730		Ring breathing	adenine
1075	v_{as}(C-C)$_T$	Asymmetric trans alkyl stretch	6-MHA
1185	C-C	Skeletal straight chain vibration for alkanes	6-MHA
1323		Ring stretch	adenine
1436	(CH$_2$) COO$^-$	Symmetric deformation Deprotonated carboxylic group	6-MHA 6-MHA
1527	v_{as}(COO$_2^-$)	Asymmetric stretch of vibration	6-MHA
1574		Ring breathing	dAMP
2924	v_{as}(CH$_2$)	Asymmetric stretch alkyl chain	6-MHA

Figure A-95: a) cathodic and b) anodic overlay spectra of 1mM adenine/0.1 M NaF solution in the presence of 6-MHA SAM, 3rd trial
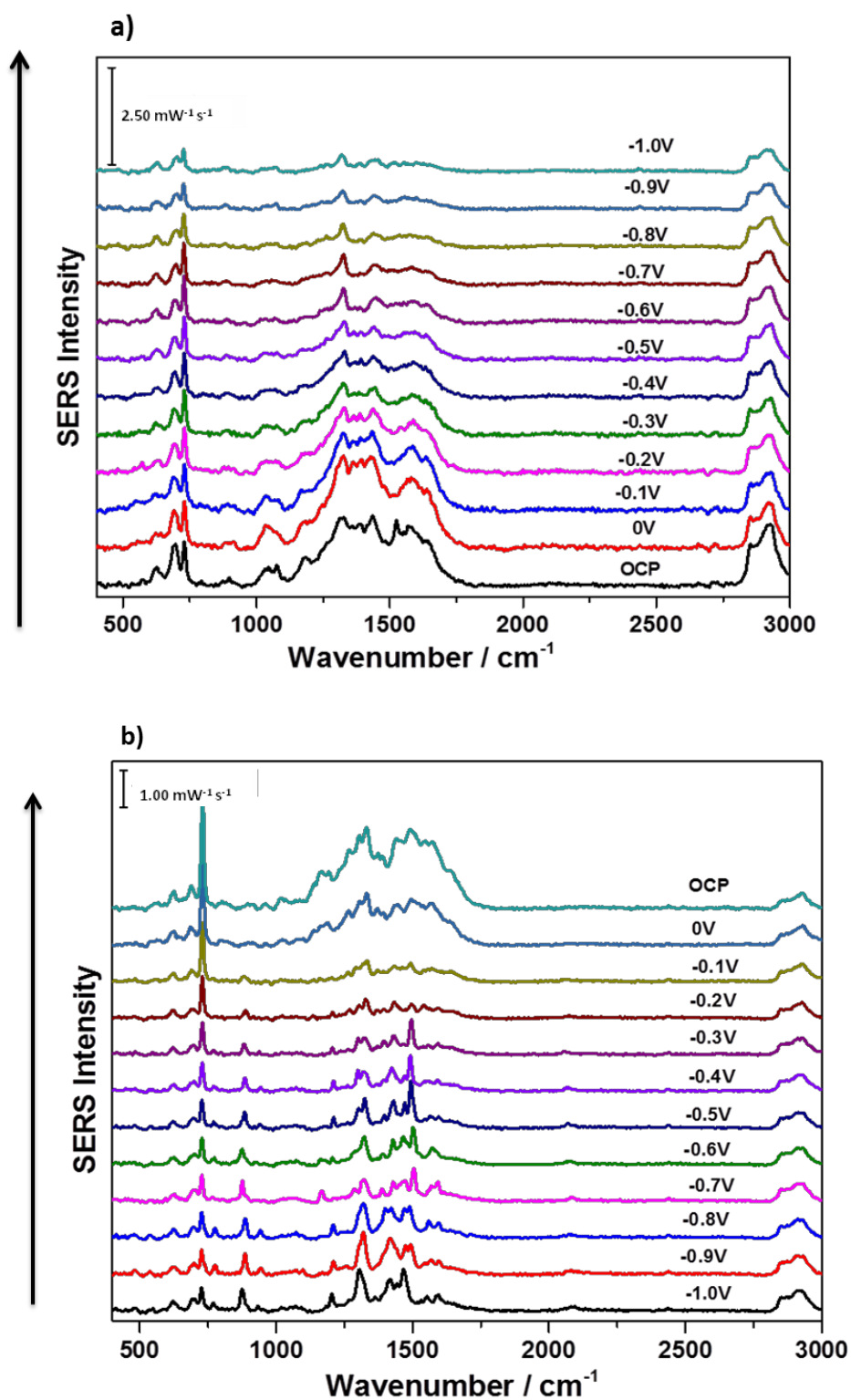
Figure A-96: CV comparison between 1mM adenine/0.1 M NaF solution in the presence of 6-MHA SAM and 0.1 M NaF solution, 3rd trial
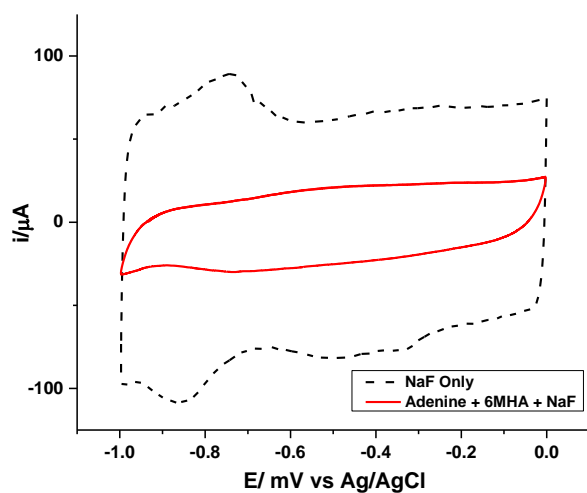
Figure A-97: In air spectrum of deposited DMPC/cholesterol (70:30) bilayer on 6-MHA SAM AgNP modified electrode, 1st trial
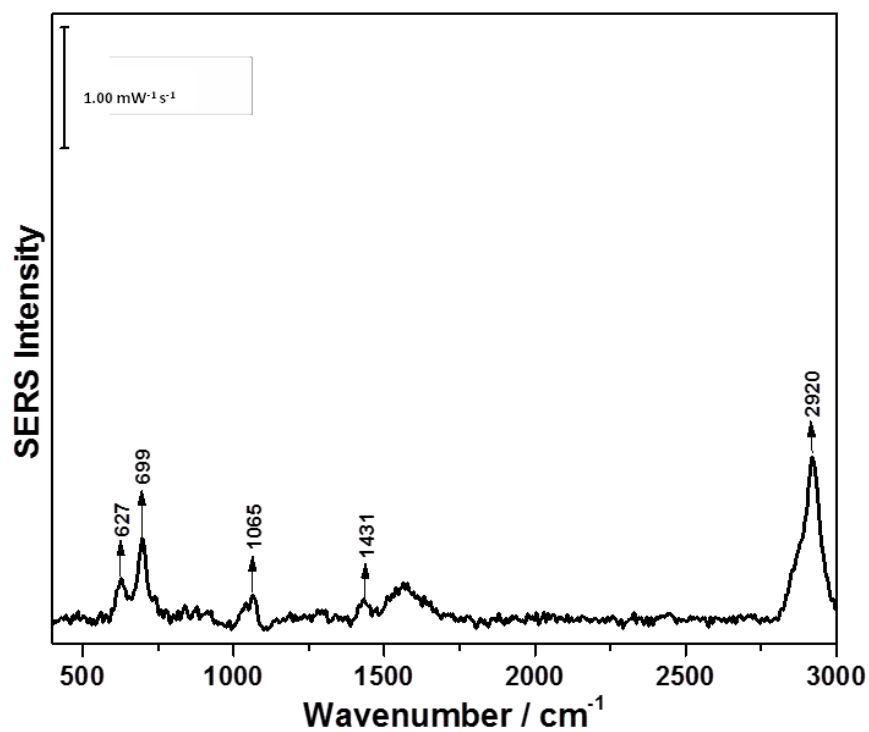
Table A-98: Peak assignment for in air spectrum of deposited DMPC/cholesterol (70:30) bilayer on 6-MHA SAM AgNP modified electrode, 1st trial

Wavenumber (cm^{-1})	Assignment	Description	Molecule
627	v(C-S)$_G$	Gauche carbon and sulphur deformation	6-MHA
699	v(C-S)$_T$	trans carbon and sulphur deformation	6-MHA
1065	v_{as}(PO$_2^-$)	Phosphate diester asymmetric stretch	DMPC
	(C-C)$_T$	Alkyl chain stretch	6-MHA
1431	(CH$_2$)	Symmetric deformation	6-MHA/DMPC
	COO$^-$	Deprotonated carboxylic	6-MHA
	δ_d(-CH$_2$)	vibration deformation for cholesterol	cholesterol
2920	v_{as}(CH$_2$)	Asymmetric stretch alkyl chain	6-MHA

Figure A-99: OCP spectrum of deposited DMPC/cholesterol (70:30) bilayer on 6-MHA SAM AgNP modified electrode in the presence of 1mM adenine/0.1 M NaF solution, 1st trial

Table A-100: Peak assignment for OCP spectrum of deposited DMPC/cholesterol (70:30) bilayer on 6-MHA SAM AgNP modified electrode in the presence of 1mM adenine/0.1 M NaF solution, 1st trial

Wavenumber (cm⁻¹)	Assignment	Description	Molecule
576	COO⁻	Carboxylic deformation	6-MHA
627	v(C-S)$_G$	Gauche carbon and sulphur deformation	6-MHA
694	v(C-S)$_T$	trans carbon and sulphur deformation	6-MHA
732		Ring breathing	adenine
1042	(C-C)$_T$	Trans alkyl chain stretch	6-MHA/DMPC
1075	v_{as}(C-C)$_T$ v(C-O-PO$_2^-$)	Asymmetric trans alkyl chain stretch Phosphate ester stretch	6-MHA DMPC
1164	C-O C-C	Ester asymmetric stretch Skeletal straight chain vibration	DMPC 6-MHA
1197	ω(CH$_2$)	Wagging for lipids or 6-MHA	6-MHA/DMPC
1249	v_{as} (PO$_2^-$)	Phosphate diester asymmetric stretch Ring breathing or stretch	DMPC adenine
1325		Ring stretch	adenine
1526	v_{as} (COO$_2^-$)	Asymmetric stretch of vibration	6-MHA
1567		Ring breathing mode	adenine
2920	v_{as}(CH$_2$)	Asymmetric stretch alkyl chain	6-MHA

Figure A-101: CV comparison between deposited DMPC/cholesterol (70:30) bilayer on 6-MHA SAM AgNP modified electrode in the presence of 1mM adenine/ 0.1 M NaF solution and 0.1 M NaF solution, 1st trial

Figure A-102: In air spectrum of deposited DMPC/cholesterol (70:30) bilayer on 6-MHA SAM AgNP modified electrode, 2nd trial

Table A-103: Peak assignment for in air spectrum of deposited DMPC/cholesterol (70:30) bilayer on 6-MHA SAM AgNP modified electrode, 2nd trial

Wavenumber (cm^{-1})	Assignment	Description	Molecule
630	v(C-S)$_G$	Gauche carbon and sulphur deformation	6-MHA
697	v(C-S)$_T$	trans carbon and sulphur deformation	6-MHA
1064	v_{as}(PO$_2^-$)	Phosphate diester asymmetric stretch	DMPC
	(C-C)$_T$	Alkyl chain stretch	6-MHA
2920	v_{as}(CH$_2$)	Asymmetric stretch alkyl chain	6-MHA

Figure A-104: OCP spectrum of deposited DMPC/cholesterol (70:30) bilayer on 6-MHA SAM AgNP modified electrode in the presence of 1mM adenine/0.1 M NaF solution, 2nd trial
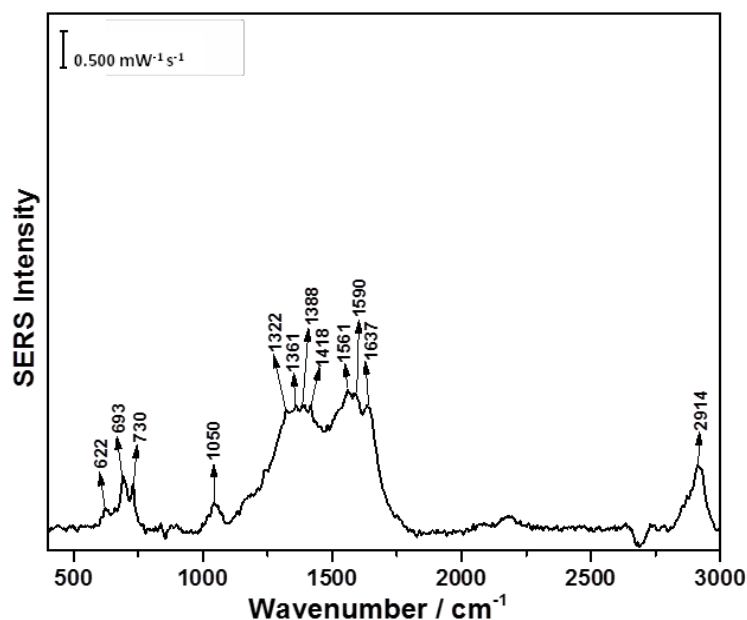
Table A-105: Peak assignment for OCP spectrum of deposited DMPC/cholesterol (70:30) bilayer on 6-MHA SAM AgNP modified electrode in the presence of 1mM adenine/0.1 M NaF solution, 2nd trial

Wavenumber (cm^{-1})	Assignment	Description	Molecule
622	v(C-S)$_G$	Gauche carbon and sulphur deformation	6-MHA
693	v(C-S)$_T$	trans carbon and sulphur deformation	6-MHA
730		Ring breathing	adenine
1050	(C-C)$_T$	Trans alkyl chain stretch	6-MHA/DMPC
1322		Ring stretch	adenine
1361		Unassigned peak	adenine
1388		Ring bending	adenine
1418	C=C	Ring alkene stretch	adenine
1561		Ring breathing mode	adenine
1590	COO$^-$	Deprotonated carboxylic group	6-MHA
	C=O	Presence of a carbonyl	6-MHA
1637	O-H	Intermolecular bending mode	water
	C=O	Presence of a carbonyl	6-MHA
2914	v_{as}(CH$_2$)	Asymmetric stretch alkyl chain	6-MHA

61

Figure A-106: a) cathodic and b) anodic overlay spectra of deposited DMPC/cholesterol (70:30) bilayer on 6-MHA SAM AgNP modified electrode in the presence of 1mM adenine/0.1 M NaF solution, 2nd trial

Figure A-107: CV comparison between deposited DMPC/cholesterol (70:30) bilayer on 6-MHA SAM AgNP modified electrode in the presence of 1mM adenine/ 0.1 M NaF solution and 0.1 M NaF solution, 2nd trial
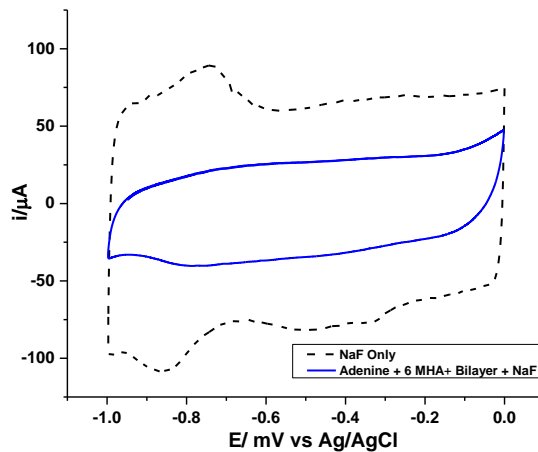
Figure A-108: In air spectrum of deposited DMPC/cholesterol (70:30) bilayer on 6-MHA SAM AgNP modified electrode, 3rd trial
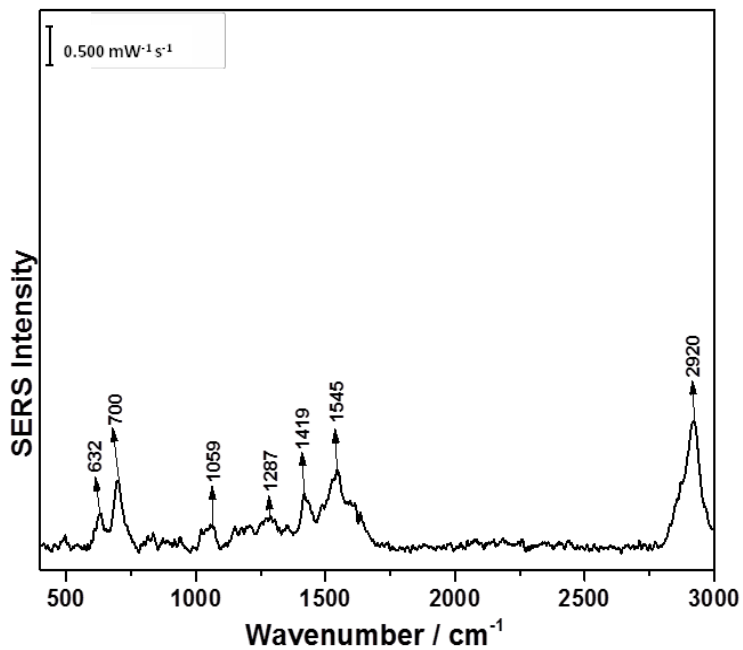
Table A-109: Peak assignment for in air spectrum of deposited DMPC/cholesterol (70:30) bilayer on 6-MHA SAM AgNP modified electrode n, 3rd trial

Wavenumber (cm^{-1})	Assignment	Description	Molecule
632	v(C-S)$_G$	Gauche carbon and sulphur deformation	6-MHA
700	v(C-S)$_T$	trans carbon and sulphur deformation	6-MHA
1059	v_{as}(PO$_2^-$)	Phosphate diester asymmetric stretch	DMPC
	(C-C)$_T$	Alkyl chain stretch	6-MHA
1287	ω(CH$_2$)	Wagging vibration	6-MHA/DMPC
1419	C=C	Ring alkene stretch	adenine
1545	v_{as} (COO$_2^-$)	Asymmetric stretch of vibration	6-MHA
2920	v_{as}(CH$_2$)	Asymmetric stretch alkyl chain	6-MHA

Figure A-110: OCP spectrum of deposited DMPC/cholesterol (70:30) bilayer on 6-MHA SAM AgNP modified electrode in the presence of 1mM adenine/0.1 M NaF solution, 3rd trial
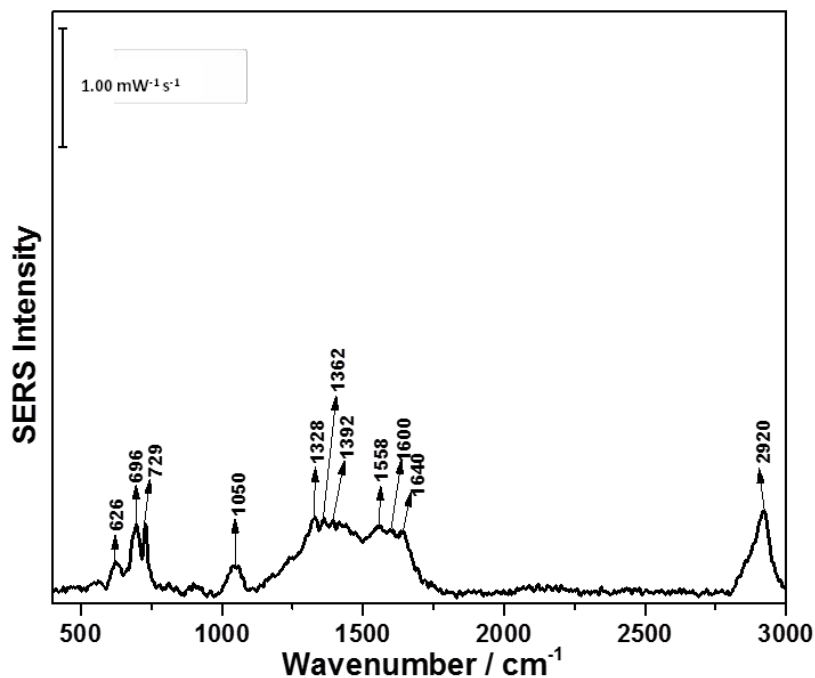
Table A-111: Peak assignment for OCP spectrum of deposited DMPC/cholesterol (70:30) bilayer on 6-MHA SAM AgNP modified electrode in the presence of 1mM adenine/0.1 M NaF solution, 3rd trial

Wavenumber (cm^{-1})	Assignment	Description	Molecule
626	v(C-S)$_G$	Gauche carbon and sulphur deformation	6-MHA
696	v(C-S)$_T$	trans carbon and sulphur deformation	6-MHA
729		Ring breathing	adenine
1050	(C-C)$_T$	Trans alkyl chain stretch	6-MHA/DMPC
1328		Ring stretch	adenine
1362		Unassigned peak	adenine
1392	v(CO$^-$) v(COO-Ag)	Deprotonated carboxylic group Carboxylic group coordinated to metal	6-MHA 6-MHA
1558		Ring breathing mode	adenine
1600	COO$^-$ C=O	Deprotonated carboxylic group Presence of a carbonyl	6-MHA 6-MHA
1640	O-H C=O	Intermolecular bending mode Presence of a	water 6-MHA
2920	v_{as}(CH$_2$)	Asymmetric stretch alkyl chain	6-MHA

Figure A-112: a) cathodic and b) anodic overlay spectra of deposited DMPC/cholesterol (70:30) bilayer on 6-MHA SAM AgNP modified electrode in the presence of 1mM adenine/0.1 M NaF solution, 3rd trial
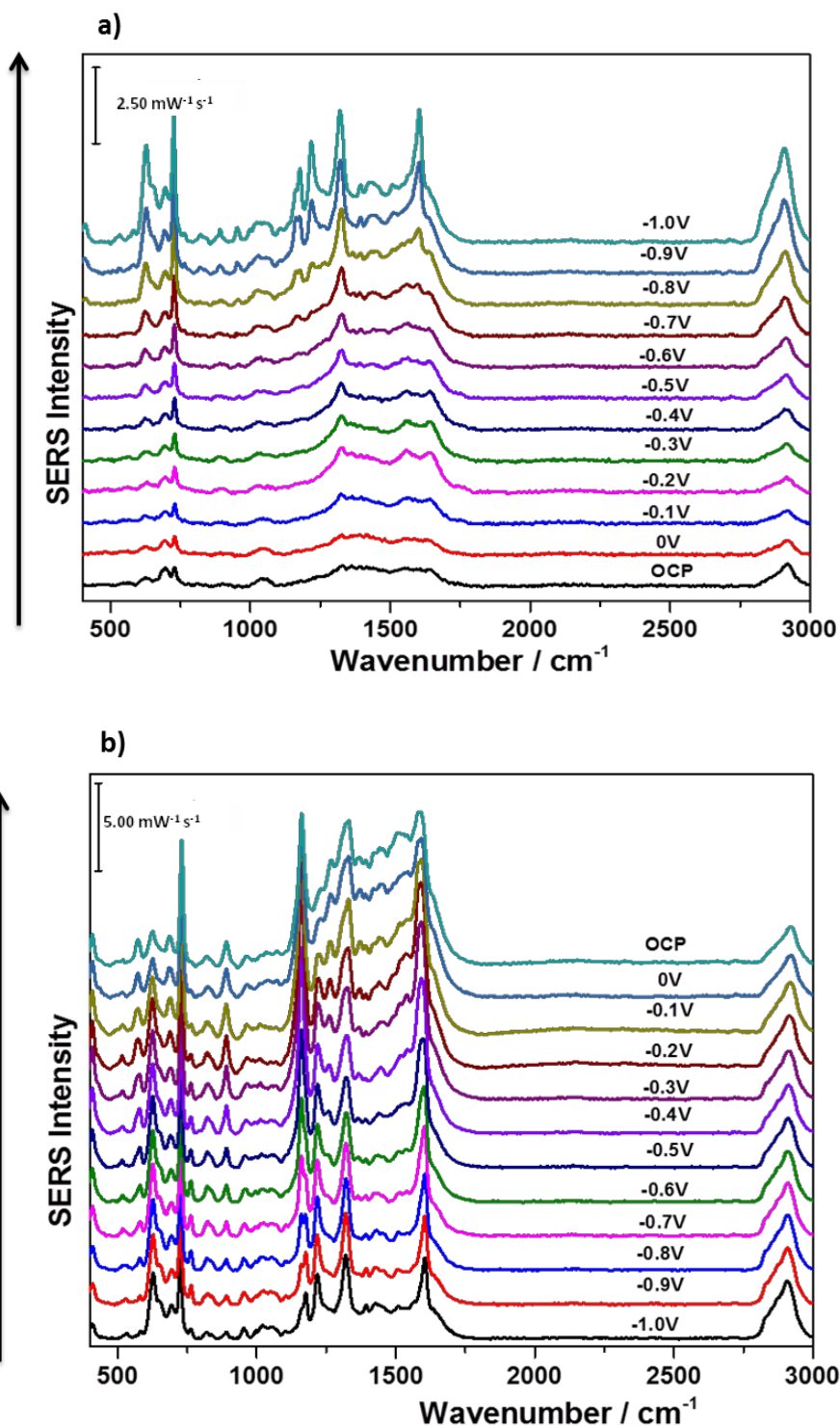
Figure A-113: CV comparison between deposited DMPC/cholesterol (70:30) bilayer on 6-MHA SAM AgNP modified electrode in the presence of 1mM adenine/ 0.1 M NaF solution and 0.1 M NaF solution, 3rd trial
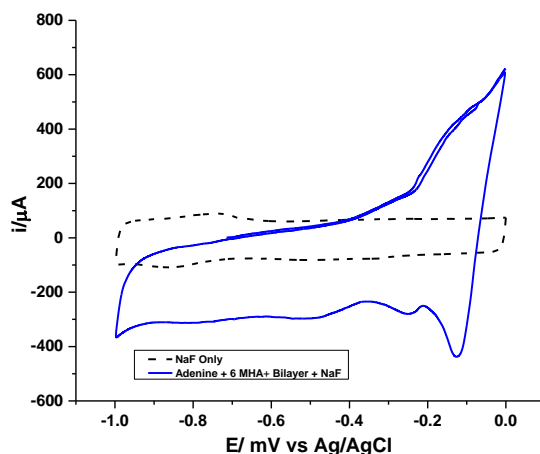
Table A-114: Peak assignment for marker peaks for 1mM aloin studies

Wavenumber (cm^{-1})	Assignment	Description	Molecule
460		Skeletal vibration	aloin
1228	δ(CH)/δ(CCC)	In-plane bending	aloin
1290	v(CO)/ v(CC)/ δ(CCC)	Stretch and in-plane bending vibration	aloin
1370	υ(CC)/ δ (COH)	In-plane bending and stretch vibration	aloin
1390	δ(COH)/ v(CC)	In-plane bending and stretch vibration	aloin
1561	υ(CC)	In-plane bending	aloin

Figure A-115: OCP spectrum of nM aloin/0.1 M NaF solution with AgNP modified electrode, 1ˢᵗ trial
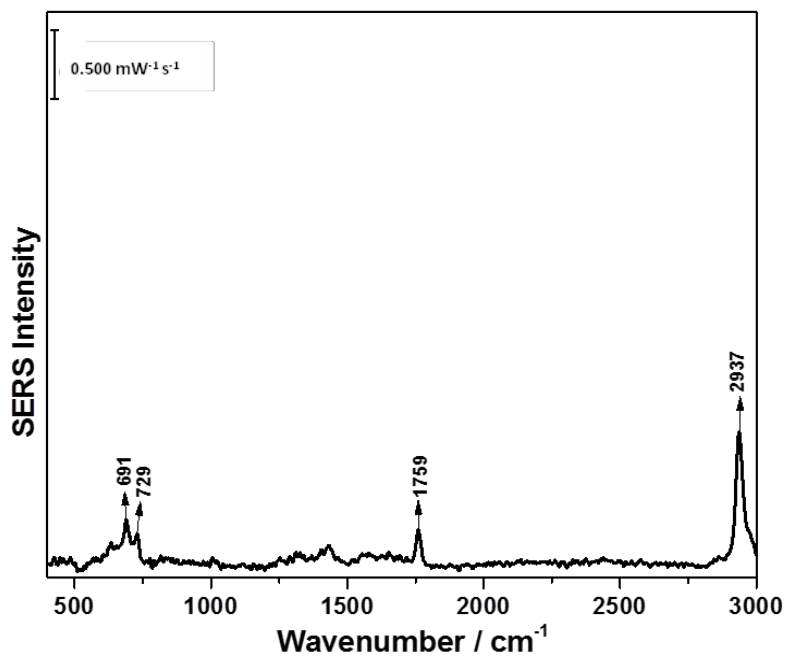
Figure A-116: Cathodic overlay spectra of 1 nM aloin/0.1 M NaF solution with AgNP modified electrode, 1ˢᵗ trial
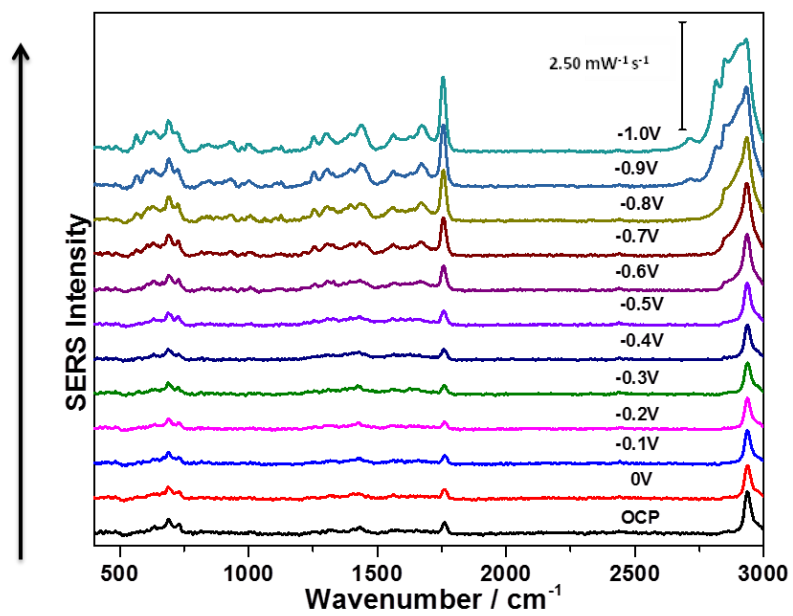
Figure A-117: CV comparison between 1 nM aloin/0.1 M NaF solution and 0.1 M NaF solution, 1st trial
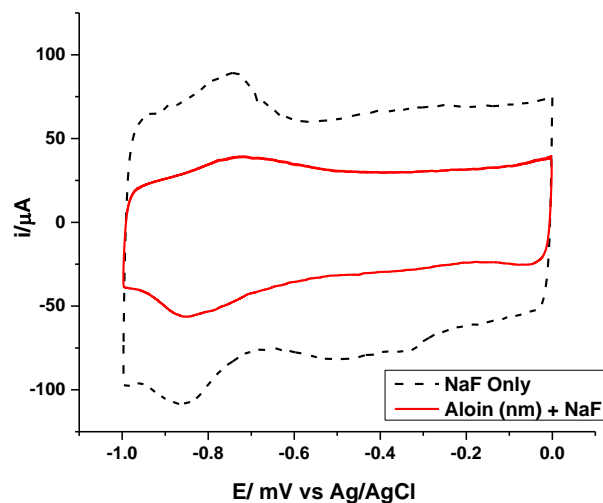
Table A-118: Peak assignment for -0.4V anodic spectrum of nM aloin/0.1 M NaF solution with AgNP modified electrode

Wavenumber (cm^{-1})	Assignment	Description	Molecule
856	δ(C=O)/δ(CCC)	In plane bending vibration	aloin
1001	ν(CC)/δ(CCC)	Stretch and in plane bending vibration	aloin
1129	ν(CC)	Stretch vibration	aloin
1401	ν(CC)/δ(CH)	Stretch and in plane bending vibration	aloin
1605	C=O/OH(ring)/CC	Stretch and in plane bending vibration	aloin
1760	C=O	Presence of a carbonyl group	aloin
2853	ν_s(CH$_2$)	symmetric stretch	aloin
2933	ν_{as}(CH$_2$)	Asymmetric stretch	aloin

Figure A-119: OCP spectrum of 1 nM aloin/0.1 M NaF solution with AgNP modified electrode, 2nd trial
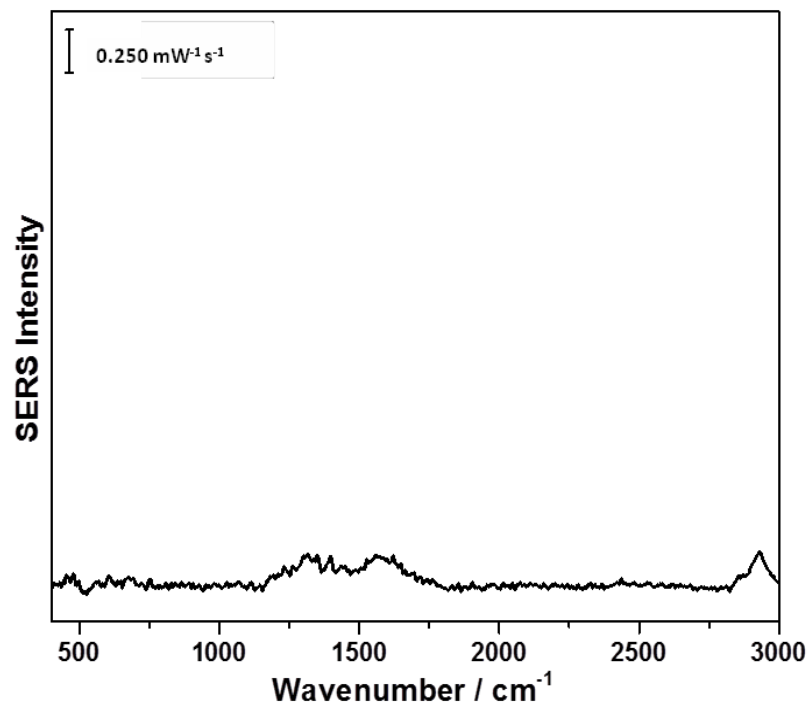
Figure A- 120: a) cathodic and b) anodic overlay spectra of nM aloin/0.1 M NaF solution with AgNP modified electrode, 2nd trial
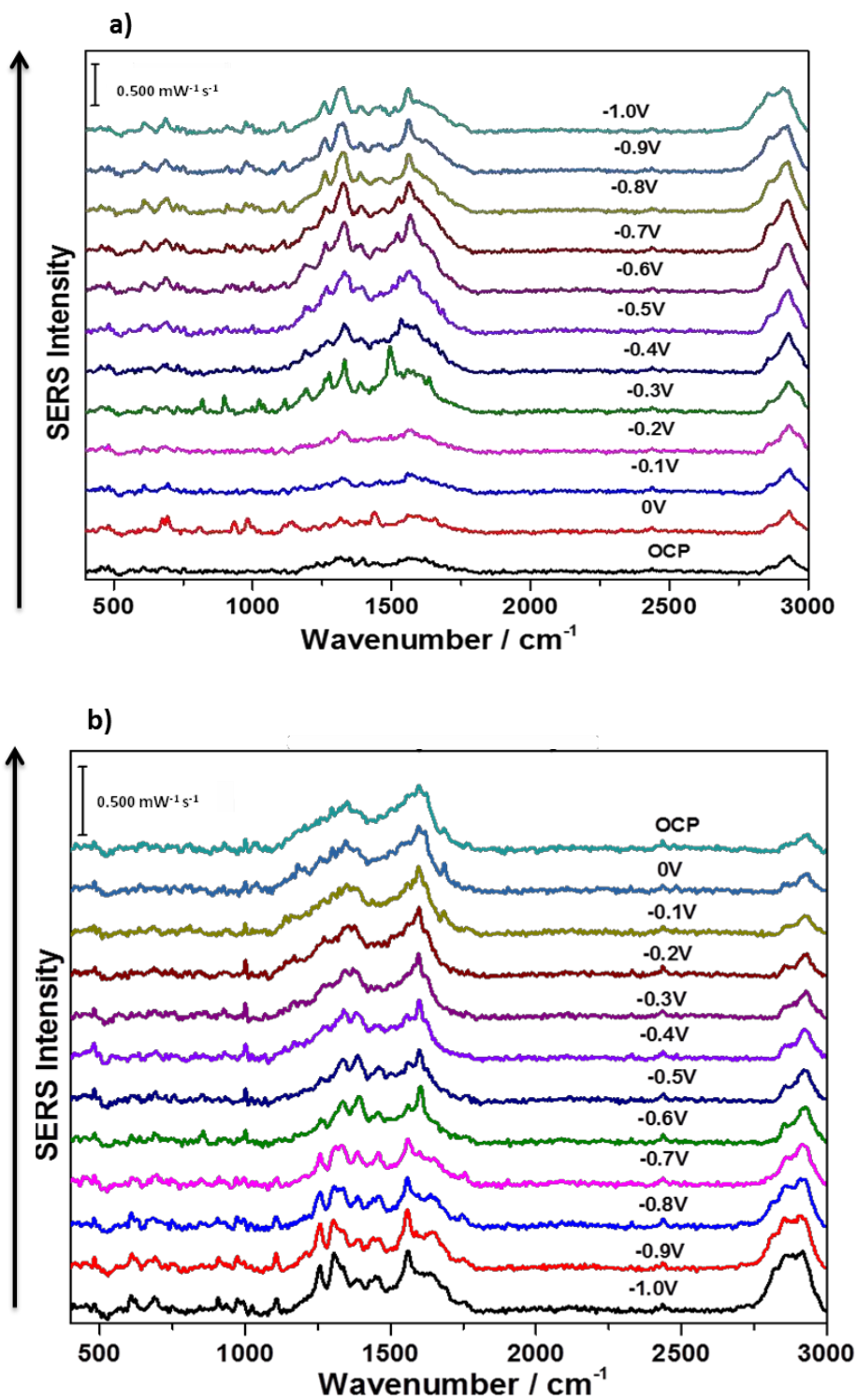
Figure A-121: CV comparison between 1 nM aloin/0.1 M NaF solution and 0.1 M NaF solution, 2nd trial
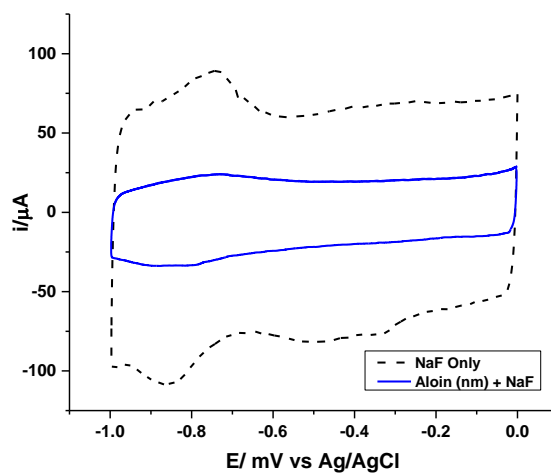
Figure A-122: OCP spectrum of nM aloin/0.1 M NaF solution with AgNP modified electrode, 3rdtrial
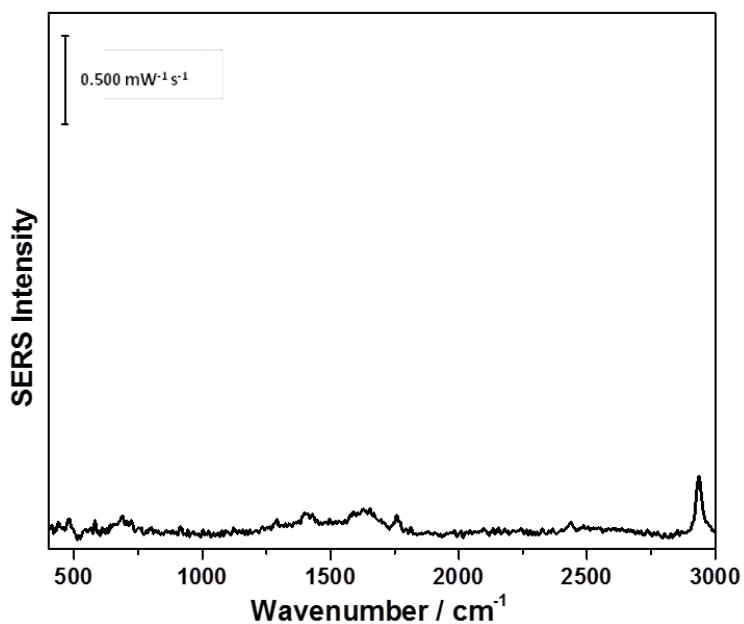
Figure A-123: a) cathodic and b) anodic overlay spectra of1 nM aloin/0.1 M NaF solution with AgNP modified electrode, 3rd trial
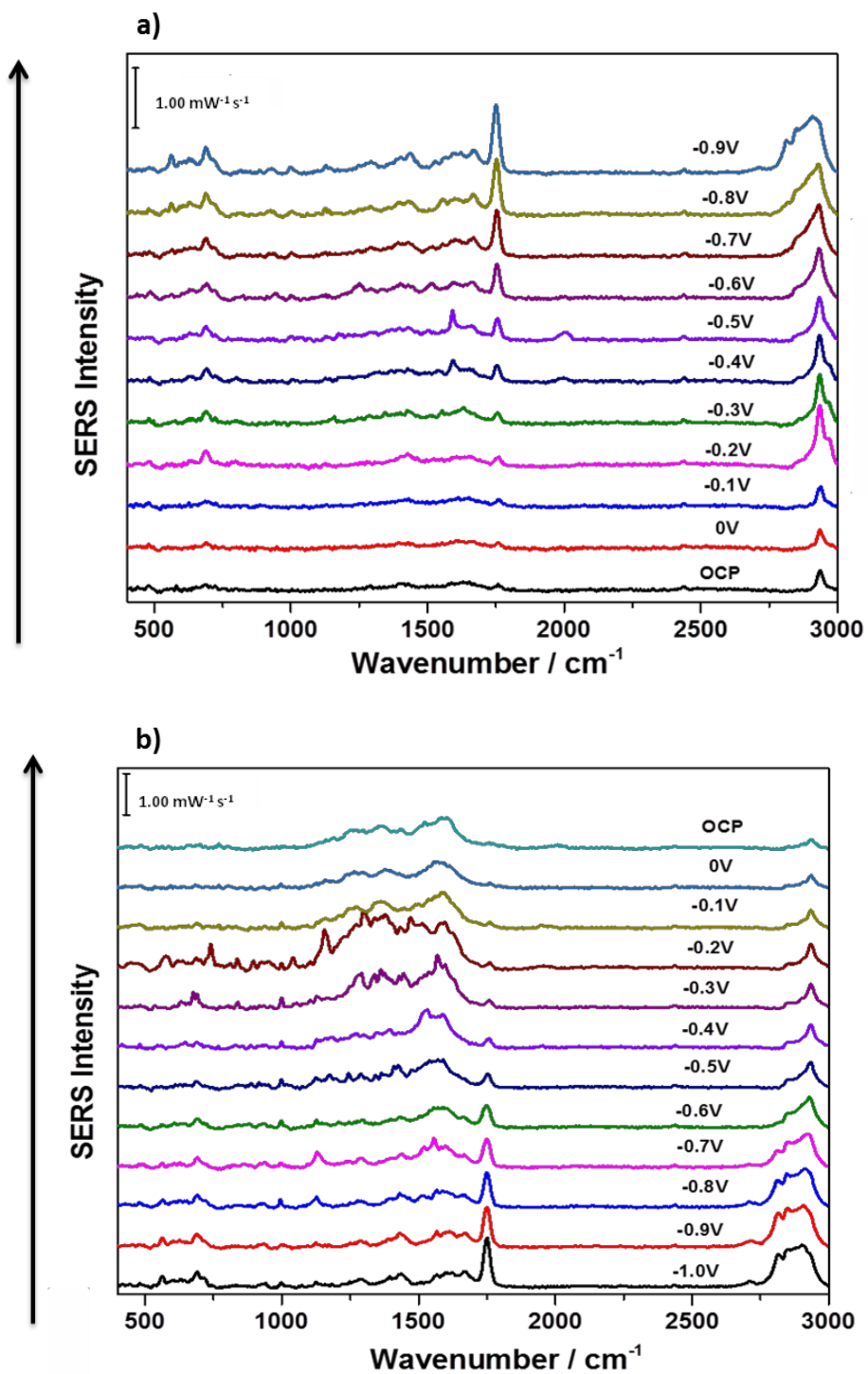
Figure A-124: CV comparison between 1 nM aloin/0.1 M NaF solution and 0.1 M NaF solution, 3rd trial
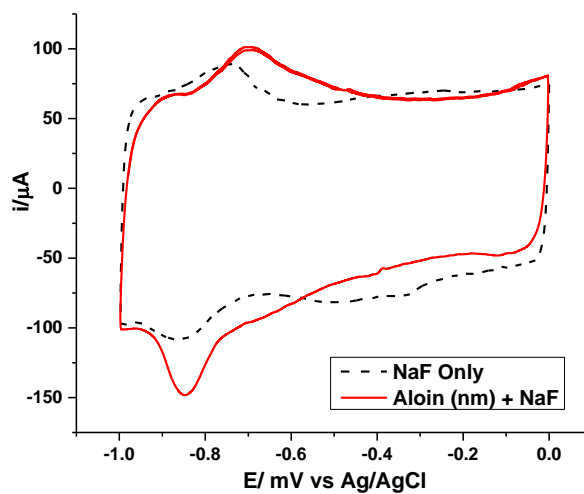
Figure A-125: OCP spectrum of 1 nM aloin/0.1 M NaF solution in the presence of 6-MHA SAM, 1st trial
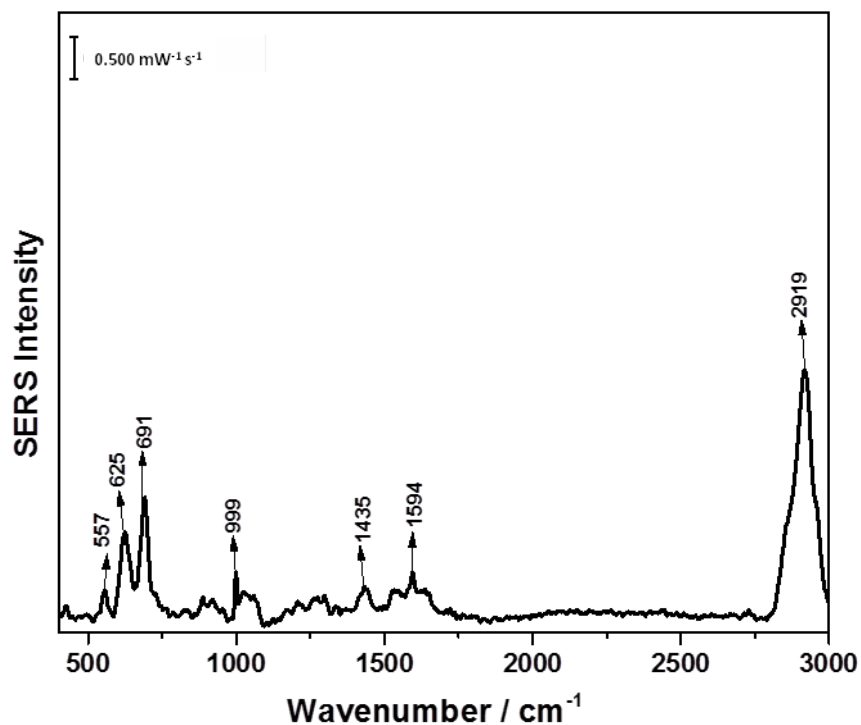
Table A-126: Peak assignment of OCP spectrum of 1 nM aloin/0.1 M NaF solution in the presence of 6-MHA SAM, 1st trial

Wavenumber (cm^{-1})	Assignment	Description	Molecule
557	γ(CCO) ω(OCO)	Out of plane bending Wagging vibration	6-MHA 6-MHA
625	v(C-S)$_G$	Gauche carbon and sulphur deformation	6-MHA
691	v(C-S)$_T$	trans carbon and sulphur deformation	6-MHA
999	C-C	Alkyl chain stretch	6-MHA
1435	(CH$_2$) COO$^-$ v(CC)/δ(CH)	Symmetric deformations Deprotonated carboxylic group Stretch and in plane bending	6-MHA 6-MHA aloin
1594	COO$^-$ C=O	Deprotonated carboxylic group interacting with positive species Presence of a carbonyl	6-MHA 6-MHA
2919	v_{as}(CH$_2$)	Asymmetric stretch alkyl chain	6-MHA/aloin

Figure A-127: CV comparison between 1 nM aloin/0.1 M NaF solution in the presence of 6-MHA SAM and 0.1 M NaF solution, 1st trial
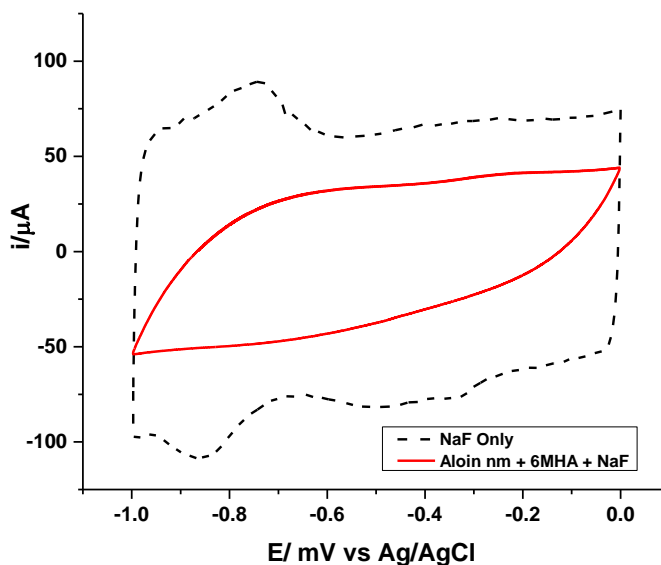
Figure A-128: OCP spectrum of 1 nM aloin/0.1 M NaF solution in the presence of 6-MHA SAM, 2nd trial
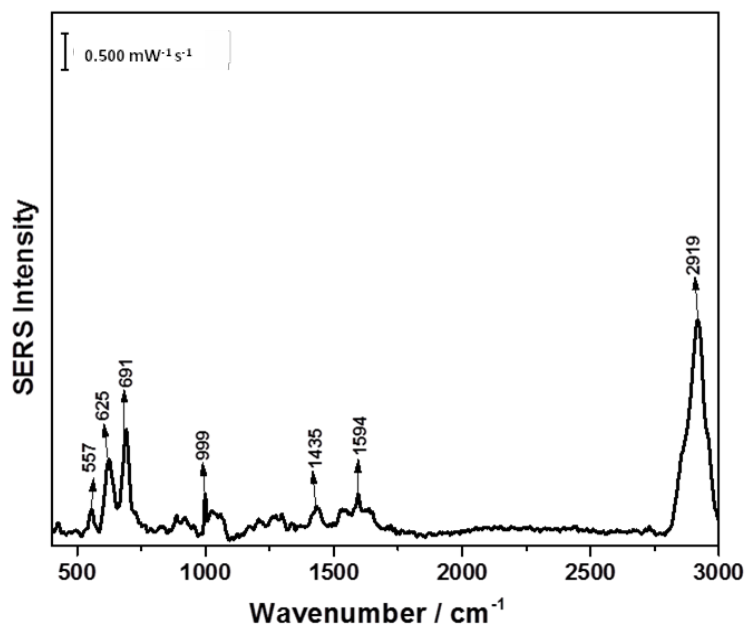
Table A-129: Peak assignment of OCP spectrum of 1 nM aloin/0.1 M NaF solution in the presence of 6-MHA SAM, 2nd trial

Wavenumber (cm^{-1})	Assignment	Description	Molecule
488	CCCC$_G$	Gauche deformation of an alkyl chain	6-MHA
557	γ(CCO) ω(OCO)	Out of plane bending Wagging vibration	6-MHA 6-MHA
632	v(C-S)$_G$	Gauche carbon and sulphur deformation	6-MHA
696	v(C-S)$_T$ γC=O	trans carbon and sulphur deformation Out of-plane bending in ring moiety	6-MHA aloin
935	v(C-COO$^-$)	Deprotonated carboxylic group	6-MHA
1025	(C-C)$_T$	Trans alkyl chain stretch	6-MHA
1175	C-C	Skeletal straight chain vibration for alkanes	6-MHA
1221	ω(CH$_2$)	Wagging vibration	6-MHA
1276	(COO$_2^-$) v(CO)/v(CC)	Vibration due to carboxylic group Stretch vibration of deprotonated ring moiety	6-MHA aloin
1535	(COO$_2^-$)	stretch of vibration	6-MHA
2918	v_{as}(CH$_2$)	Asymmetric stretch alkyl chain	6-MHA/aloin

Figure A-130: a) cathodic and b) anodic overlay spectra of 1 nM aloin/0.1 M NaF solution in the presence of 6-MHA SAM, 2nd trial
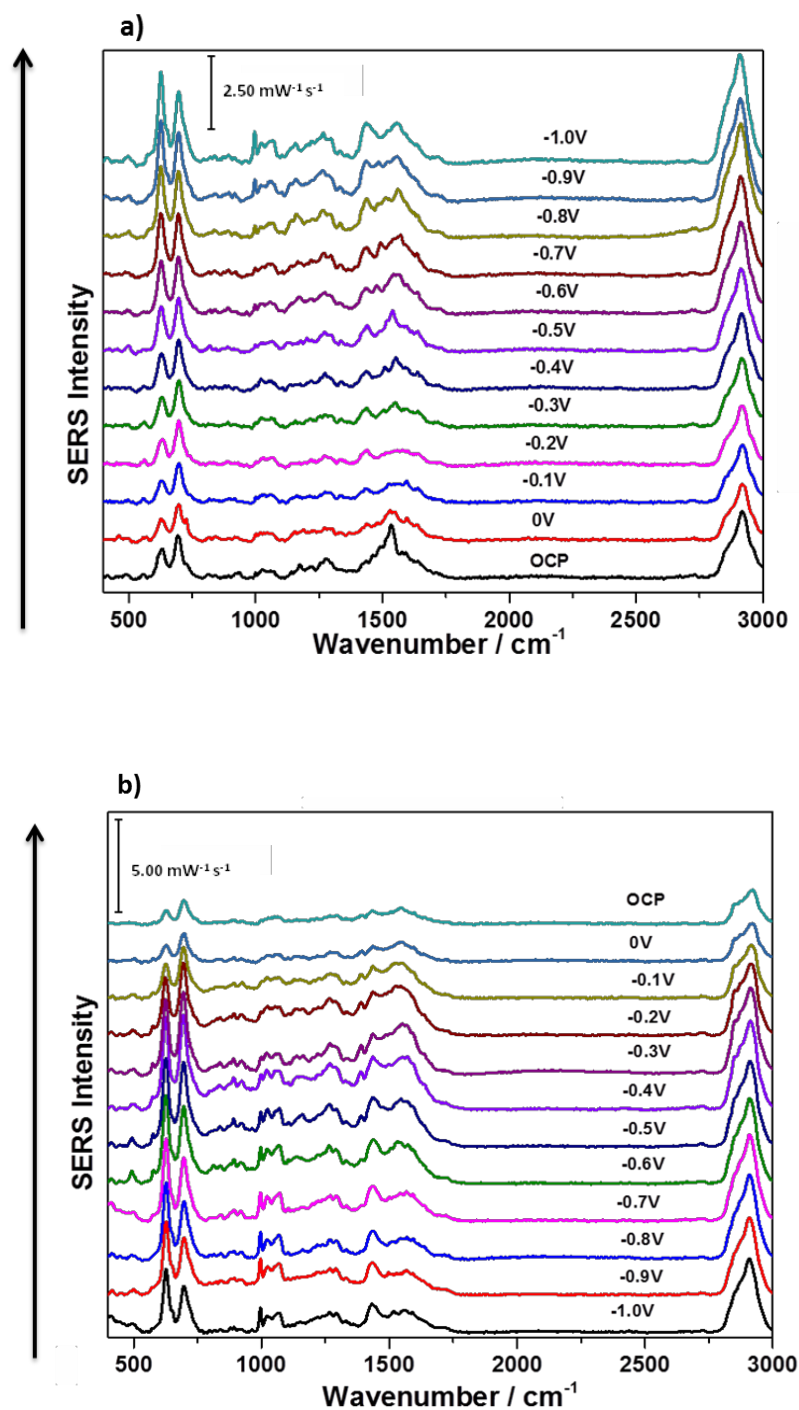
Figure A-131: CV comparison between 1 nM aloin/0.1 M NaF solution in the presence of 6-MHA SAM and 0.1 M NaF solution, 2ⁿᵈ trial
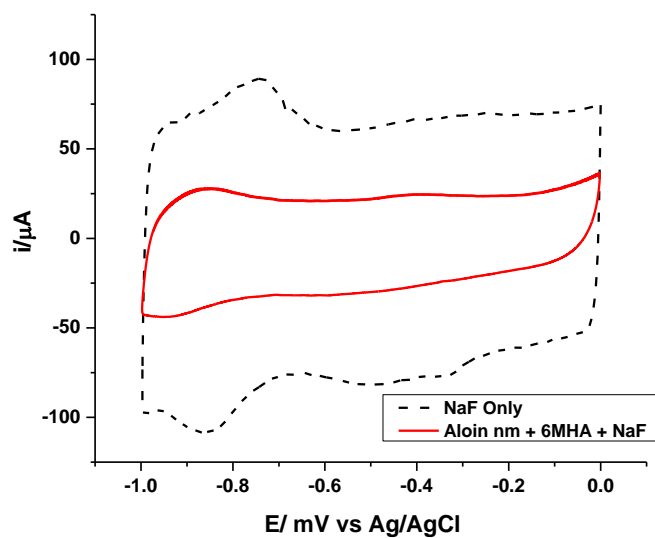
Figure A-132: OCP spectrum of 1 nM aloin/0.1 M NaF solution in the presence of 6-MHA SAM, 3ʳᵈ trial
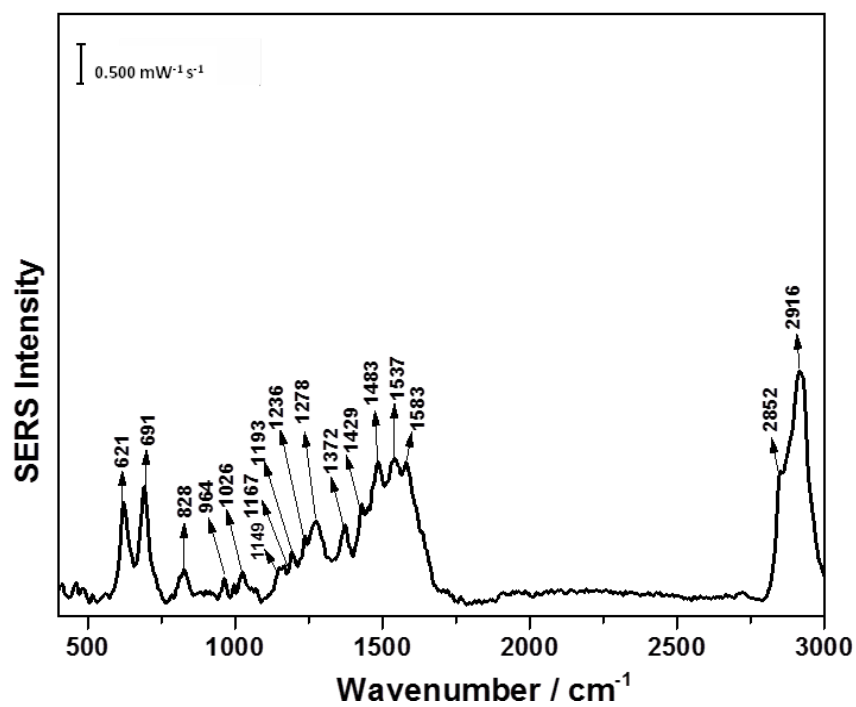
Table A-133: Peak assignment of OCP spectrum of 1 nM aloin/0.1 M NaF solution in the presence of 6-MHA SAM, 3rd trial

Wavenumber (cm^{-1})	Assignment	Description	Molecule
621	v(C-S)$_G$	Gauche carbon and sulphur deformation	6-MHA
691	v(C-S)$_T$	trans carbon and sulphur deformation	6-MHA
828	-C-C-C-	Straight chain alkyl vibration	6-MHA
964	v(C-COO$^-$)	Deprotonated carboxylic group	6-MHA
1026	(C-C)$_T$	Trans alkyl chain stretch	6-MHA
1149	C-C v(CC)/δ(CH)	Skeletal straight chain vibration Stretch and in plane bending vibration	6-MHA aloin
1167	C-C	Skeletal straight chain vibration	6-MHA
1193	ω(CH$_2$)	Wagging vibration	6-MHA
1236		Unassigned peak	
1278	(COO$_2$$^-$) v(CO)/v(CC)	Vibration due to carboxylic group Stretch vibration of ring moiety	6-MHA aloin
1372	υ (CC)/ δ (COH)	In-plane bending and stretch vibration	aloin
1429	(CH$_2$) COO$^-$ v(CC)/δ(CH)	Symmetric deformations Deprotonated carboxylic group Stretch and in plane bending vibration	6-MHA 6-MHA aloin
1483	NH$_3$$^+$	Choline	DMPC
1537	(COO$_2$$^-$)	Stretch of vibration	6-MHA
1583	υ (CC)/ δ (OH) COO$^-$	deformations and stretch vibration deprotonated carboxylic group	aloin 6-MHA
2852	v_s(CH$_2$)	symmetric stretch	6-MHA/aloin
2916	v_{as}(CH$_2$)	Asymmetric stretch	6-MHA/aloin

Figure A-134: a) cathodic and b) anodic overlay spectra of 1 nM aloin/0.1 M NaF solution in the presence of 6-MHA SAM, 3rd trial
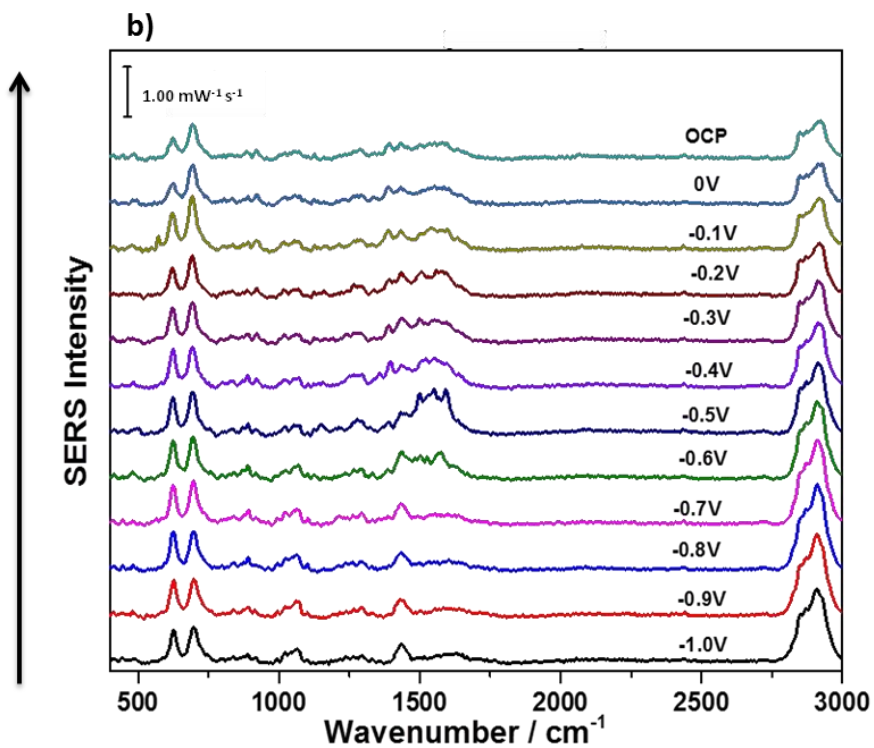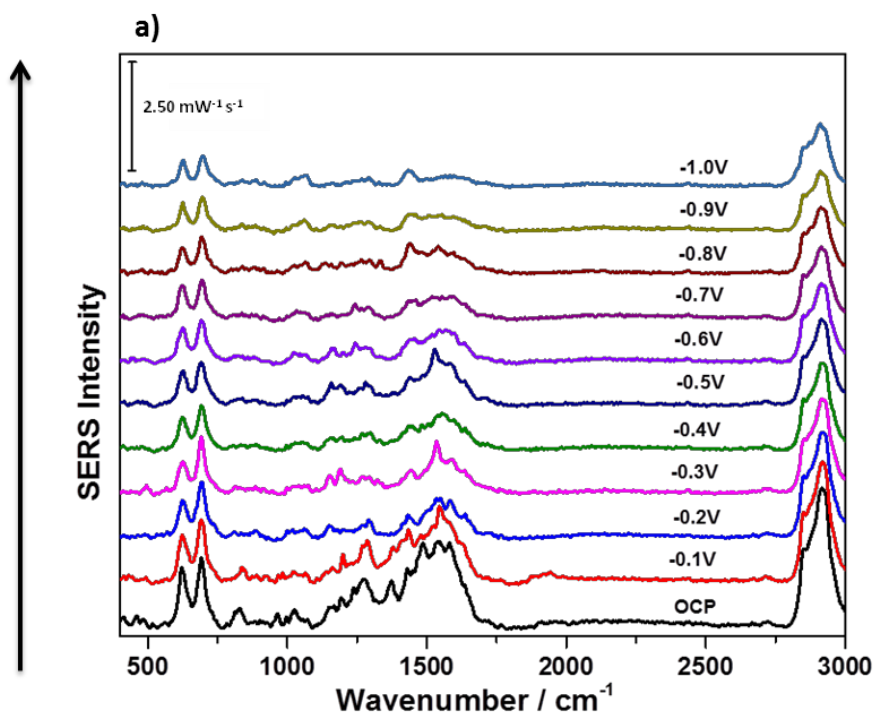
Figure A-135: CV comparison between 1 nM aloin/0.1 M NaF solution in the presence of 6-MHA SAM and 0.1 M NaF solution, 3rd trial
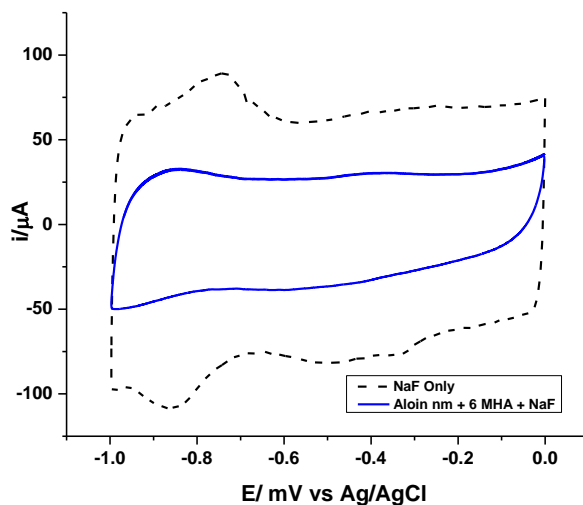
Figure A-136: In air spectrum of deposited DMPC/cholesterol (70:30) bilayer on 6-MHA SAM AgNP modified, 1st trial
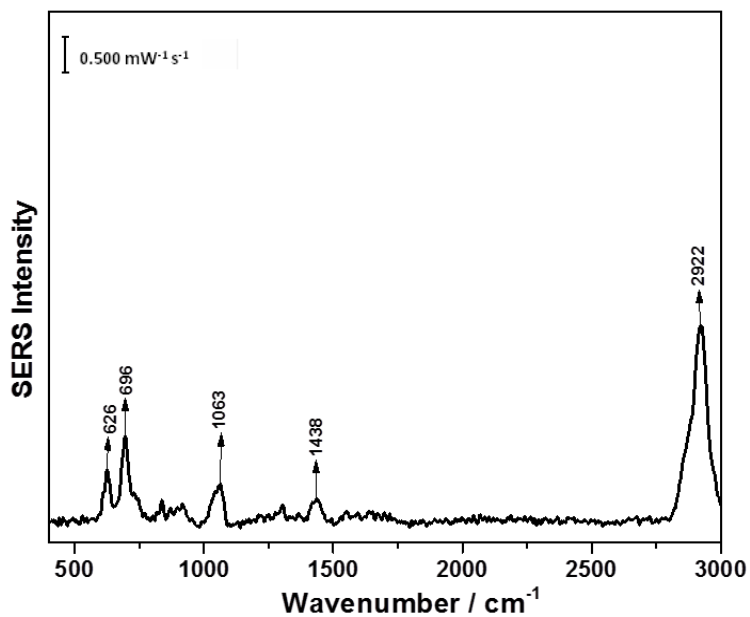
Table A-137: Peak assignment for in air spectrum of deposited DMPC/cholesterol (70:30) bilayer on 6-MHA SAM AgNP modified electrode, 1st trial

Wavenumber (cm^{-1})	Assignment	Description	Molecule
626	v(C-S)$_G$	Gauche carbon and sulphur deformation	6-MHA
696	v(C-S)$_T$	trans carbon and sulphur deformation	6-MHA
1063	v_{as}(PO$_2^-$)	Phosphate diester asymmetric stretch	DMPC
	(C-C)$_T$	Alkyl chain stretch	6-MHA
1438	(CH$_2$)	Symmetric deformations	6-MHA
	COO$^-$	Deprotonated carboxylic group	6-MHA
2922	v_{as}(CH$_2$)	Asymmetric stretch	6-MHA/DMPC

Figure A-138: OCP spectrum of deposited DMPC/cholesterol (70:30) bilayer onto 6-MHA SAM in the presence of 1 nM aloin/0.1 M NaF solution, 1st trial
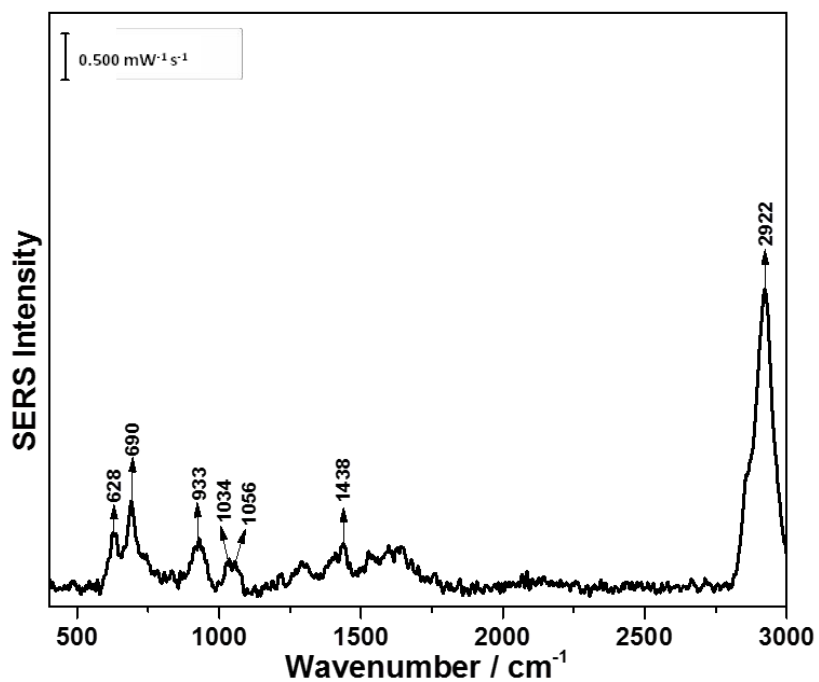
Table A-139: Peak assignment for OCP spectrum of deposited DMPC/cholesterol (70:30) bilayer 6-MHA SAM in the presence of 1 nM aloin/0.1 M NaF solution, 1st trial

Wavenumber (cm^{-1})	Assignment	Description	Molecule
626	v(C-S)$_G$	Gauche carbon and sulphur deformation	6-MHA
690	v(C-S)$_T$	trans carbon and sulphur deformation	6-MHA
933	COO$^-$	Deprotonated carboxylic group	6-MHA
1034	C-C CH$_2$CH$_3$	Alkyl chain stretch Bending of lipids	6-MHA DMPC
1056	v_{as}(PO$_2^-$) (C-C)$_T$	Phosphate diester asymmetric stretch Alkyl chain stretch	DMPC 6-MHA
1438	(CH$_2$) COO$^-$	Symmetric deformations Deprotonated carboxylic group	6-MHA 6-MHA
2922	v_{as}(CH$_2$)	Asymmetric stretch	6-MHA/DMPC

Figure A-140: CV comparison between deposited DMPC/cholesterol (70:30) bilayer on 6-MHA SAM AgNP modified electrode in the presence of 1 nM aloin/0.1 M NaF solution and 0.1 M NaF solution, 1st trial
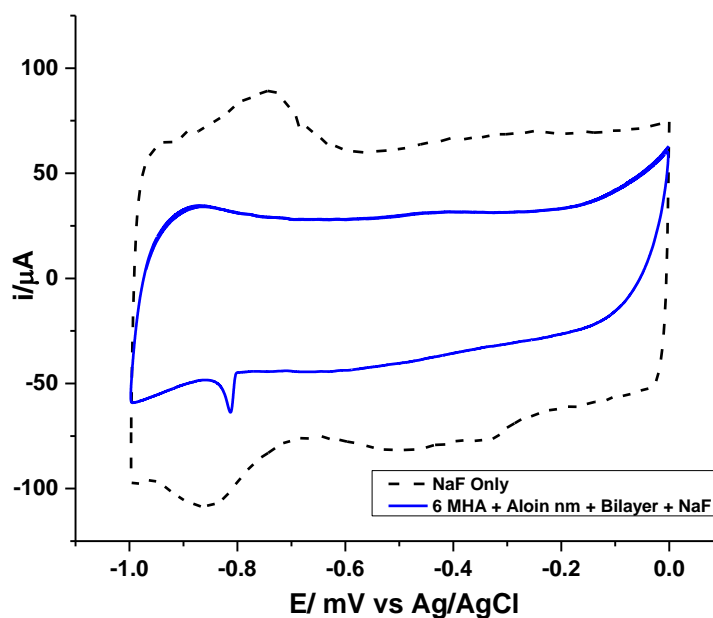
Figure A-141: In air spectrum of deposited DMPC/cholesterol (70:30) bilayer on 6-MHA SAM AgNP modified electrode, 2nd trial
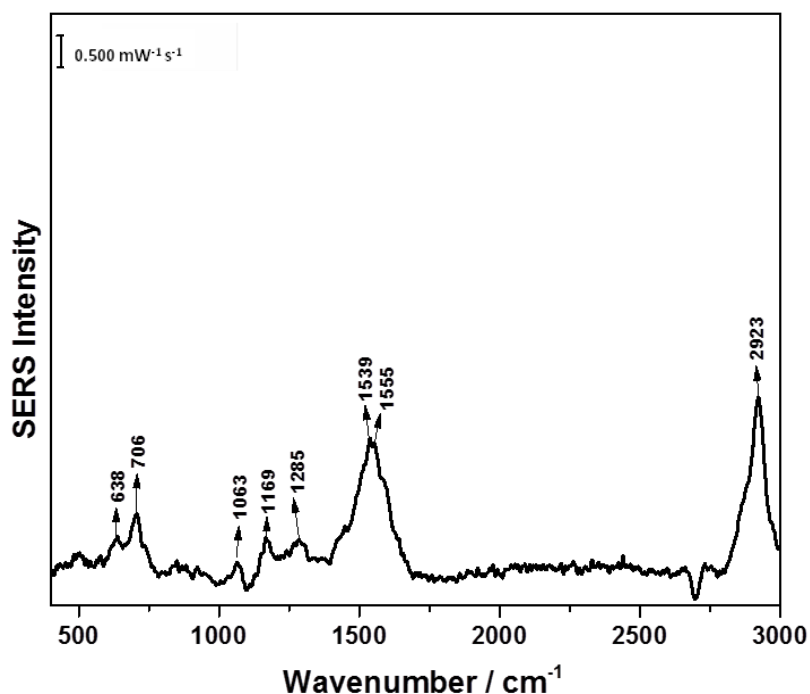
Table A-142: Peak assignment for in air spectrum of deposited DMPC/cholesterol (70:30) bilayer on 6-MHA SAM AgNP modified electrode , 2nd trial

Wavenumber (cm^{-1})	Assignment	Description	Molecule
638	v(C-S)$_G$	Gauche carbon and sulphur deformation	6-MHA
706	v(C-S)$_T$	trans carbon and sulphur deformation	6-MHA
1063	v_{as}(PO$_2^-$)	Phosphate diester asymmetric stretch	DMPC
	(C-C)$_T$	Alkyl chain stretch	6-MHA
1169	C-O	Ester asymmetric stretch	DMPC
	C-C	Skeletal straight chain vibration	6-MHA
1285	ω(CH$_2$)	Wagging vibration	6-MHA/DMPC
1539	v_{as} (COO$_2^-$)	Asymmetric stretch of vibration	6-MHA
1555	v_{as} (COO$_2^-$)	Asymmetric stretch of vibration	6-MHA
2923	v_{as}(CH$_2$)	Asymmetric stretch	6-MHA/DMPC

Figure A-143: OCP spectrum of deposited DMPC/cholesterol (70:30) bilayer on 6-MHA SAM AgNP modified electrode in the presence of 1 nM aloin/0.1 M NaF solution, 2nd trial
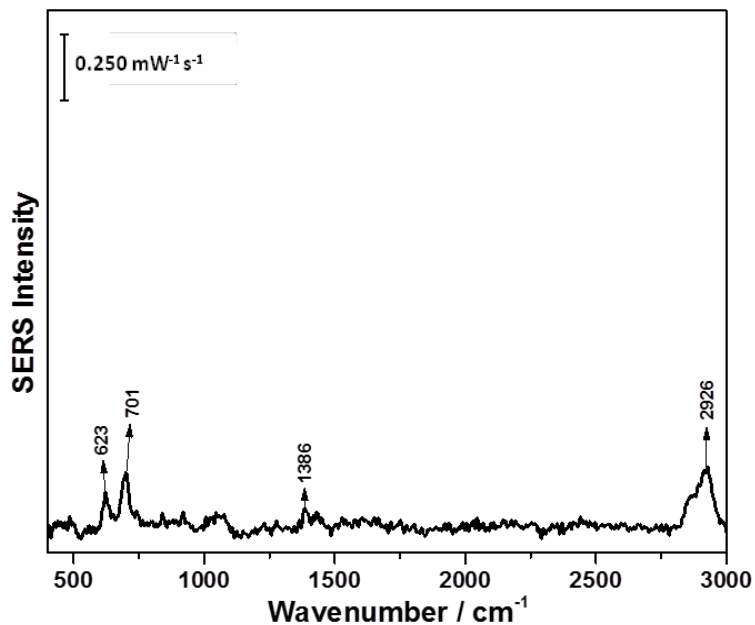
Table A-144: Peak assignment for OCP spectrum of deposited DMPC/cholesterol (70:30) bilayer on 6-MHA SAM AgNP modified electrode in the presence of 1 nM aloin/0.1 M NaF solution, 2nd trial

Wavenumber (cm^{-1})	Assignment	Description	Molecule
623	ν(C-S)$_G$	Gauche carbon and sulphur deformation	6-MHA
701	ν(C-S)$_T$	trans carbon and sulphur deformation	6-MHA
1396	δ(COH)/ ν(CC) ν(COO-Ag)	In-plane bending and stretch Carboxylic group co-ordinated to metal	aloin 6-MHA
2926	ν_{as}(CH$_2$)	Asymmetric stretch	6-MHA/DMPC

Figure A-145: a) cathodic and b) anodic overlay spectra of deposited DMPC/cholesterol (70:30) bilayer on 6-MHA SAM AgNP modified electrode in the presence of 1 nM aloin/0.1 M NaF solution, 2nd trial
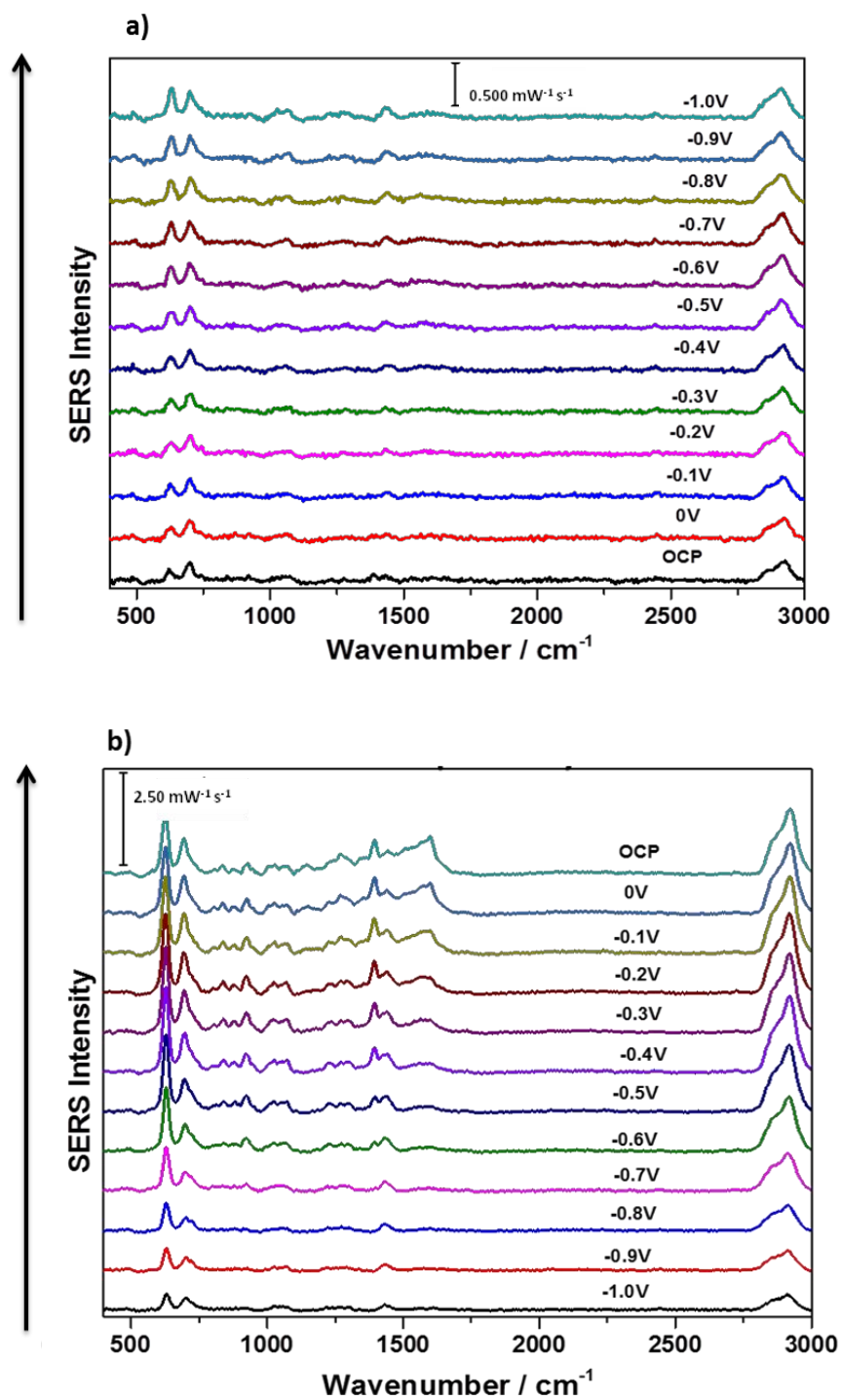
Figure A-146: CV comparison between deposited DMPC/cholesterol (70:30) bilayer on 6-MHA SAM AgNP modified electrode in the presence of 1 nM aloin/0.1 M NaF solution and 0.1 M NaF solution, 2nd trial
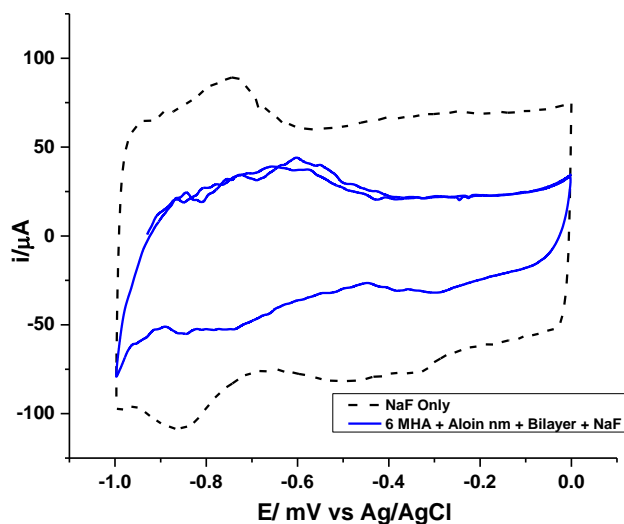
Figure A-147: In air spectrum of deposited DMPC/cholesterol (70:30) bilayer on 6-MHA SAM AgNP modified electrode, 3rd trial
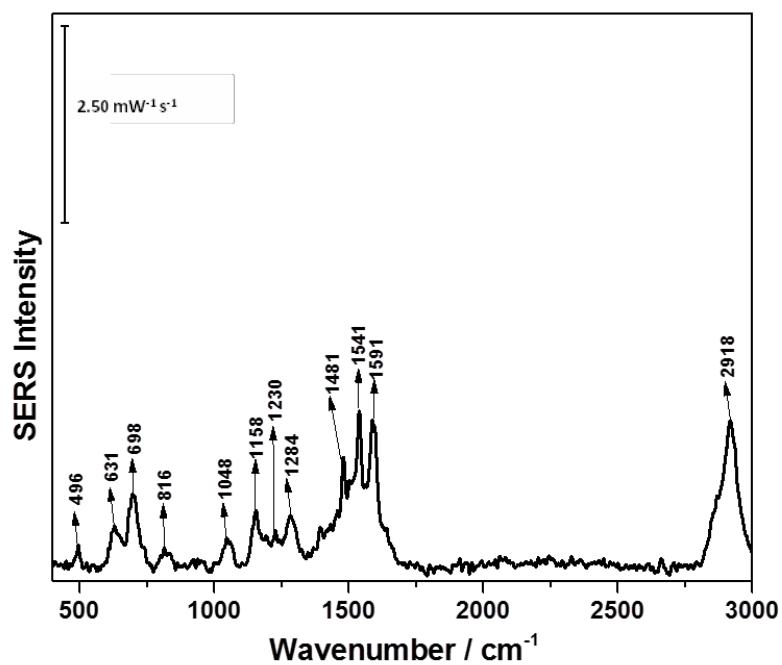
Table A-148: Peak assignment of in air spectrum of deposited DMPC/cholesterol (70:30) bilayer on 6-MHA SAM AgNP modified electrode , 3rd trial

Wavenumber (cm^{-1})	Assignment	Description	Molecule
496	-C-C-C-	Straight chain alkyl vibration	6-MHA
631	v(C-S)$_G$	Gauche carbon and sulphur deformation	6-MHA
698	v(C-S)$_T$	trans carbon and sulphur deformation	6-MHA
816	C-C	Stretch	6-MHA/DMPC
1048	v_{as}(PO$_2^-$)	Phosphate diester asymmetric stretch	DMPC
	(C-C)$_T$	Alkyl chain stretch	6-MHA
1158	C-C	Skeletal straight chain vibration	6-MHA
1230	v_{as}(PO$_2^-$)	Phosphate diester asymmetric stretch	DMPC
1284	ω(CH$_2$)	Wagging vibration	6-MHA/DMPC
1481	NH$_3^+$	Choline	DMPC
1541	v_{as} (COO$_2^-$)	Asymmetric stretch of vibration	6-MHA
1591	v_{as} (COO$_2^-$)	Asymmetric stretch of vibration	6-MHA
2918	v_{as}(CH$_2$)	Asymmetric stretch	6-MHA/DMPC

Figure A-149: OCP spectrum of deposited DMPC/cholesterol (70:30) bilayer on 6-MHA SAM AgNP modified electrode in the presence of 1 nM aloin/0.1 M NaF solution, 3rd trial
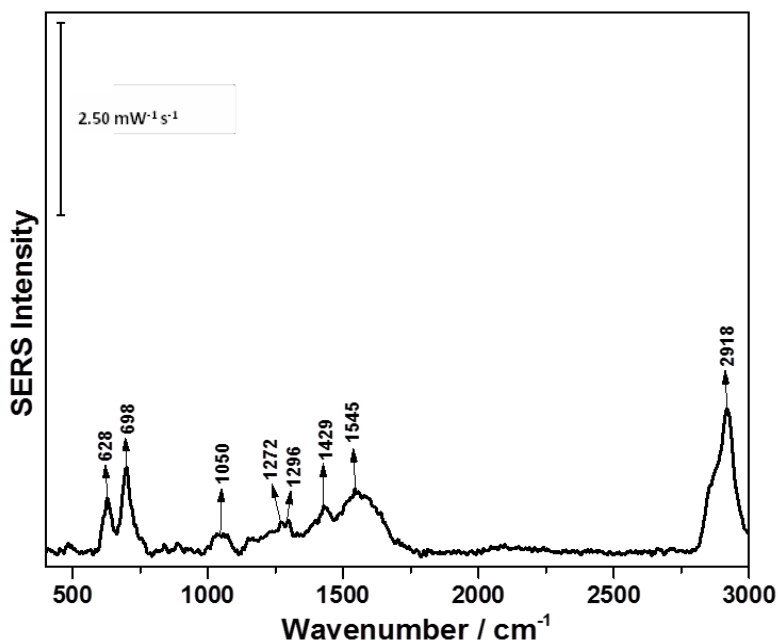
Table A-150: Peak assignment of OCP spectrum of deposited DMPC/cholesterol (70:30) bilayer on 6-MHA SAM AgNP modified electrode in the presence of 1 nM aloin/0.1 M NaF solution, 3rd trial

Wavenumber (cm^{-1})	Assignment	Description	Molecule
628	v(C-S)$_G$	Gauche carbon and sulphur deformation	6-MHA
698	v(C-S)$_T$	trans carbon and sulphur deformation	6-MHA
1050	v_{as}(PO$_2^-$)	Phosphate diester asymmetric stretch	DMPC
	(C-C)$_T$	Alkyl chain stretch	6-MHA
1272		Presence of a phospholipid	DMPC
		Unassigned 6-MHA monolayer peak	6-MHA
1296	ω(CH$_2$) v(CO)/ v(CC)/ δ(CCC)	Wagging vibration Stretch and in-plane bending vibration	6-MHA aloin
1429	(CH$_2$) COO$^-$ δ_d(-CH$_2$)	Symmetric deformation Deprotonated carboxylic deformation for cholesterol	6-MHA/DMPC 6-MHA cholesterol
1545	v_{as} (COO$_2^-$)	Asymmetric stretch of vibration	6-MHA
2918	v_{as}(CH$_2$)	Asymmetric stretch	6-MHA/DMPC

Figure A-151: a) cathodic and b) anodic overlay spectra of deposited DMPC/cholesterol (70:30) bilayer on 6-MHA SAM AgNP modified electrode in the presence of 1 nM aloin/0.1 M NaF solution, 3rd trial
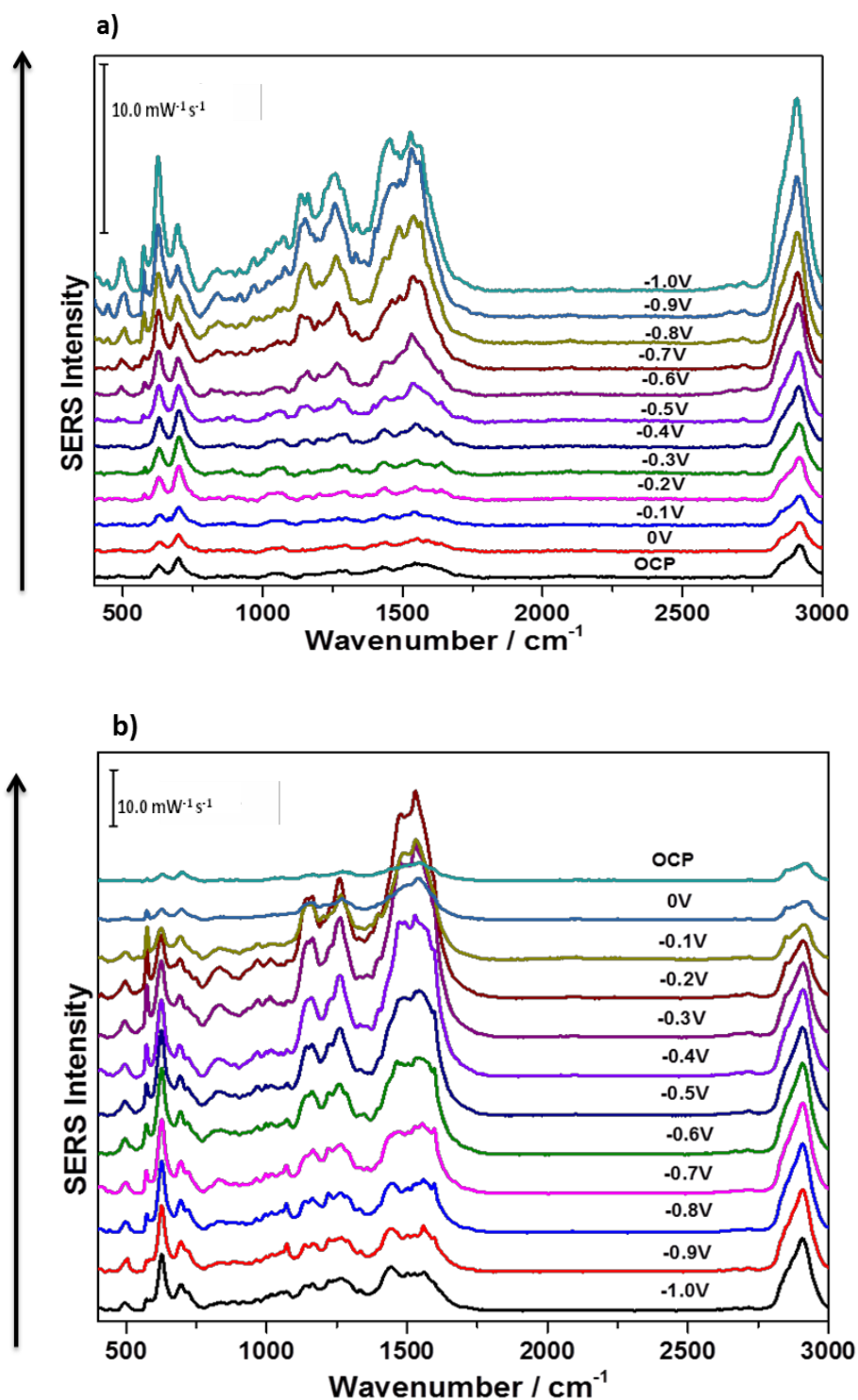
Figure A-152: CV comparison between deposited DMPC/cholesterol (70:30) bilayer on 6-MHA SAM AgNP modified electrode in the presence of 1 nM aloin/0.1 M NaF solution and 0.1 M NaF solution, 3rd trial
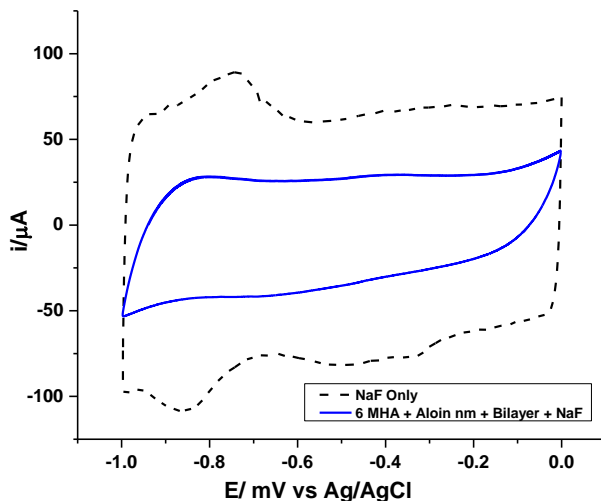
Figure A-153: Anodic OCP spectrum of 1 µM aloin/0.1 M NaF solution with AgNP modified electrode, 1sttrial
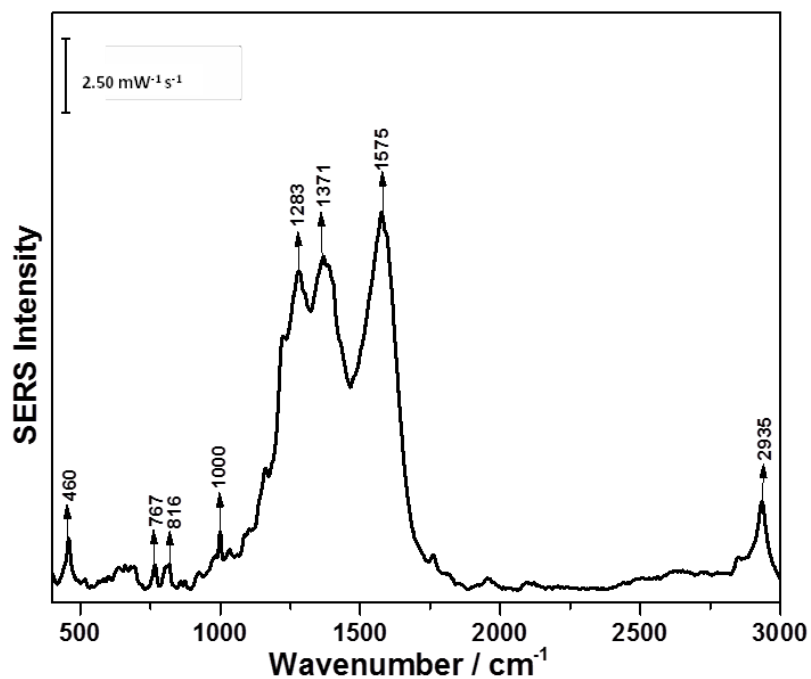
Table A-154: Peak assignment for OCP anodic spectrum of 1 µM aloin/0.1 M NaF solution with AgNP modified electrode, 1ˢᵗtrial

Wavenumber (cm⁻¹)	Assignment	Description	Molecule
460		Skeletal vibration	aloin
767	γ(CH)/ γ(C=O)/τ(CCC)	Out of plane and torsion vibration	aloin
816	ν(CC)/δ(OH)	Stretch and in plane bending vibration	aloin
1000	ν(CC)/δ(CCC)	Stretch and in plane bending vibration	aloin
1283	δ(OH)/ν(CC)	In-plane bending and stretch vibration	aloin
1371		Presence of glucose and OH stretch	aloin
1575	δ(OH)/ν(CC)/δ(CH)	In-plane bending and stretch vibration	aloin
2935	ν_{as}(CH$_2$)	Asymmetric stretch	aloin

Figure A-155: CV comparison between 1 µM aloin/0.1 M NaF solution and 0.1 M NaF solution, 1ˢᵗtrial
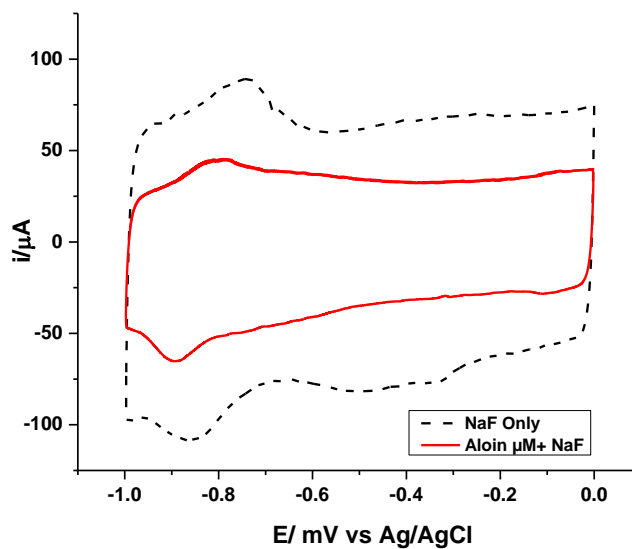
Figure A-156: Anodic OCP spectrum of 1 µM aloin/0.1 M NaF solution with AgNP modified electrode, 2nd trial
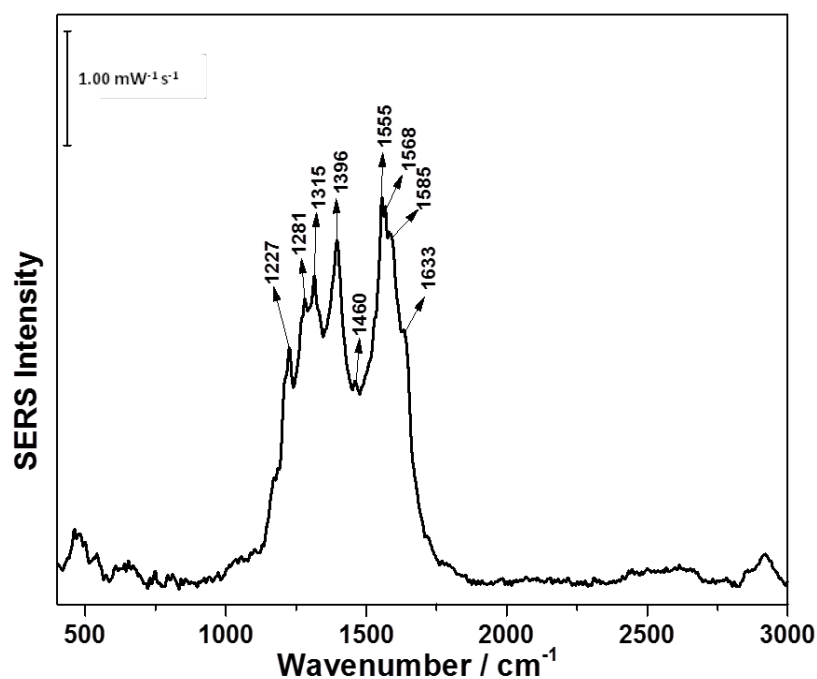
Table A-157: Peak assignment for OCP anodic spectrum of 1 µM aloin/0.1 M NaF solution with AgNP modified electrode, 2nd trial

Wavenumber (cm^{-1})	Assignment	Description	Molecule
460		Skeletal vibration	aloin
623		Skeletal vibration Presence of citrate	aloin citrate
689	γC=O	Out of-plane bending in ring Presence of citrate	aloin citrate
814	ν(CC)/δ(OH)	Stretch and in plane bending vibration	aloin
1014	ν(CC)/δ(CC)	Stretch and in plane bending vibration	aloin
1227	δ(OH)/ν(CC)/δ(CH$_{Glu}$)	In-plane bending and stretch vibration	aloin
1279	δ(OH)/ν(CC)	In-plane bending and stretch vibration	aloin
1400	ν(CC)/δ(CH)	Stretch and in plane bending vibration	aloin
1432	ν(CC)/δ(CH)	Stretch and in plane bending vibration	aloin

Figure A-158: a) cathodic and b) anodic overlay spectra of 1 µM aloin/0.1 M NaF solution with AgNP modified electrode, 2nd trial
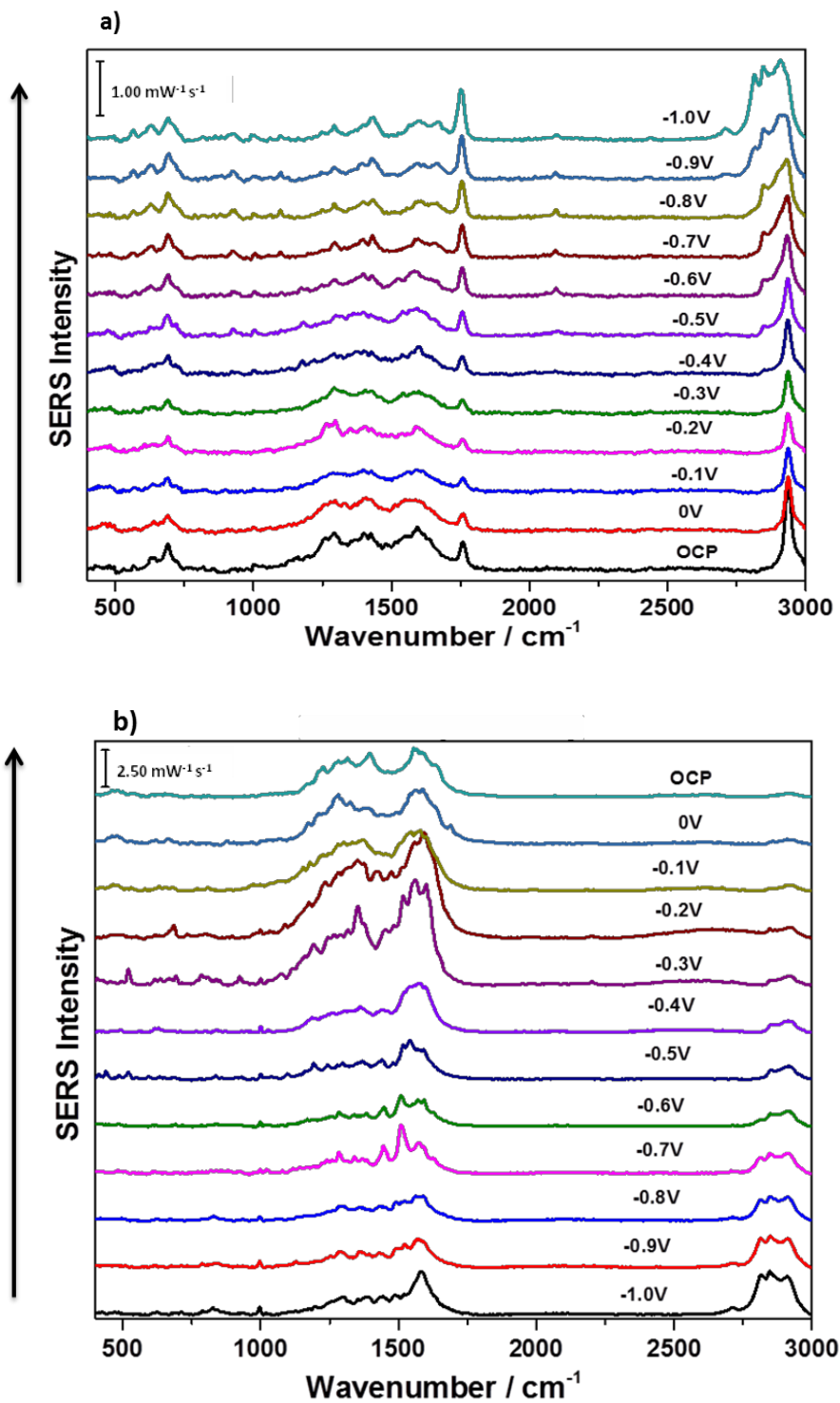
Figure A-159: CV comparison between 1 μM aloin/0.1 M NaF solution and 0.1 M NaF solution, 2nd trial
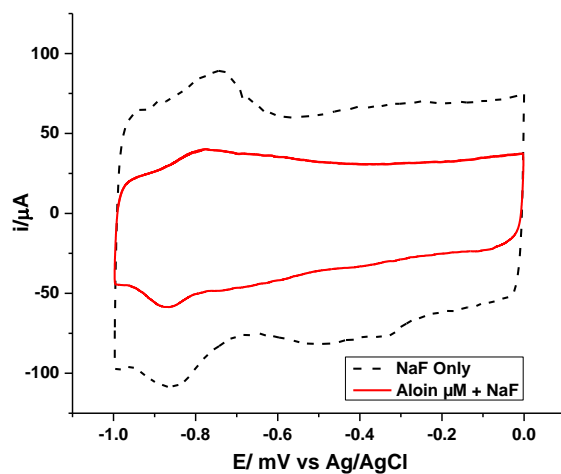
Figure A-160: Anodic OCP spectrum of 1 μM aloin/0.1 M NaF solution with AgNP modified electrode, 3rd trial
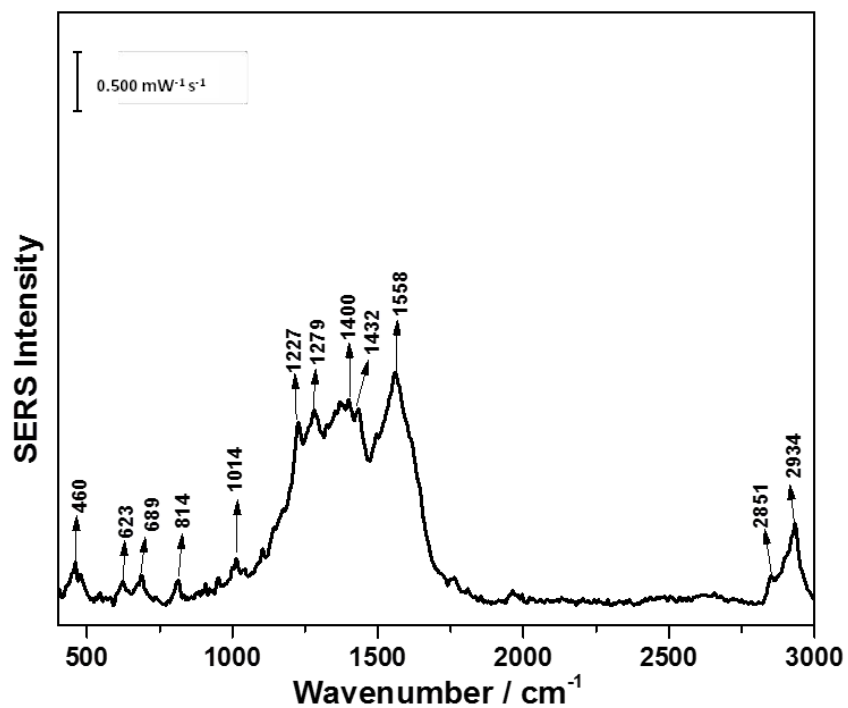
Table A-161: Peak assignment for OCP anodic spectrum of 1 µM aloin/0.1 M NaF solution with AgNP modified electrode, 3rd trial

Wavenumber (cm^{-1})	Assignment	Description	Molecule
1227	δ(OH)/ν(CC)/δ(CH$_{Glu}$)	In-plane bending and stretch vibration	aloin
1281	δ(OH)/ν(CC)	In-plane bending and stretch vibration	aloin
1315	δ(OH)/ν(CC)	In-plane bending and stretch vibration	aloin
1396	ν(CC)/δ(CH)	Stretch and in plane bending vibration	aloin
1460	δ(OH)/ν(CC)	In-plane bending and stretch vibration	aloin
1555	δ(OH)/ν(CC)	In-plane bending and stretch vibration	aloin
1568	ν(CC)	In-plane bending and stretch vibration	aloin
1585	δ(OH)/ν(CC)	In-plane bending and stretch vibration	aloin
1633	C=O	Presence of a carbonyl group	aloin

Figure A-162: a) cathodic and b) anodic overlay spectra of 1 μM aloin/0.1 M NaF solution with AgNP modified electrode, 3rd trial
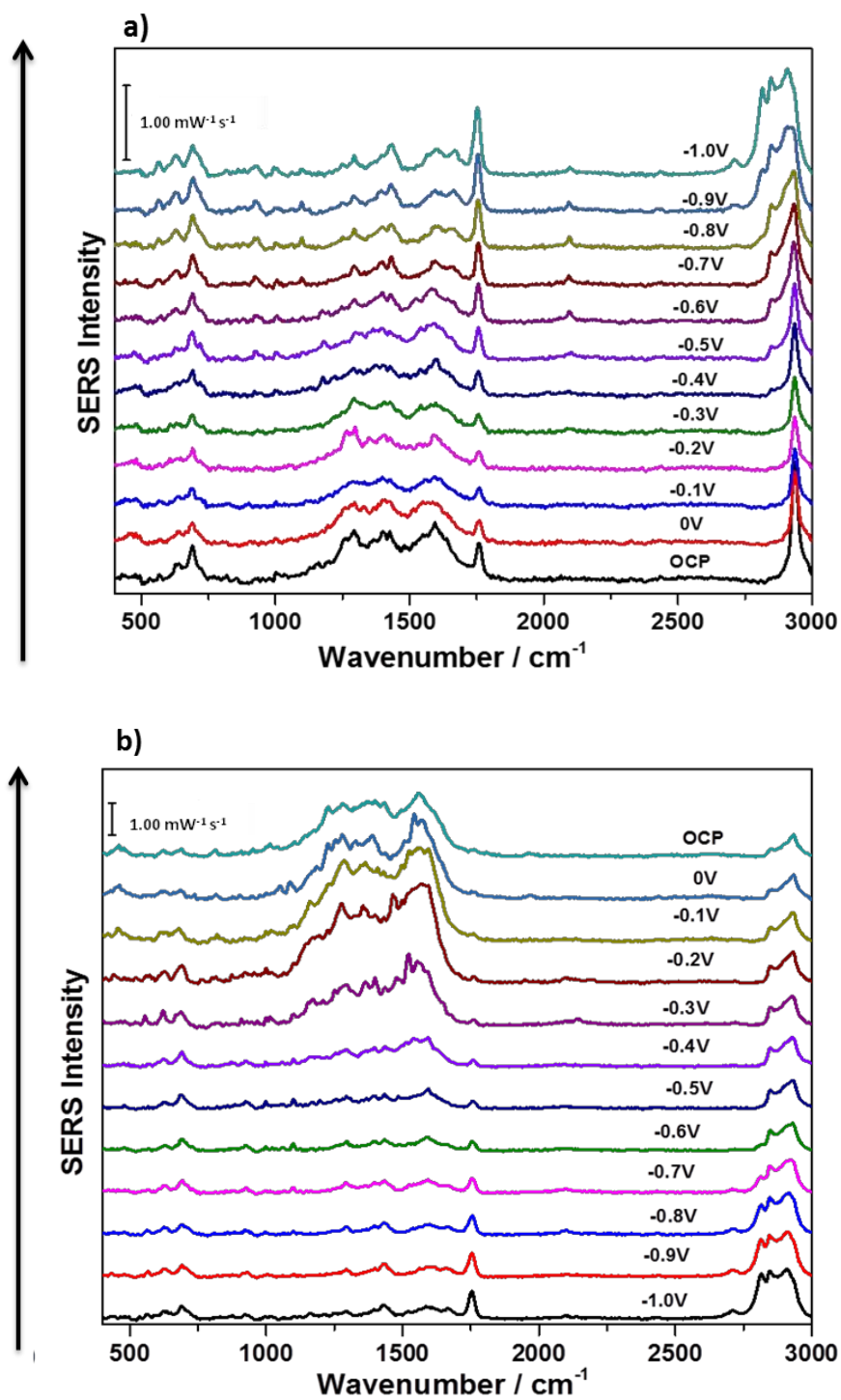
Figure A-163: CV comparison between 1 µM aloin/0.1 M NaF solution and 0.1 M NaF solution, 3rd trial
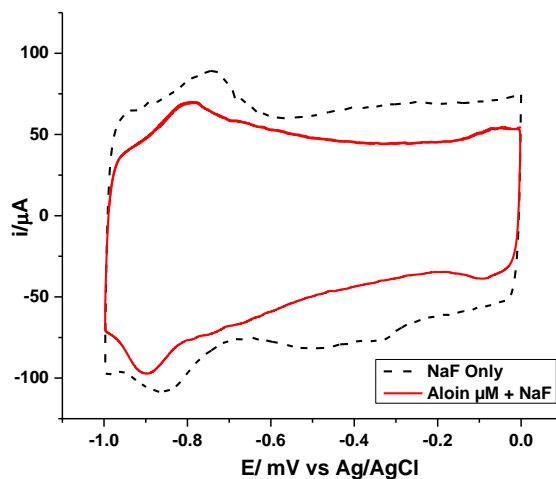
Figure A-164: OCP spectrum of 1 µM aloin/0.1 M NaF solution in the presence of 6-MHA SAM, 1st trial
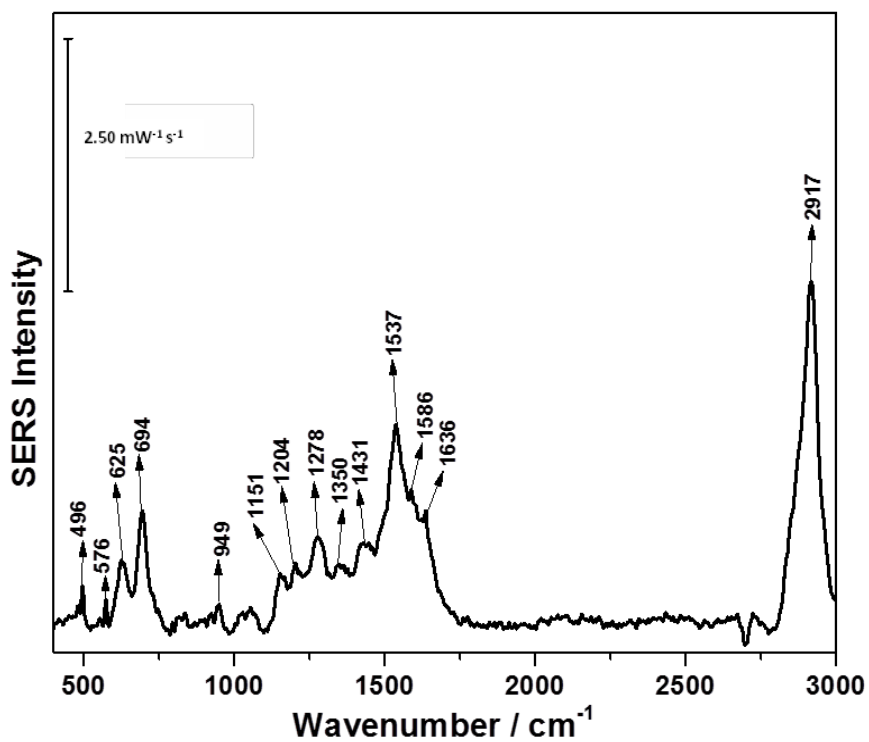
Table A-165: Peak assignment of OCP spectrum of 1 μM aloin/0.1 M NaF solution in the presence of 6-MHA SAM, 1st trial

Wavenumber (cm^{-1})	Assignment	Description	Molecule
496	(-C-C-C-)$_G$	gauche straight chain vibration	6-MHA
576	γ(CCO)/ω(OCO)	Wagging and out of plane bending	6-MHA
625	v(C-S)$_G$	Gauche carbon and sulphur deformation	6-MHA
694	v(C-S)$_T$	trans carbon and sulphur deformation	6-MHA
949	v(C-COO$^-$)	Deprotonated carboxylic group	6-MHA
1151	(CC)/υ(CH)	Stretch and in-plane bending vibration	aloin
1204	ω(CH$_2$)	Wagging vibration	6-MHA
1278	ω(CH$_2$) υ(CC)/δ(CH)/CO	Wagging vibration In-plane bending vibration	6-MHA aloin
1350	CC/COH	Stretch vibration	aloin
1431	(CH$_2$) COO$^-$	Symmetric deformations Deprotonated carboxylic group	6-MHA 6-MHA
1537	v_{as} (COO$_2^-$)	Asymmetric stretch of vibration	6-MHA
1586	COO$^-$ C=O	Deprotonated carboxylic group Presence of a carbonyl	6-MHA 6-MHA
1636	C=O	Presence of a carbonyl group	6-MHA
2917	v_{as}(CH$_2$)	Asymmetric stretch	6-MHA/aloin

Figure A-166: CV comparison between 1 μM aloin/0.1 M NaF solution in the presence of 6-MHA SAM and 0.1 M NaF solution, 1st trial
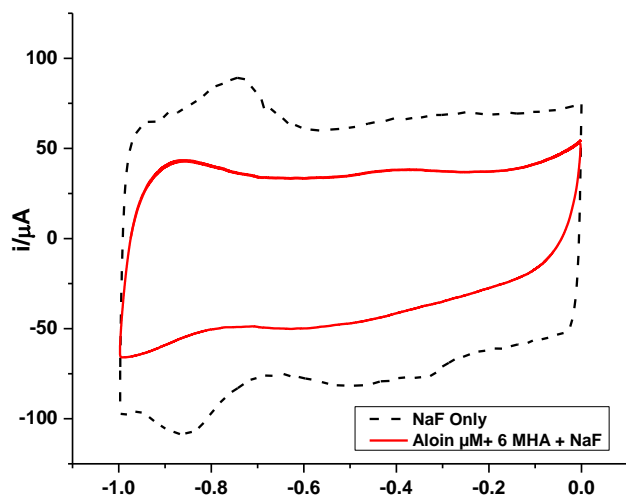
Figure A-167: OCP spectrum of 1 μM aloin/0.1 M NaF solution in the presence of 6-MHA SAM, 2nd trial
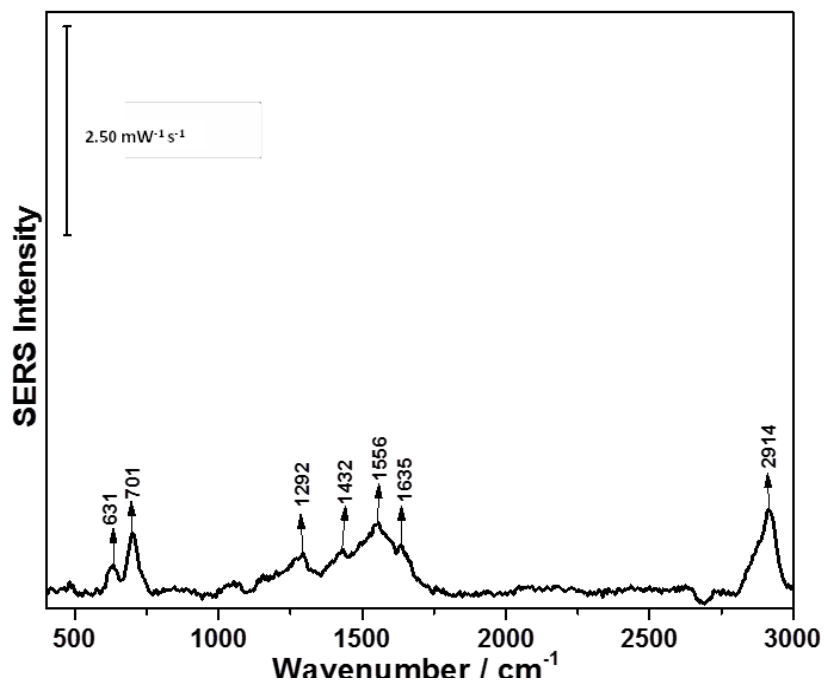
Table A-168: Peak assignment of OCP spectrum of 1 µM aloin/0.1 M NaF solution in the presence of 6-MHA SAM, 2nd trial

Wavenumber (cm^{-1})	Assignment	Description	Molecule
631	v(C-S)$_G$	Gauche carbon and sulphur deformation	6-MHA
701	v(C-S)$_T$	trans carbon and sulphur deformation	6-MHA
1292	ω(CH$_2$) v(CO)/ v(CC)/ δ(CCC)	Wagging vibration Stretch and in-plane bending vibration	6-MHA aloin
1432	(CH$_2$) COO$^-$	Symmetric deformations Deprotonated carboxylic group	6-MHA 6-MHA
1566	COO$^-$ v(CC)	Deformations of carboxyl group In plane bending	6-MHA aloin
1635	C=O	Presence of a carbonyl group	6-MHA
2914	v_{as}(CH$_2$)	Asymmetric stretch	6-MHA/aloin

Figure A-169: a) cathodic and b) anodic overlay spectra of 1 μM aloin/0.1 M NaF solution in the presence of 6-MHA SAM, 2nd trial
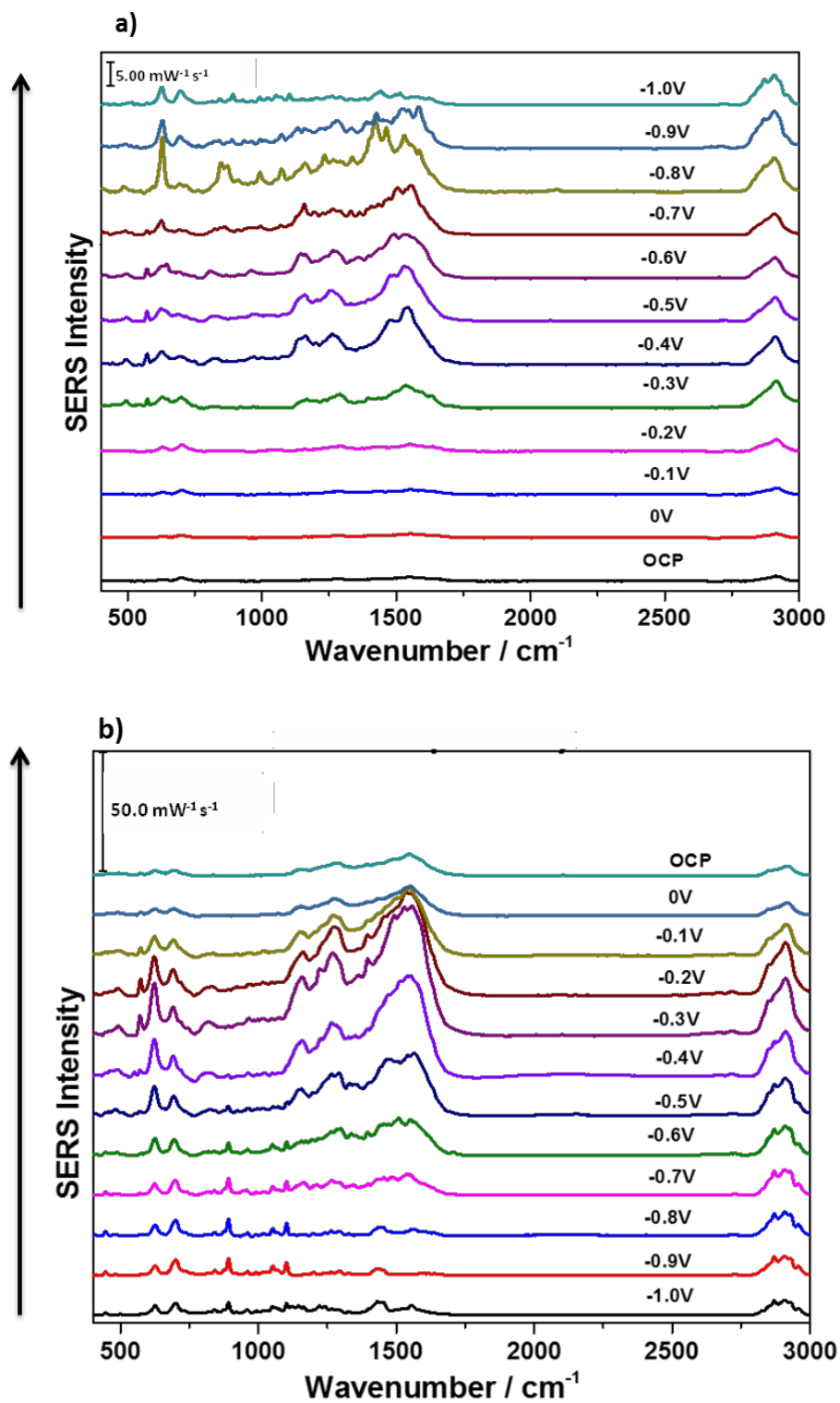
Figure A-170: CV comparison between aloin 1 µM aloin/0.1 M NaF solution in the presence of 6-MHA SAM and 0.1 M NaF solution, 2ⁿᵈ trial
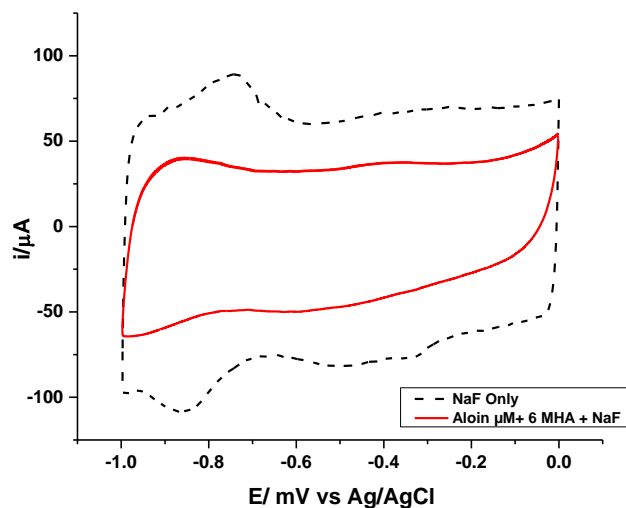
Figure A-171: In air spectrum of deposited DMPC/cholesterol (70:30) bilayer on 6-MHA SAM AgNP modified electrode, 1ˢᵗ trial
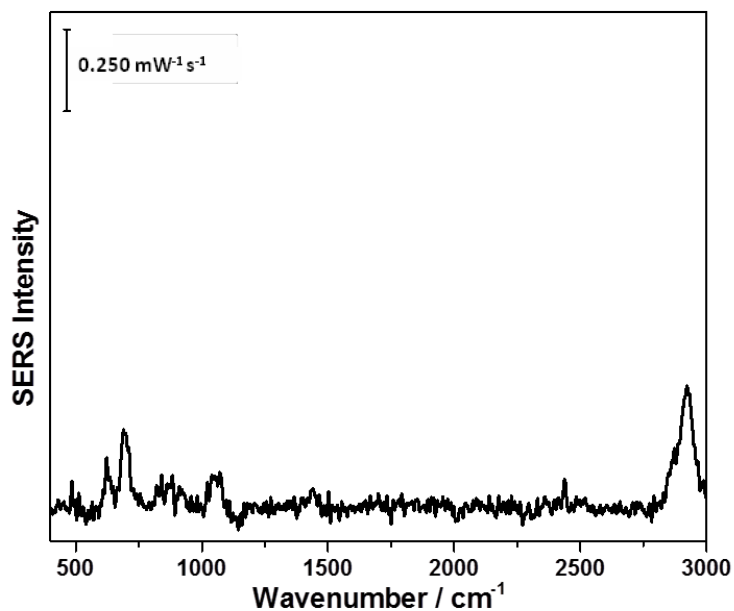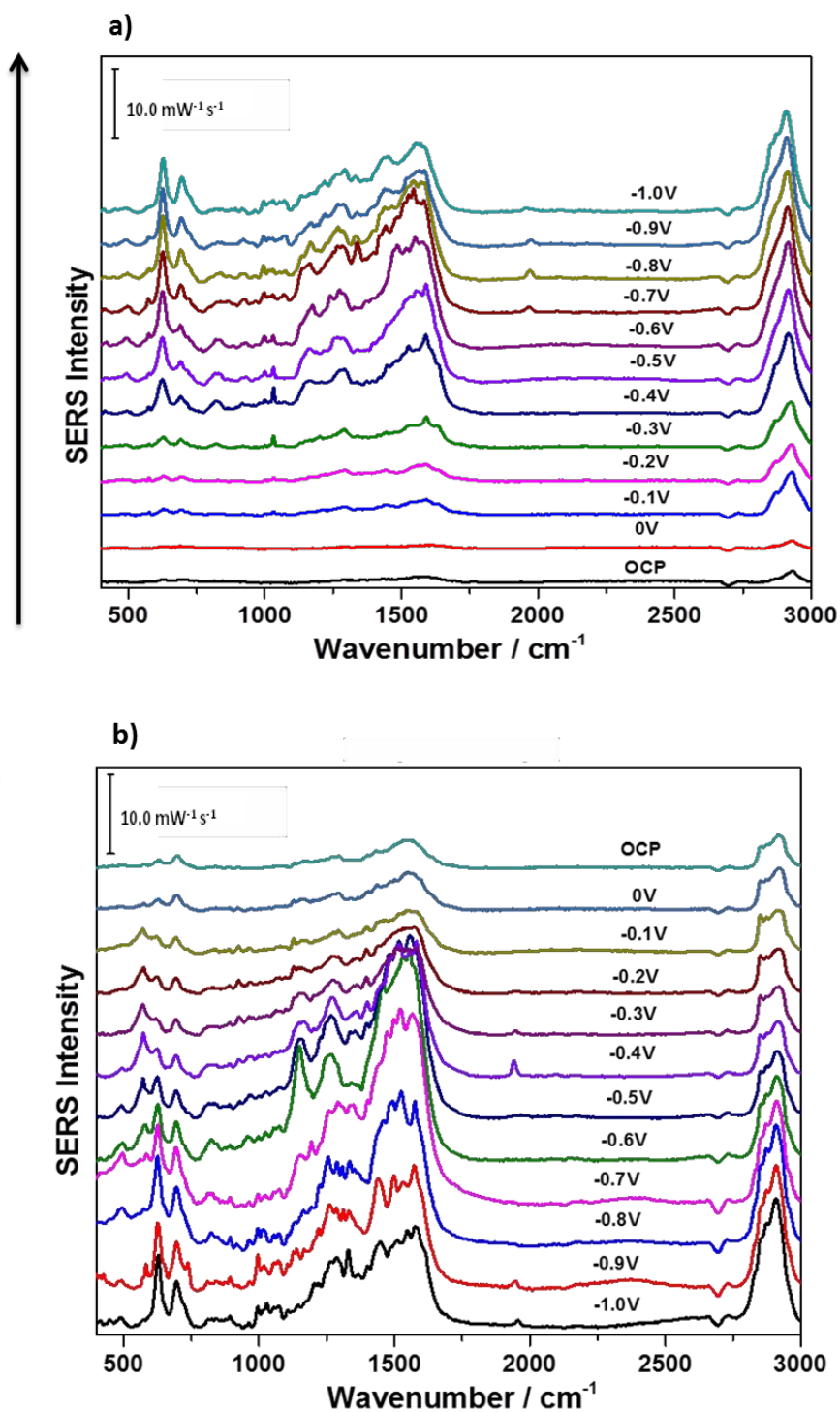
Figure A-172: OCP spectrum of deposited DMPC/cholesterol (70:30) bilayer on 6-MHA SAM AgNP modified electrode in the presence of 1 μM aloin/0.1 M NaF solution, 1st trial
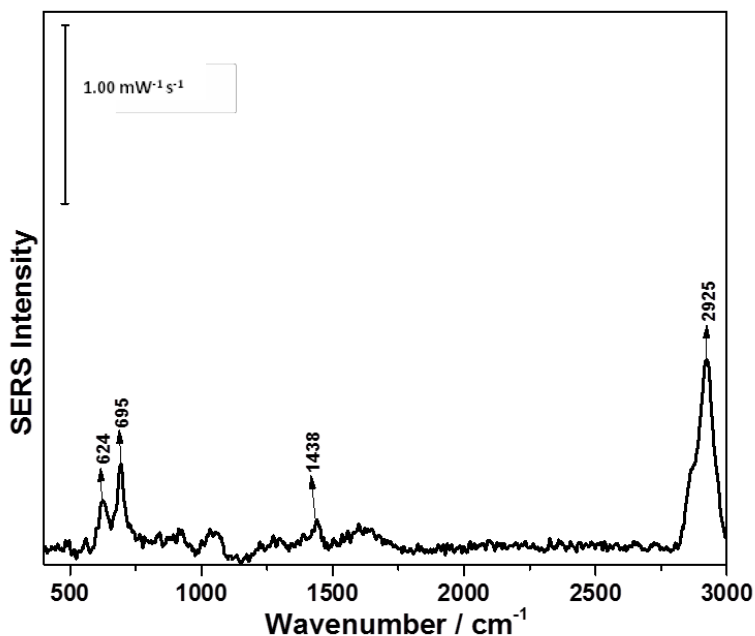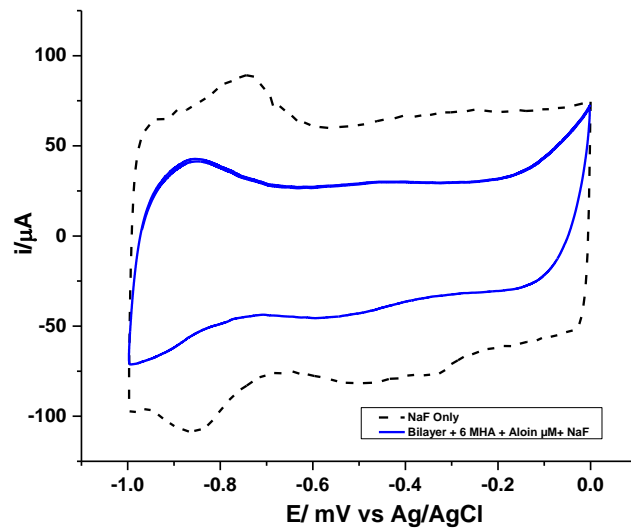

Table A-173: Peak assignment of OCP spectrum of deposited DMPC/cholesterol (70:30) bilayer 6-MHA SAM in the presence of 1 μM aloin/0.1 M NaF solution, 1st trial

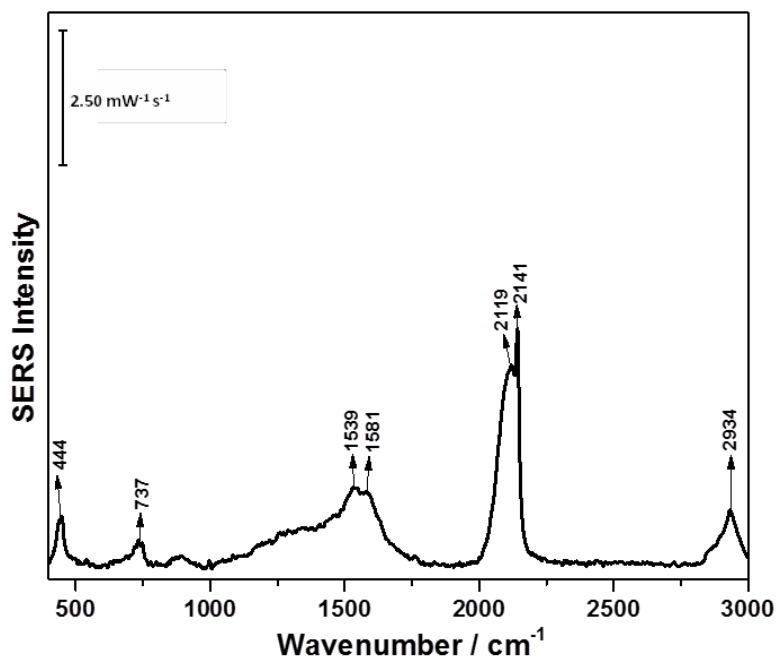| Wavenumber (cm^{-1})	Assignment	Description	Molecule
624	v(C-S)$_G$	Gauche carbon and sulphur deformation	6-MHA
695	v(C-S)$_T$	trans carbon and sulphur deformation	6-MHA
1438	(CH$_2$) COO$^-$ δ_d(-CH$_2$)	Symmetric deformation Deprotonated carboxylic deformation for cholesterol	6-MHA/DMPC 6-MHA cholesterol
2925	v_{as}(CH$_2$)	Asymmetric stretch	6-MHA/DMPC

Figure A-174: CV comparison between deposited DMPC/cholesterol (70:30) bilayer on 6-MHA SAM AgNP modified electrode in the presence of 1 μM aloin/0.1 M NaF solution and 0.1 M NaF solution, 1sttrial
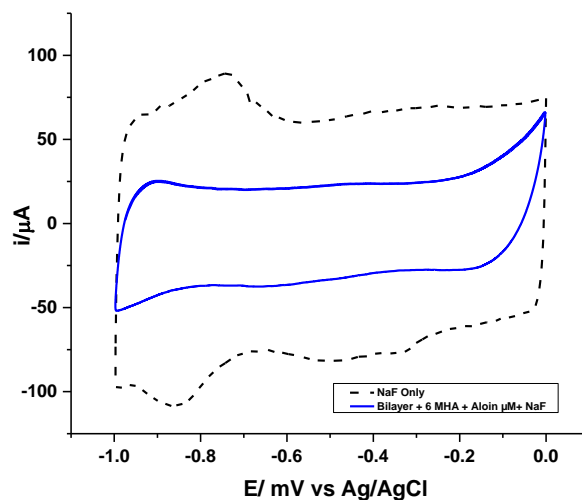

Figure A-175: In air spectrum of deposited DMPC/cholesterol (70:30) bilayer on 6-MHA SAM AgNP modified electrode, 2ndtrial
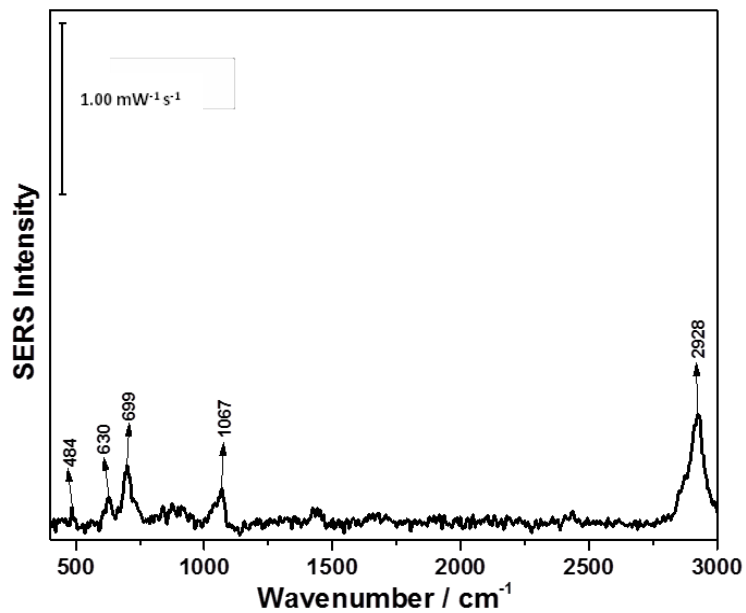
Table A-176: Peak assignment of in air spectrum of deposited DMPC/cholesterol (70:30) bilayer on 6-MHA SAM AgNP modified electrode, 2[nd]trial

Wavenumber (cm^{-1})	Assignment	Description	Molecule
484	$(-C-C-C-)_G$	gauche straight chain alkyl vibration	6-MHA
630	$v(C-S)_G$	Gauche carbon and sulphur deformation	6-MHA
699	$v(C-S)_T$	trans carbon and sulphur deformation	6-MHA
1067	$v_{as}(PO_2^-)$	Phosphate diester asymmetric stretch	DMPC
	$(C-C)_T$	Alkyl chain stretch	6-MHA
2924	$v_{as}(CH_2)$	Asymmetric stretch	6-MHA/DMPC

Figure A-177: OCP spectrum of deposited DMPC/cholesterol (70:30) bilayer on 6-MHA SAM AgNP modified electrode in the presence of 1 μM aloin/0.1 M NaF solution, 2[nd]trial
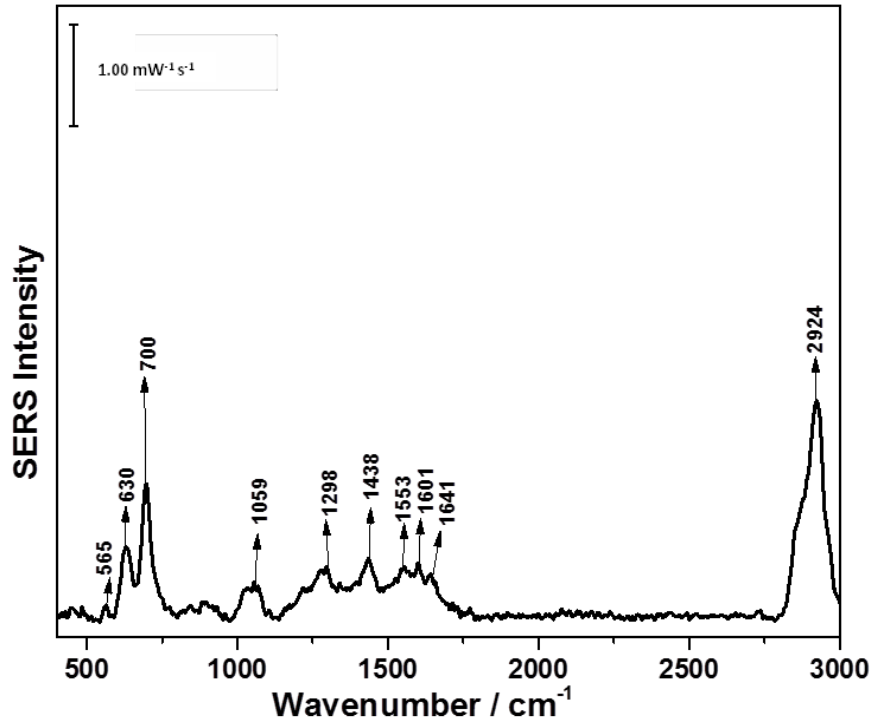
Table A-178: Peak assignment of OCP spectrum of deposited DMPC/cholesterol (70:30) bilayer on 6-MHA SAM AgNP modified electrode in the presence of 1 μM aloin/0.1 M NaF solution, 2nd trial

Wavenumber (cm^{-1})	Assignment	Description	Molecule
565	COO$^-$	Carboxylic deformations	6-MHA
630	v(C-S)$_G$	Gauche carbon and sulphur deformation	6-MHA
700	v(C-S)$_T$	trans carbon and sulphur deformation	6-MHA
1059	v_{as}(PO$_2^-$)	Phosphate diester asymmetric stretch	DMPC
	(C-C)$_T$	Alkyl chain stretch	6-MHA
1298	ω(CH$_2$) v(CO)/ v(CC)/ δ(CCC)	Wagging vibration Stretch and in-plane bending vibration	6-MHA aloin
1438	(CH$_2$) COO$^-$ δ_d(-CH$_2$)	Symmetric deformation Deprotonated carboxylic deformation for cholesterol	6-MHA/DMPC 6-MHA cholesterol
1553	v_{as} (COO$_2^-$)	Asymmetric stretch of vibration	6-MHA
1601	v_{as} (COO$_2^-$) C=C	Asymmetric stretch of vibration Presence of a double bond	6-MHA cholesterol
1641	O-H C=O	Intermolecular bending mode Presence of a carbonyl	Water 6-MHA
2924	v_{as}(CH$_2$)	Asymmetric stretch	6-MHA/DMPC

Figure A-179: a) cathodic and b) anodic overlay spectra of deposited DMPC/cholesterol (70:30) bilayer on 6-MHA SAM AgNP modified electrode in the presence of 1 μM aloin/0.1 M NaF solution, 2nd trial
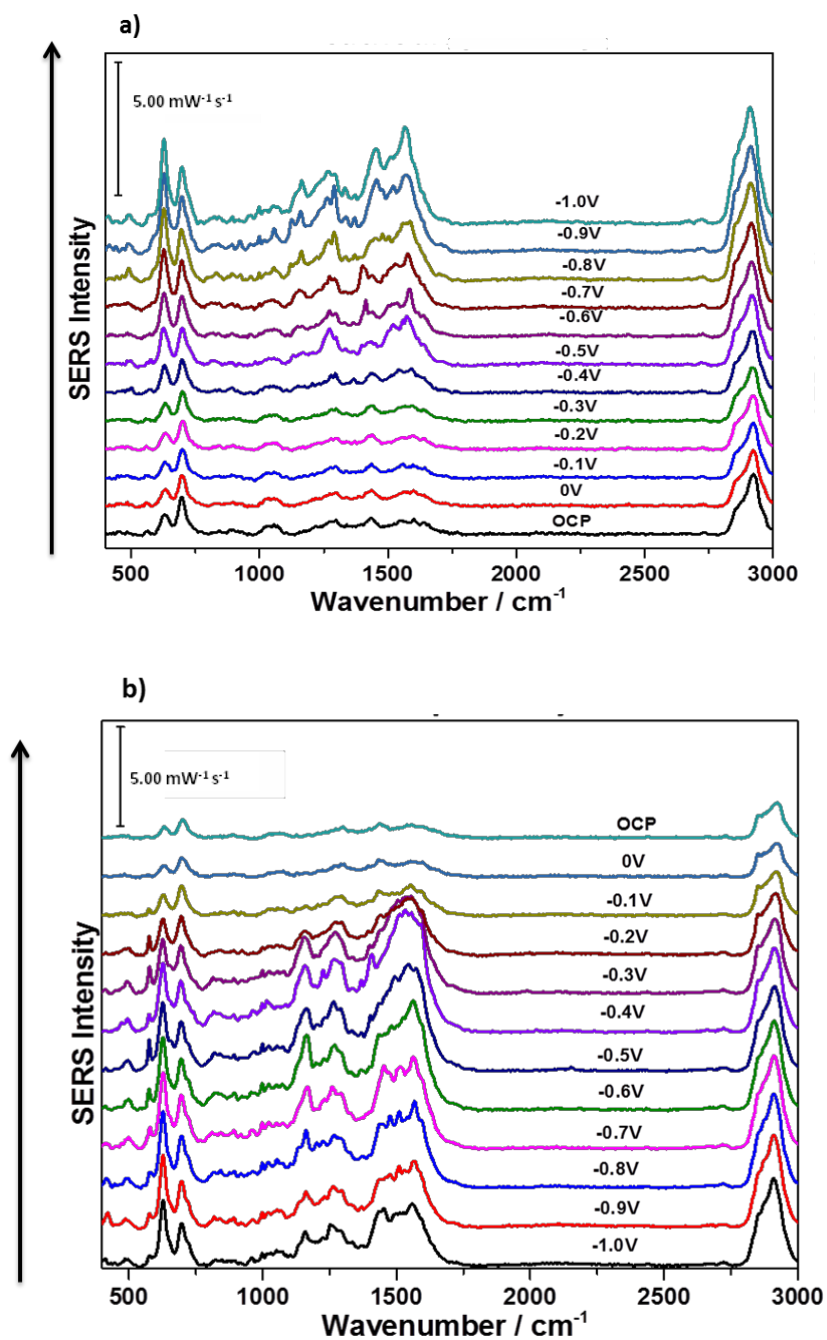
Figure A-180: CV comparison between deposited DMPC/cholesterol (70:30) bilayer on 6-MHA SAM AgNP modified electrode in the presence of 1 µM aloin/0.1 M NaF solution and 0.1 M NaF solution, 2nd trial
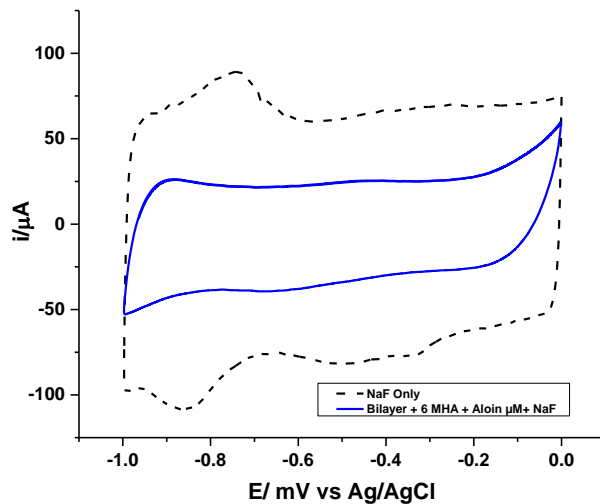
Figure A-181: In air spectrum of deposited DMPC/cholesterol (70:30) bilayer on 6-MHA SAM AgNP modified electrode, 3rd trial
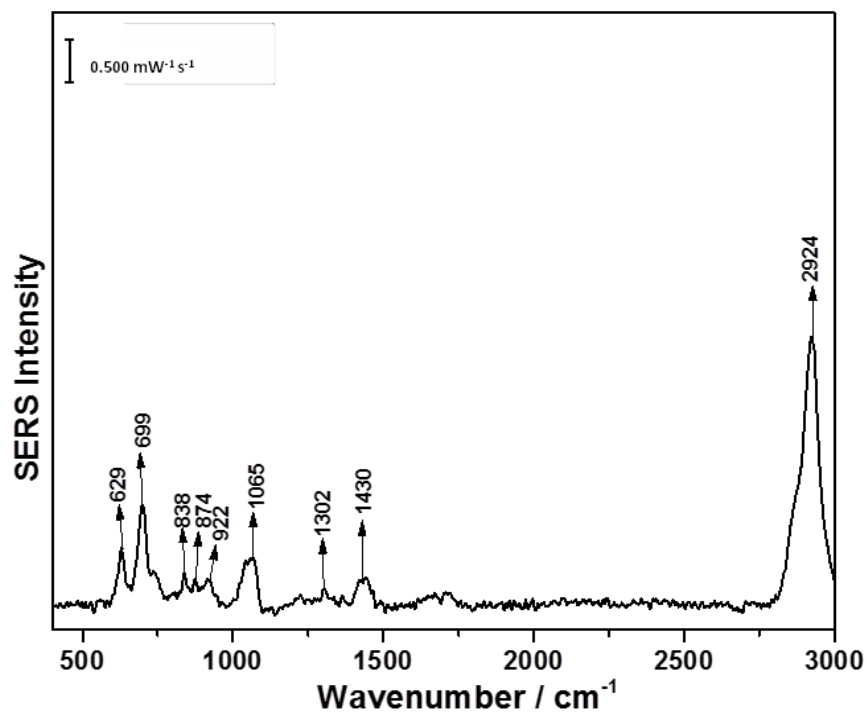
Table A-182: Peak assignment of in air spectrum of deposited DMPC/cholesterol (70:30) bilayer on 6-MHA SAM AgNP modified electrode, 3rd trial

Wavenumber (cm^{-1})	Assignment	Description	Molecule
629	v(C-S)$_G$	Gauche carbon and sulphur deformation	6-MHA
699	v(C-S)$_T$	trans carbon and sulphur deformation	6-MHA
838	(CH$_2$)$_G$ O-P-O	Methylene rocking Stretch vibration	6-MHA DMPC
874	C-N$^+$(CH$_3$)	Antisymmetric choline stretch vibration	DMPC
922	COO$^-$	Deprotonated carboxyl group	6-MHA
1065	v_{as}(PO$_2^-$) (C-C)$_T$	Phosphate diester asymmetric stretch Alkyl chain stretch	DMPC 6-MHA
1302	ω(CH$_2$)	Wagging vibration	6-MHA
1430	(CH$_2$) COO$^-$ δ$_d$(-CH$_2$)	Symmetric deformation Deprotonated carboxylic group deformation for cholesterol	6-MHA/DMPC 6-MHA cholesterol

Figure A-183: OCP spectrum of deposited DMPC/cholesterol (70:30) bilayer on 6-MHA SAM AgNP modified electrode in the presence of 1 μM aloin/0.1 M NaF solution, 3rd trial
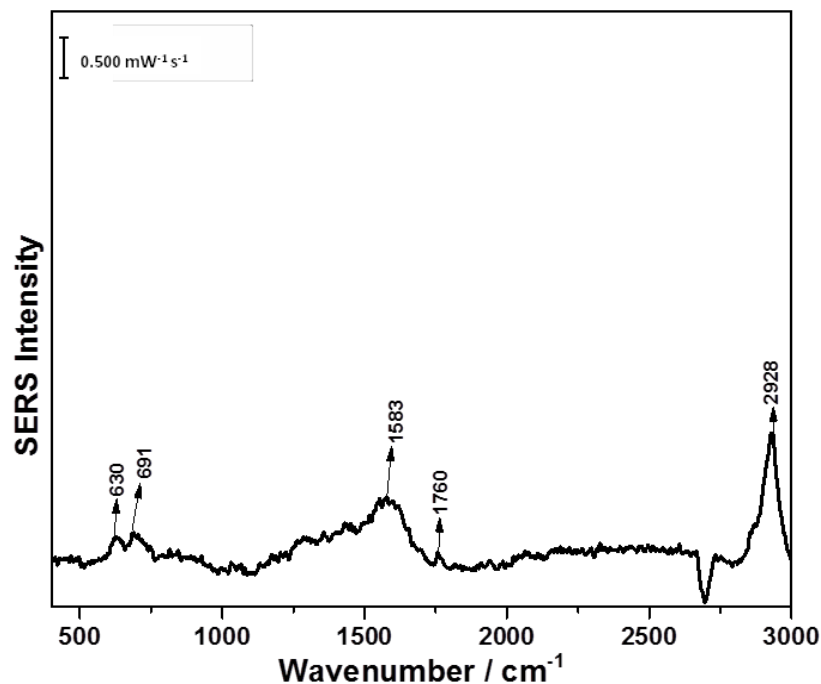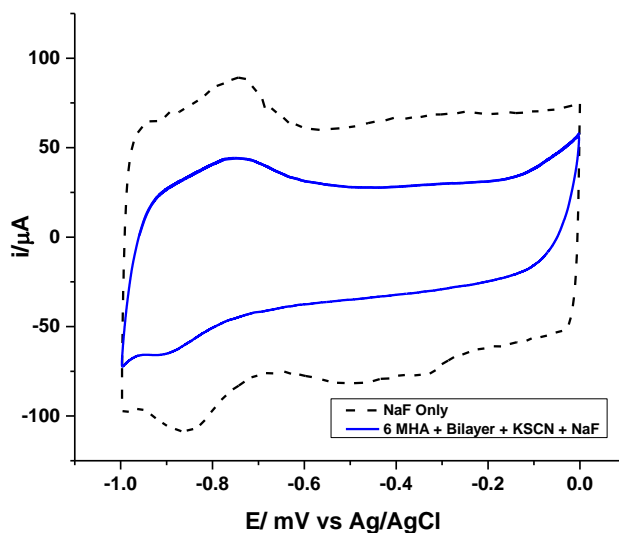

Table A-184: Peak assignment of OCP spectrum of deposited DMPC/cholesterol (70:30) bilayer on 6-MHA SAM AgNP modified electrode in the presence of 1 μM aloin/0.1 M NaF solution, 3rd trial

Wavenumber (cm^{-1})	Assignment	Description	Molecule
630	v(C-S)$_G$	Gauche carbon and sulphur deformation	6-MHA
691	v(C-S)$_T$	trans carbon and sulphur deformation	6-MHA
1583	v_{as}(COO$_2^-$)	Asymmetric stretch of vibration	6-MHA
1760	v(C=O)	Ester carbonyl stretch	DMPC
2928	v_{as}(CH$_2$)	Asymmetric stretch	6-MHA/DMPC

Figure A-185: a) cathodic and b) anodic overlay spectra of deposited DMPC/cholesterol (70:30) bilayer on 6-MHA SAM AgNP modified electrode in the presence of 1 μM aloin/0.1 M NaF solution, 3rd trial

Figure A-186: CV comparison between deposited DMPC/cholesterol (70:30) bilayer on 6-MHA SAM AgNP modified electrode in the presence of 1 μM aloin/0.1 M NaF solution and 0.1 M NaF solution, 3rd trial

Figure A-187: OCP spectrum of 1 mM KSCN/0.1 M NaF solution with AgNP modified electrode, 1st trial

Table A-88: Peak assignment of OCP spectrum of 1 mM KSCN/0.1 M NaF solution with AgNP modified electrode, 1st trial

Wavenumber (cm^{-1})	Assignment	Description	Molecule
444	-C≡N$^-$	Bending vibration	thiocyanate
737	C-S	Stretch vibration	thiocyanate
1539	COO$^-$	Presence of citrate	citrate
1581	COO$^-$	Presence of citrate	citrate
2119	-C≡N$^-$	Asymmetric stretch	thiocyanate
2141	-C≡N$^-$	Asymmetric stretch	thiocyanate
2934	$v_{as}(CH_2)$	Asymmetric stretch	citrate

Figure A-189: CV comparison between KSCN 1 mM KSCN/0.1 M NaF solution and 0.1 M NaF solution, 1st trial
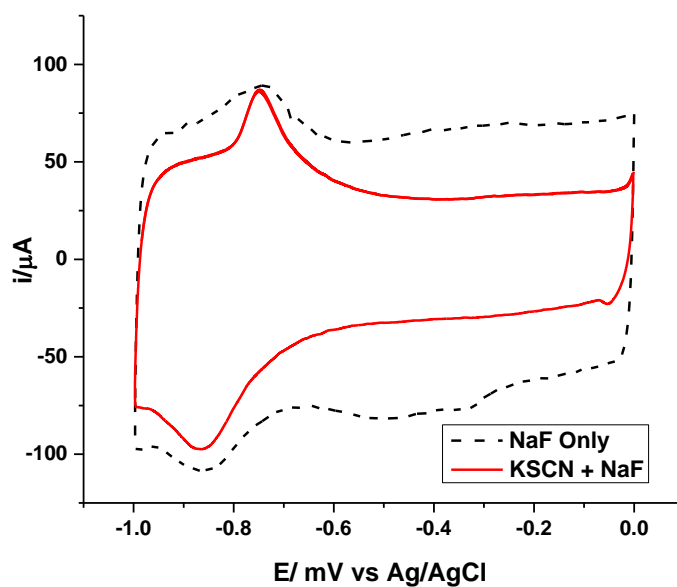
Figure A-190: OCP spectrum of 1 mM KSCN/0.1 M NaF solution with AgNP modified electrode, 2nd trial
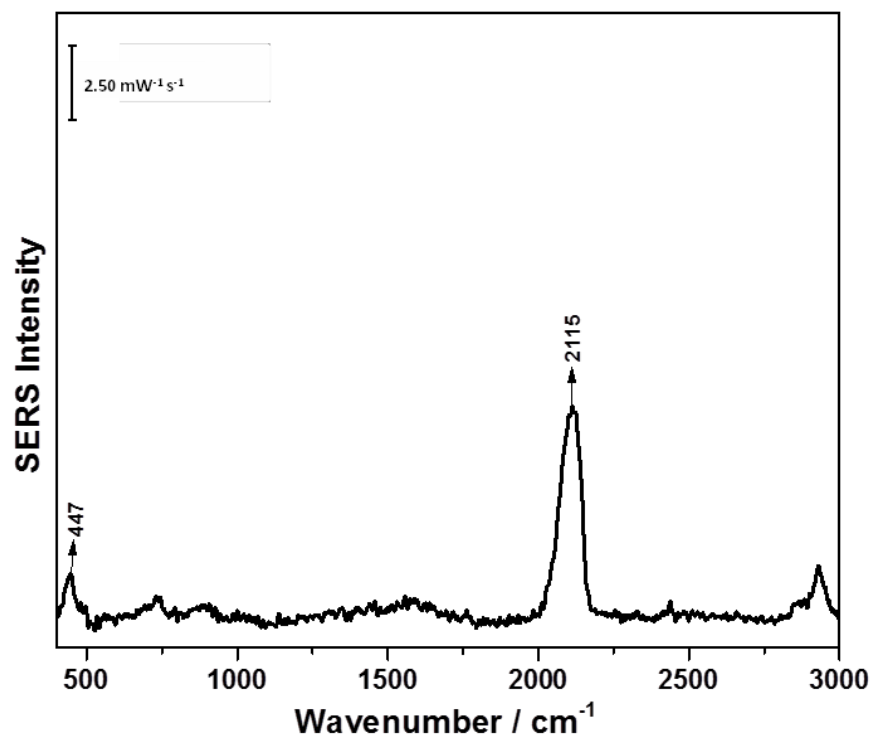
Figure A-191: a) cathodic and b) anodic overlay spectra of 1 mM KSCN/0.1 M NaF solution with AgNP modified electrode, 2nd trial
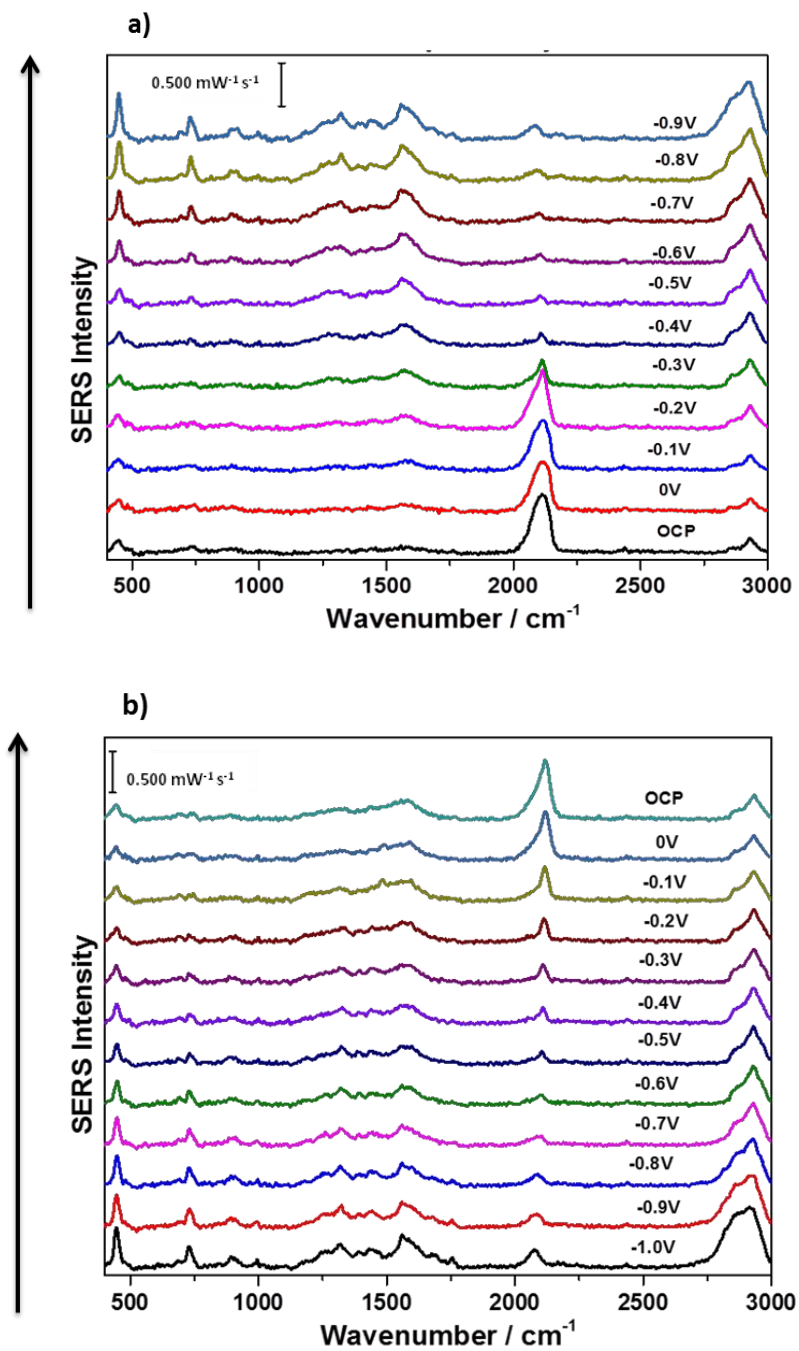
Figure A-192: CV comparison between 1 mM KSCN/0.1 M NaF solution and 0.1 M NaF solution, 2nd trial
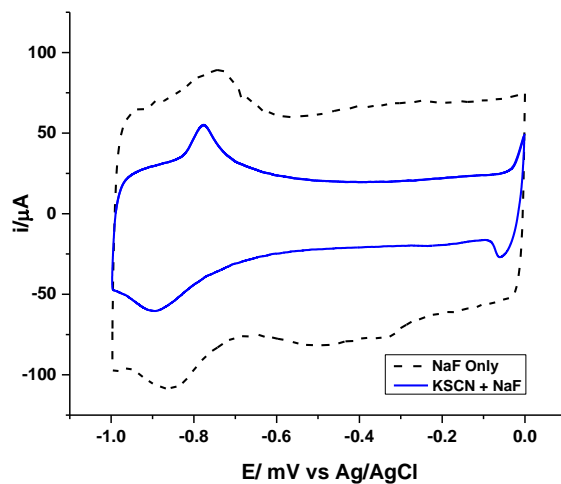
Figure A-193: OCP spectrum of 1 mM KSCN/0.1 M NaF solution with AgNP modified electrode, 3rd trial
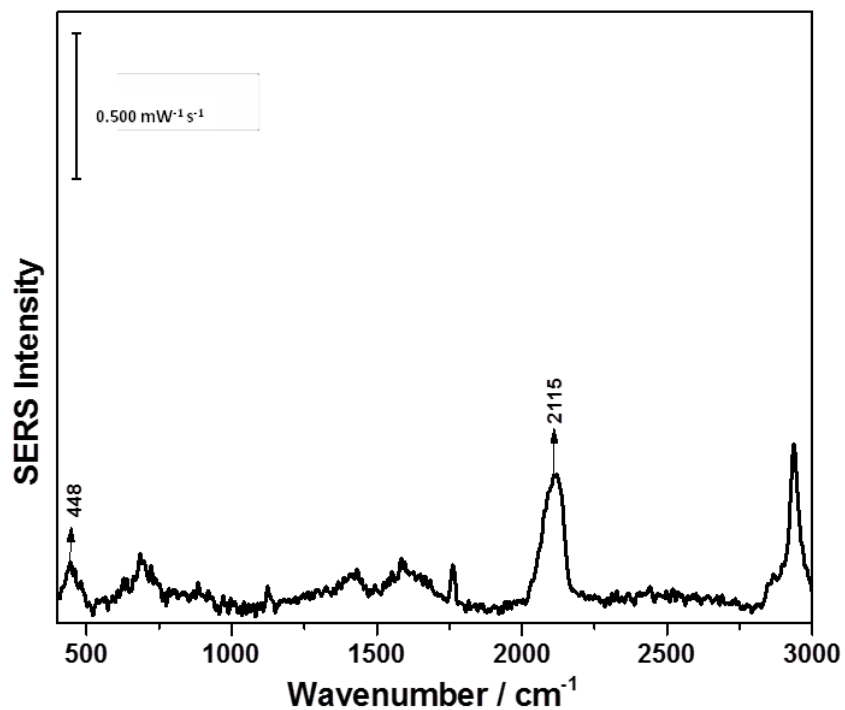
Figure A-194: a) cathodic and b) anodic overlay spectra of 1 mM KSCN/0.1 M NaF solution with AgNP modified electrode, 3rd trial
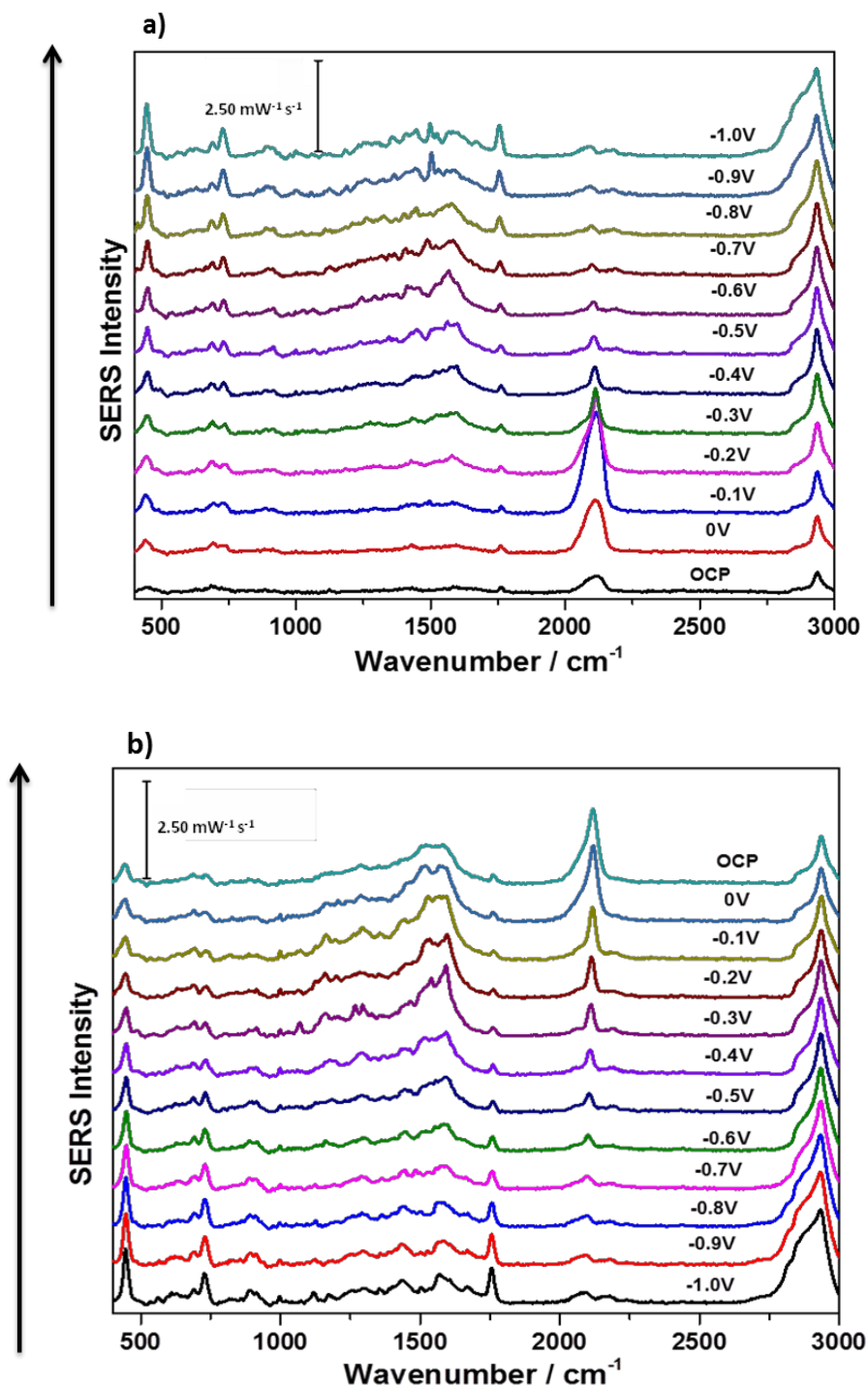
Figure A-195: CV comparison between 1 mM KSCN/0.1 M NaF solution with AgNP modified electrode and 0.1 M NaF solution, 3rd trial
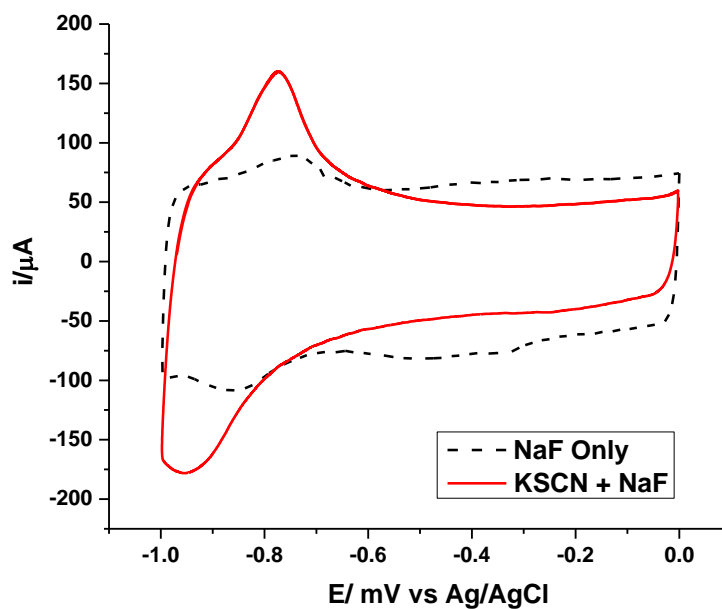
Figure A-196: a) cathodic and b) anodic overlay spectra of 1 mM KSCN/0.1 M NaF solution in the presence of 6-MHA SAM, 2nd trial
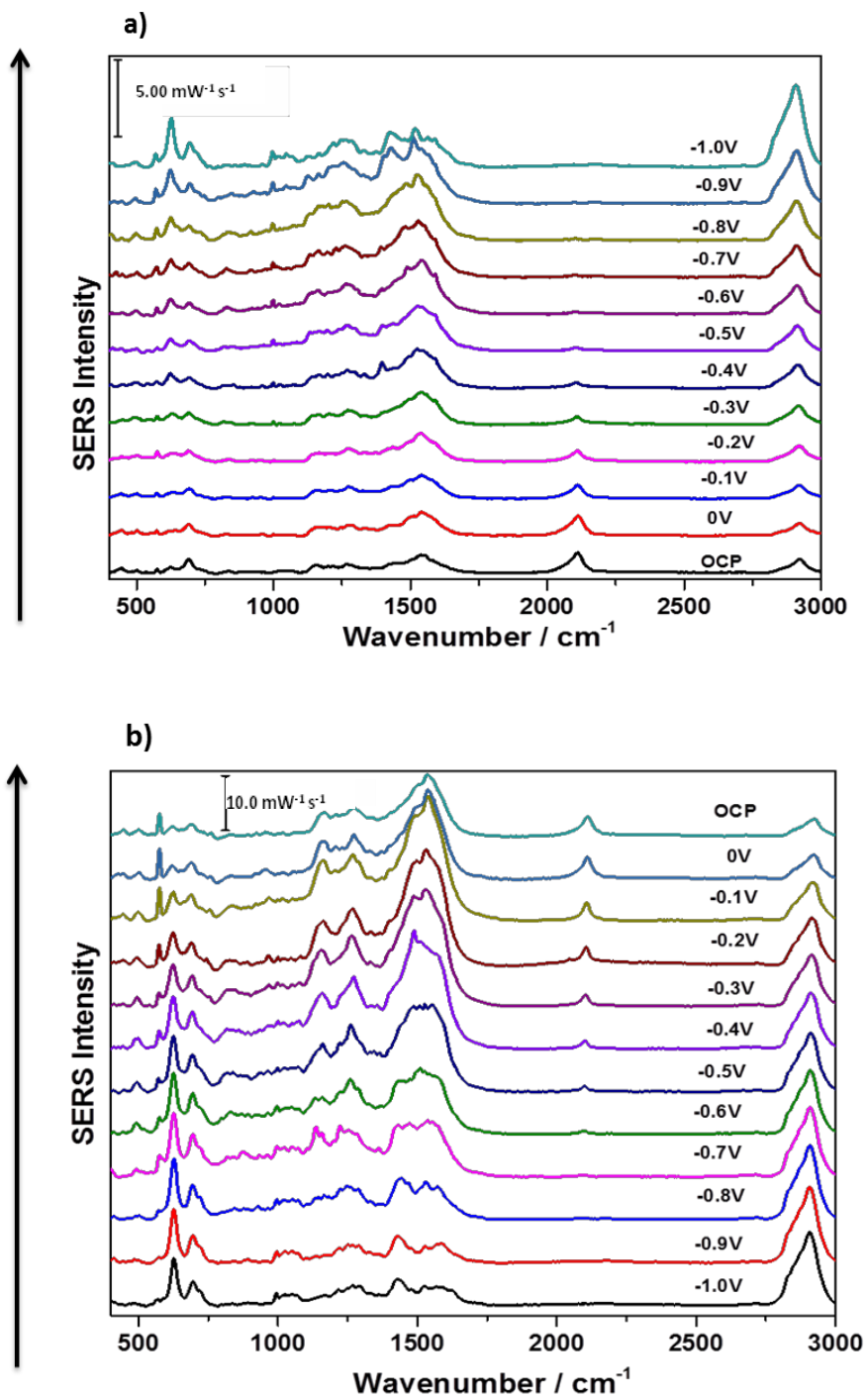
Figure A-197: CV comparison between 1 mM KSCN/0.1 M NaF solution in the presence of 6-MHA SAM and 0.1 M NaF solution, 2ⁿᵈ trial
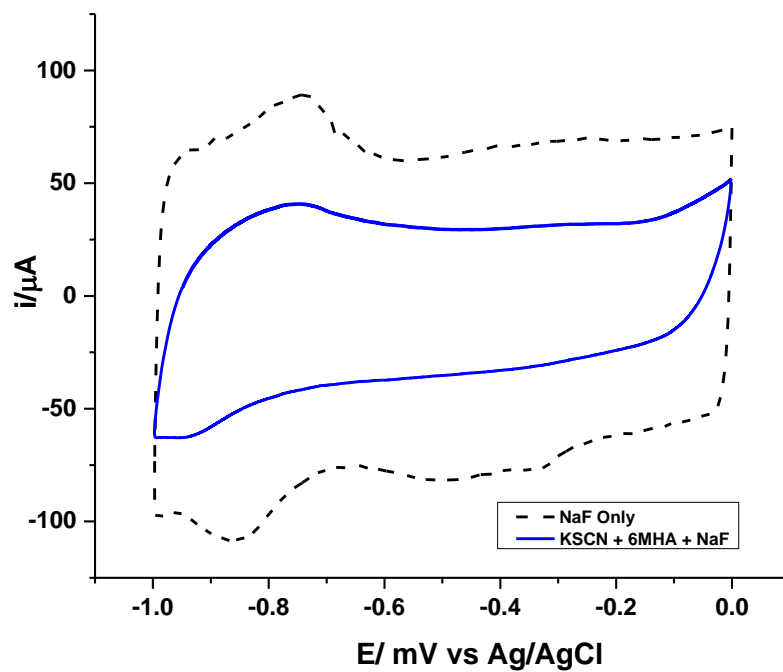
Figure A-198: a) cathodic and b) anodic overlay spectra of 1 mM KSCN/0.1 M NaF solution in the presence of 6-MHA SAM, 3rd trial
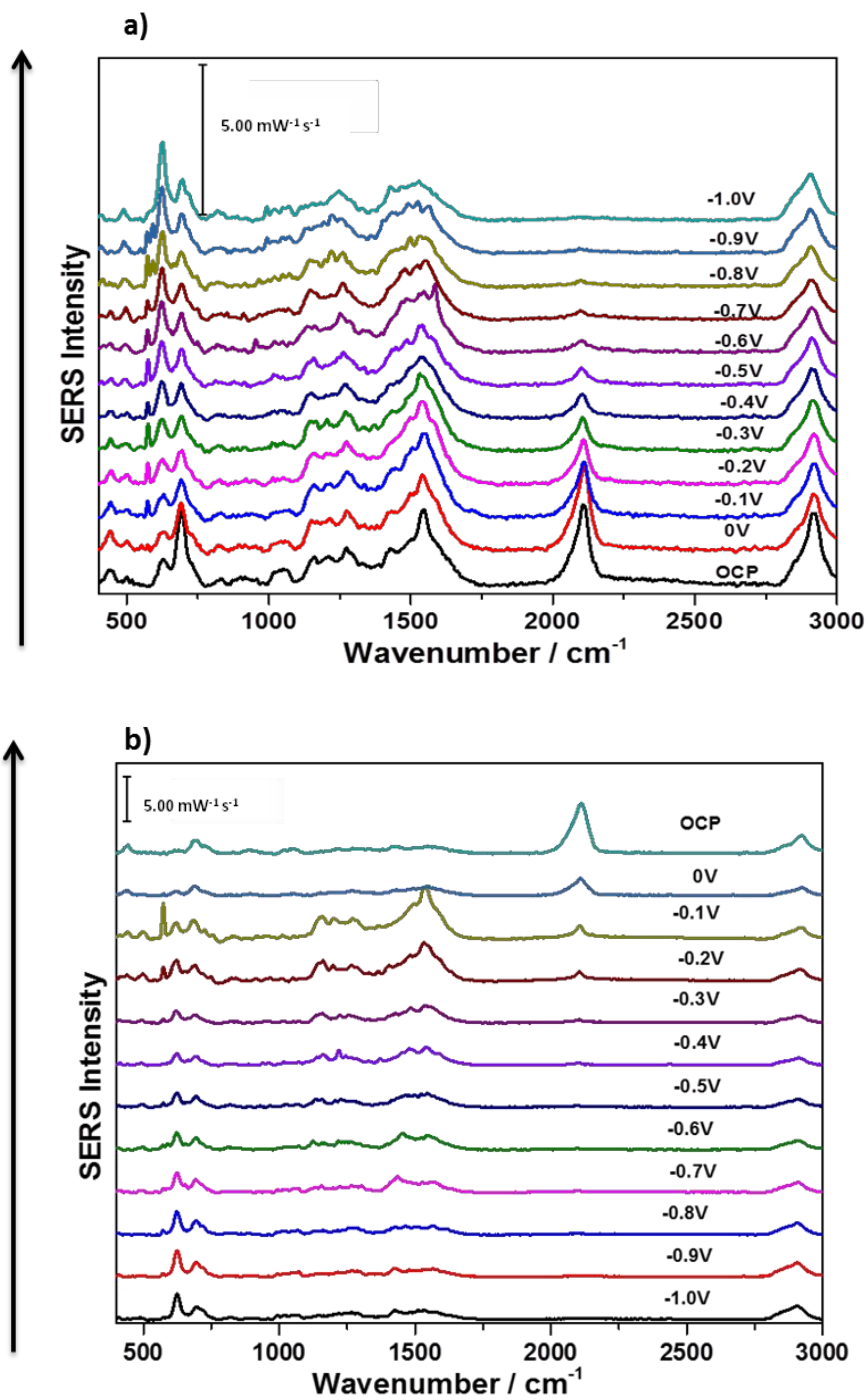
Figure A-199: CV comparison between 1 mM KSCN/0.1 M NaF solution in the presence of 6-MHA SAM and 0.1 M NaF solution, 3rd trial
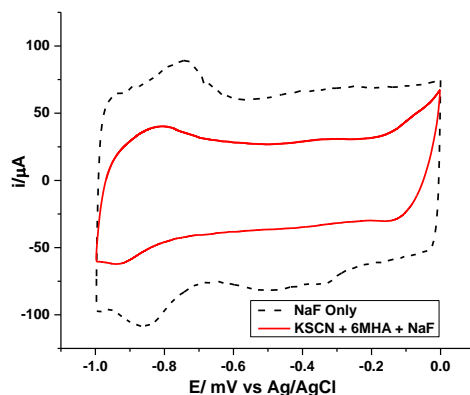
Figure A-200: In air spectrum of deposited DMPC/cholesterol (70:30) bilayer on 6-MHA SAM AgNP modified, 1st trial
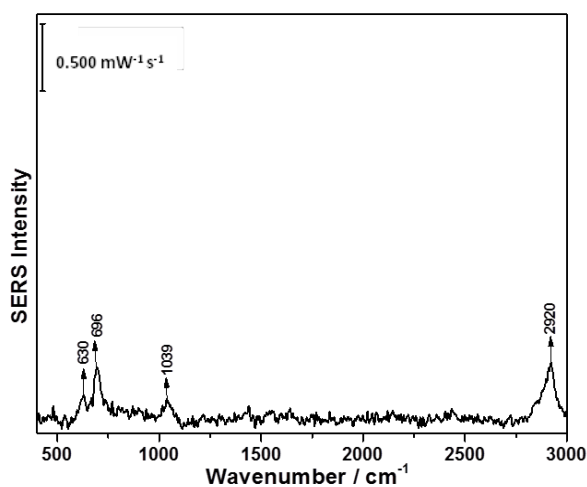
Table A-201: Peak assignment for in air spectrum of deposited DMPC/cholesterol (70:30) bilayer on 6-MHA SAM AgNP modified electrode , 1st trial

Wavenumber (cm^{-1})	Assignment	Description	Molecule
630	v(C-S)$_G$	Gauche carbon and sulphur deformation	6-MHA
696	v(C-S)$_T$	trans carbon and sulphur deformation	6-MHA
1039	C-C CH$_2$CH$_3$	Alkyl chain stretch Bending of lipids	6-MHA DMPC
2920	v_{as}(CH$_2$)	Asymmetric stretch	6-MHA/DMPC

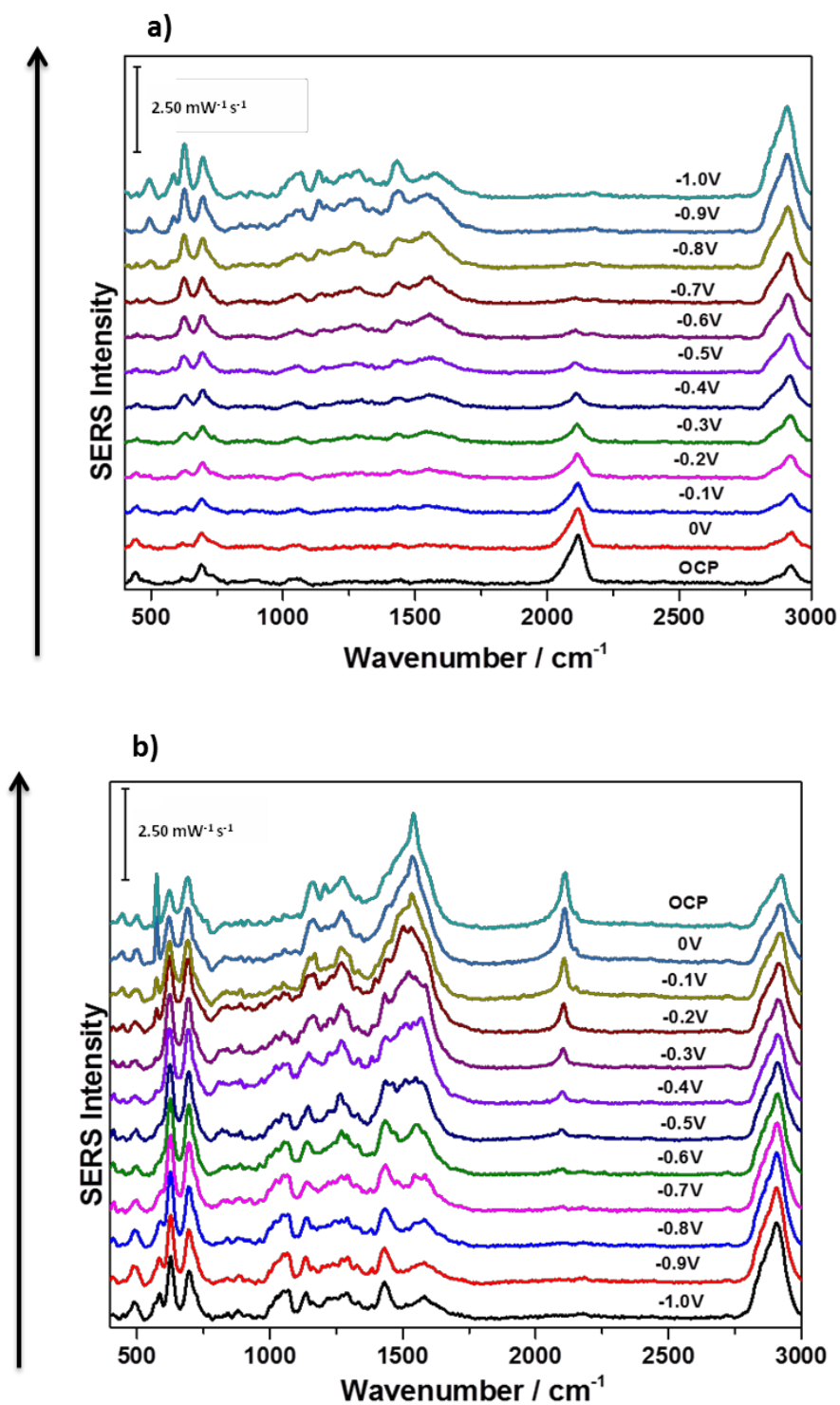**Figure A-202: Anodic overlay spectra of deposited DMPC/cholesterol (70:30) bilayer on 6-MHA SAM AgNP modified electrode in the presence of 1 mM KSCN/0.1 M NaF solution, 1st trial**
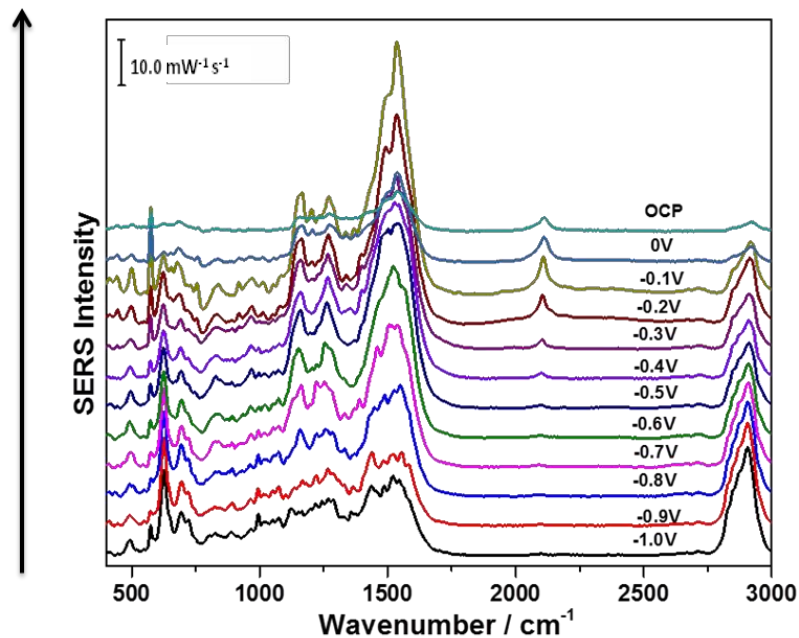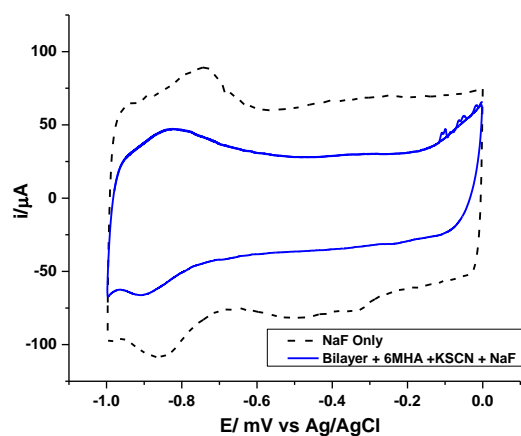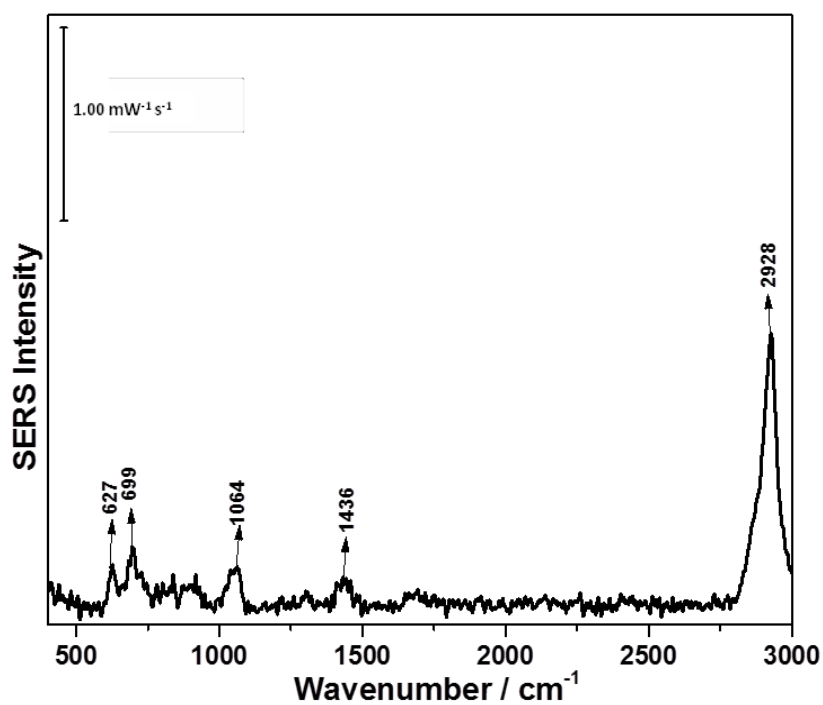

Figure A-203: CV comparison between deposited DMPC/cholesterol (70:30) bilayer on 6-MHA SAM AgNP modified electrode in the presence of 1 mM KSCN/ 0.1 M NaF solution and 0.1 M NaF solution, 1st trial
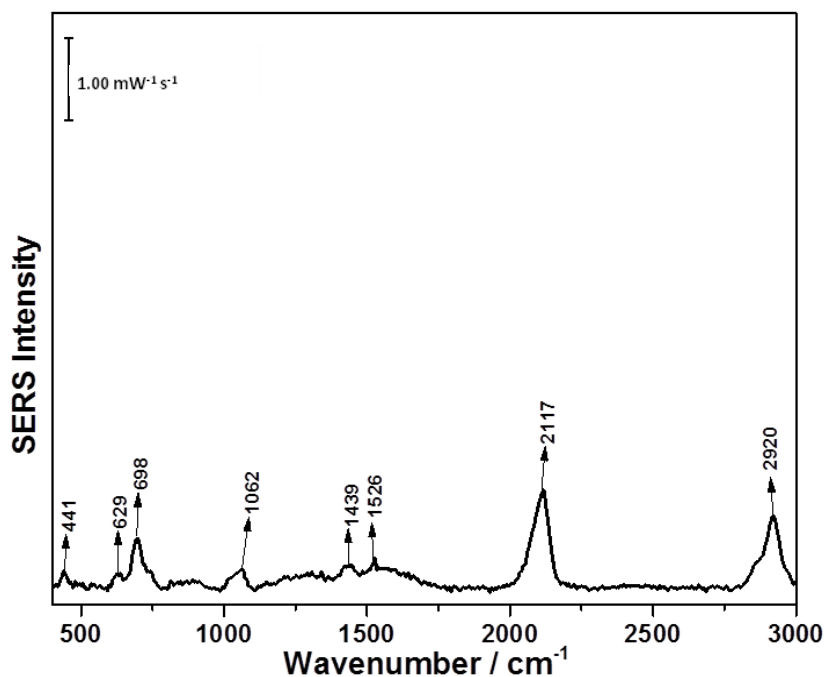
Table A-204: Peak assignment for OCP spectrum of deposited DMPC/cholesterol (70:30) bilayer 6-MHA SAM in the presence of 1 mM KSCN/0.1 M NaF solution, 1st trial

Wavenumber (cm^{-1})	Assignment	Description	Molecule
443	-C≡N$^-$	Bending vibration	thiocyanate
501	(-C-C-C-)$_G$	gauche straight chain vibration	6-MHA
574	COO$^-$	Carboxylic deformation	6-MHA
656	v(C-S)$_G$	Gauche carbon and sulphur deformation	6-MHA
695	v(C-S)$_T$	trans carbon and sulphur deformation	6-MHA
828	-C-C-C-	Straight chain alkyl vibration	6-MHA
956	v(C-COO$^-$)	Deprotonated carboxylic group Presence of cholesterol	6-MHA cholesterol
1152	C-C	Skeletal straight chain vibration for alkanes	6-MHA
1205	ω(CH$_2$)	Wagging vibrations	6-MHA
1276	ω(CH$_2$)	Wagging vibrations	6-MHA/DMPC
1543	v_{as} (COO$_2^-$)	Asymmetric stretching of vibration	6-MHA
2114	-C≡N$^-$	Asymmetric stretch	thiocyanate
2926	v_{as}(CH$_2$)	Asymmetric stretch	6-MHA/DMPC

Figure A-205: In air spectrum of deposited DMPC/cholesterol (70:30) bilayer on 6-MHA SAM AgNP modified electrode, 2nd trial
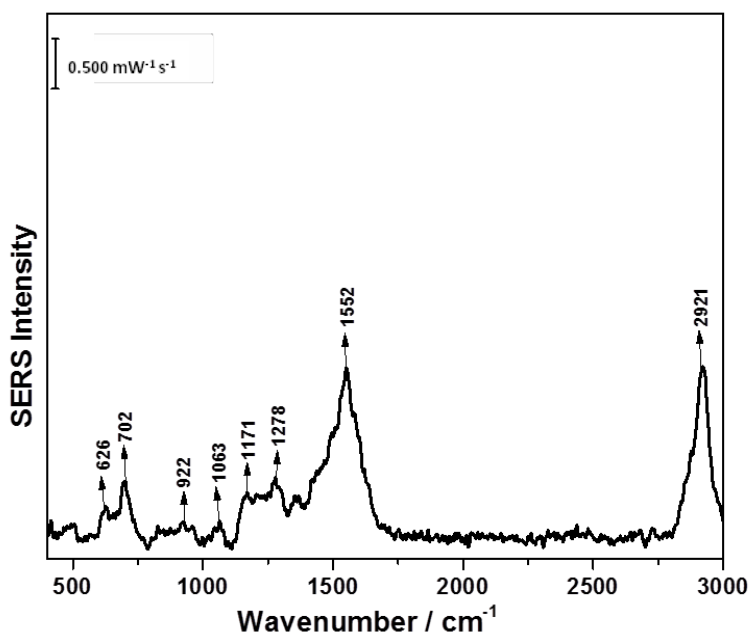
Table A-206: Peak assignment for in air spectrum of deposited DMPC/cholesterol (70:30) bilayer on 6-MHA SAM AgNP modified electrode, 2nd trial

| Wavenumber (cm^{-1})	Assignment	Description	Molecule
626	v(C-S)$_G$	Gauche carbon and sulphur deformation	6-MHA
702	v(C-S)$_T$	trans carbon and sulphur deformation	6-MHA
922	COO$^-$	Deprotonated carboxyl group	6-MHA
1063	v_{as}(PO$_2^-$)	Phosphate diester asymmetric stretch	DMPC
	(C-C)$_T$	Alkyl chain stretch	6-MHA
1171	C-O	Ester asymmetric stretch	DMPC
	C-C	Skeletal straight chain vibration	6-MHA
1278	ω(CH$_2$)	Wagging vibration Unassigned peak from 6-MHA studies	6-MHA/DMPC 6-MHA
1552	v_{as}(COO$_2^-$)	Asymmetric stretching of vibration	6-MHA
2921	v_{as}(CH$_2$)	Asymmetric stretch	6-MHA/DMPC

126

Figure A-207: OCP spectrum of deposited DMPC/cholesterol (70:30) bilayer on 6-MHA SAM AgNP modified electrode in the presence of 1 mM KSCN/0.1 M NaF solution, 2nd trial
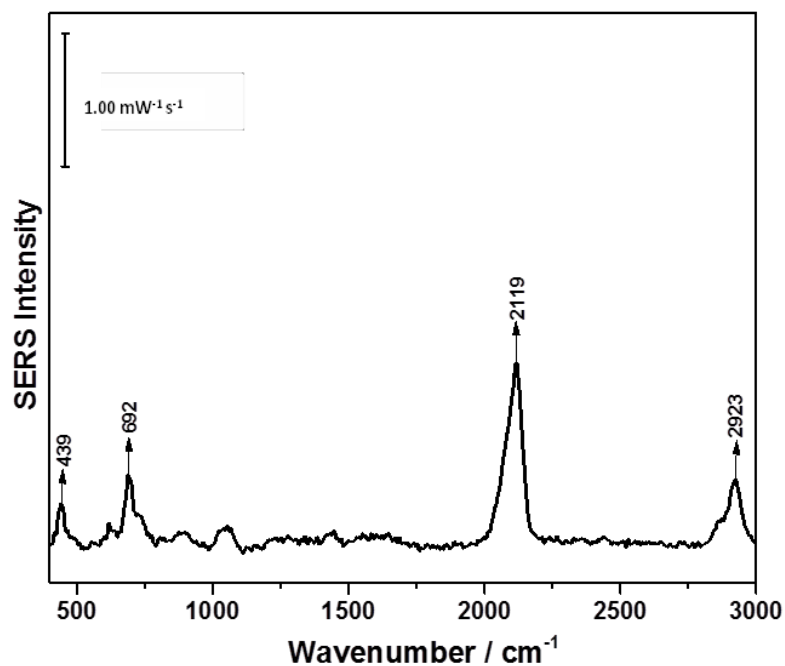
Table A-208: Peak assignment for OCP spectrum of deposited DMPC/cholesterol (70:30) bilayer on 6-MHA SAM AgNP modified electrode in the presence of 1 mM KSCN/0.1 M NaF solution, 2nd trial

Wavenumber (cm^{-1})	Assignment	Description	Molecule
439	-C≡N$^-$	Bending vibration	thiocyanate
692	v(C-S)$_T$	trans carbon and sulphur deformation	6-MHA
2119	-C≡N$^-$	Asymmetric stretch	thiocyanate
2923	v_{as}(CH$_2$)	Asymmetric stretch	6-MHA/DMPC

Figure A-209: a) cathodic and b) anodic overlay spectra of deposited DMPC/cholesterol (70:30) bilayer on 6-MHA SAM AgNP modified electrode in the presence of 1 mM KSCN/0.1 M NaF solution, 2nd trial

Figure A-210: CV comparison between deposited DMPC/cholesterol (70:30) bilayer on 6-MHA SAM AgNP modified electrode in the presence of 1 mM KSCN/ 0.1 M NaF solution and 0.1 M NaF solution, 2nd trial


Figure A-211: In air spectrum of deposited DMPC/cholesterol (70:30) bilayer on 6-MHA SAM AgNP modified electrode, 3rd trial

Table A-212: Peak assignment for air spectrum of deposited DMPC/cholesterol (70:30) bilayer on 6-MHA SAM AgNP modified electrode in the presence of 1 mM KSCN/0.1 M NaF solution, 3rd trial

Wavenumber (cm^{-1})	Assignment	Description	Molecule
627	v(C-S)$_G$	Gauche carbon and sulphur deformation	6-MHA
699	v(C-S)$_T$	trans carbon and sulphur deformation	6-MHA
1064	v_{as}(PO$_2^-$)	Phosphate diester asymmetric stretch	DMPC
	(C-C)$_T$	Alkyl chain stretch	6-MHA
1436	(CH$_2$)	Symmetric deformation	6-MHA/DMPC
	COO$^-$	Deprotonated carboxylic	6-MHA
	δ_d(-CH$_2$)	deformation for cholesterol	cholesterol
2928	v_{as}(CH$_2$)	Asymmetric stretch	6-MHA/DMPC

Figure A-213: OCP spectrum of deposited DMPC/cholesterol (70:30) bilayer on 6-MHA SAM AgNP modified electrode in the presence of 1 mM KSCN/0.1 M NaF solution, 3rd trial

Table A-214: Peak assignment for OCP spectrum of deposited DMPC/cholesterol (70:30) bilayer on 6-MHA SAM AgNP modified electrode in the presence of 1 mM KSCN/0.1 M NaF solution, 3rd trial

Wavenumber (cm^{-1})	Assignment	Description	Molecule
441	-C≡N$^-$	Bending vibration	thiocyanate
629	v(C-S)$_G$	Gauche carbon and sulphur deformation	6-MHA
698	v(C-S)$_T$	trans carbon and sulphur deformation	6-MHA
1062	v_{as}(PO$_2^-$)	Phosphate diester asymmetric stretch	DMPC
	(C-C)$_T$	Alkyl chain stretch	6-MHA
1439	(CH$_2$) COO$^-$ δ_d(-CH$_2$)	Symmetric deformation Deprotonated carboxylic deformation for cholesterol	6-MHA/DMPC 6-MHA cholesterol
1526	v_{as} (COO$_2^-$)	Asymmetric stretching of vibration	6-MHA
2117	-C≡N$^-$	Asymmetric stretch	thiocyanate
2920	v_{as}(CH$_2$)	Asymmetric stretch	6-MHA/DMPC

Figure A-215: a) cathodic and b) anodic overlay spectra of deposited DMPC/cholesterol (70:30) bilayer on 6-MHA SAM AgNP modified electrode in the presence of 1 mM KSCN/0.1 M NaF solution, 3rd trial
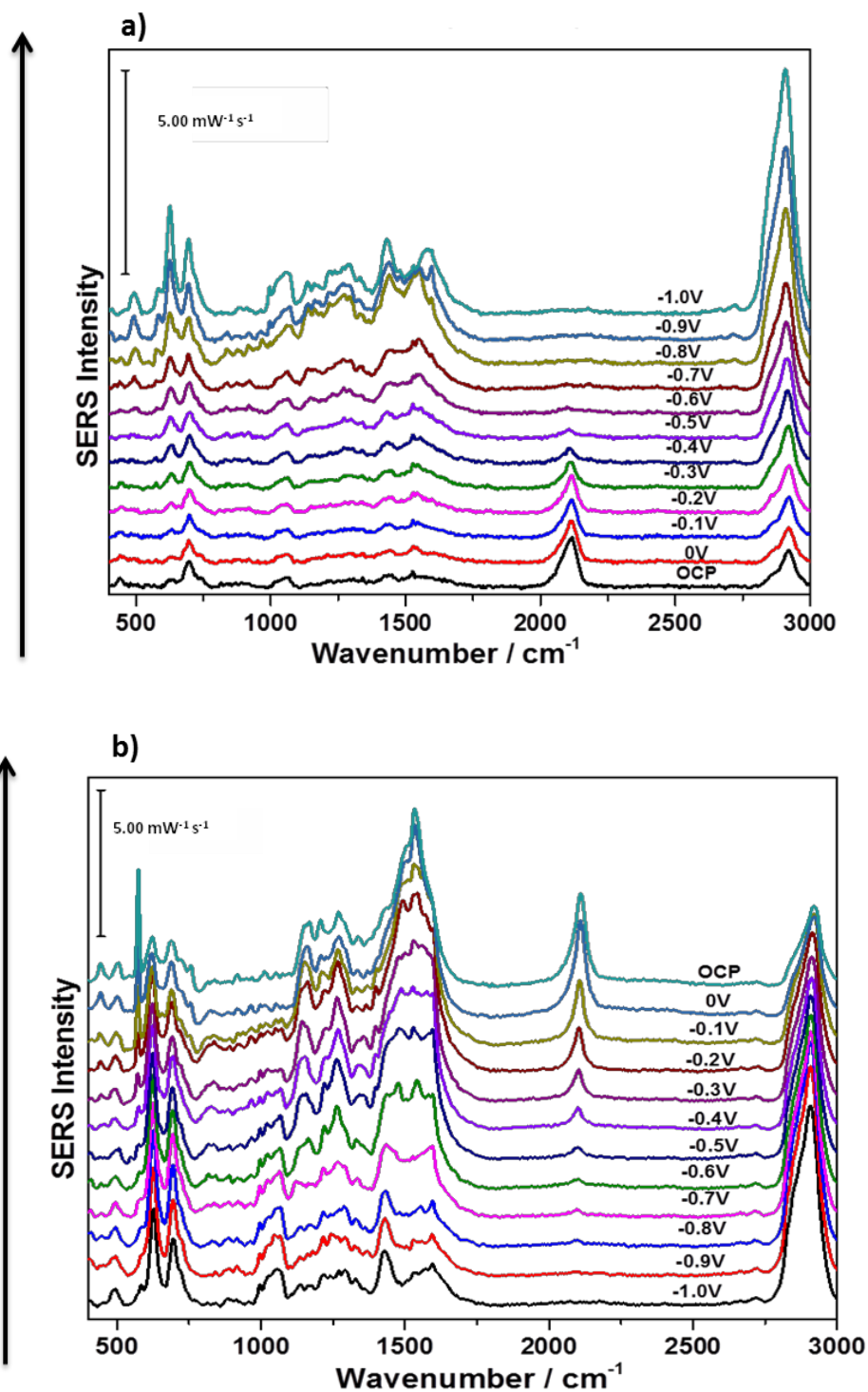
Figure A-216: CV comparison between deposited DMPC/cholesterol (70:30) bilayer on 6-MHA SAM AgNP modified electrode in the presence of 1 mM KSCN/ 0.1 M NaF solution and 0.1 M NaF solution, 3rd trial
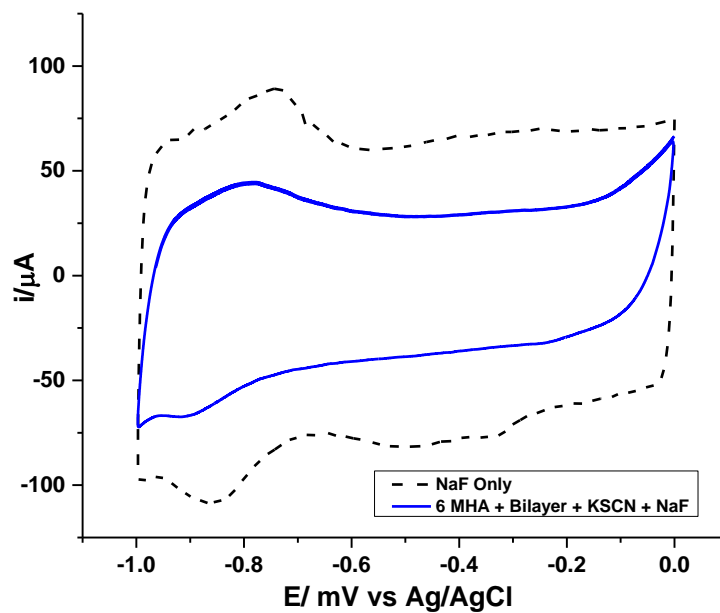
Figure A-217: a) cathodic and b) anodic overlay spectra of basic 1 mM KSCN/ 0.1 M NaF solution with AgNP modified electrode, 1st trial

a)

b)
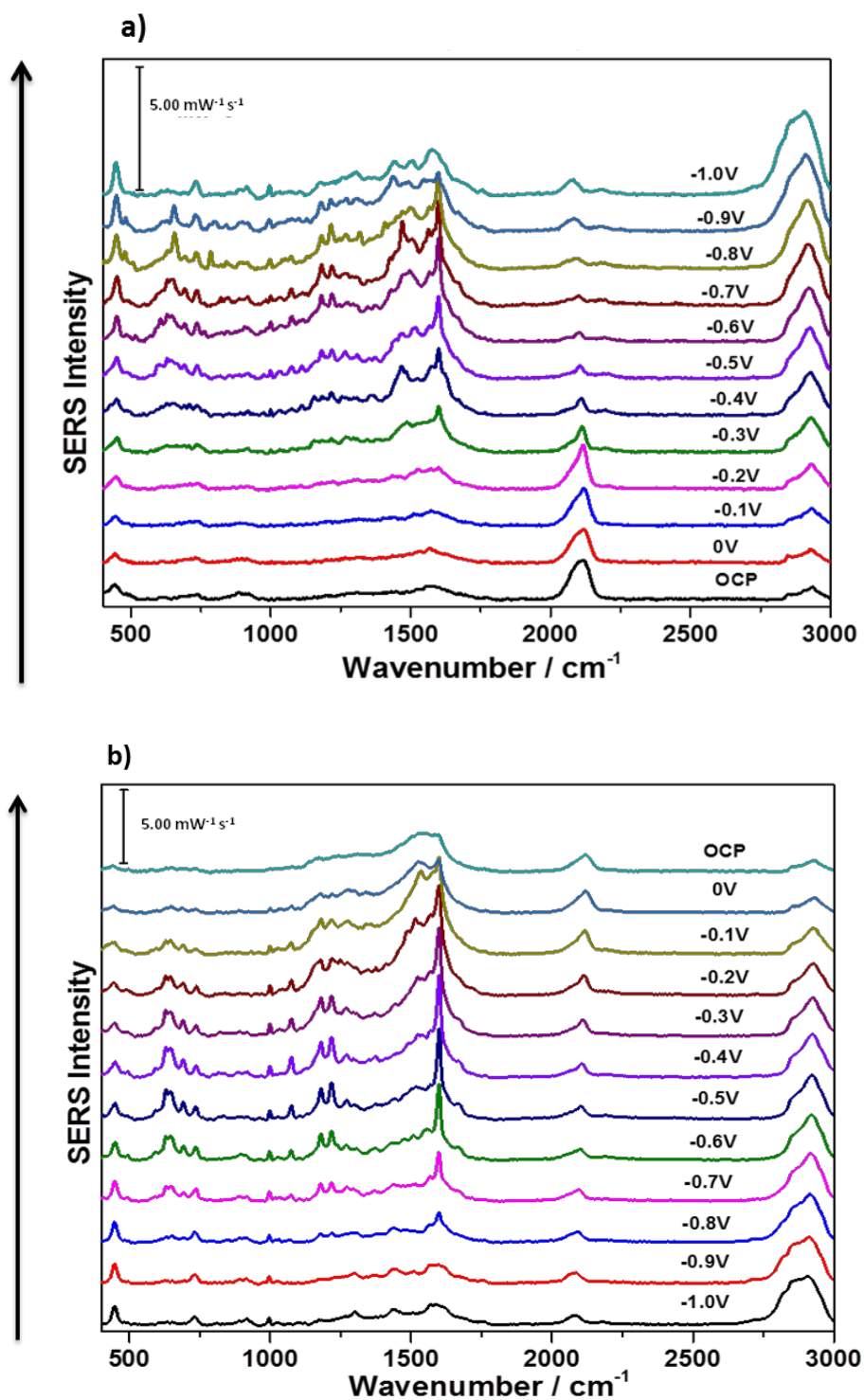
Figure A-218: CV comparison between basic 1 mM KSCN/0.1 M NaF solution and 0.1 M NaF solution, 1st trial
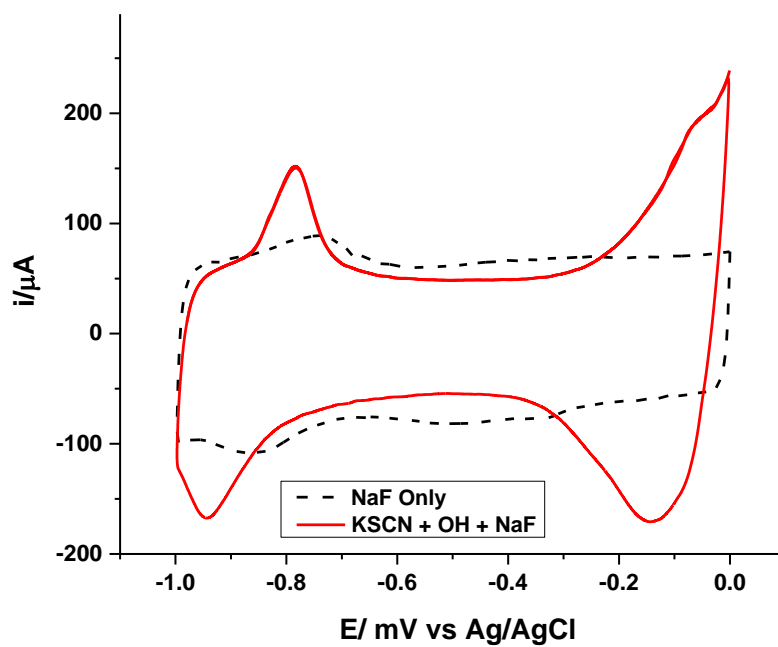
Figure A-219: a) cathodic and b) anodic overlay spectra of basic 1 mM KSCN/ 0.1 M NaF solution with AgNP modified electrode, 2nd trial
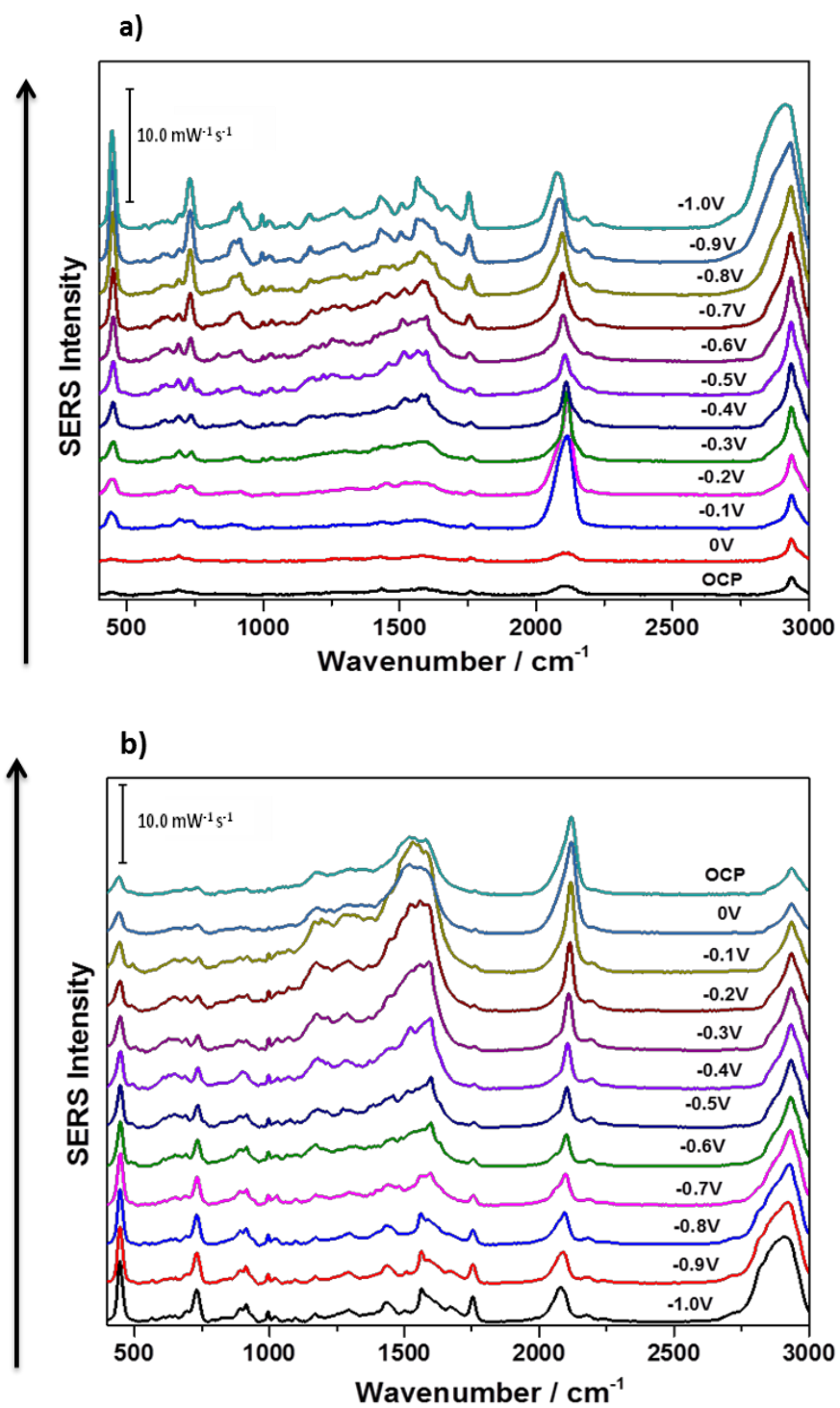
Figure A-220: CV comparison between basic 1 mM KSCN/0.1 M NaF solution and 0.1 M NaF solution, 2nd trial
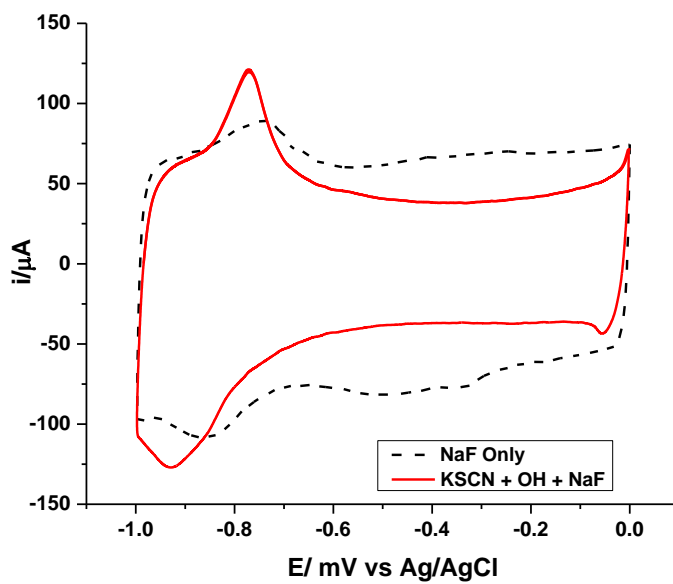
Figure A-221: a) cathodic and b) anodic overlay spectra of basic 1 mM KSCN/ 0.1 M NaF solution with AgNP modified electrode, 3rd trial
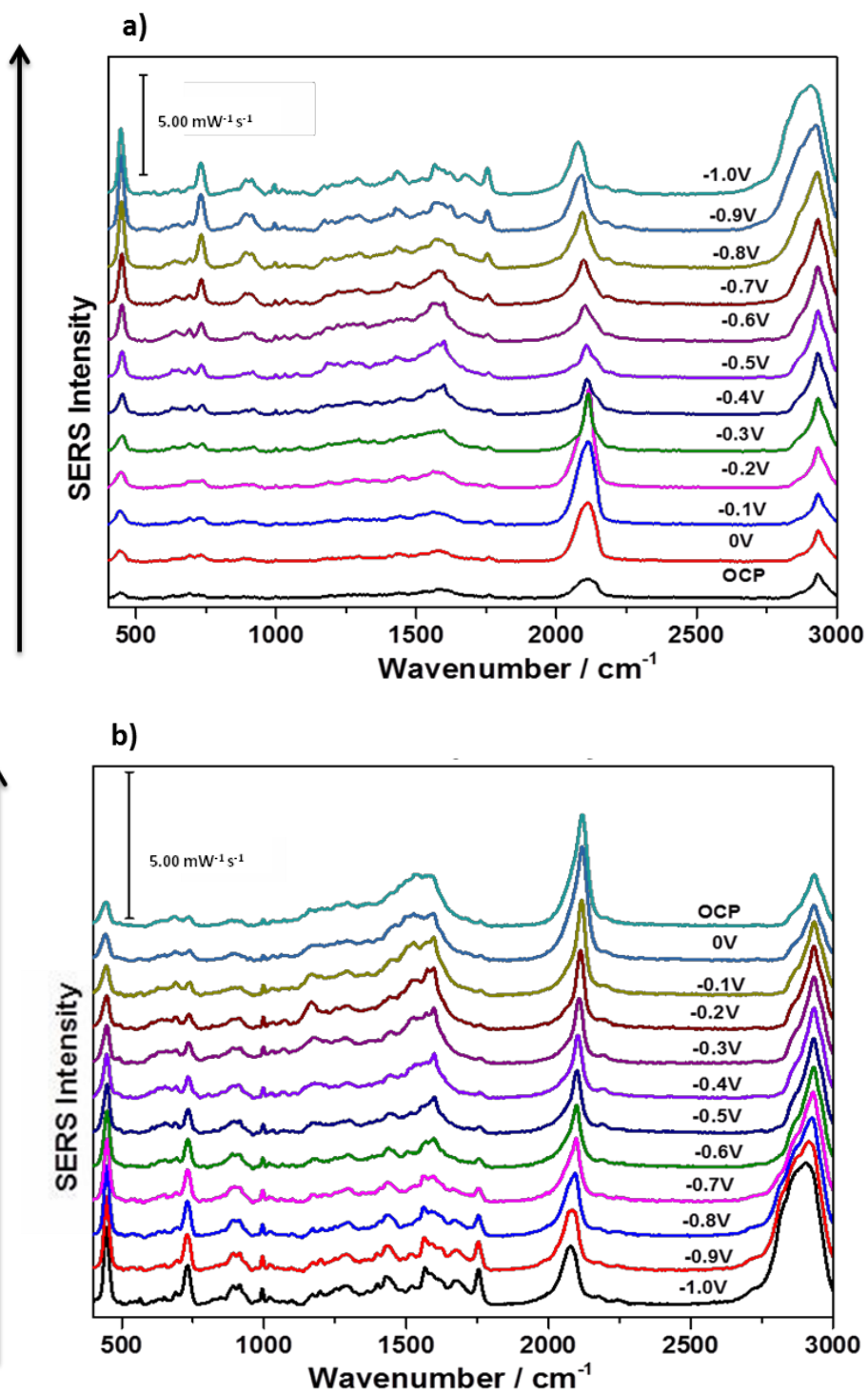
Figure A-222: CV comparison between basic 1 mM KSCN/0.1 M NaF solution and 0.1 M NaF solution, 3rd trial
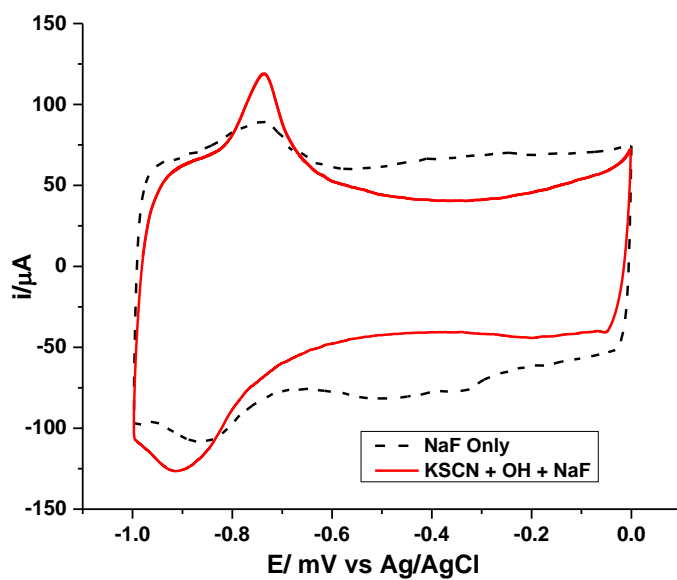
Figure A-223: a) cathodic and b) anodic overlay spectra of basic 1 mM KSCN/0.1 M NaF solution in the presence of 6-MHA SAM, 1st trial
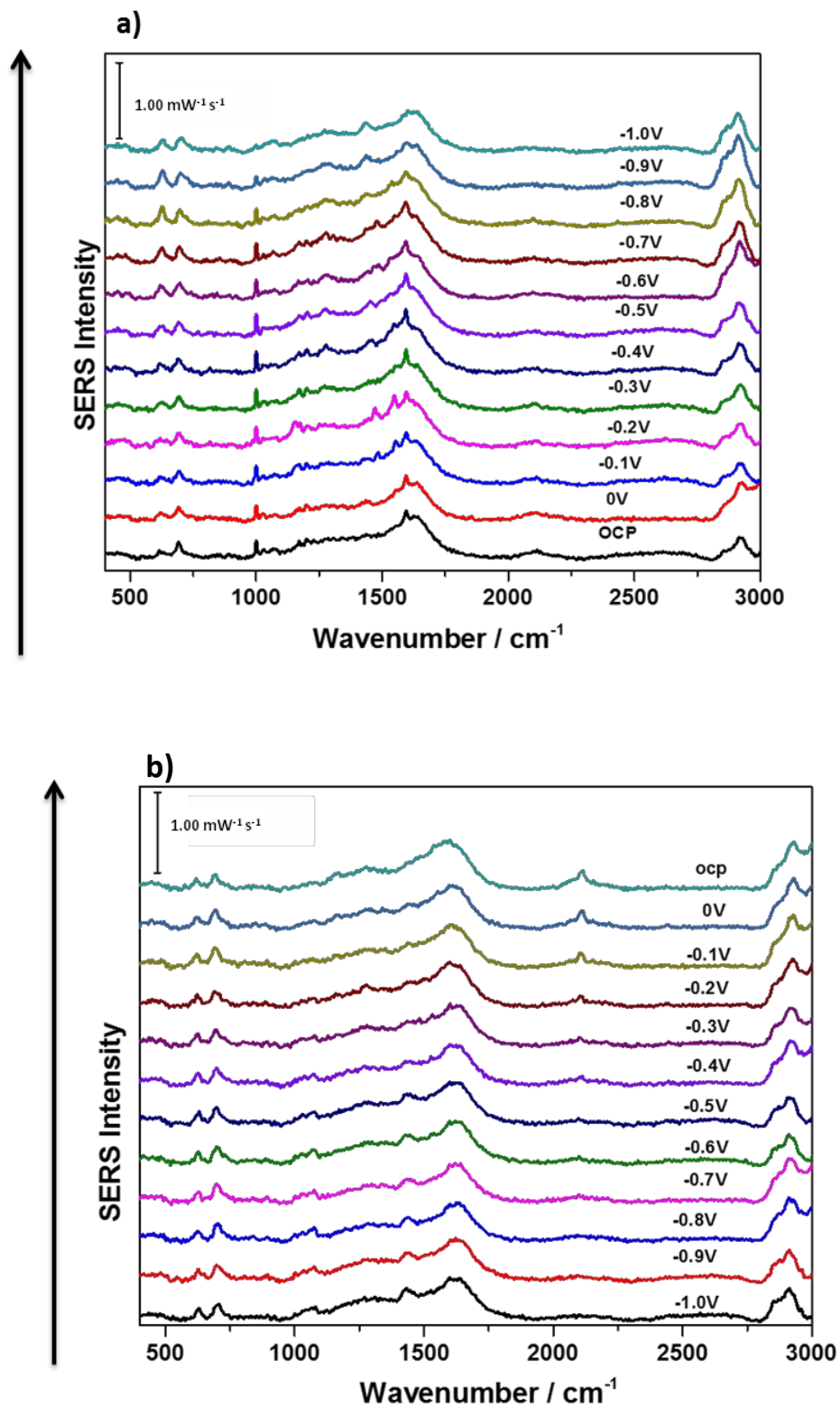
Figure A-224: CV comparison between b a s i c 1 mM KSCN/0.1 M NaF solution in the presence of 6-MHA SAM and 0.1 M NaF solution, 1st trial
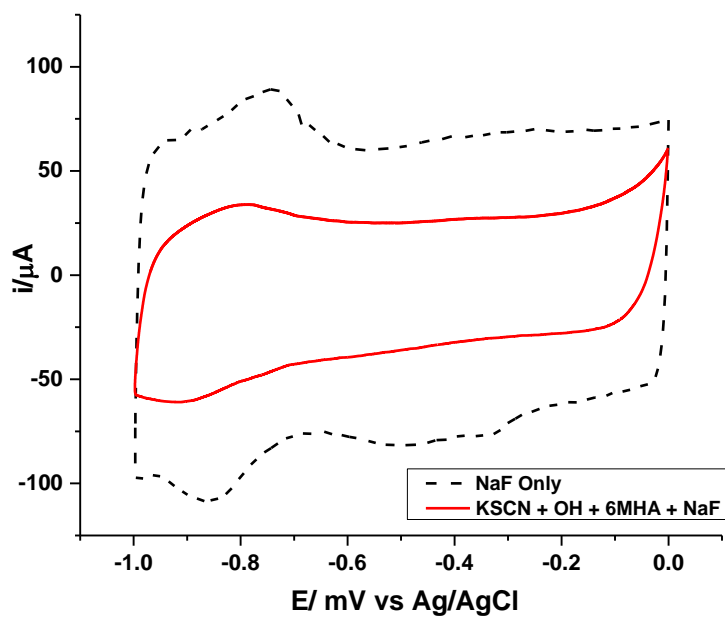
Figure A- 225: a) cathodic and b) anodic overlay spectra of basic 1 mM KSCN/0.1 M NaF solution in the presence of 6-MHA SAM, 2nd trial
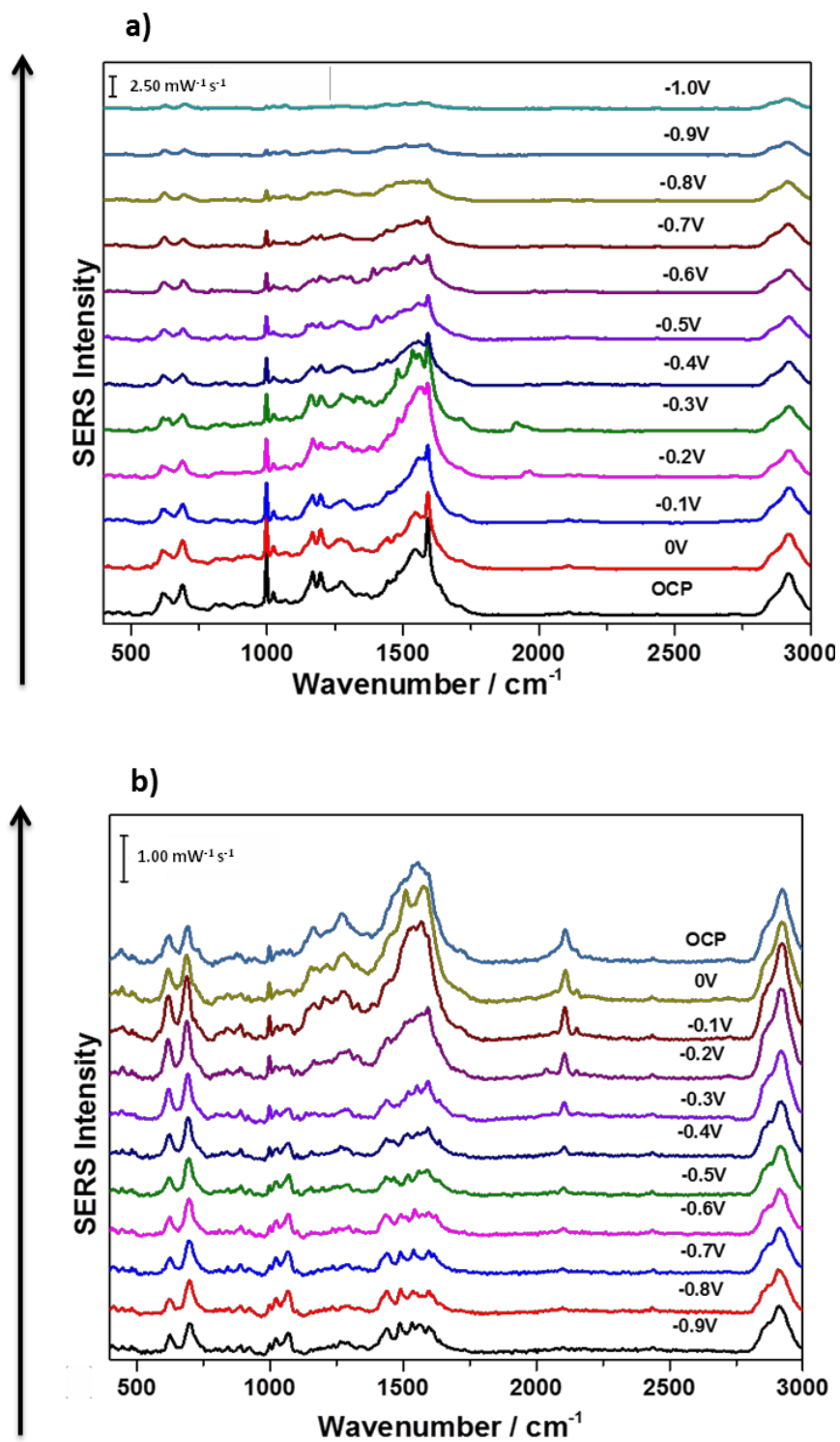
Figure A-226: CV comparison between basic 1 mM KSCN/0.1 M NaF solution in the presence of 6-MHA SAM and 0.1M NaF solution, 2nd trial
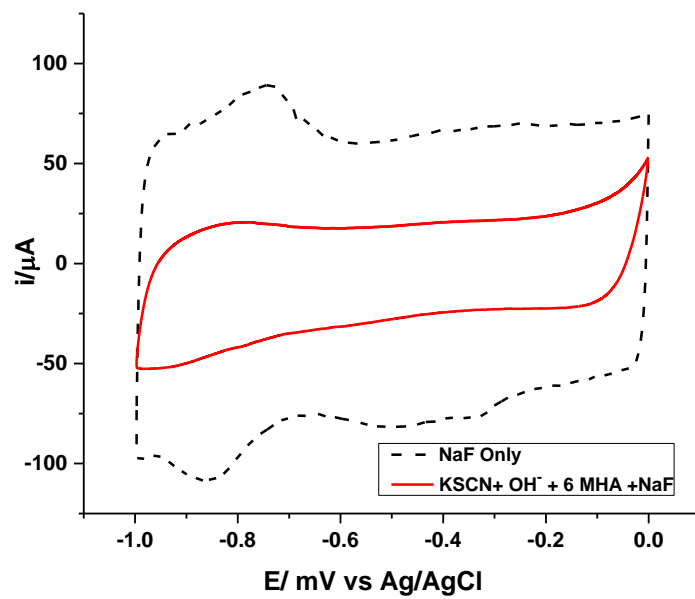
Figure A- 227: a) cathodic and b) anodic overlay spectra of basic 1 mM KSCN/0.1 M NaF solution in the presence of 6-MHA SAM, 3rd trial
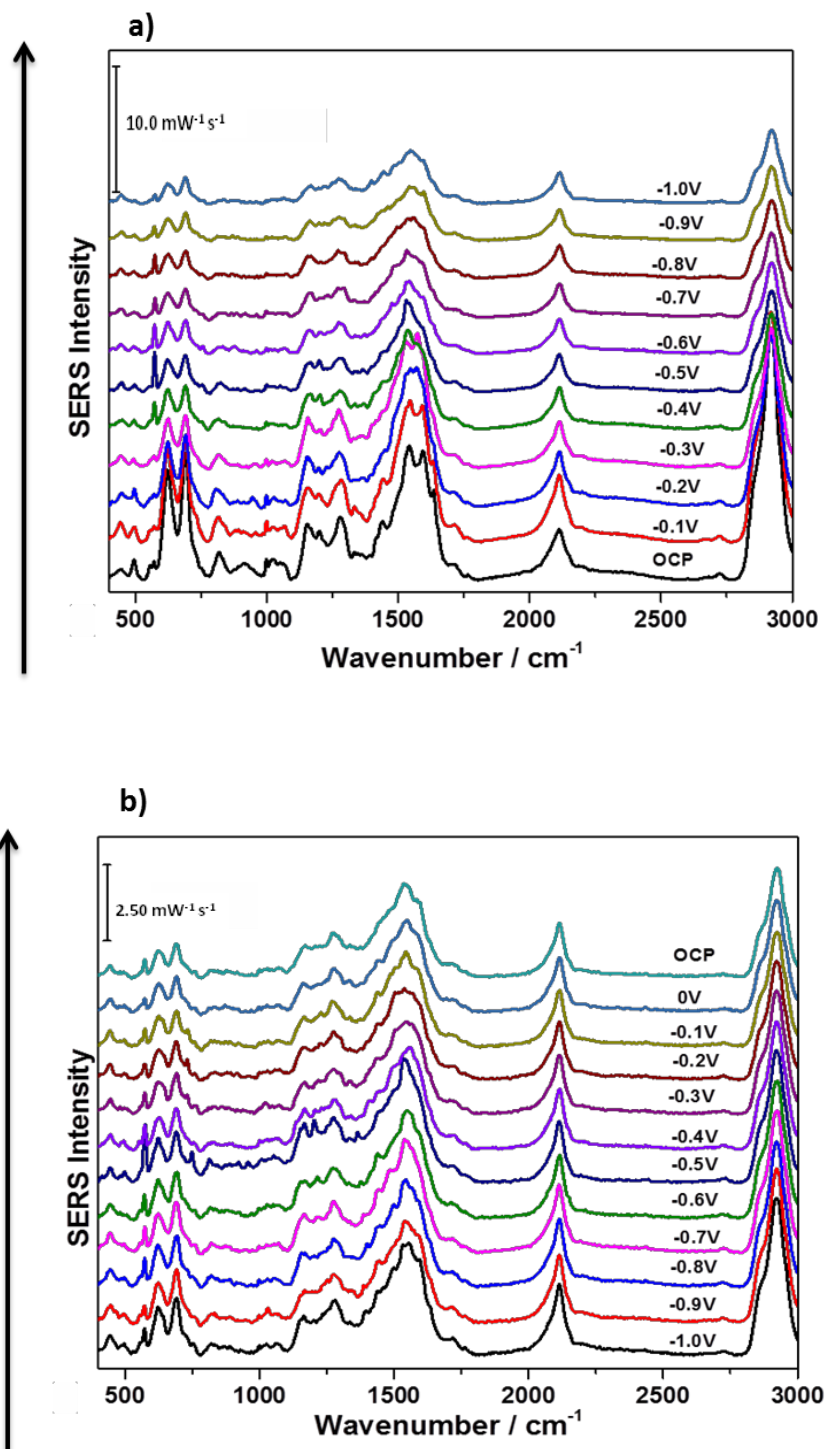
Figure A-228: CV comparison between basic 1 mM KSCN/0.1 M NaF solution in the presence of 6-MHA SAM and 0.1 M NaF solution, 3rd trial
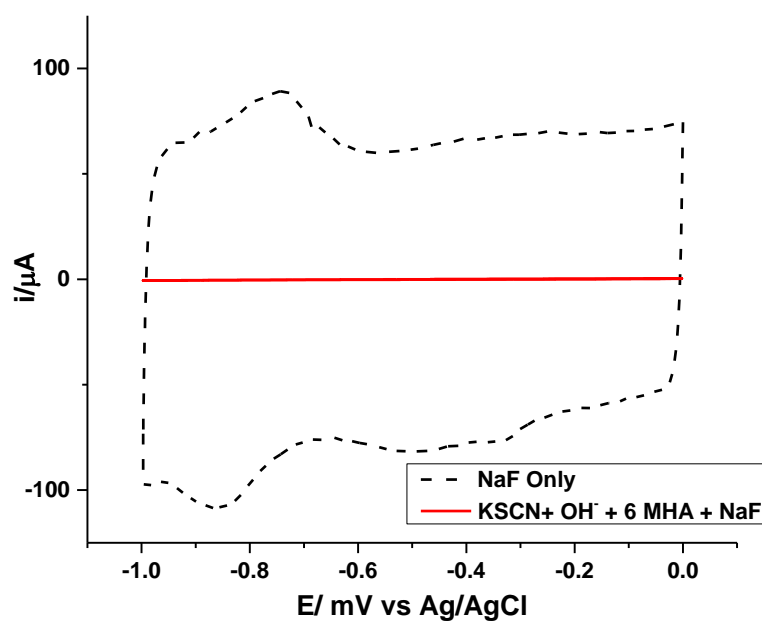
Figure A-229: a) cathodic and b) anodic overlay spectra of deposited DMPC/cholesterol (70:30) bilayer on 6-MHA SAM AgNP modified electrode in the presence of basic 1 mM KSCN/0.1 M NaF solution, 1st trial
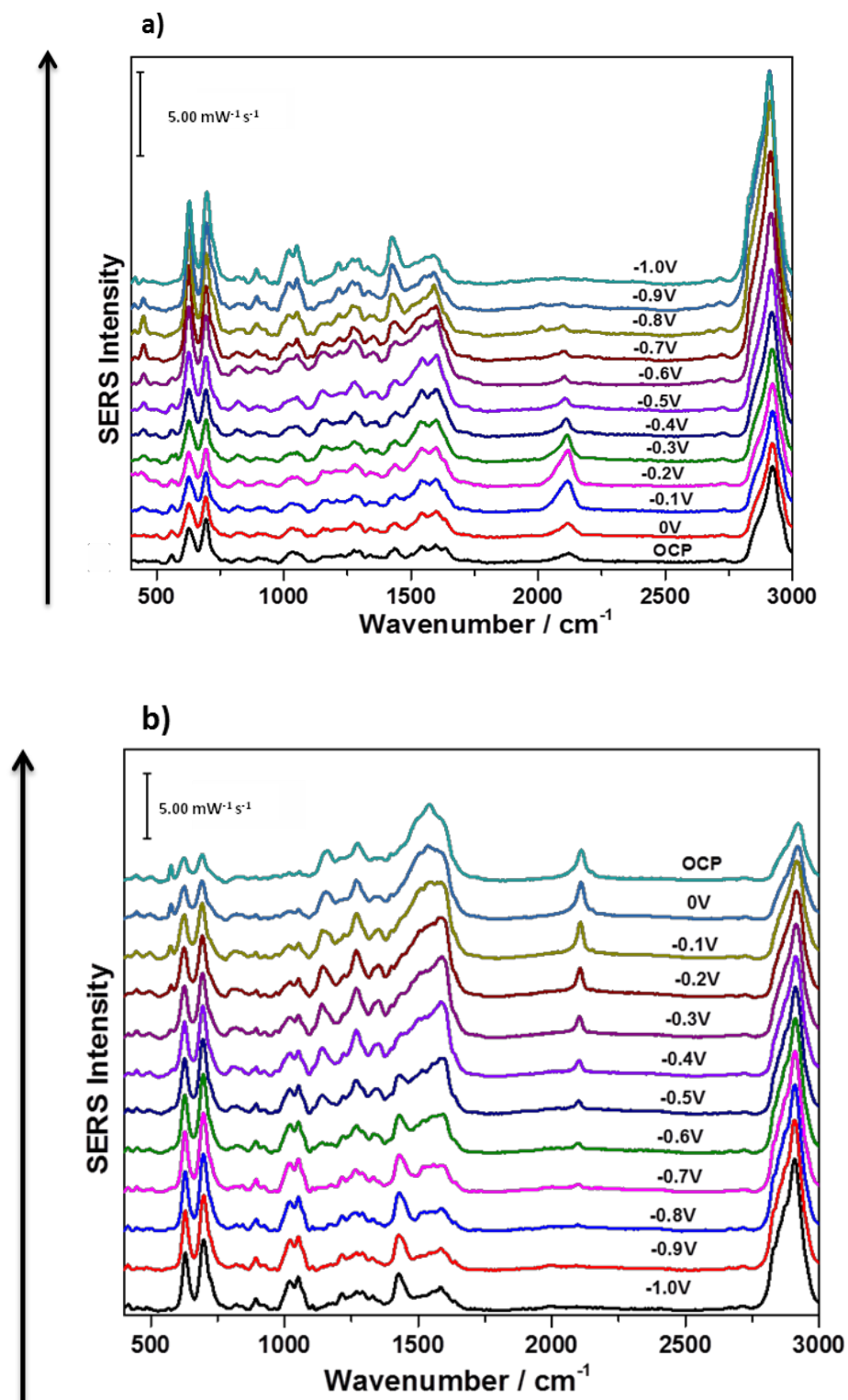
Figure A-230: CV comparison between deposited DMPC/cholesterol (70:30) bilayer on 6-MHA SAM AgNP modified electrode in the presence of basic 1 mM KSCN/ 0.1 M NaF solution and 0.1 M NaF solution, 1st trial
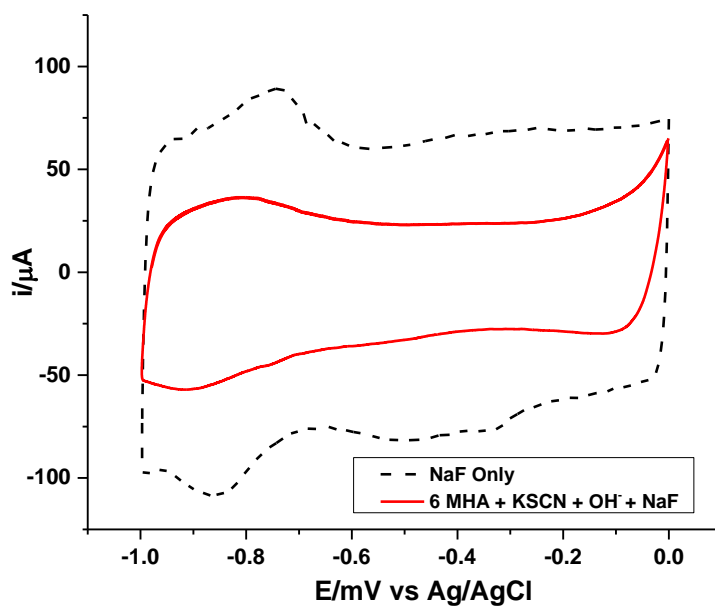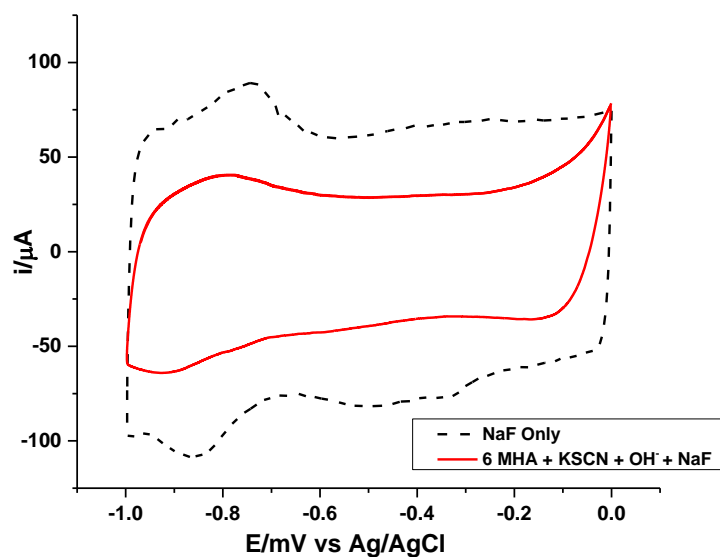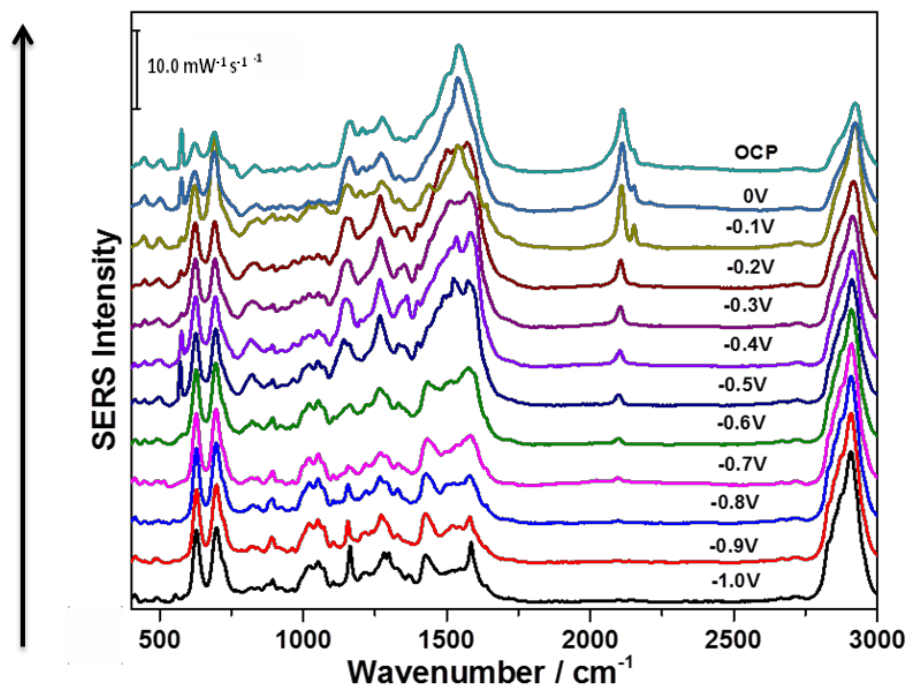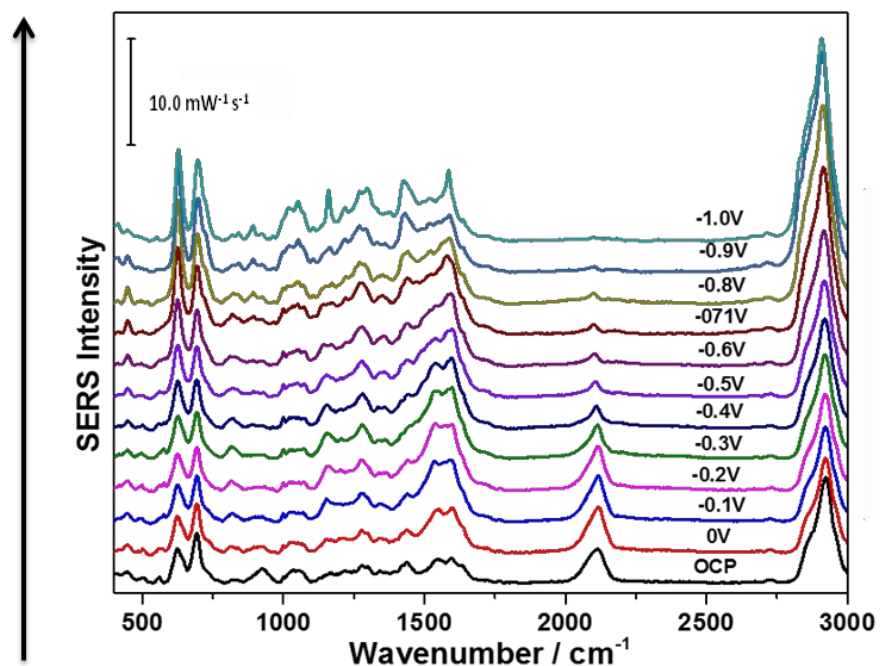
Figure A-231: a) cathodic and b) anodic overlay spectra of deposited DMPC/cholesterol (70:30) bilayer on 6-MHA SAM AgNP modified electrode in the presence of basic 1 mM KSCN/0.1 M NaF solution, 2nd trial
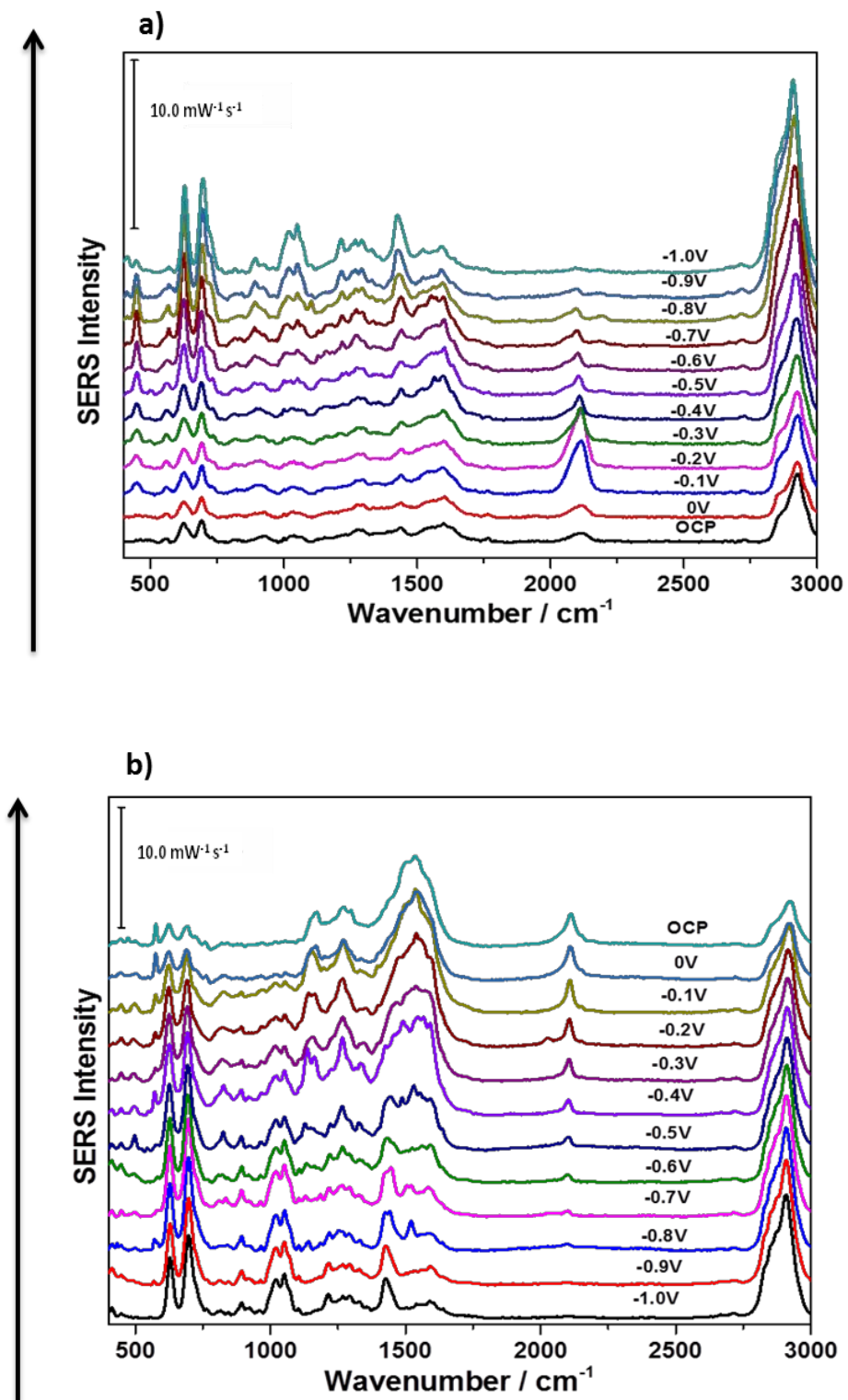
Figure A-232: CV comparison between deposited DMPC/cholesterol (70:30) bilayer on 6-MHA SAM AgNP modified electrode in the presence of basic 1 mM KSCN/ 0.1 M NaF solution and 0.1 M NaF solution, 2nd trial

Figure A-233: a) cathodic and b) anodic overlay spectra of deposited DMPC/cholesterol (70:30) bilayer on 6-MHA SAM AgNP modified electrode in the presence of basic 1 mM KSCN/0.1 M NaF solution, 3rd trial

Figure A-234: CV comparison between deposited DMPC/cholesterol (70:30) bilayer on 6-MHA SAM AgNP modified electrode in the presence of basic 1 mM KSCN/ 0.1 M NaF solution and 0.1 M NaF solution, 3rd trial
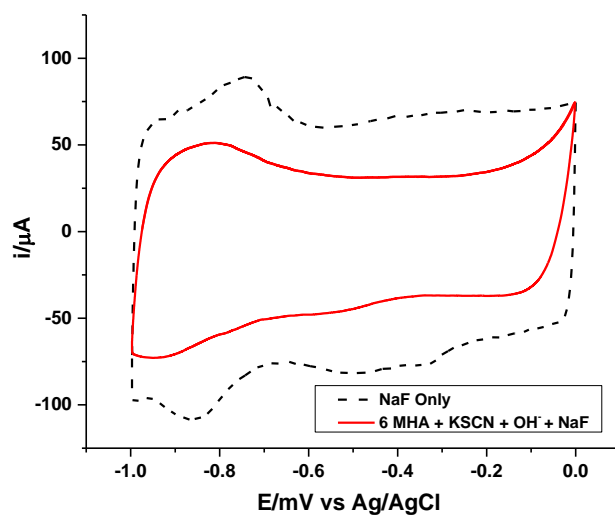
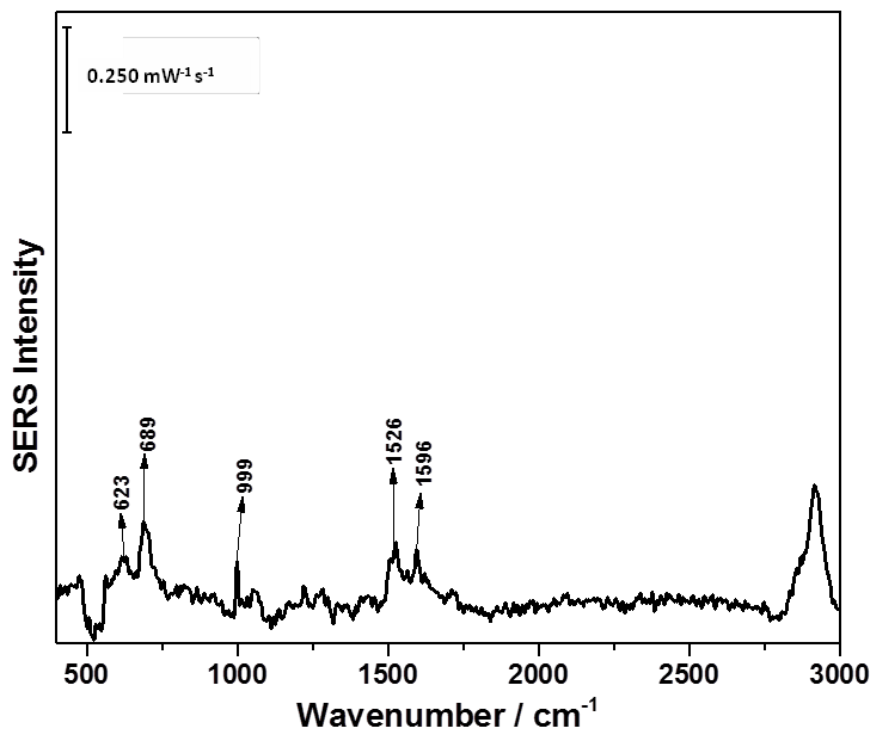**Figure A-235: OCP spectrum of 0.1M CaSO$_4$ solution in the presence of 6-MHA SAM**

Figure A-236: OCP spectrum of 0.1M NaCl solution in the presence of 6-MHA SAM
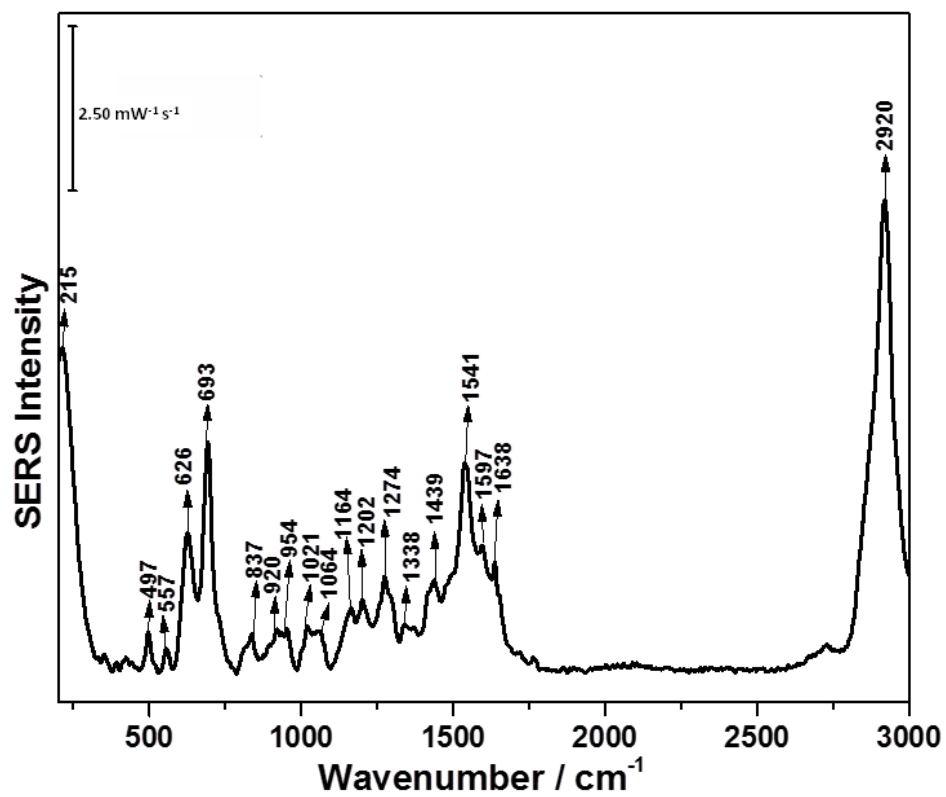
Figure A-237: a) OCP anodic and b) -1.0V cathodic spectra of 0.1 M NaF solution in the presence of 6-MHA SAM
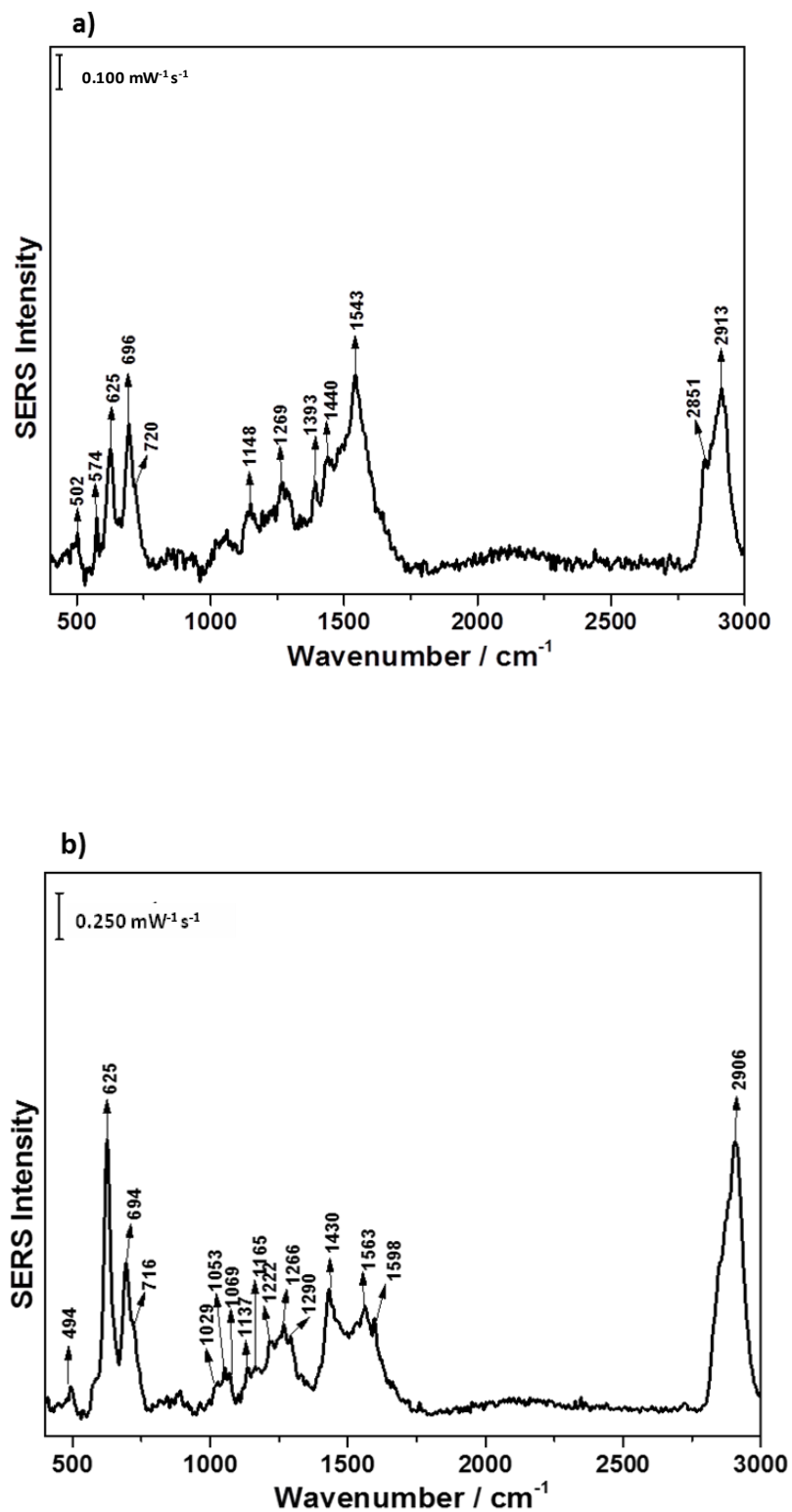
Figure A-238: a) OCP and b) anodic spectra of 0.1 M NaF solution in the presence of 6-MHA SAM